SIMULATION AND ASSESSMENT OF ENGINE KNOCK EVENTS

Von der Fakultät für Maschinenbau, Elektro- und Energiesysteme der Brandenburgischen Technischen Universität Cottbus-Senftenberg zur Erlangung des akademischen Grades eines Doktors der Ingenieurwissenschaften genehmigte Dissertation

vorgelegt von

Master of Science

Corinna Netzer

geboren am 23. Oktober 1987 in Freiburg im Breisgau

Vorsitzender: Prof. Dr.-Ing. Christoph Egbers
Gutachter: Prof. Dr.-Ing. Fabian Mauß
Gutachter: Prof. Dr. Fabio Bozza
Tag der mündlichen Prüfung: 29.04.2019

Abstract

Sophisticated engine knock modeling supports the optimization of the thermal efficiency of spark ignition engines. For this purpose the presented work introduces the resonance theory (Bradley and co-workers, 2002) for three-dimensional Reynolds-Averaged Navier-Stokes (RANS) and for the zero-dimensional Spark Ignition Stochastic Reactor Model (SI-SRM) simulations. Hereby, the auto-ignition in the unburnt gases is investigated directly instead of the resulting pressure fluctuations. Based on the detonation diagram auto-ignition events can be classified to be in acceptable deflagration regime or possibly turn to a harmful developing detonation.

Combustion is modeled using detailed chemistry and formulations for turbulent flame propagation. The use of detailed chemistry caters for the prediction of physical and chemical properties, such as the octane rating, C:H:O-ratio or dilution. For both models, the laminar flame speed is retrieved from surrogate specific look-up tables compiled using the reaction mechanism for Ethanol containing Toluene Reference Fuels by Seidel (2017). In the fresh gas zone, the scheme is used for auto-ignition prediction. For this purpose, the G-equation coupled with a Well-Stirred-Reactor model is applied in RANS. In analogy, in the SI-SRM the combustion is modeled using a two zone model with stochastic mixing between the particles.

RANS is used to develop the knock classification methodology and to analyze in detail location, size and shape of the auto-ignition kernels. RANS estimates the ensemble average of the process and therefore cannot reproduce a developing detonation. Hence, Large Eddy Simulation (LES) is used to verify the methodology. Studies using wide ranges of surrogates with different octane rating and cycle-to-cycle variations are carried out using the computationally efficient SI-SRM. Cyclic variations are predicted based on stochastic mixing, stochastic heat transfer to the wall, varying exhaust gas recirculation composition and imposed probability density functions for the inflammation time and the scaling of the mixing time retrieved from RANS.

The methodology is verified for spark timing and octane rating. It is shown that the surrogate

formulation has an important impact on knock prediction. RANS is suitable to predict the mean strength of auto-ignition in the unburnt gas if the thermodynamic and chemical state of the ignition kernel is analyzed instead of the pressure gradients. The probability of the transition to knocking combustion can be determined. Good agreement between RANS and SI-SRM are obtained. The combination of both tools gives insights of local effects using RANS and the distribution of auto-ignition in the whole pressure range of an operating point using SI-SRM with reasonable computationally cost for development purposes.

Kurzfassung

Detaillierte Klopfmodelle unterstützen den Entwicklungsprozess zur Optimierung des thermischen Wirkungsgrads von Ottomotoren. Die vorliegende Arbeit diskutiert einen neuen Ansatz zur Bewertung von motorischen Klopfen mittels der Resonanztheorie (Bradley und Kollegen, 2002) für die Nutzung in dreidimensionalen Reynolds-Averaged Navier-Stokes Simulationen (RANS) und im nulldimensionalen Spark Ignition Stochastic Reactor Model (SI-SRM). Hierbei wird, anstatt der resultierenden Druckwelle, die Selbstzündung in den unverbrannten Gasen direkt untersucht. Mit Hilfe des Detonationsdiagramms können Selbstzündungen klassifiziert und der mögliche Übergang zu einer schädlichen, sich aufbauenden Detonation (Klopfen) bestimmt werden.

Die vorgemischte Verbrennung wird mittels detaillierter Chemie modelliert. Diese ermöglicht die Vorhersage physikalischer und chemischer Prozesse abhängig von der Oktanzahl, dem C:H:O-Verhältniss oder der Verdünnung. Für beide Modelle wird die laminare Flammengeschwindigkeit aus Tabellen abgerufen, die unter Verwendung des Reaktionsmechanismus für Ethanol haltige Toluol-Referenzkraftstoffe (ETRF) von Seidel (2017) ersatzkraftstoffspezifisch erstellt werden. In den unverbrannten Gasen wir der Reaktionsmechanismus für die Simulation der Selbstzündung genutzt. Zu diesem Zweck wird in RANS die G-Gleichung mit dem Well-Stirred-Reactor (WSR) Modell gekoppelt. In Analogie wird im SI-SRM ein Zwei-Zonen-Modell mit stochastischer Mischung der Partikel verwendet.

RANS wird zur Entwicklung der Methodik zur Klopfbewertung und zur detaillierten Analyse von Position, Größe und Form der Zündungskerne verwendet. RANS liefert ensemblegemittelte Größen und kann daher eine entstehende Detonation nicht auflösen. Daher wird die Methodik mit Large Eddy Simulationen (LES) verifiziert. Für Studien, die verschiede Ersatzkraftstoffe oder zyklische Schwankungen untersuchen, wird das SI-SRM aufgrund der kurzen Rechenzeiten genutzt. Zyklische Schwankungen werden mittels stochastischen Mischens der virtuellen Partikeln, stochastischen Wärmeübergangs zur Wand, variierender Zusammensetzung der zurück geführten Abgase und vorgegeben Verteilungsfunktionen für Entflammung und Mischungszeit modelliert.

Die Methodik wurde hinsichtlich Zündzeitpunktes und Oktanzahl verifiziert. RANS ist geeignet, die mittlere Stärke der Selbstzündung im unverbrannten Gas vorherzusagen, wenn der thermodynamische und chemische Zustand des Zündkerns analysiert wird anstatt des Druckgradientens. Die Wahrscheinlichkeit des Übergangs zum motorischen Klopfen kann bestimmt werden. Die Ergebnisse von RANS und SI-SRM stimmen gut überein. Die Kombination beider Werkzeuge ermöglicht die Untersuchung lokaler Effekte (RANS) und die Verteilung der Selbstzündung über die gesamte Ausdehnung des maximalen Druckes eines Betriebspunktes (SI-SRM) mit vertretbarem rechnerischem Aufwand für den Einsatz in der Motorenentwicklung.

Authored and Co-Authored Peer Reviewed Publications

Introduction of the Methodology

Netzer, C., Seidel, L., Pasternak, M., Lehtiniemi, H., Perlman, C., Ravet, F., Mauss, F., Three-dimensional computational fluid dynamics engine knock prediction and evaluation based on detailed chemistry and detonation theory, *Int J Engine Res, 19(1):33-44*, 2018.

Netzer, C., Seidel, L., Pasternak, M., Klauer, C., Perlman, C., Ravet, F., Mauss, F., Engine Knock Prediction and Evaluation Based on Detonation Theory Using a Quasi-Dimensional Stochastic Reactor Model, *SAE Technical Paper 2017-01-0538*, 2017.

Seidel, L., Netzer, C., Hilbig, M., Mauss, F., Klauer, C., Pasternak, M., Matrisciano, M., Systematic Reduction of Detailed Chemical Reaction Mechanisms for Engine Applications, *J Eng Gas Turbines Power, 139(9):091701-091701-9*, 2017.

Netzer, C., Lehtiniemi, H., Seidel, L., Ravet, F., Mauss, F., Assessment of the Validity of RANS Knock Prediction, *Int J Engine Res*, 2019 – In Press, doi 10.1177/1468087419846032.

Netzer, C., Pasternak, M., Seidel, L., Ravet, F., Mauss, F., Computationally Efficient Prediction of Cycle-to-Cycle Variations in Spark Ignition Engines, *Int J Engine Res*, 2019 – In Press, doi 10.1177/1468087419856493.

Application and Further Analysis

Netzer, C., Franken, T., Seidel, L., Lehtiniemi, H., Kulzer, A., Mauss, F., Numerical Analysis of the Impact of Water Injection on Combustion and Thermodynamics in a Gasoline Engine using Detailed Chemistry, *SAE Int J Engines 11(6):1151-1166*, 2018.

Pasternak, M., Netzer, C., Mauss, F., Fischer, M., Sens, M. and Riess, M., Simulation of the effects of spark timing and external EGR on gasoline combustion under knock-limited operation at high speed and load. *In: Guenther, M. and Sens, M. (eds.): Knocking in Gasoline Engines, IAV Automotive Engineering, 121-142, Berlin (Book chapter)*, 2017.

Netzer, C., Seidel, L., Ravet, F., Mauss, F., Impact of the Surrogate Formulation on 3D CFD Engine Knock Prediction using Detailed Chemistry, *Fuel 254:115678*, 2019 - In Press, doi.org/10.1016/j.fuel.2019.115678.doi.

Franken, T., Netzer, C., F., Mauss, Pasternak, M., Seidel, L., Borg, A., Lehtiniemi, H., Matrisciano, A., Kulzer, A., Multi-objective Optimization of Water Injection in SI Engines using the Stochastic Reactor Model with Tabulated Chemistry, *Int J Engine Res*, 2019 – In Press, doi 10.1177/1468087419857602.

Contents

Abstract **1**

Kurzfassung **3**

Authored and Co-Authored Peer Reviewed Publications **5**

1 Introduction **9**

2 Combustion Processes in Spark Ignition Engines **12**
2.1 Turbulent Premixed Combustion 12
2.2 Laminar Flame Speed 13
2.3 Abnormal Combustion - Engine Knock 17
2.4 Engine Knock Detection 23
2.5 Resonance Theory and Detonation Diagram 24

3 Modeling of Turbulent Premixed Combustion Processes **30**
3.1 Conservation Equations 32
3.2 Turbulence Models 34
3.2.1 Reynolds-Averaged Navier-Stokes Simulation - RANS 36
3.2.2 Large Eddy Simulation - LES 39
3.3 Combustion Models 42
3.3.1 Laminar Flame Speed 44
3.3.2 Turbulent Flame Speed 45
3.3.3 The G-Equation Model 48
3.3.4 The Well Stirred Reactor Model 51
3.4 The Stochastic Reactor Model for SI Engines 52
3.4.1 Physical Model 53
3.4.2 Mixing Time and Model 55
3.4.3 Two Zone Approach 57
3.5 Model Choice and Interaction 59

4 Detailed Chemistry **61**
4.1 Kinetic Model . . . 62
4.2 Surrogate Formulation . . . 64
4.3 Laminar Flame Speed Tables . . . 67

5 Resonance Theory in Three-Dimensional Engine Simulations **71**
5.1 Methodology . . . 71
5.2 Sensitivity to Spark Timing . . . 73
5.3 Sensitivity to Octane Rating . . . 78
5.4 Verification of the RANS Methodology using LES . . . 84
5.5 Impact of the Surrogate Formulation . . . 95

6 Resonance Theory in Zero-Dimensional Engine Simulations **112**
6.1 Methodology . . . 112
6.2 Verification of the Methodology . . . 115
6.3 Analysis of Surrogates . . . 119
6.4 Analysis of Cycle-to-Cycle Variations . . . 125

7 Summary and Outlook **139**

Nomenclature **142**

Bibliography **146**

1 Introduction

Climate change and global warming are human made phenomena that need short term actions and engineering solutions. Traffic is one of the contributors to the global carbon dioxide (CO_2) emissions. The graphs in Figure 1.1 shows that the majority, with more than 95%, of the new licensed passenger cars in Europe in 2017 are using internal combustion engines burning Diesel (44.8 %), gasoline (49.4 %) and natural gas or Liquefied Petroleum Gas (LPG, 1.6 %). For heavy duty vehicles the percentage is even higher. Even if the production of electric vehicles will be doubled in the next years, a significant number of cars will be running on fossil fuels. This points out, how important it is to optimize the next sold internal combustion engine generation regarding their emissions, independent of their configuration as main propulsion or in a hybrid application.

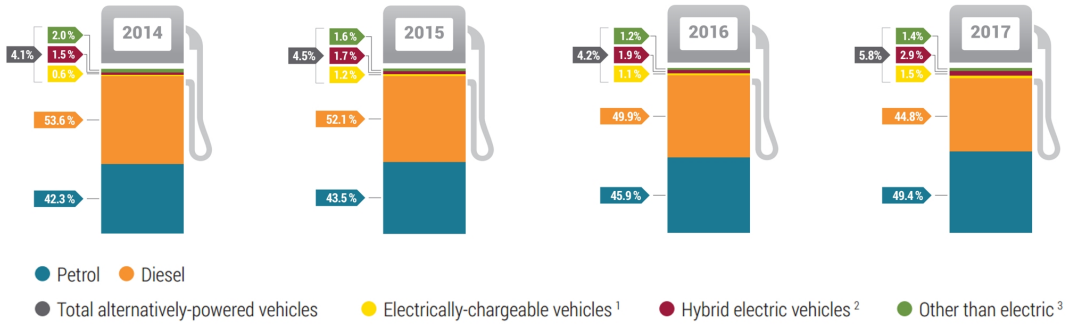

Figure 1.1: Sold new passenger cars in the European Union by fuel type. (1) inlcudes Battery Electric Vehicles (BEV), Extended-Range Electric Vehicles (EREV), Plug-in Hybrid Electric Vehicles (PHEV) and Fuel Cell Electric Vehicles (FCEV) (2) Includes full and mild hybrids (3) Includes Natural Gas Vehicles (NGV), LPG-fueled vehicles and ethanol (E85) vehicles. Figure reprinted from [1].

The products of incomplete combustion, such as carbon monoxide (CO), nitrogen oxidizes (NO_x), unburnt hydrocarbons (uHC) and particulate matter (PM), can be reduced applying catalytic after treatment and particle filter. The emission of CO_2 can be reduced by improving

the thermal efficiency of an internal combustion engine only, since it depends directly on the carbon amount of the injected fuel that is needed to generate the power. For Spark Ignition (SI) engines the development tends towards direct injection engines (Gasoline Direct injection or Direct Injection Spark Ignition) with increased compression ratios and higher boost pressure (downsizing in combination with downspeeding). An alternative is upsizing and the use of very high compression rations. Those methods lead to higher pressures and temperatures in the cylinder, which promote abnormal combustion (engine knock). Frequently occurring knock or super knock can destroy parts in the combustion cylinder. In modern SI engines, sensors control the occurrence of knocking combustion to the detriment of fuel efficiency. Being the main obstacle in making SI engines more efficient, engine knock is the focus of researchers and development engineers of SI engines.

Developing more sophisticated knock models supports the development process. The use of three-dimensional (3D) Computational Fluid Dynamics (CFD) is well established in automotive engineering to optimize flows or study heat transfer and combustion. Zero-dimensional (0D) models are typically used to investigate large parameter studies or applied embedded in full engine or car optimization tools. Detailed chemistry schemes are a key to predict combustion and to analyze fuel effects. In this work, a methodology based on detailed chemistry that consist of three-dimensional CFD and a stochastic zero-dimensional simulations is developed. In CFD, the location and the dimensions of a predicted auto-ignition can be analyzed in detailed. The zero-dimensional Spark Ignition Stochastic Reactor Model (SI-SRM) is used to analyze cycle-to-cycle variations (CCV) computationally efficient. For both models, a methodology to classify predicted auto-ignitions using the resonance theory by Bradley and colleagues [2, 3, 4, 5, 6, 7] is developed.

Within this work, all CFD simulations (Reynolds-Averaged Navier-Stokes simulations - RANS and Large Eddy Simulation - LES) are performed using Converge v2.2 - v2.4 [8]. The LOGEsoft package (LOGEreserach v.1.8 - v1.10 [9] and LOGEengine v2.0 - v3.0 [10]) is used for the calculation of freely propagating flames, constant volume or pressure reactor simulations, rapid compression machine simulations and zero-dimensional SI-SRM engine simulations. Results from engine experiments are provided by Renault [11], other experiments are reference in the text.

The thesis is structured as follows: Chapter 2 introduces the combustion process in SI engines. The laminar flame speed s_l and the octane rating are introduced as main characteristics of turbulent premixed flames and abnormal combustion modeling. Further, the resonance theory is reviewed and the detonation diagram introduced. Chapter 3 presents the three-dimensional

and zero-dimensional turbulence and combustion models. A comment on the model choice concludes this chapter. The discussion in chapter 4 on the applied detailed chemistry and the surrogate formulation complete the model approach. In chapter 5, the resonance theory for RANS is introduced and discussed. The first part of this chapter is based on Netzer et al. [12] and analyzes the sensitivity to spark timing and octane rating. The applicability of the approach is verified by comparing to LES (published in Netzer et al. [13]). Further, the importance of the surrogate formulation is argued (published in Netzer et al. [14]). Chapter 6 introduces the same methodology for the SI-SRM based on Netzer et al. [15]. Surrogate effects and stochastic cycle-to-cycle variations are investigated and discussed (published in Netzer et al. [16]). The chapter ends with a comparison of the results obtained with RANS and the SI-SRM. The different steps are illustrated in Figure 1.2.

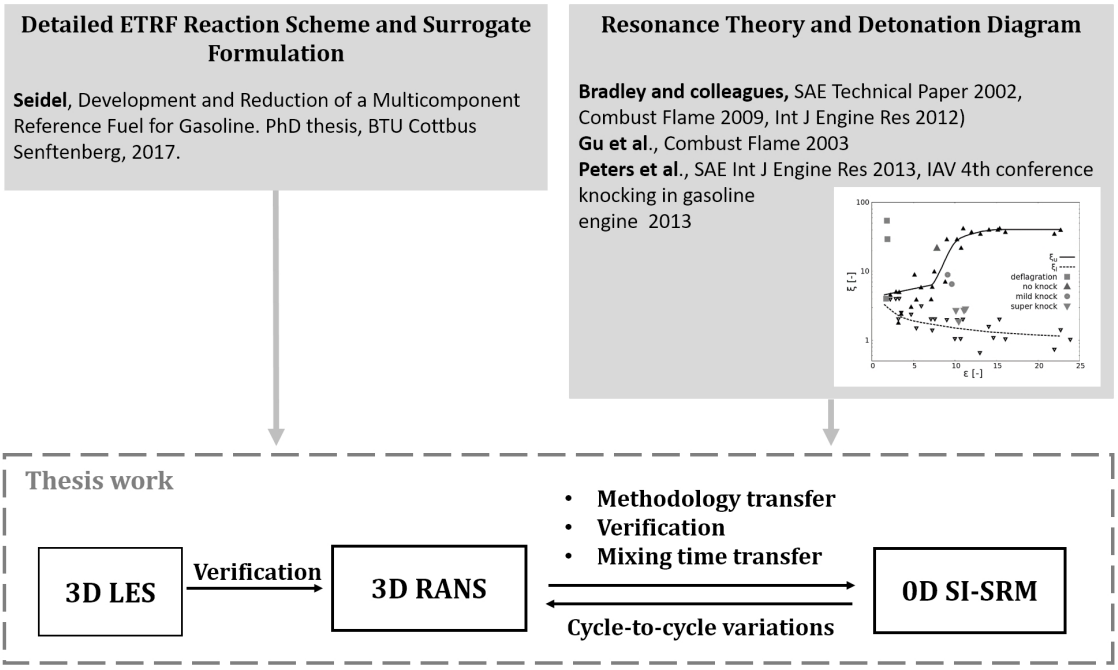

Figure 1.2: Illustration of the thesis.

2 Combustion Processes in Spark Ignition Engines

2.1 Turbulent Premixed Combustion

The SI engine is the prime example for turbulent premixed combustion, which is characterized by the complete mixing of fuel and oxidizer prior to combustion. This mixing takes place at temperatures that are low enough that low temperature chemistry is "frozen" or very slow and the ignition process is not induced, since the chain branching mechanism can not be initiated [17]. This premixed state is within the flammability limits metastable and a sufficient strong energy or heat source can initiate the combustion. After this external ignition, a flame front is propagating trough the premixed fuel/oxidizer-mixture. While the flame front travels trough the mixture, the burnt gases behind the flame front reach rapidly a state close to equilibrium, whereas the unburnt gases ahead of the flame front remain in the metastable state [17]. Therefore, premixed combustion is characterized by its two zones, often called the unburnt and burnt gases. These two zones coexists and are spatially separated by the flame front at which the transition from the unburnt to burnt gases happens.
In classical SI engines, the fuel is injected in the intake port or carburetor, where it mixes with air and is sucked as a mixture into the combustion chamber. In modern concepts, the fuel is injected directly in the cylinder during the inlet valve closure. With both injection strategies the fuel, air and residual gases form a rather homogeneous mixture latest at about 40 to 20 crank angle degree (°CA) before top dead center (TDC) [17]. Close to TDC, optimized to obtain the maximum torque, the charge is ignited via a spark plug, which gives SI engines its name. The energy source forms first a small laminar flame kernel, which turns very rapidly into a turbulent flame front. The flame front travels then from the spark plug spherically trough the cylinder. Figure 2.1 shows Schlieren photographs of a spark ignition process of a gasoline/air mixture. At 40 μs the ignition kernel appears laminar, whereas at 1800 μs the flame front is fully turbulent. The speed of the traveling flame front through the premixed charge is a dominating quantity in premixed combustion. Even though, the flame front propagates turbulent, the characteristic property that is used to describe the flame propagation velocity of a specific fuel is the lam-

inar flame speed (discussed in section 2.2). This is because changes in laminar flame speed are carried through to the regime of turbulent flame propagation [18]. Experimental results of turbulent flame speed measurements show that the turbulent flame speed s_t can be correlated to the laminar flame speed s_l, as for example in [18]. The authors obtain the turbulent flame speed s_t using the strain rate χ and the Karlovitz factor that includes dependencies on the turbulent Reynolds number Re_t and the laminar flame speed s_l. In general, it is found that [19]:

$$\frac{s_t}{s_l} = f(u', l_t, \phi) \tag{2.1}$$

where u' is the fluctuation of the turbulent velocity and l_t is the turbulent length scale.
Since the unburnt zone remains in the ignitable metastable state, it is very likely that trough any change of that state an auto-ignition occurs locally. This ignition can be initiated by: a hot wall, changes of the thermodynamic state, due to the compression of the unburnt zone by the flame propagation or the moving piston, local inhomogeneity of the mixture or residuals with different auto-ignition behavior such as oil droplets. This phenomena is called abnormal combustion and discussed in section 2.3.

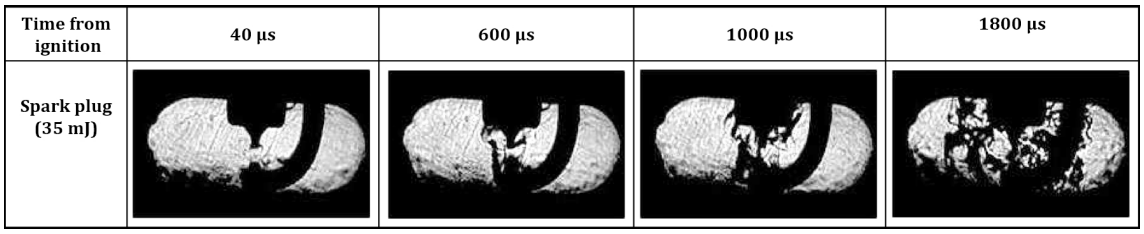

Figure 2.1: Schlieren photographs of the early stage of an ignition by a spark plug and the subsequent flame propagation in an engine operated with a stoichiometric mixture of gasoline and air [20].

2.2 Laminar Flame Speed

"The most important quantity in premixed combustion is the velocity at which the flame front propagates normal to itself and relative to the flow into the unburnt mixture." - Peters, 2000, p. 69 [17] This velocity is the laminar flame speed s_l. In literature also called the flame velocity, burning velocity or normal combustion velocity [21].
Different theories have been developed to describe and quantify this property. They are subdivided in thermal, diffusion and comprehensive theories. Thermal theories are based on the concept of Mallard and LeChatelier [22], (described in [21]), who stated that the heat transfer from the flame front into the unburnt gas layers is the controlling mechanism of flame propagation. Figure 2.2 shows the temperature profile of an one-dimensional idealized premixed flame. Over the flame coordinate the temperature is rising from the temperature in the unburnt

zone T_u approximately linear until it reaches the adiabatic flame temperature T_f. Simultaneously, the fuel is consumed until the equilibrium composition is reached in the burnt gases. The flame front is characterized by high reaction rates $\dot{\omega}$. According to Mallard and LeChatelier, the flame is divided into two regions: the burning region (zone I) with the flame thickness δ and the conduction region (zone II) in which the unburnt gases are heated up. An enthalpy balance can be used to derive an equation for the flame speed using the mass flow rate $\dot{m}$ of the unburnt gas into the combustion wave, and the ignition temperature T_i [21]:

$$\dot{m}c_p(T_i - T_0) = \lambda \frac{(T_f - T_i)}{\delta} A \tag{2.2}$$

The mass flow rate in a tube is given by $\dot{m} = \rho_u A u_u$. The velocity of the flame front consuming the unburnt mass can only be as fast as the mass flowing into the combustion wave, so that by definition $s_l = u_u$. Introducing those two terms in the enthalpy balance, the surface A drops and for the laminar flame speed s_l follows:

$$s_l = \left[\frac{\lambda}{\rho_u c_p} \frac{(T_f - T_i)}{(T_i - T_0)} \frac{1}{\delta} \right] \tag{2.3}$$

Assuming complete combustion (stoichiometric conditions), the mass that enters the combustion wave with s_l needs to be burnt within the flame with the thickness δ. Therefore, s_l and δ are related to the reaction rate $\dot{\omega}$:

$$\rho s_l = \dot{\omega}\delta \tag{2.4}$$

In other words, the faster $\dot{\omega}$, the thinner is the reaction zone. Eliminating the flame thickness δ with this relation yields a quadratic equation for the laminar flame speed [21]:

$$s_l = \left[\frac{\lambda}{\rho_u c_p} \frac{(T_f - T_i)}{(T_i - T_0)} \frac{\dot{\omega}}{\rho_u} \right]^{\frac{1}{2}} \tag{2.5}$$

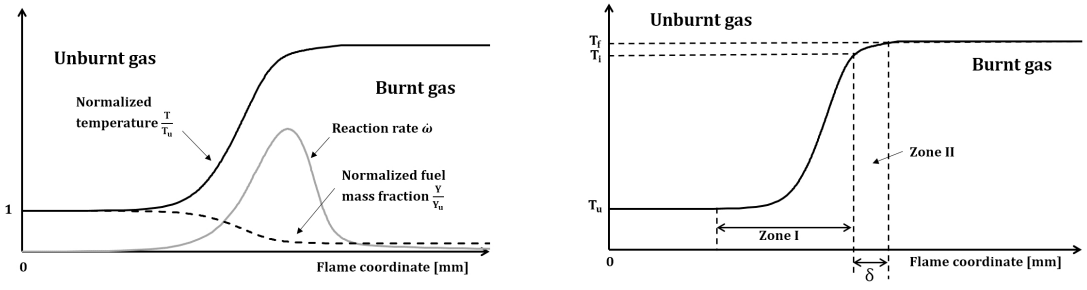

(a) One-dimensional flame.

(b) Flame thickness.

Figure 2.2: Schematically illustration of an one-dimensional premixed flame and the zones in the theory of Mallard and LeChatelier. Graph based on figures in [23].

Analyzing equation (2.5), it follows that the laminar flame speed is increasing with reaction rate $\dot{\omega}$ and with thermal conductivity $\alpha = \lambda/(\rho_u c_p)$ of the unburnt gases since the preheated zone gets smaller. The reaction rates depend on the available oxidizer, so that s_l, T_i and T_f depend on the air-fuel equivalence ratio ϕ. Therefore, s_l is limited by the fuel lean and fuel rich limit. The flammability limit is typically in the range of $0.5 < \phi < 1.5$ [17]. At the flammability limits T_i and T_f converge, so that s_l turns to zero. The real lean flammability limit is, compared to the theoretic, at slightly higher equivalence ratios due to radiation losses. The fuel rich flammability limit is extended to higher equivalence ratios by pyrolysis. The maximum laminar flame speed (Figure 2.3 (a) and (b)) occurs, as well as the maximum adiabatic flame temperature T_f for slightly rich mixtures $1.0 < \phi < 1.1$, because of the higher carbon monoxide (CO) level present at those conditions. Equation (2.5) shows further that s_l is increasing with the unburnt temperature T_u, which is in the numerator. In case $T_u \geq T_i$, the mixture is exploding. There is no flame speed defined since the mixture ignites homogeneously, however the flame speed of an apparent flame front grows rapidly. The dependency on T_u is shown exemplary for gasoline in Figure 2.3 (c).

Later the theory by Mallard and LeChatelier was extended by the diffusion of molecules by Zeldovich and Frank-Kamenetskii, while the diffusion of free radicals and atoms have still be neglected [21]. This was overcome by Lewis and von Elbe who found that reactions are not only affected by heat, but also radicals [21]. Low-atomic, light molecules can diffuse into the flame and reinforce reactions. However, the diffusion terms are connected by the governing equations for mass and temperature. It holds, that the higher the unburnt temperature, the higher is the final temperature and the higher is the reaction rate and flame velocity. While the higher the temperature, the more effective are dissociation reactions, the greater is the amount of radicals that diffuse back. This sequence also ends up with a faster flame velocity [21]. Hirschfelder concluded that thermal effects dominate, but diffusion of all species must be respected in flame speed formulations and predictions [21].

Peters and co-workers [24, 25] identified using an asymptotic analysis three different layers, namely the fuel consumption or inner layer, the H_2-, CO-non-equilibrium layer and the H_2-, CO-oxidation layer. The inner layer is smaller than the H_2-, CO-oxidation layer and has a characteristic temperature. This temperature is a function of three kinetic rates only and pressure, but not of the preheated zone.

Figure 2.3 (b) and (d) show the pressure dependency of s_l. At lower pressures the main chain branching reaction is [26]:

$$H + O_2 \rightleftarrows OH + O$$

and at high pressures the following reaction sequence [26]:

$$HO_2 + HO_2 \rightleftarrows H_2O_2 + O_2$$

$$H_2O_2 + M \rightleftarrows OH + OH + M$$

The dominating chain termination reaction is at both pressure levels [26]:

$$H + O_2 + M \rightleftarrows HO_2 + M$$

This termination step is weak at low pressures, the chain branching reactions dominate the flame propagation and s_l is the highest. With increasing pressure, the chain termination reaction gets faster, $\dot{\omega}$ and s_l slower, until chain branching and termination reaction are neutral at very high pressures. The temperature and pressure dependency can be expressed by [23]:

$$s_l(p,T) = s_l(p_0,T_0)\left(\frac{p}{p_0}\right)^{\alpha_p}\left(\frac{T}{T_0}\right)^{\alpha_T} \tag{2.6}$$

where p_0 and T_0 are reference pressure and temperature respectively and the exponents $\alpha_p < 0$ and $\alpha_T > 1$.

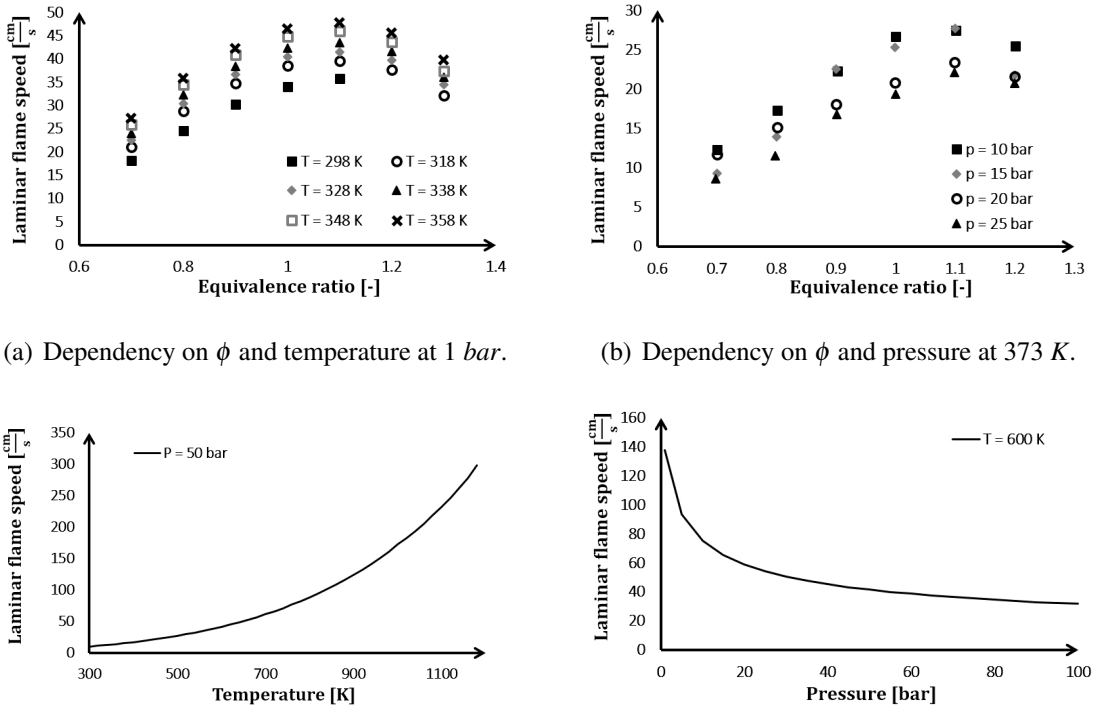

(a) Dependency on ϕ and temperature at 1 *bar*.

(b) Dependency on ϕ and pressure at 373 *K*.

(c) Temperature dependency at 50 *bar* and $\phi = 1$.

(d) Pressure dependency at 600 *K* and $\phi = 1$.

Figure 2.3: Laminar flame speed dependency on equivalence ratio ϕ, unburnt temperature T_u and pressure p. (a) Flat flame adiabatic burner measurements for gasoline in air [27]. (b) Spherically expanding flame measurements for gasoline in air [28]. (c) and (d) Predicted laminar flame speeds for *iso*-octane in air using the laminar flame speed skeletal scheme from Seidel [29].

Since the laminar flame speed affects directly the turbulent flame propagation, there is also direct proportionality to engine performance: a fuel with higher s_l leads to a faster combustion. A faster burning fuel is desirable because the whole torque curve can be shifted to higher torque and earlier spark timings [30]. Cracknell et al. [30] carried out engine measurements using commercial gasoline (RON 95) mixed with 20 *vol%* of paraffins, olefins and aromatics that increase the laminar flame speed of the base gasoline. In those experiments the spark timing was fixed, so that all gain in performance are found to be solely due to the change of s_l. They found that a faster laminar flame speed correlates well with increased performance. The modified faster burning fuels showed a gain of 3% in engine performance compared to the commercial gasoline with lower laminar flame speed.

2.3 Abnormal Combustion - Engine Knock

The flame propagating due to the ignition with an external source is called normal combustion. An undesired auto-ignition of the unburnt zone prior or after that controlled ignition is called abnormal combustion. The reason of this uncontrolled ignition can be very different: local conditions such as increased temperature and pressure or inhomogeneity of the mixture can lead to auto-ignition of the charge due to the promotion of chain branching reactions. It is also likely that the unburnt charge is ignited at hot surfaces such as the valves and the electrode of the spark plug or due to deposits with a higher tendency to auto-ignite. An overview of the different phenomena is given in Figure 2.4. Those local spontaneous auto-ignitions have the potential to grow to a second very rapid flame front that interferes the main flame propagation or to result in local very high temperatures and pressure gradients. Those high pressure gradients can lead to detonation waves traveling across the cylinder which can be seen as pressure fluctuations in measurements (Figure 2.6). Those pressure waves are accompanied by a metallic noise, which gives the phenomena its name [31]: engine knock or knocking combustion. Beside the unwanted noise, long term exposure to knock or occurrence of super knock damage cylinder and piston parts (Figure 2.5) and therefore needs to be avoided.

Those auto-ignitions are difficult to control since they depend on combustion chamber design and engine operating conditions [31, 33, 34]. The appearance of this irregular combustion phenomenon is a direct consequence of too high temperatures and pressures in the unburnt gases. In general, an increasing knock tendency with load and compression ratio and a decreasing tendency with charge cooling and cylinder wall cooling is observed. Long combustion duration, e.g. caused by low engine speeds or cylinder geometry, can promote auto-ignition [34]. This limits the range of operating conditions and therefore the efficiency of spark ignited engines. Future concepts of internal combustion engine design and operating conditions are targeted to enhance fuel efficiency and reduce pollutant emissions. The efficiency improvement of modern

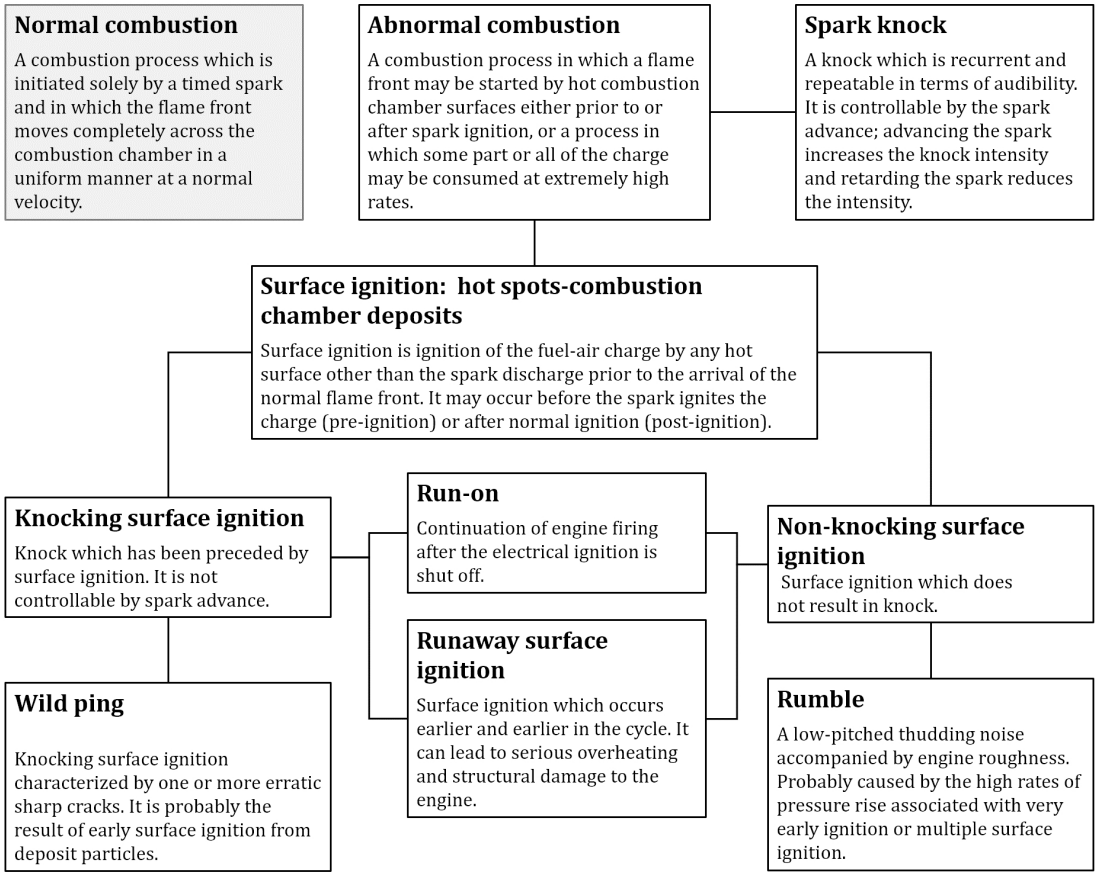

Figure 2.4: Definitions of normal and abnormal combustion phenomena in SI engines according to [31].

Figure 2.5: Damaged cylinder parts due to super knock [32].

(turbocharged) SI engines is an ongoing effort. Downsizing of the SI engine yields the reduction of fuel consumption at a constant power level. Examples of methods to increase the engine efficiency are the use of the Miller cycle, cylinder deactivation, friction and weight reduction [35]. In addition to these technologies, the operation of the SI engine with higher boost levels and higher compression ratios is investigated [36]. Both strategies result in a significant increase in

cylinder gas temperature and hence higher knock or pre-ignition tendency. Summarizing, one of the main challenges in SI engine development is that the targeted operating conditions prone engine knock (Figure 2.6 (b)).

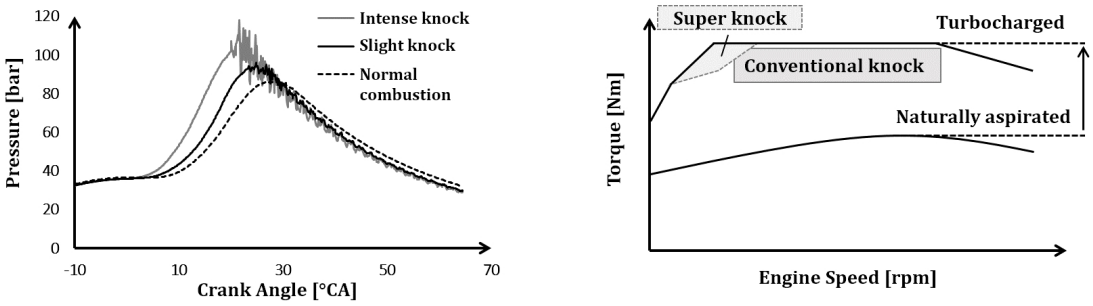

(a) Cylinder pressure for normal combustion, slight and intense knock.

(b) Regions of knock and super knock in the engine map.

Figure 2.6: Characteristic pressure traces and operating conditions of knock occurrence. Figure according to [32].

However, in modern SI engines knock sensors are used to control "spark knock", which is controllable by the ignition timing. In case knock is detected, the spark timing is delayed since this reduces temperatures and pressures in the unburnt gas. This enables to safely operate close at the Knock Limit Spark Advance (KLSA), but results in lower torque for a given amount of fuel [37]. Therefore, the trade-off of fuel efficiency and avoiding knocking combustion is one of the key issues in SI engine development. To enable the safe operation at high load, the air/fuel-mixture is enriched to cool the cylinder gas. However, this second injection and delaying the spark timing increase fuel consumption and exhaust out emissions. To reduce the cylinder gas temperature and knock tendency without additionally injected fuel, strategies such as two-stage turbocharger with intercooler, external cooled exhaust gas recirculation (EGR) and water injection are investigated and used [36, 38].

Beside operating mode and engine design, the fuel properties have a major impact on engine knock [31, 33, 34]. The fuels' resistance to auto-ignition is characterized by its octane rating. The octane rating relates the tested commercial fuel against a mixture of *iso*-octane and *n*-heptane, called Primary Reference Fuel (PRF). Depending on the test conditions, given in Table 2.2, the Research Octane Number (RON) or Motored Octane Number (MON) are found. RON and MON are defined as the *iso*-octane volume fraction of the PRF that leads to the same knock reading as the tested fuel. By definition is:

$$RON_{iso\text{-}octane} = MON_{iso\text{-}octane} = 100$$
$$RON_{n\text{-}heptane} = MON_{n\text{-}heptane} = 0.$$

RON and MON are determined using a Cooperative Fuel Research (CFR) engine, which is a standardized single-cylinder test motor (Table 2.1), following a test procedure that is defined in ASTM D2699 / D2700 and EN ISO 5163 / 5164 [31, 34]: First, the compression ratio (CR) of the CFR engine operated with the tested gasoline fuel is increased until engine knock occurs. Then, the air number λ is set so that maximum knock intensity occurs. Subsequently, the test engine is operated with the PRF. The *iso*-octane content is varied until the same knock reading as during operation with the tested gasoline fuel is found.

Table 2.1: Cooperative Fuel Research (CFR) engine geometry and valve timing for the RON and MON test [39].

Bore	82.6 mm
Stroke	114.3 mm
Connecting rod length	265.2 mm
Displacement	611.7 cm^3
Inlet valve opening (IVO)	350°CA bTDC
Inlet valve closing (IVC)	146°CA bTDC
Exhaust valve opening (EVO)	140°CA aTDC
Exhaust valve closing (EVC)	375°CA aTDC

Table 2.2: Test conditions for the octane rating tests [31, 34, 40].

	RON	**MON**
Engine speed	600 rpm	900 rpm
Compression ratio (CR)	4 - 10	4 - 10
Ignition angle	13°CA bTDC	varies with CR 26°CA bTDC for CR = 4 14°CA bTDC for CR = 10
Mixture preheating	none	149°C
Intake air temperature	52°C	25°C
Air-fuel equivalence ratio	adjusted for maximum knock intensity	adjusted for maximum knock intensity
Measurement accuracy	± 1 %	± 1 %

By definition the RON and MON of a PRF are the same, but commercial gasolines have higher RON than MON. The difference of the commercial fuel compared to the PRF is given by the fuel sensitivity *S*:

$$S = RON - MON \tag{2.7}$$

The reason for this difference is the pronounced negative temperature coefficient (NTC) region of alkanes. The PRF species *iso*-octane and *n*-heptane have this NTC region whereas it does not or only little appears for other components of commercial gasoline such as *cyclo*-alkanes, olefins and aromatics. As a result, *iso*- and *n*-alkanes are more resistant against auto-ignition under MON conditions, which results in higher MON for the PRF as for the commercial gasoline . To respect this discrepancy, the combination of RON and MON to the anti-knock index *AKI* is used [41]:

$$AKI = \frac{1}{2}(RON + MON) \tag{2.8}$$

In modern direct injection spark ignition engines (DISI, manufactured after 1990) and under modern operating conditions, such as downsizing and turbo-charging, valve overlapping and charge cooling, the temperatures of the unburnt zone are today 100 K below the RON test conditions and 250 K below the MON conditions for a given end gas pressure under knocking conditions. However, those numbers depend on the boosting level, scavenging and charge cooling [37]. Therefore, the knock tendency prediction moves away from MON. RON gets more dominating whereas the auto-ignition tendency is lower than in the CFR engine [37, 42]. To reflect the impact of the operating conditions on the knock probability, the octane index (OI) using the *K*-factor was developed [42, 43]:

$$OI = RON - K(RON - MON) \tag{2.9}$$

K depends on engine and operating conditions and needs therefore to be determined empirically for each engine [42]. In experiments, the KLSA for different fuels with different octane sensitivity is determined and K correlated. For modern engines, K is mostly negative, which leads to $OI > RON$, or to small positive values $K < 0.2$ [43]. Higher speeds lead to an increase of K, hence the MON contribution to OI increases with speed [42]. This conclusion is also drawn form Yates et al. [40]. They compared expected ignition delay times (predicted using chemistry models) against predicted KLSA for different engine types and operating modes (Figure 2.7). They concluded that for engines equipped with a carburetor, common for the decade when RON and MON test have been established, the RON value for low speed and the MON value for high speed operation, agree well with the knocking tendency found in the engine. Whereas for modern engine concepts, the RON values is the more reliable measure, but overestimates the knock tendency since the threshold beyond RON with $K < 0$ is entered.

The octane rating plays an important role for increasing fuel efficiency, therefore gasoline fuels are further investigated and optimized. From equation 2.9 follows, assuming $K < 0$ (for DISI engines as discussed above), that fuels with a given RON, but small MON and high fuel sensitivity respectively, are more resistant to auto-ignition than fuels with higher MON and low sensitivity and could be aimed in future fuel optimization. Prakash et al. [37] investigated

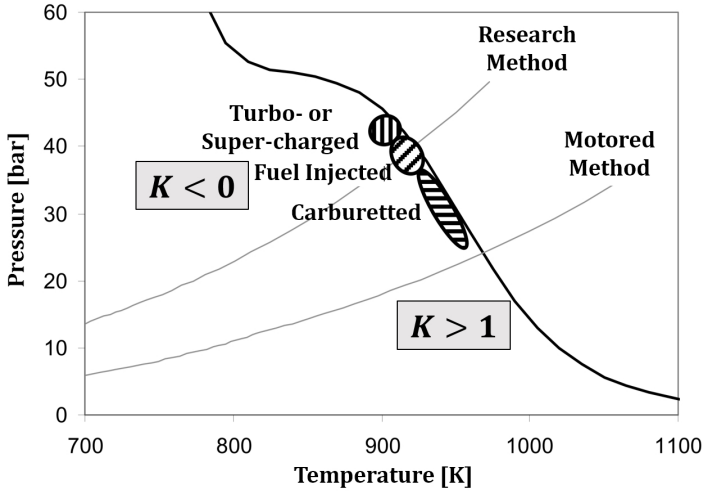

Figure 2.7: Zones of auto-ignition for different SI engine types and operating conditions. Black solid line is the predicted ignition delay time for a commercial gasoline with a octane sensitivity of S=10 [40]. K value ranges added from [44].

different fuels with same RON, but different fuel sensitivities in the range from 5 to 15 in a DISI engine regarding their impact on efficiency η. Hereby, the efficiency has been calculated from the lower heating value and the indicated specific fuel consumption. The authors found that a fuel sensitivity increase of 10 points, leads to an efficiency increase of 1.9 - 3.9 % at a compression ratio of 11.5 and RON=92. This impact is weaker for fuels with higher octane rating (RON=98). A test increasing the RON, but fixing MON, showed an efficiency increase of 3.6 - 5.3 %. The authors found that the knock resistance with increased fuel sensitivity is higher than expected from the RON and MON test. Further, both octane sensitivity and RON improve the efficiency, whereas RON has a larger impact. A combination of both results in earlier combustion phasing and lower exhaust temperatures. The authors state, that in future the optimization of both properties could increase the fuel efficiency. Other methods to improve the knock resistance is adding organometallic additives or components with $RON > 100$. The organometallic compounds decompose at high pressure and high temperature where the metal vapor is acting as a reaction-inhibiting catalyst during the ignition delay because of its high surface area [34]. Ethanol is added depending on country up to 25 $vol\%$ because of its high RON ($RON = 109$), but also since it can be carbon dioxide (CO_2) neutral produced from biomass [45]. In modern concepts engines and fuels are optimized together [46].

2.4 Engine Knock Detection

In the original RON and MON test, the knock event is detected using a bouncing pin (changed today). Opposite to modern knock sensor, that use the pressure fluctuations or vibrations for knock detection, a bouncing pin detects the rise in combustion rate prior the onset of the pressure fluctuations. This detection of changes in the burn rate is only applicable for the rather low speeds in ON tests and are a rather rough detection of heavy knock events. The detection of small changes in the auto-ignition strength and an operation close to the KLSA, where non-knocking auto-ignitions and mild knock needs to be detected, as it is needed and applied today, is not possible [40]. According to Yates et al. [40] this is an additional reason, why RON and MON overestimates the knock tendency in modern SI engines.

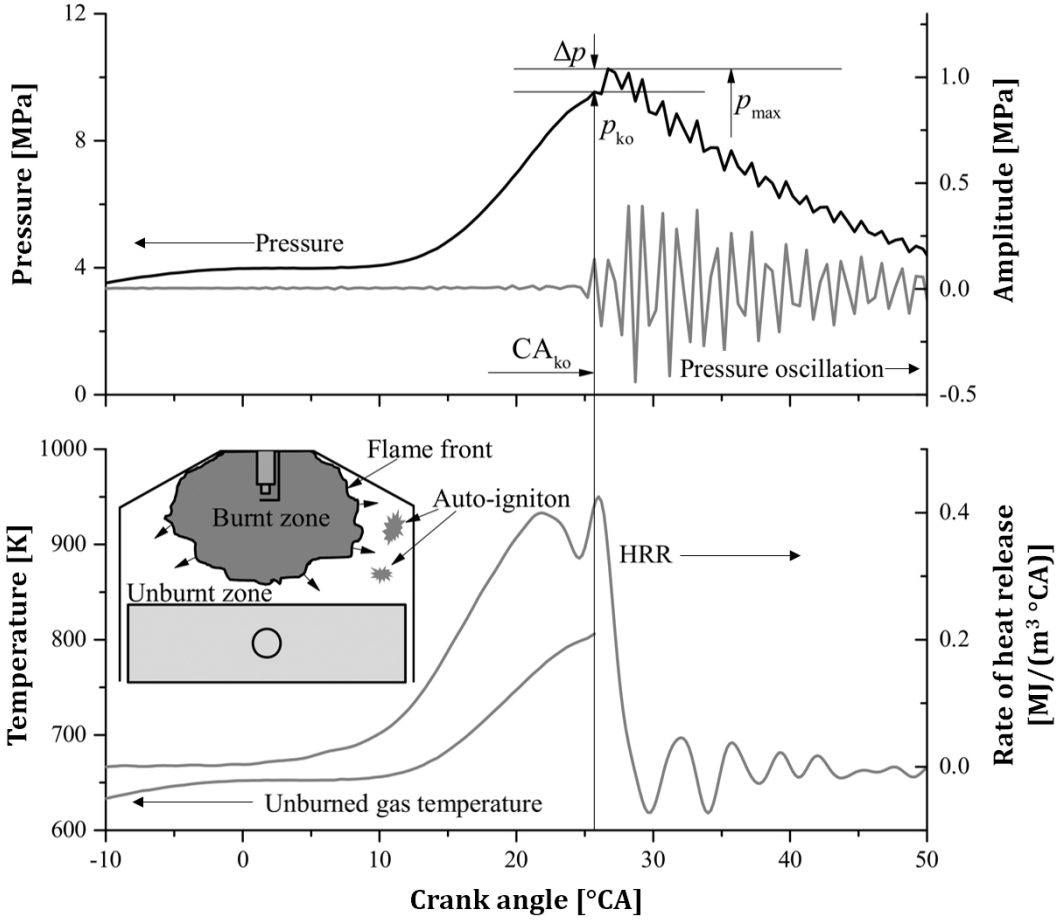

Figure 2.8: Combustion characteristics that can be used to identify knocking combustion [47].

However, in engine development and simulations it is not only important to detect knock as it is done on board, but also to investigate and quantify the strength of auto-ignitions, since not every auto-ignition leads to engine knock [34]. A key issue is to estimate the transition from

harmless deflagration to knocking combustion. In literature, several indexes are proposed to evaluate the strength of auto-ignitions [48]. Typically, they are developed based on experimental pressure traces using the gradient of the in-cylinder pressure or the filtered pressure signal [48, 49]. A variety of knock indexes are available, for example, the Maximum Amplitude of Pressure Oscillations (MAPO) [50] or the Integrated Modulus of Pressure Oscillations (IMPO) and their further development and combination to dimensionless indexes as the Logarithmic Knock Intensity (LKI) [51] and the Dimensionless Knock Indicator (DKI) [52]. Using these indexes, it is possible to determine the onset and to quantify the intensity of knock and the KLSA [48]. These indexes are especially usable for engine test benches and are adopted in engine simulations. Nevertheless, reference values need to be determined during calibration procedures. Those values are potentially dependent on the engine parameters and operating conditions, why they are not directly transferable to other engines. Nowadays, the aim of engine simulations is to support the engine development and the analysis of experiments. The analysis of auto-ignitions in simulations is not limited to the investigation of the resulting pressure wave, which follows an auto-ignition event. Rather, the origin of the pressure wave, namely, the ignition hotspot, and the strength of this ignition can be investigated and quantified.

Researchers are working owing to these advantages on knock indexes and knock probability prediction especially for simulations. First, global combustion parameters such as the pressure trace [53], the mass fraction of burned fuel [54] or the rate of heat release [55, 56] are used to determine knock onset or knock criteria. The typical appearance of those global parameters are for a knocking cycle shown in Figure 2.8. Second, the analysis is extended to include local effects such as local pressure gradients and the local rate of heat transfer to the walls due to an auto-ignition in the end gas [57]. It is concluded that the local auto-ignition event needs to be analyzed in detail, since not every auto-ignition event will lead to engine knock. One of the key issues is therefore to determine the combustion regime of the auto-ignition kernel as described by Zeldovich [58]. This analysis became available through the work and development of the detonation diagram by Bradley and colleagues [2, 4, 5], Gu et al. [3] and Peters et al. [6, 7]. This methodology enables to evaluate the knock intensity based on chemical and physical processes without any calibration or dependencies on the engine operating conditions and is discussed in detail in the following section.

2.5 Resonance Theory and Detonation Diagram

Bradley and co-workers [2, 3], developed the “detonation diagram”, in which the conditions for the occurrence of developing detonation beside other flame regimes are defined using two dimensionless parameters: the resonance parameter ξ and the reactivity parameter ε.

The resonance parameter ξ determines the mode of the propagating flame following an auto-ignition based on the regime classification by Zeldovich [58]. The reactivity parameter ε includes the initial radius of the hotspot r_0 and is a measure for the hotspot reactivity.

In an ideally, uniform, fully homogeneous air/fuel mixture the reaction rates are the same over the whole mixture. Once the ignition delay time τ is overcome, the whole mixture ignites everywhere at the same time. The pressure rise resulting from such an auto-ignition is rapid and uniform. There are no pressure pulses or spatial gradients. The regime following those characteristics is called thermal explosion [2]. However, in SI engines, there is no such fully homogeneous mixture. Temperature gradients appear due to charge stratification, at the cylinder walls or incomplete mixing with residual gases. Therefore, local hotspots appear in the charge of a SI engine. Those hotspots are local regions with increased temperature or increased concentration of a reactive species. Hence, those hotspots have an enhanced chemical reactivity. If the reaction rates are high enough, a hotspot can auto-ignite with the flame front developing out of this hotspot or ignition kernel with radius r into the surrounding mixture. It is important to note, that the flame propagates into a mixture, in which the ignition delay time τ increases with increasing distance from the hotspot [2]. Such an auto-ignition imposes an additional gas velocity u_a relative to the surrounding unburnt mixture [3]. This imposed velocity u_a is inverse relative to the ignition delay time τ [3]:

$$u_a = \left(\frac{\partial \tau}{\partial r} \right)^{-1} \tag{2.10}$$

Since the flame propagates from a region with shorter ignition delay time into a mixture with lower temperatures and accordingly longer ignition delay times, the velocity u_a can be expressed as function of this temperature gradient $(\partial T_0/\partial r)$ [3]:

$$u_a = \left(\frac{\partial \tau}{\partial T_0} \frac{\partial T_0}{\partial r} \right)^{-1} \tag{2.11}$$

Following Zeldovich [58], such an auto-ignition event is in the spontaneous regime and if the gradient $(\partial T_0/\partial r)$ reaches the critical value $(\partial T_0/\partial r)_c$, a developing detonation occurs, because such an auto-ignition and the accompanying heat release generate a pressure wave. If the temperature gradient is at its critical value $(\partial T_0/\partial r)_c$, the imposed velocity u_a equals the speed of sound a. In this scenario, the two waves combine, reinforce and propagate together at high velocity, release pressure spikes and result in a developing detonation [2, 58, 59]. This incident is called resonance and yield by [3]:

$$u_a = \left(\frac{\partial \tau}{\partial T_0} \right)^{-1} \left[\left(\frac{\partial T_0}{\partial r} \right)_c \right]^{-1} = a \tag{2.12}$$

From this balance the critical temperature gradient $(\partial T_0/\partial r)_c$ can be found [3]:

$$\left(\frac{\partial T_0}{\partial r}\right)_c = \frac{1}{a}\left(\frac{\partial \tau}{\partial T_0}\right)^{-1} \tag{2.13}$$

The actual temperature gradient can be normalized and the resonance parameter ξ be defined [2, 3]:

$$\xi = \left(\frac{\partial T_0}{\partial r}\right)\left(\frac{\partial T_0}{\partial r}\right)_c^{-1} = \frac{a}{u_a} \tag{2.14}$$

$(\partial T_0/\partial r)_c$ is hereby the boundary condition for the resonance of the two wave with $\xi = 1$. Especially, for longer ignition delay times and slower flame propagation, the surrounding of the early flame kernel might change its state due to diffusion, thermal conduction and chemical processes. Therefore, the developing detonation regime is not only limited to $\xi = 1$, but to a certain range around. Gu et al. [3] introduced the lower ξ_l and upper ξ_u limit for the reactivity parameter ξ. $\xi = 0$ corresponds to a thermal explosion. If the auto-ignition wave is running ahead of the sound wave, there is no link between the wave, the gas velocity u_a can propagate unrestricted. This corresponds to the range $0 < \xi < \xi_l$. For values $\xi > \xi_u$, u_a is rather small and cannot compete with the speed of sound. In case the gas velocity u_a is smaller than the laminar burning velocity s_l, the flame propagation is driven by molecular transport, s_l dominates. The flame is in subsonic deflagration mode. The regimes after Bradley and co-workers [2, 3] are given in Table 2.3 .

Table 2.3: Combustion modes following Bradley and co-workers [2, 3].

Range of ξ			**Regime**
	ξ	$= 0$	thermal explosion
$0 <$	ξ	$< \xi_l$	supersonic auto-ignitive wave ahead of acoustic wave
$\xi_l \leq$	ξ	$< \xi_u$	developing and developed detonation
$\xi_l \leq$	ξ	$< \frac{a}{s_l}$	subsonic auto-ignitive deflagration
	ξ	$\geq \frac{a}{s_l}$	laminar burning deflagration with s_l

Bradley and co-workers [2, 3] performed Direct Numerical Simulations (DNS) of auto-ignitions of a single hotspot and the combustion wave originating from the hotspot in an infinitely large volume solving the transport equations in one-dimensional spherical form. At the center of the hotspot there is a temperature elevation ΔT_0 related to the uniform distributed initialed temperature T_0 of the surrounding domain. From its maximum in the center, ΔT_0 decreases linearly until the edge of the kernel. Three different hotspot sizes have been analyzed (0.5 *mm*, 1 *mm* and 3 *mm*). Auto-ignition and combustion wave have been predicted using detailed chemistry, syngas-air ($CO/H_2/air$) and hydrogen-air mixtures. Figure 2.9 shows a

typical result of their work: the transition from a subsonic auto-ignitive deflagration wave (iv), over a developing and developed detonation (iii) to a supersonic auto-ignitive deflagration wave (ii), which results in a thermal explosion (i) [3]. This transition can be followed up by five characteristic time steps: At time step **1** (1.4011 *ms*) the first significant reactions occur. As a result of the ignition, the velocity of the reaction front wave first increases, but drops thereafter and propagates as steady flame. Starting form time step **2** (1.4188 *ms*) the flame changes its regime. The ignition delay time $\tau(r)$ has changed during the induction time mainly due to heat conduction, but also due to diffusion and gas expansion. As the temperature wave reaches the edge of the kernel $r_0 = 3mm$ in time step **2**, it rises rapidly, fuses with the pressure pulse and imposes the gas velocity u_a. The maximum pressure rises until time step **3** (1.4202 *ms*), the detonation is developing. At time step **4** (1.4213 *ms*), the flame becomes a supersonic deflagration and finally thermal explodes at time step **5** (1.4217 *ms*).

From their studies Bradley and co-workers [2, 3] conclude, that small temperature elevations (starting from $\Delta T_0 > 0.1\ K$) can form developing detonations. Further, they found that for higher unburnt temperatures, the temperature elevations needs to be larger than for lower unburnt temperatures of the surrounding mixture. An important finding is also that, not only the ignition delay time τ and the critical temperature gradient $(\partial T_0/\partial r)_c$, but also the rate of how fast the chemical energy can be uploaded to the acoustic wave is essential to form the resonance of the two waves. The measure of the release of the chemical energy is the excitation time τ_e, which is defined as the time from 5 % heat release until the maximum heat release of a homogeneous mixture. Only if the energy can be transfered within the acoustic time frame, the two waves reinforce. For an auto-ignition kernel this time is given by r_0/a, which leads to the definition of the reactivity parameter ε [2]:

$$\varepsilon = \frac{r_0}{a\tau_e} \tag{2.15}$$

Summarizing and generalizing their simulation results, Bradley and co-workers [2, 3] developed the detonation diagram shown in Figure 2.10 (a), which shows the detonation peninsula enclosed with the upper and lower limit of ξ as function of the reactivity parameter ε.
The detonation diagram was developed for syngas- and hydrogen-air mixtures although the aim was to understand and investigate knock and super knock in gasoline engines. To understand, if the detonation transition boundaries, developed using syngas, are applicable to engine simulation, Peters et al. [7] repeated the calculation for *n*-heptane/air-mixtures and *iso*-octane/air-mixtures since those surrogate fuels are the components of PRF. Figure 2.10 (b) shows the result for *n*-heptane. Peters et al. [7] verified the transition boundaries ξ_l and ξ_u to be the same for *n*-heptane and *iso*-octane as for syngas and also the minimum reactivity parameter to from a developing detonation to be $\varepsilon = 1.6$. A fuel with negative temperature coefficient and a pronounced low temperature chemistry is more likely to develop an auto-ignition, but a

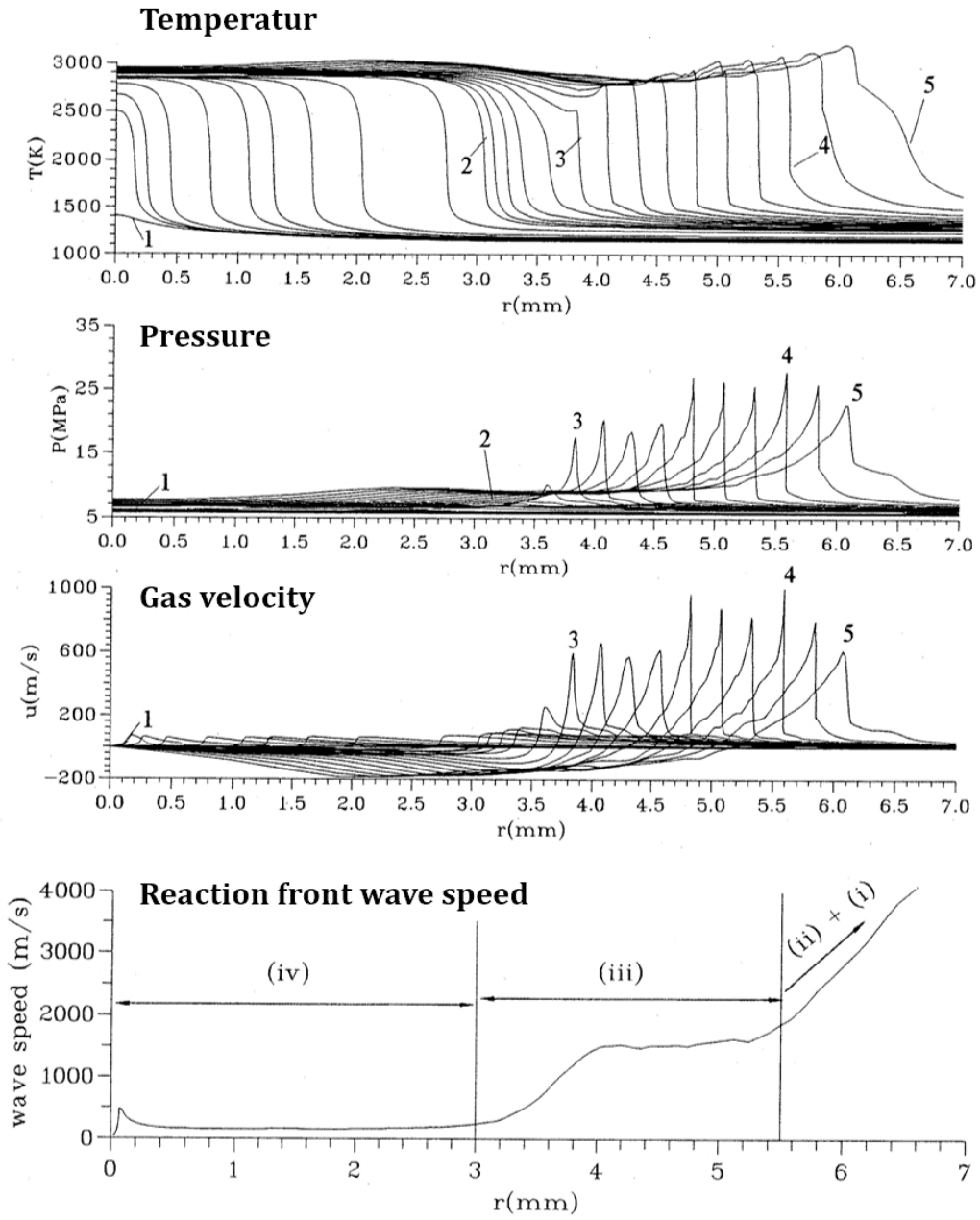

Figure 2.9: Simulation result taken from Gu et al. [3]. Sequence of subsonic auto-ignitive deflagration wave (iv), developing and developed detonation (iii), supersonic auto-ignitive deflagration wave (ii)and thermal explosion (i). Initial conditions: $\xi = 10$, $r_0 = 3\ mm$, $\Delta T_0 = 1.689\ K$, $\tau = 1.4225\ ms$.

developed and visible ignition kernel with significant heat release already passed through the low temperature regime. The ignition of this kernel that may lead to a developing detonation is driven by the high temperature regime. Therefore, the high temperature chemistry is the reason for the apparent fuel independence of the transition boundaries, since the high temperature chemistry is similar for the analyzed fuels as found in [7].

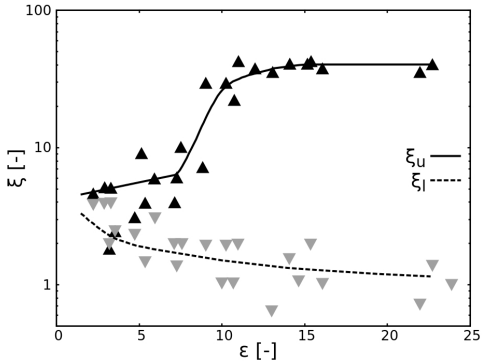

(a) Data from Bradley et. al. [2].

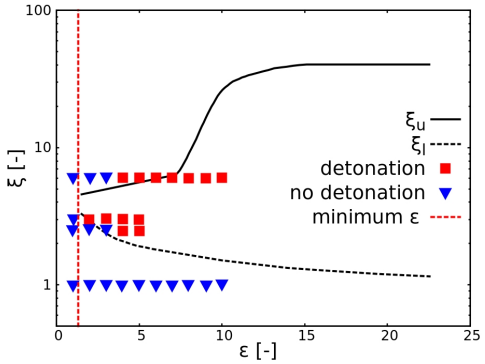

(b) Verification for *n*-heptane and *iso*-octane data from Peters et. al. [7].

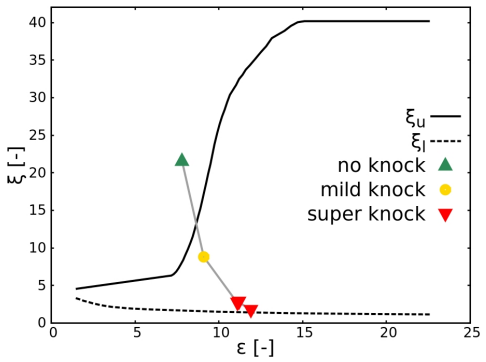

(c) Data from Kalghatgi et. al. [5].

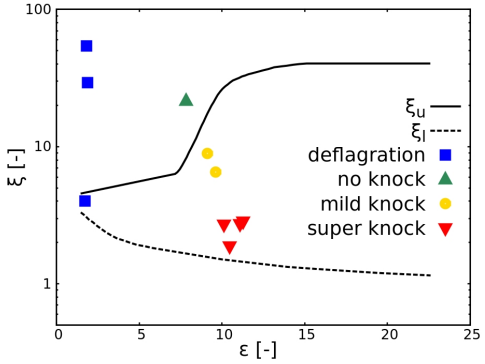

(d) Data from Bates et. al. [60], data from Kalghatgi et al. [5] included.

Figure 2.10: Detonation diagram peninsula and corresponding engine conditions.

Kalghatgi and Bradley [5] analyzed super knock events of measurements from which pressure p_0 and temperature T_0 have been derived. A hotspot size of $r_0 = 5mm$ as consequence of an analysis of the geometry and turbulent length scale l_t and a temperate gradient of $\partial T/\partial r = -2 \quad K/mm$ have been assumed. Evaluating the thermodynamic state in the engine prior auto-ignition onset and the calculation of the corresponding ignition delay time τ and excitation time τ_e, ξ and ε are calculated for the different knock events in the experiment. The transition of a non-knocking to a mild knocking cycle to a cycle with occurrence of super knock can in this way followed up in the detonation diagram 2.10 (c). Bates et al. [60] reported further LES results for the different knock regimes within the detonation diagram 2.10 (d).

3 Modeling of Turbulent Premixed Combustion Processes

The flow in engines is turbulent and reactive. It covers vast ranges of turbulent and chemical length- and timescales. Additionally, there is a two-way-interaction of turbulence and combustion. The elementary reactions need to be described by hundreds of species and thousands of reactions. This complexity is a challenging modeling task, particularly since not all phenomena are fundamentally understood today.

The energy content of turbulent flows is described by the eddy cascade hypothesis. In engines, the scales of this cascade cover the size of the larger eddies at the integral length scale l down to the Kolmogorov scale η_K, where the energy is dissipated. Between those two scales (l and η_K, inertial range) lie two orders of magnitude. Accounting for the bore of an internal combustion engine, the length scales of the problem covers three orders of magnitude, that need to be accounted for in modeling [17]. Table 3.1 gives an example for the length scales in a typical engine simulation performed within this work.

The Navier-Stokes Equations were developed for non-reacting, iso-thermal flows with constant density. For turbulent reacting flows, with high temperature and density gradients, further models, simplifications and assumptions need to be introduced. The eddy cascade hypothesis builds the basis for the turbulence models. Based on the scale invariance of energy transfer and eddy size, the Navier Stokes-Equations are solved down to a certain eddy size at which closure assumptions are introduced [17, 23].

Strain and shear at eddy interfaces govern large gradients of temperature and reactant concentrations. Those interfaces and the increased diffusion processes due to the gradients can promote or prohibit combustion. The high gradients of temperature and consequently of density and kinematic viscosity can accelerate turbulence. However, combustion occurs at various chemical timescales. In thin reaction fronts, combustion occurs at molecular scales, which are smaller than the Kolmogorov scale, where the chemical timescales are fast compared

Table 3.1: Example of occurring length- and timescales in a SI engine simulation without modeled injection.

	Compression	**Combustion**	**Expansion**
Crank angle [°CA aTDC]	-10	20	100
Bore [mm]	72.0	72.0	72.0
Turbulent length scale [mm]	0.7	0.4	2.0
Kolmogorov length scale [μm]	4.0	10.0	70.0
360°CA (2500 rpm) [ms]	24.0	24.0	24.0
Turbulent timescale [ms]	0.8	0.6	5.0
Kolmogorov timescale [μm]	8.0	17.0	210.0

to the turbulence timescales. The other extreme, in case of slow reactions, the combustion is controlled by the mixing due to turbulence. This difference in magnitude between scales, leads to one of the basic strategies in modeling of turbulent reacting flows: the separation of turbulent and chemical scales. The chemical timescales are faster than the turbulent scales and can therefore not affect the inertial range scales. This holds for large Damköhler numbers (Da $\gg 1$), which determines the ratio between turbulent and chemical timescales, but not for scales of the same order Da ≈ 1. The scale separation is an important assumption that simplify the modeling of turbulent combustion and is therefore used in almost all turbulent combustion models [17, 23].

In the following, the combustion and turbulence models applied in this work are presented. The combustion models are based on detailed reaction schemes. The reaction mechanism is discussed in chapter 4. The different characteristics of knocking combustion - the flame propagation of the main flame and the auto-ignition ahead of the flame front - are modeled separately, since they occur as a result of different chemical and physical processes. For the turbulence prediction different approaches are applied. The main purpose of this work is the prediction and assessment of the development of engine knock based on detailed chemistry for the use in SI engine development and optimization. For this purpose, three-dimensional RANS simulations are carried out. Thanks to the model assumptions (section 3.3) this approach can offer results based on detailed chemistry in reasonable computational times. However, the stochastics of the flow cannot be captured. To verify if the conclusions drawn from the simulations are physically reasonable, the developed methodology for auto-ignition prediction and evaluation within RANS is compared to the more physically detailed LES approach. Cyclic variations in SI engines result mainly from the stochastics of the flow and are a dominant effect on auto-ignition occurrence. As mentioned, RANS cannot reproduce the stochastics of the flow and accordingly no cyclic variations. Therefore it is used to analyze the mean cycle and fuel

effects in detail. LES predicts cycle-to-cycle variations, but is, especially if detailed chemistry is applied, computationally too expensive for development and optimization applications. To study the impact of cyclic variations and the stochastics of the flow, the zero-dimensional SI-SRM is applied in this work. Due to reduction of spatial dimensionality, detailed chemistry can be solved efficiently. Therefore several consecutive cycles can be predicted, analyzed and compared to experiments.

This chapter introduces first the conservation equation in their laminar form, followed by their formulation for three-dimensional turbulent flows. The same combustion modeling approach is used in RANS and LES. The components of the combustion model are discussed in the following order: laminar and turbulent flame speed model, flame propagation model and auto-ignition model. The last section describes the zero-dimensional model with special emphasis on stochastic modeling.

3.1 Conservation Equations

The conservation equations are listed here for a control volume (Figure 3.1) in index notation and in Cartesian coordinates. Index $i = 1,2,3$ denotes the three spatial directions, $k = 1,...,n_k$ the number of species. Each of the conservation equations consist of a term for the temporal change ($\partial/\partial t$), for convection ($\partial u_i/\partial x_i$), diffusion processes with the diffusion velocity $V_{k,i}$, a source or sink $\dot{\Psi}$ and external forces $f_{k,i}$.

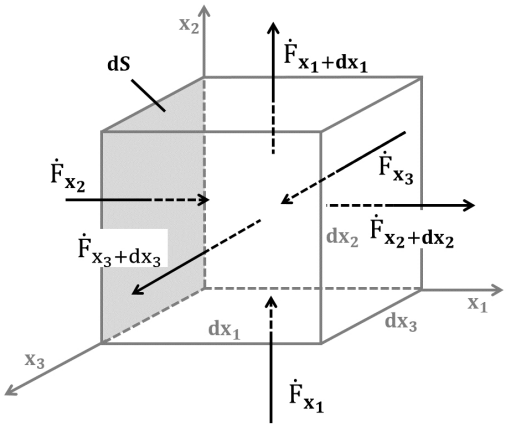

Figure 3.1: Illustration of a control volume V_c.

Mass Conservation The mass conservation equation, often referred to as continuity the equation, is given by [23, 61]:

$$\frac{\partial \rho}{\partial t} + \frac{\partial}{\partial x_i}(\rho u_i) = \dot{\rho}_s \tag{3.1}$$

From left to right, the terms govern the temporal mass change in the control volume, the mass flux over the boundaries and the source term $\dot{\rho}_s$. Since mass conservation holds, the source or sink term in equation 3.1 has to be zero. However, a mass increase in the system, due to fuel injection $\dot{\rho}_s$ needs to be considered for engine simulations.

Species Mass Conservation Since chemical reactions form and consume species, the species mass density is not conserved, for a species k therefore results [23, 61]:

$$\frac{\partial}{\partial t}(\rho Y_k) + \frac{\partial}{\partial x_i}(\rho (u_i + V_{k,i}) Y_k) = M_k \dot{\omega}_k + \delta_{ki} \dot{\rho}_{k,s} \tag{3.2}$$

Where the diffusion flux $V_{k,i}$ is the diffusion velocity vector of species k. The terms on the right hand side are the consumption or formation rate due to chemical reactions $M_k \dot{\omega}_k$, obtained from the combustion model (section 3.3), and the spray source term $\dot{\rho}_{k,s}$. The spray source term has to be present for the species that are injected $\delta_{ki} = 1$, which are the fuel species and others such as water in modern concepts, but vanishes for all other species $\delta_{ki} = 0$.

Momentum Conservation The momentum transport equation results in [23, 61]:

$$\frac{\partial}{\partial t}(\rho u_i) + \frac{\partial}{\partial x_j}(\rho u_i u_j) = -\frac{\partial p}{\partial x_j} + \frac{\partial \tau_{ij}}{\partial x_i} + \rho \sum_{k=1}^{n_k} Y_k f_{k,j} + \dot{s}_{u,i} \tag{3.3}$$

with

$$\tau_{ij} = -\frac{2}{3}\mu \frac{\partial u_k}{\partial x_k}\delta_{ij} + \mu \left(\frac{u_i}{\partial x_j} \frac{\partial u_j}{\partial x_i} \right) \tag{3.4}$$

The momentum change due to the pressure tensor is represented here with the pressure gradient and τ_{ij} that includes the deformation and viscous stress tensors. For $i = j$ the Kronecker delta is $\delta_{ij} = 1$, for $i \neq j$ holds $\delta_{ij} = 0$. External forces and sources are the volume forces $f_{k,j}$ that act on species k and the spray source term $\dot{s}_{u,i}$. The flow in engines is turbulent, so that the viscosity μ becomes the effective viscosity $\mu_{eff} = \mu_t + \mu_{mol}$, which is the sum of turbulent and molecular viscosity. μ_t needs to be obtained using turbulence models (section 3.2).

Energy Conservation The conservation equation for the total energy e is given by [23]:

$$\frac{\partial}{\partial t}(\rho e) + \frac{\partial}{\partial x_i}(\rho u_i e) = -\frac{\partial q_i}{\partial x_i} + \frac{\partial}{x_j}(\sigma_{ij} u_i) + \rho \sum_{k=1}^{n_k} Y_k f_{k,i}(u_i + V_{k,i}) + \dot{Q} \tag{3.5}$$

with

$$\sigma_{ij} = \tau_{ij} - p\delta_{ij} \tag{3.6}$$

and the diffusion term including Fourier's law for thermal diffusion and accounting for diffusion of species with different enthalpy [23]:

$$q_i = -\lambda \frac{\partial T}{\partial x_i} + \rho \sum_{k=1}^{n_k} h_k Y_k V_{k,i} \tag{3.7}$$

$\dot{Q}$ is an external energy source, i.e. the spark plug in SI engines. For reacting flows, the sensible enthalpy h_s conservation equation emphasizes the influence of the heat release during combustion $\dot{\omega}_T$ [23]:

$$\begin{aligned} \frac{\partial}{\partial t}(\rho h_s) + \frac{\partial}{\partial x_i}(\rho h_s u_i) = \dot{\omega}_T + \frac{\partial p}{\partial t} + \frac{\partial}{\partial x_i}(p u_i) + \frac{\partial}{\partial x_i}\left(\lambda \frac{\partial T}{\partial x_i}\right) \\ - \frac{\partial}{\partial x_i}\left(\rho \sum_{k=1}^{n_k} h_{s,k} Y_k V_{k,i}\right) + \tau_{ij}\frac{\partial u_i}{\partial x_j} + \dot{Q} + \rho \sum_{k=1}^{n_k} Y_k f_{k,i} V_{k,i} \end{aligned} \tag{3.8}$$

The heat release is determined using the standard enthalpy of formation $\Delta h^0_{f,k}$ and reaction rate $\dot{\omega}_k$:

$$\dot{\omega}_T = -\sum_{k=1}^{n_k} \Delta h^0_{f,k} \dot{\omega}_k \tag{3.9}$$

3.2 Turbulence Models

There are in general three different approaches to solve or model the turbulence in CFD: Direct Numerical Simulation (DNS), Large Eddy Simulation (LES) and Reynolds Averaged Navier-Stokes Simulations (RANS). Those approaches are distinguished by the wave number k_w spectrum that is solved or modeled (Figure 3.2). Defined by $k_w = (2\pi)/l_{eddy}$, is the wave number inversely proportional to the eddy size l_{eddy} [62]. In a turbulent flow, the energy is passed down from the larger eddies towards ever smaller eddies until the Kolmogorov scale η_k. Here, the energy is dissipated by molecular viscosity [63]. In the modeling of turbulent flow it is of interest how much energy the turbulent structures contain. The energy that is passed from a larger eddy to a smaller and the accompanying change in wave number dk_w is given by $E(k_w)dk_w$. The turbulent kinetic energy k of a turbulent flow is hence given as integral over the eddies [62]:

$$k = \int_0^\infty E(k_w) dk_w. \tag{3.10}$$

First, the average of the flow motion can be considered as it is done for RANS. This average can be over time for stationary flows, over a non-shifting coordinate or over a volume element. Averaging is called one-point closure, since it is based on single point averages. The averaging procedure leads to an unclosed system of partial differential equations. Modeling is needed to close the system. The turbulence models introduce a model description of the turbulent

viscosity. In those turbulence models, certain terms and correlations are closed by the use of approximations [23, 64]. Properties as turbulent kinetic energy k and dissipation of turbulent kinetic energy ϵ are calculated as function of the integral length scale l. Properties in the range down to the Kolmogorov scale η_K are modeled as function of them [17]. The RANS concept is an engineering approach with rather coarse meshes compared to the other approaches. Due to its comparably low computational cost and well validated turbulences models for different applications, it can be applied in complex geometries, needed for modeling of engines with moving valves and piston. RANS simulations yield the ensemble average for each grid cell and therefore resolve not the instantaneous flame front itself, but the mean location over several engine cycles [23]. However, those simplifications are not necessarily a drawback: simulations based on detailed chemical schemes need transport equations and chemical source terms for each included species, which can lead to a quadratic increase of the simulation time with the number of species. Such simulations are typically targeted to find the exhaust out emissions of an engine operating point or the average behavior of hundreds of combustion strokes. The mean values obtained of a system can be compared consistently to an experiment, since experiments are usually repeated several times and averaged. For such applications RANS becomes a very powerful and usable engineering tool.

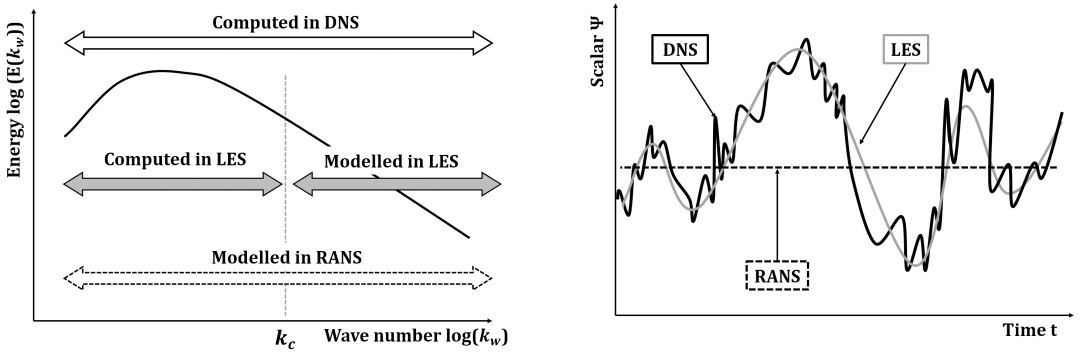

(a) Solved and modeled spatial frequency ranges.

(b) Time evolution of a scalar Ψ, for example at a fixed spatial position.

Figure 3.2: Comparison of the basic characteristics of the DNS, LES and RANS approach. Figures according to [23].

Second, the transport equations can be solved directly without any approximations, which is called Direct Numerical Simulation. Grid size and time step need to respect the smallest possible length- and timescales of all processes involved. This method is the most exact since it solves every motion of the flow, but needs huge computational resources, so that only small parts of a flow problem can be calculated. The solution of DNS can be treated as a single

realization of small scale laboratory experiment and offers a lot of important information [64]. The computational costs make DNS inapplicable for the simulation and the optimization of in-cylinder combustion, but the results are used for further scientific understanding of physics and chemistry. Based on DNS results, models for other simulation approaches can be developed and verified. With increasing availability and performance of modern computers the application fields of DNS increases, allowing today engine-like simulations such as the flow for a fixed valve lift [65].

LES is a compromise of the other two approaches. As it is shown in Figure 3.2, down to a certain eddy size, the critical wave number k_c, the turbulent flow is solved directly as in DNS simulations. Below k_c, the transport equations are filtered, which leads, as in the RANS approach, to an unclosed system of equations. As in RANS, closure of the system of equations is needed. In LES, a so-called sub-grid model is required. Different than in RANS, the equations are not filtered in time, but in space. Cell sizes, accuracy and computational costs are ranged between RANS and DNS [23, 64]. Whereas RANS simulations govern by the same boundary conditions always exact the same results, LES can capture the stochastics in the motion of the flows, since it averages, or filters, in space and not over time and leads therefore to different mean values and smaller fluctuations [17]. Since cycle-to-cycle variations are an important phenomenon in SI engines, which is mainly originating from the turbulent field around the spark plug, that can promote or prohibit the ignition of the charge, LES is increasingly used in SI engine development. However, to obtain the same conclusion on mean exhaust out emissions or behavior of an operating point, at least 30 consecutive computationally expensive cycles need to be calculated. The LES concept poses additional challenges compared to RANS. Models that have been developed for RANS are not necessarily consistent with the LES approach [66]. In literature, LES with different modeling assumptions can be found. Scientific approaches, in which the models for the combustion or spray have been developed recently, such as the G-equation formulation by Pitsch [67], are based on the original formulation in RANS by Peters [17]. Rather an engineering hybrid-approach, is the combination of a LES turbulence model with RANS sub-grid models. Hereby, the idea is that the LES turbulence model improves the turbulence prediction and therefore the boundary conditions for the other models. In those hybrid approaches the stochastic nature of the flow field is represented more physically than in regular RANS [66].

3.2.1 Reynolds-Averaged Navier-Stokes Simulation - RANS

Reynolds or time averaging means splitting any property Ψ into its mean $\overline{\Psi}$ and fluctuation Ψ' [61]:

$$\Psi(x_i,t) = \overline{\Psi}(x_i,t) + \Psi'(x_i,t) \quad with \quad \overline{\Psi'} = 0 \tag{3.11}$$

Applying this average to the mass conservation equation (3.1) yields [23]:

$$\frac{\partial \overline{\rho}}{\partial t} + \frac{\partial}{\partial x_i}\left(\overline{\rho}\overline{u}_i + \overline{\rho' u_i'}\right) = 0 \tag{3.12}$$

The terms $\overline{\rho' \overline{u}_i}$ and $\overline{\overline{\rho} u_i'}$ occurring in the averaging process are zero due to $\overline{\Psi'} = 0$. An outcome of the Reynolds average procedure are the unclosed correlations, such as $\overline{\rho' u_i'}$. Averaging the remaining conservation equations and for variable density flows further correlations $\overline{\rho' \Psi_i'}$ are introduced and need closure. Therefore, for flows with variable density (combustion processes), the Favre average is introduced, which is a density-weighted average of the form [61]:

$$\widetilde{\Psi} = \frac{\overline{\rho \Psi}}{\overline{\rho}} \tag{3.13}$$

$$\Psi(x_i,t) = \widetilde{\Psi}(x_i,t) + \Psi''(x_i,t) \quad with \quad \overline{\rho \Psi''} = 0 \tag{3.14}$$

Averaging equation (3.1) leads to [23]:

$$\frac{\partial \overline{\rho}}{\partial t} + \frac{\partial}{\partial x_i}(\overline{\rho}\tilde{u}_i) = \overline{\dot{\rho}_s} \tag{3.15}$$

Since

$$\frac{\partial \overline{\rho u_i''}}{\partial x_i} = 0$$

and

$$\frac{\partial \overline{\rho''}}{\partial t} + u_i \frac{\partial \overline{\rho''}}{\partial x_i} = 0.$$

Assuming that molecular transport and terms needed for shock waves or detonations can be neglected against turbulent transport and assuming equal diffusivity for all species, averaging equations (3.2), (3.3) and for equation (3.8) yields [23]:

$$\frac{\partial}{\partial t}(\overline{\rho}\tilde{Y}_k) + \frac{\partial}{\partial x_i}(\overline{\rho}\tilde{u}_i\tilde{Y}_k) + \frac{\partial}{\partial x_i}\left(\overline{\rho} D_k \frac{\partial \widetilde{Y}_k}{\partial x_i} + \overline{\rho \widetilde{u_i'' Y_k''}}\right) = \overline{M_k \dot{\omega}_k} + \overline{\delta_{ki} \dot{\rho}_{k,s}} \tag{3.16}$$

$$\frac{\partial}{\partial t}(\overline{\rho}\tilde{u}_i) + \frac{\partial}{\partial x_j}(\overline{\rho}\tilde{u}_i\tilde{u}_j) = -\frac{\partial \overline{p}}{\partial x_i} + \frac{\partial}{\partial x_i}\left[\mu_t\left(\frac{\partial \tilde{u}_i}{\partial x_j} + \frac{\partial \tilde{u}_j}{\partial x_i}\right) - \frac{2}{3}\mu_t \frac{\partial \tilde{u}_k}{\partial x_k}\delta_{ij}\right] + \frac{\partial \tau_{ij}}{\partial x_j} + \overline{\dot{s}_{u,i}} \tag{3.17}$$

where

$$\tau_{ij} = -\overline{\rho \widetilde{u_i' u_j'}} \tag{3.18}$$

$$\frac{\partial}{\partial t}(\overline{\rho}\tilde{h}) + \frac{\partial}{\partial x_i}(\overline{\rho}\tilde{h}\tilde{u}_i) = \frac{\partial \overline{p}}{\partial t} + \widetilde{u}_i \frac{\partial \overline{p}}{\partial u_i} + \frac{\partial}{\partial x_i}\left(\overline{\lambda}\frac{\partial \widetilde{T}}{\partial x_i} - \overline{\rho \widetilde{u_i'' h''}}\right) + \overline{\tau_{ij}\frac{\partial u_i}{\partial x_j}} + \overline{\dot{q}_r} + \overline{\dot{\omega}_T} \tag{3.19}$$

It should be noted that in Converge the energy conservation equation is formualted and solved in terms of the total energy e [8]. To close the system, an equation of state needs to be applied. In this work, the equation of state by Redlich-Kwong is used. $\overline{M_k \dot{\omega}_k}$ is obtained from the combustion model. Anyway, unclosed terms as result of the averaging procedure occur: $\overline{\rho}\widetilde{u_i'' u_j''}$, $\overline{\rho}\widetilde{u_i'' Y_k''}$, $\overline{\rho}\widetilde{u_i'' h''}$. Whereas species and enthalpy fluxes can be approximated using a gradient assumption, the Reynold stresses $\overline{\rho}\widetilde{u_i'' u_j''}$ need to be modeled using a turbulence model since they are essential for the prediction of turbulent flows. To model the Reynolds stresses detailed models (Reynolds stress models) are available, but require long computational times, so that eddy viscosity models are preferred [68]. The viscous stress tensor τ_{ij} and the turbulent viscosity μ_t result from the turbulence models [23, 64]:

$$\overline{\rho}\widetilde{u_i'' u_j''} = \tau_{ij} = -\mu_t \left(\frac{\partial \widetilde{u}_i}{\partial x_j} + \frac{\partial \widetilde{u}_j}{\partial x_i} \right) - \frac{2}{3}\delta_{ij}\overline{\rho}k \tag{3.20}$$

where k is the turbulent kinetic energy [64]:

$$k = \frac{1}{2}\widetilde{u_i'' u_i''} \tag{3.21}$$

To solve the turbulent viscosity μ_t zero-equation models, such as the Prandtl mixing length-model, and one- and two-equation models have been developed. For those models one or two additional equations for the turbulent kinetic energy k and the dissipation of turbulent kinetic energy ϵ respectively, are introduced. In this work, the Re-Normalization Group RNG k-ϵ model is used and therefor discussed in the following. In such two equation k-ϵ models the eddy viscosity is estimated by [23]:

$$\mu_t = \mu + \overline{\rho} C_\mu \frac{k^2}{\epsilon} \tag{3.22}$$

In RANS it holds that $\mu_{eff} = \mu_t$, since the molecular viscosity μ_{mol} is negligible compared to μ_t. For the turbulent kinetic energy k a transport equation from the momentum conservation (equation (3.3)) multiplied by u_i to obtain the velocity correlations is derived. It yields [23]:

$$\frac{\partial}{\partial t}(\overline{\rho}k) + \frac{\partial}{\partial x_i}(\overline{\rho}\widetilde{u}_i k) = \frac{\partial}{\partial x_i}\left(\frac{\mu_t}{\sigma_k} \frac{\partial k}{\partial x_i} \right) + P_k - \overline{\rho}\epsilon \tag{3.23}$$

Where P_k is a source term and ϵ the turbulent dissipation, which is given by [17]:

$$\epsilon = -\mu_t \overline{\frac{\partial u_i''}{x_j} \frac{\partial u_i''}{x_j}} \tag{3.24}$$

and therefore needs further modeling. To model ϵ a transport equation can be formulated connected to the turbulent kinetic energy. Since there is no direct derivation possible the whole equation (3.25) should be regarded as a model [17]. To physically limit the growth of k (via the gradient $(\partial u_i / \partial x_i)$), ϵ needs to grow proportionally. The other way around, if k decreased ϵ

needs to decrease, since not more energy can be dissipated than what is available in the system. The transport equation for the turbulent dissipation ϵ results in [23]:

$$\frac{\partial}{\partial t}(\overline{\rho}\epsilon)+\frac{\partial}{\partial x_i}(\overline{\rho}\widetilde{u_i}\epsilon)=\frac{\partial}{\partial x_i}\left(\frac{\mu_t}{\sigma_\epsilon}\frac{\partial \epsilon}{\partial x_i}\right)+C_{\epsilon,1}\frac{\epsilon}{k}P_k-C_{\epsilon,2}\overline{\rho}\frac{\epsilon^2}{k}-\overline{\rho}R \tag{3.25}$$

with [8]

$$R=\frac{C_\mu\eta^3\left(1-\eta/\eta_0\right)}{1+\beta\eta^3}\frac{\epsilon^2}{k} \tag{3.26}$$

and

$$\eta=\frac{k}{\epsilon}\left(2S_{ij}S_{ij}\right)^{1/2}\quad with\quad S_{ij}=\frac{1}{2}\left(\frac{\partial\widetilde{u_i}}{\partial x_j}+\frac{\partial\widetilde{u_j}}{\partial x_i}\right) \tag{3.27}$$

P_k is a source term and C_μ - the turbulent viscosity coefficient, the Prandtl numbers σ_k and σ_ϵ, the turbulence dissipation constant $C_{\epsilon,1}$ and $C_{\epsilon,2}$, and the RNG k-ϵ model specific constant β and η_0 are model constants and given for an engine simulation in Table 3.2.

Table 3.2: RNG k-ϵ model constants for the flow prediction in internal combustion engines [8].

C_μ	$1/\sigma_k$	$1/\sigma_\epsilon$	$C_{\epsilon,1}$	$C_{\epsilon,2}$	β	η_0
0.0845	1.39	1.39	1.42	1.68	0.012	4.38

Applying eddy viscosity models, the turbulent length scale $l_t=k^{3/2}/\epsilon$ and turbulent time scale $t_t=l/\epsilon$ needed for the combustion models are determined as well. Anyhow, the model has some limitations that have to be noted: the transport equations for k and ϵ are closed using assumptions that are only valid for high Reynolds numbers and homogeneous and isotropic turbulence. The Reynold stresses for source terms as P_k need algebraic formulations especially for the near wall zones [23].

3.2.2 Large Eddy Simulation - LES

For the derivation of the LES equations a scalar is spitted into its filtered $\widehat{\Psi}$ and the the sub-grid Ψ' part as in RANS [66]:

$$\Psi=\widehat{\Psi}+\Psi' \tag{3.28}$$

Eddies that are larger than the filter length Δ are solved as in DNS, while smaller sub-grid eddies are modeled. Different than in RANS (compare equation (3.11)), the filtered perturbation in LES is not zero [23]:

$$\widehat{\psi'}\neq 0 \tag{3.29}$$

$\widehat{\Psi}$ and Ψ' depend on the filter size Δ. If the filter size decreases, the impact of the sub-grid models decreases and the solution becomes more accurate [66]. The filter cut-off length is typically chosen in a way, that the large energy-containing eddies are solved [67]. The filter

can be applied in spectral space (Figure 3.3 (a)) or in physical space (Figure 3.3 (b) and (c)). A filtered property $\widehat{\psi}(x)$ is given as function of the LES filter F [23]:

$$\widehat{\psi}(x) = \int \psi(x')F(x-x')dx' \tag{3.30}$$

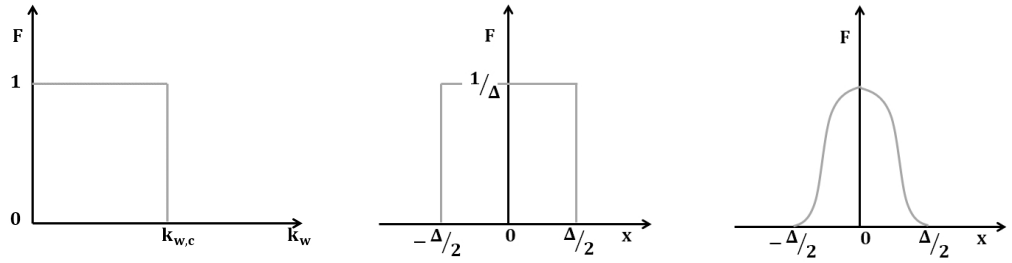

(a) Cut-off filter. (b) Box filter. (c) Gaussian filter.

Figure 3.3: Examples for used filters in LES. Figures according to [23].

As an example, a box filter in physical space that corresponds to a cubic box with an edge length of Δ, is defined by [23].

$$F(x_i) = \begin{cases} \frac{1}{\Delta^3} & \text{if } |x_i| \leq \frac{\Delta}{2} \\ 0 & \text{otherwise} \end{cases} \tag{3.31}$$

Often implicit filtering is applied, which means that the filter size equals the mesh grid points [66]. Independent of the filter choice, the filters are normalized and for combustion modeling Favre averaged [23]:

$$\int_{-\infty}^{+\infty}\int_{-\infty}^{+\infty}\int_{-\infty}^{+\infty} F(x_i)dx_1dx_2dx_3 = 1 \tag{3.32}$$

$$\overline{\rho}\,\widehat{\psi}(x_i) = \int \rho\,\psi(x')F(x-x')dx' \tag{3.33}$$

Applying the filtering method to the conservation equations results in [23].

$$\frac{\partial\overline{\rho}}{\partial t} = \frac{\partial}{\partial x_i}(\overline{\rho}\widehat{u_i}) = 0 \tag{3.34}$$

$$\frac{\overline{\rho}\widehat{u_i}}{\partial t} + \frac{\partial}{\partial x_i}(\overline{\rho}\widehat{u_i}\widehat{u_j}) = -\frac{\partial\overline{p}}{\partial x_j} + \frac{\partial}{\partial x_i}\left[\overline{\tau_{ij}} - \overline{\rho}(\widehat{u_iu_j} - \widehat{u_i}\widehat{u_j})\right] \tag{3.35}$$

$$\frac{\partial(\overline{\rho}\widehat{Y_k})}{\partial t} + \frac{\partial}{\partial x_i}(\overline{\rho}\widehat{u_i}\widehat{Y_k}) = \frac{\partial}{\partial x_i}\left[-\overline{\rho}\overline{D_k}\frac{\partial\widehat{Y_k}}{\partial x_i} - \overline{\rho}\left(\widehat{u_iY_k} - \widehat{u_i}\widehat{Y_k}\right)\right] + \overline{M_k\dot{\omega}_k} \tag{3.36}$$

$$\frac{\overline{\rho}\widehat{h}}{\partial t} + \frac{\partial}{\partial x_i}(\overline{\rho}\widehat{u_i}\widehat{h}) = \frac{\partial\overline{p}}{\partial t} + \widehat{u_i}\frac{\overline{p}}{\partial x_i} + \frac{\partial}{\partial x_i}\left[\overline{\lambda}\frac{\partial\widehat{T}}{\partial x_i} - \overline{\rho}\left(\widehat{u_ih} - \widehat{u_i}\widehat{h}\right)\right] + \overline{\tau_{ij}\frac{u_i}{\partial x_j}} + \overline{\dot{q}_r} + \overline{\dot{\omega}}_T \tag{3.37}$$

As for the final RANS transport equations, a gradient assumption for the laminar diffusion fluxes has been introduced and the pressure velocity term was approximated by $\widehat{u}_i(\partial\overline{p}/\partial x_i)$ [23]. Unclosed terms are the Reynolds stresses $(\widehat{u_i u_j} - \widehat{u}_i\widehat{u}_j)$ and $(\widehat{u_i Y_k} - \widehat{u}_i\widehat{Y}_k)$ as well as $(\widehat{u_i h} - \widehat{u}_i\widehat{h})$. Whereas for the closure of the Reynolds stresses a turbulence model needs to be applied, the remaining two terms can be approximated using a gradient assumption as in RANS, e.g. [23]:

$$\widehat{u_i Y_k} - \widehat{u}_i\widehat{Y}_k = \frac{\mu_t'}{\sigma_k}\frac{\partial\widehat{Y}_k}{\partial x_i} \tag{3.38}$$

Equations (3.34) to (3.37) are formally similar to the transport equations for RANS, but the physical meaning of the single terms can be very different [66]. The main difference in the equation set for LES and RANS is the modeling of the turbulent viscosity μ_t [23, 66]. Different than in RANS, where $\mu_{mol} \ll \mu_t$ and therefore neglected, in LES the treatment of μ_{mol} needs to be accounted for, especially for the near wall modeling. The fluid properties have a dominating role under the non-slip condition [62]. Approaches of different detail are available to model and close the sub-grid turbulence. Common zero-equation models are the Smagorinsky model [69] and the Germano dynamic model [70]. One-equation models are based on the transport of the turbulent kinetic energy k and an approximation of ϵ.

In this work the dynamic Smagorinsky model [70, 71, 72] is applied, which provides an automatic prediction of the Smagorinsky coefficient, that varies for different flow regimes. In those models is the filter size calculated from the cell volume $\Delta = (V_{cell})^{1/3}$. The Smagorinsky model estimates the sub-grid stress tensor τ_{ij}' and the turbulent viscosity μ_t' as function of the strain rate tensor S_{ij} [8]:

$$\tau_{ij}' = -2\mu_t'\widehat{S_{ij}} \quad \text{with } \mu_t' = C_s^2\Delta^2\left(S_{ij}S_{ij}\right)^{1/2}, \tag{3.39}$$

where C_s is a model constant that needs to be provided by the user depending on the flow regime or can be calculated applying the dynamic Smagorinsky model [8]. For this dynamic approach in addition to the regular sub-grid filter Δ a test level filter $\widehat{\widehat{\Delta}}$ with the size $\widehat{\widehat{\Delta}} \approx 2\Delta$ is applied. For the eddies close to but larger than the filter wave number k_c, the Leonard stress tensor L_{ij} is known (Figure 3.4). Based on this knowledge the stress tensor of the test filter range T_{ij} and the sub-grid range τ_{ij}' are calculated. They are defined as [8]:

$$\tau_{ij}' = \left(\widehat{u_i u_j} - \widehat{u}_i\widehat{u}_j\right) \tag{3.40}$$

$$T_{ij} = \left(\widehat{\widehat{u_i u_j}} - \widehat{\widehat{u}}_i\widehat{\widehat{u}}_j\right) \tag{3.41}$$

The two stress tensors are connected by the Germano identity [23, 70]:

$$L_{ij} = T_{ij} - \widehat{\widehat{\tau_{ij}'}} = \left(\widehat{\widehat{u_i u_j}} - \widehat{\widehat{u}}_i\widehat{\widehat{u}}_j\right) \tag{3.42}$$

The sub-grid stress tensor can finally be approximated by [8]:

$$\tau'_{ij} = -2C_{s,dyn}\widehat{\Delta}^2 \left|\widehat{S}\right| \widehat{S_{ij}} \tag{3.43}$$

where $C_{s,dyn}$ is calculated by [8]:

$$C_{s,dyn} = \frac{M_{ij}L_{ij}}{M_{kl}M_{kl}} \quad \text{with } M_{ij} = 2\widehat{\widehat{\Delta}}^2 \widehat{\widehat{|S|\,S_{ij}}} - 2\widehat{\widehat{\Delta}}\left|\widehat{\widehat{S}}\right| \widehat{\widehat{S_{ij}}} \tag{3.44}$$

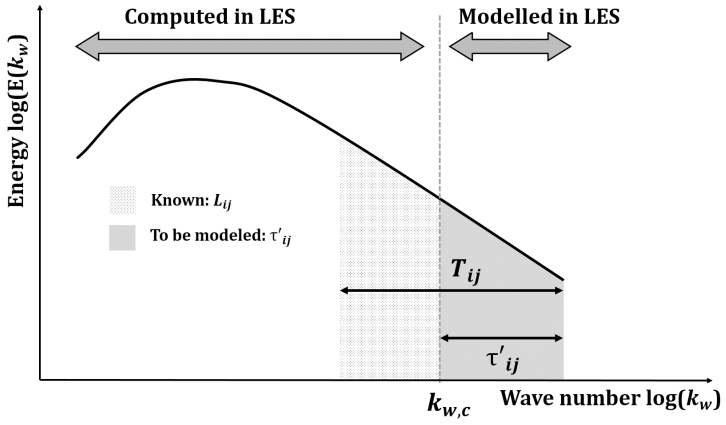

Figure 3.4: Concept of the dynamic Smagorinsky model. Figure according to [23].

3.3 Combustion Models

The flow field in engine cylinders is highly turbulent. The flame front is wrinkled due to the interactions with the eddies. A turbulent flame has therefore an increased flame area and propagates with the turbulent flame speed s_t. It holds that $s_t > s_l$. Different model approaches are available to model turbulent premixed flames. Those models can be classified in Eddy-Break-Up models, flamelet models, fractal models and flame area evolution models [73]. Alternatively, one can distinguish between combustion models assuming finite-rate chemistry and those assuming infinite-rate chemistry.

The Eddy-Break-Up Model [74] and Eddy Dissipation model [75] transfer the energy cascade concept to turbulent combustion. The underlying assumption is that the turbulent mixing is the rate limiting step. Following this assumption, combustion is determined from the rate at which the eddies are broken down within the flame brush. In those models no microscale information of length- or timescale of combustion are considered [63].

Flamelet models account, thanks to the flamelet assumption, for macro- and microscales. This assumptions states that even though the flame is wrinkled by turbulence, it can be treated as laminar on a local scale if the flame front is thin, the chemistry fast ($Da \gg 1$) and the turbulent scales are larger than the flame thickness ($\mathrm{Ka} < 1$). The flamelet model includes fast chemistry at the large turbulent scales and non-equilibrium chemistry in the thin stoichiometric layer. The greatest advantage of flamelet models is that the solution of flow field and chemistry can be decoupled whereas the flame stretch is modeled using the scalar dissipation rate. The solution of the chemical rates can be outsourced and stored in pre-compiled look-up tables, which makes the combustion model computationally very efficient [63, 73].

Flame area evolution models introduce a comprehensive formulation of the flame surface area using an additional transport equation. The Bray-Moss-Libby model (BML) [76] introduces in the progress variable transport equation terms for the laminar flame speed s_l and the flame surface density Σ. Whereas Σ is solved on the turbulent length scales, s_l is governed as microscale model [63]. The Coherent Flame Model (CFM) [77] and its extensions (ECFM) [78, 79] account for a local flame wrinkling factor and the local mean reaction rate on combustion progress.

The G-equation model differs from the flame surface density models by introducing an explicit model for the turbulent flame propagation. Hereby, the turbulent flame model accounts for the information from the macro- and microscales [63]. The interface of unburnt and burnt zone is given by the non-reacting scalar G. In turbulent reacting flows with variable density, such as in combustion, the diffusion of scalars and species are enhanced. As a result of turbulence enhanced transport, species and heat are transported parallel with, but in counter direction to their mean gradient. Different than for the regular gradient diffusion. This phenomena is called counter-gradient diffusion and is a challenging modeling task since the gradient flux assumption does not hold [80]. Models that introduce combustion progress variables do not need to introduce counter-gradient diffusion. A further benefit of the model formulation is that no closure of the transport equations is needed since G is a non-reactive scalar. The CFM and G-equation model lead both to satisfactory results for the simulation of SI engines [73] and provide more detail of the flame structure than the previous discussed models. Further, the CFM model can be viewed as an infinite-rate combustion model, and the G-equation model as finite-rate model.

The use of detailed chemistry enables to model and investigate physical effects, i.e. cooling strategies, and chemical effects, such as ignition promoting radicals on the auto-ignition occurrence. In this work, the flame propagation models are therefore based on flame speed tables that are accounting for a complex fuel surrogate formulation. This allows for considering

the effect of different surrogates. For this purpose in CFD the G-equation model is applied and for zero-dimensional modeling the two zone SI-SRM.

Besides the capability to predict flame propagation, the combustion model needs to predict auto-ignition in the unburnt zone, which is a prerequisite for engine knock prediction. The G-equation model includes no formulation for the prediction of auto-ignition. Anyway, flame propagation and auto-ignition in the unburnt zone, are from the chemical point of view independent processes that do not need to be modeled with the same combustion model. Since the unburnt zone is rather homogeneous in SI engines, a homogeneous approach - the Well-Stirred-Reactor (WSR) model - is applied for the prediction of auto-ignition based on a detailed reaction scheme. Each cell in the unburnt zone is treated as a WSR, hence with sufficient discretization local inhomogeneities are accounted for. For SI engines, this approach is well established and widely used, see for example [81, 82, 83, 84] and references therein. The models applied in CFD are discussed in the following.

The same strategy, to split the description of the flame propagation based on provided flame speed look-up tables and a homogeneous approach in the unburnt zone, is applied for the zero-dimensional modeling and discussed in section 3.4.

3.3.1 Laminar Flame Speed

As discussed in chapter 2.2, the laminar flame speed is a dominating and important parameter for the prediction of the flame propagation of a premixed flame. It is used as input parameter for the turbulent flame propagation model and needs therefore be modeled with certain care. In this work, the laminar flame speed is calculated based on detailed chemistry and stored in look-up tables (see section 4.3). For this purpose s_l is calculated for a given p, T_u and ϕ using a planar steady-state flame normal to the x_1-coordinate. Fresh gases are defined to be at $x_1 \mapsto -\infty$ and the burnt combustion products at $x_1 \mapsto +\infty$. The transport equations have to be solved for one dimension [17, 9]:

$$\frac{\partial(\rho u_1)}{\partial x_1} = 0 \tag{3.45}$$

$$\rho u_1 \frac{\partial Y_k}{\partial x} = -\frac{\partial j_k}{\partial x_1} + M_k \dot{\omega}_k \tag{3.46}$$

$$c_{p,mix} \rho u_1 \frac{\partial T}{\partial x_1} = \frac{\partial}{\partial x_1}\left(\lambda \frac{\partial T}{\partial x_1}\right) - \sum_{i=1}^{n} c_{p,k} j_k \frac{\partial T}{\partial x_1} - \sum_{i=1}^{n} h_k \dot{\omega}_k + \dot{q}_R \tag{3.47}$$

Since the mass flow rate through the flame surface is constant (equation (3.45)) the laminar

flame speed is given by the flow field velocity at $-\infty$ [17]:

$$(\rho u_1)_{-\infty} = (\rho s_l)_u \tag{3.48}$$

The diffusion flux $j_{k,i}$ is given by Fick's law accounting for species diffusion in one dimension:

$$j_k = -\rho D_k \frac{\partial Y_k}{\partial x_1} \tag{3.49}$$

Whereas in CFD usually same diffusivity for all species is assumed since the turbulence dominates the mixing, is the treatment in laminar flames important. For the generation of the laminar flame speed look-up tables multispecies diffusion is accounted. For this, the mixture-averaged diffusion coefficient of species k into the the remaining mixture, denoted with j, is calculated [23]:

$$D_k = \frac{(1-Y_k)}{\sum_{j \neq k} X_j / D_{jk}} \tag{3.50}$$

3.3.2 Turbulent Flame Speed

Damköhler [85] derived a ratio between laminar s_l and turbulent flame speed s_t considering a pipe with cross sectional area A. Damköhler stated that the mass flux through the pipe of the turbulent flame surface area A_t moving with the laminar burning velocity s_l, must equal the mass flux trough A moving with s_t. This balance is schematically shown in Figure 3.5 and leads to [17]:

$$\dot{m} = \rho_u s_l A_t = \rho_u s_t A \tag{3.51}$$

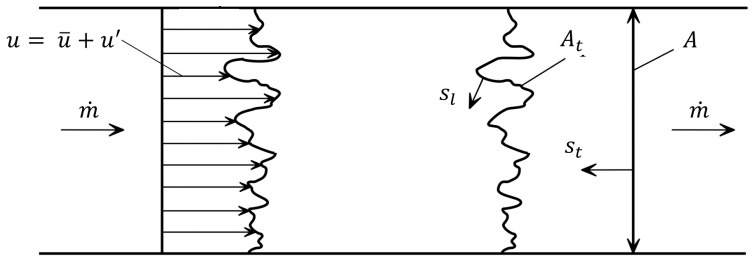

Figure 3.5: Schematically illustration of a ideal premixed flame in a tube [17].

Assuming the density to be constant leads to the ratio of laminar s_l and turbulent flame speed s_t of the discussed two areas [17]:

$$\frac{s_t}{s_l} = \frac{A_t}{A} \tag{3.52}$$

Using this ratio, the balance from equation (3.51), the continuity equation and the analogy to the turbulent dissipation ϵ, a relation to the flow can be found. For the turbulent dissipation it

is known from the energy cascade, that it is invariant in the range between integral length scale l and Kolmogorov scale η_K since the energy is transferred form the large eddies down to the eddies with η_K. Therefore, ϵ can be calculated based on the eddies on the integral length scale. Hence, ϵ is fixed for a certain state of turbulence. From equation (3.24) results accordingly, that the velocity gradient $\overline{\partial u_i''/\partial x_j}$ needs to increase if μ_t is decreasing. Filtering s_t and A with a filter of any size between the integral length scale l and Kolmogorov scale η_K and applying continuity, it results that the product of the filtered $\hat{s}_t$ and $\hat{A}$ needs to be the same as the terms in equation (3.51). Hence $\hat{s}_t\hat{A}$ is invariant over the considered length scales, just as ϵ, and can therefore be determined form the integral scales $s_t A$. Further, the turbulent flame surface area A_t has to increase as s_l decreases analog to μ_t and $\overline{\partial u_i''/\partial x_j}$ [17]. Applying the analogy to turbulence modeling, the high Reynolds number limit can be adopted with u'/s_l, which leads to the relations [17]:

$$\frac{A_t}{A} \sim \frac{u'}{s_l} \tag{3.53}$$

and consequently:

$$s_t \sim u' \tag{3.54}$$

In the thin reaction front regime, according to Damköhler, the turbulence affects the transport from the reaction front to the unburnt gas, but not the chemical time scales t_c. For laminar and turbulent flame speed yields [17]:

$$s_l \sim \left(\frac{D_l}{t_c}\right)^{1/2} \quad and \quad s_t \sim \left(\frac{D_t}{t_c}\right)^{1/2} \tag{3.55}$$

The combination of those relations and with $D_t \sim u'l$, $D_l \sim s_l$ and $D_l \sim \delta$ results in [17]:

$$\frac{s_t}{s_l} \sim \left(\frac{D_t}{D_l}\right)^{1/2} = \left(\frac{u'}{s_l}\frac{l}{\delta}\right)^{1/2} \tag{3.56}$$

This relation can only empirically be adopted to experiments. Equation (3.57) correlates the turbulent flame speed s_t to the laminar flame speed s_l and u' using the constant C which is a function of l/δ and the model constant n in the range $0.5 < n < 1.0$ [17]:

$$\frac{s_t}{s_l} = 1 + C\left(\frac{u'}{s_l}\right)^n \tag{3.57}$$

For the limiting case $u' \mapsto 0$, which corresponds to a pure laminar flow, the term in brackets goes to zero, so that $s_l \mapsto s_t$. A variety of correlations are available in literature. The applied correlations for the turbulent flame speed for RANS and LES simulations in this work are discussed below.

Turbulent Flame Speed Model for RANS Environment The turbulent flame model by Peters [17] is derived form the flame thickness δ and based on the Damköhler number Da. It contains properties from macro- and microscales. The model constants a_4, b_1 and b_2 can be used to calibrate the turbulent flame propagation. Due to the formulation using the mean values of turbulent kinetic energy k and dissipation ϵ, the model is applicable for RANS simulations only. Peters [17] suggested $a_4 = 0.78$ based on the ratio of turbulent diffusion and turbulent viscosity and $b_3 = 1$ following Damköhler. From experiments $b_1 = 2$ was found [17]. The constant b_1 is therefore the only parameter that can be used for calibration. In this work it is set to $b_1 = 2.9$, which is explained by the use of the RNG k-ε model, that results in lower turbulence levels than the standard k-ε model. The applied values are summarized in Table 3.3. The following equations are taken from [8]:

$$s_t = s_l + u' \left\{ -\frac{a_4 b_3^2}{2b_1} Da + \left[\left(\frac{a_4 b_3^2}{2b_1} Da \right)^2 + a_4 b_3^2 Da \right]^{1/2} \right\} \tag{3.58}$$

$$Da = \frac{s_l l_t}{u' \delta} \tag{3.59}$$

$$\delta = \frac{\lambda_0 / c_{p,0}}{\rho_u / s_l} \tag{3.60}$$

$$l_t = C_\mu^{3/4} \frac{k^{3/2}}{\epsilon} \tag{3.61}$$

Turbulent Flame Speed Model for LES The model by Pitsch [67] is derived in analogy to equation (3.58), but in the LES context using the dynamic Smagorinsky number $C_{s,dyn}$ and the turbulent Schmidt number Sc_t [8]:

$$s_t = s_l \left\{ -\frac{b_3^2 C_{s,dyn}}{2b_1 Sc_t} \frac{\Delta}{\delta} + \left[\left(\frac{b_3^2 C_{s,dyn}}{2b_1 Sc_t} \right)^2 + \frac{b_3^2 D_t}{s_l \delta} \right]^{1/2} + 1 \right\} \tag{3.62}$$

Table 3.3: Turbulent flame speed model constants for the model by Peters and by Pitsch.

a_4	b_1	b_3
0.78	2.9	1.0

3.3.3 The G-Equation Model

The main characteristic of premixed combustion is, as discussed before, the coexistence of the unburnt and burnt gases, separated by the flame front. That main characteristic is reproduced by using the Level-Set-Approach by Sethian [86], further developed by Peters [17]. The flame front is hereby represented by an iso-scalar surface with the value G_0, where G is a nonreactive scalar [17]:

$$G(x_i,t) = G_0 \tag{3.63}$$

The unburnt gases are represented by $G < G_0$ and the burnt gases by $G > G_0$. Figure 3.6 illustrates the model approach. Equation (3.66) is called the G-equation and was first introduced by William in 1985 [87]. The G-equation is applicable to premixed combustion processes with thin flame structures and well defined burning velocities. In these structures, the flame is embedded in a quasi-laminar flow field [17]. Those characteristics are found in the corrugated flamelet regime with Reynolds numbers $Re > 1$ and turbulent Karlovitz numbers $Ka < 1$. Under these conditions is the flame front thickness δ smaller than the Kolmogorov scale η_K. This proportion implies that the flow at the flame front is quasi-laminar and the flame structure quasi-steady.

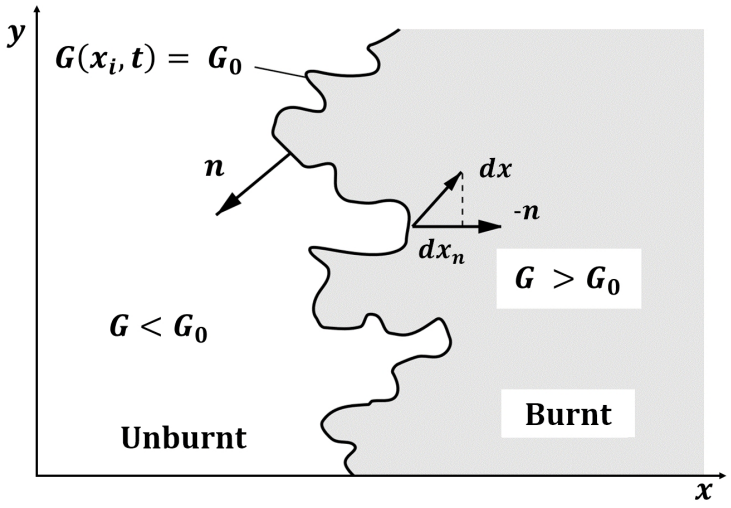

Figure 3.6: Schematically illustration of the G-equation model approach [17].

In a premixed flame, the flame front (G_0) propagates with a certain velocity u_f. This velocity depends on the flow velocity u_i of the surrounding and the laminar burning velocity s_l. Considering the kinematic balance of those velocities and a three-dimensional flow field for the propagation velocity u_f results in [17]:

$$\frac{du_f}{dt} = u_i + n_i s_l \tag{3.64}$$

Where s_l contributes in the normal direction to the flame front expressed by the normal vector n_i (Figure 3.6) [17]:

$$n_i = -\frac{\partial G/\partial x_i}{|\partial G/\partial x_i|} \tag{3.65}$$

In a three-dimensional flow, the time derivative of the iso-scalar surface (equation (3.63)) yields [17]:

$$\frac{\partial G}{\partial t} + u_i \left(\frac{\partial G}{\partial x_i}\right) = s_l \left|\frac{\partial G}{\partial x_i}\right|, \tag{3.66}$$

where velocity u_f has been set to the velocity of the surrounding flow field u_i. Equation (3.66) has no diffusion term, different from other transport equations, because it is based on the two-dimensional kinematic balance that results from equation (3.64). Therefore, G is defined at the flame front, but not in the surrounding three-dimensional field (G-field). However, the gradient of G towards the flame front is needed to define the curvature κ of the iso-surface G_0. This gradient is introduced using the differential of G towards the burnt gas in normal direction (Figure 3.6) [17]:

$$dx_n = -n_i dx = \frac{\partial G/\partial x_i}{|\partial G/\partial x_i|} \tag{3.67}$$

Equation (3.66) is derived for a perfect spherical flame that propagates with s_l. However, flame stretch needs to be accounted for. In engine simulations, the flame front cannot be assumed to be quasi steady, as introduced above, and therefore a valid G-equation formulation for the thin reaction zone regimes needs to be defined. For this formulation the flame front is thin, but of finite thickness [17]. The inner layer of a flame (Zone II in Figure 2.2) governs the reaction progress. Its position is determined by a certain temperature T_0. The position of this temperature, identifies in analogy with equation (3.63) an iso-surface [17]:

$$T(x_i, t) = T_0 \tag{3.68}$$

Introducing the flame curvature κ and strain rate S, and identifying the temperature iso-surface with the G iso-surface, the G-equation in its applicable form to turbulent combustion in SI engines is obtained [8]:

$$\frac{\partial G}{\partial t} + u_i \frac{\partial G}{\partial x_i} = s_t \left|\frac{\partial G}{\partial x_i}\right| - D\kappa \left|\frac{\partial G}{\partial x_i}\right| \tag{3.69}$$

Where the turbulent flame speed s_t is modeled as discussed above.The G-equation formulation for RANS and LES are given in following. In Converge v2.4 [8] different implementations of the G-equation formulation combining a chemical equilibrium solver (CES) and a Well-Stirred-Reactor (WSR, see next section) model are available (Table 3.4). In this work option 3.) is applied since the aim is to predict auto-ignition in the unburnt gases. Further, the chemistry is solved in the burnt zone, to predict exhaust out emissions and treat the thermodynamics based

on physically reasonable conditions. Option 4.) was not available in earlier versions that have been used to develop the methodology to predict and evaluate auto-ignition. To be consistent, the combustion modeling approach was not changed. However, emission prediction is limited by the chosen combustion approach since the flame front passes chemical equilibrium. For a proper emission prediction, the combustion approach should be changed. Anyway, the auto-ignition prediction ahead of the flame front is not affected. The spark is modeled introducing a source-term for the non-reactive scalar G. The source is assumed to be spherical and can move with the flow field.

Table 3.4: Available combinations of the G-equation and chemistry solver in Converge v2.4 [8].

	Flame front	**Unburnt zone**	**Burnt zone**
1.)	CES	CES	CES
2.)	CES	WSR	CES
3.)	CES	WSR	WSR
4.)	WSR	WSR	WSR

G-Equation Formulation for RANS

The G-equation for turbulent premixed combustion in RANS framework is govern using the turbulent flame speed s_t and curvature κ [8]:

$$\frac{\partial\left(\overline{\rho}\widetilde{G}\right)}{\partial t}+\frac{\partial\left(\overline{\rho}\widetilde{u}_i\widetilde{G}\right)}{\partial x_i}=\overline{\rho}_u s_t\left|\frac{\partial\widetilde{G}}{\partial x_i}\right|+D_t'\kappa\left|\frac{\partial\widetilde{G}}{\partial x_i}\right| \tag{3.70}$$

The variance of the non-reactive G'' results in [8]:

$$\frac{\partial\left(\overline{\rho}\widetilde{G''^2}\right)}{\partial t}+\frac{\partial\left(\overline{\rho}\widetilde{u}_i\widetilde{G''^2}\right)}{\partial x_i}=\frac{\partial}{\partial x_i}\left(\overline{\rho}D_t\frac{\partial\widetilde{G''^2}}{\partial x_i}\right)+2\overline{\rho}D_t\frac{\partial\widetilde{G}}{\partial x_i}\frac{\partial\widetilde{G}}{\partial x_i}-C_s\overline{\rho}\widetilde{G''^2}\frac{\epsilon}{k} \tag{3.71}$$

where curvature κ and turbulent diffusions coefficient are given by [8]:

$$\kappa=\frac{\partial}{\partial x_i}\left(\frac{\partial\widetilde{G}/\partial x_i}{\left|\partial\widetilde{G}/\partial x_i\right|}\right) \tag{3.72}$$

$$D_t=\frac{C_\mu}{Sc}\frac{k^2}{\epsilon} \tag{3.73}$$

$$D_t'=\left(C_s\frac{k}{2}\frac{C_\mu}{Sc}G''^2\right)^{1/2} \tag{3.74}$$

G-Equation Formulation for LES

Pitsch [67] transfered the G-equation formulation by Peters [17] to the LES context. A formulation for the filtered flame front position and closures for the conditioned flame front velocity and the sub-grid laminar flame speed s_l' are included.

$$\widehat{G}(x_f,t) = G_0 \tag{3.75}$$

$$\widehat{n} = -\frac{\partial\widehat{G}/\partial x_i}{\left|\partial\widehat{G}/\partial x_i\right|} \tag{3.76}$$

$$\frac{\partial(\overline{\rho}\widehat{G})}{\partial t} + \frac{\partial\left(\overline{\rho}\widehat{u}_i\widehat{G}\right)}{\partial x_i} = \left(\widehat{s}_l + s_t - D\widehat{\kappa} - D_t Da_\Delta^{-2}\widehat{\kappa}\right)\left|\frac{\partial\widehat{G}}{\partial x_i}\right| \tag{3.77}$$

for $Da < 1$ the last term in the bracket on the right hand side becomes $D_t\widehat{\kappa}$.

3.3.4 The Well Stirred Reactor Model

The unburnt gases ahead of the flame front are in average homogeneous, however, small gradients of temperature or species concentrations are always present and play an import role in the auto-ignition formation process. To predict auto-ignition in the unburnt zone, each computational cell can be treated as a Well Stirred Reactor (WSR) with constant volume. The name giving model assumption of a WSR is that within the reactor the mixture is well or perfectly stirred, so that it is fully homogeneous. Therefore, on cell level, the three-dimensional problem is broken down a to zero-dimensional problem. No transport of the momentum is needed within the cell. However, the transport of species between cells or WSR is governed by the species transport equation (equation (3.2)). Species and temperature are time dependent only (equations (3.82) and (3.85)), source terms can be calculated from a provided reaction scheme. Such a reaction scheme describes a set of reactions n_r and the number of chemical species n_k [26]:

$$\sum_{k=1}^{n_k} \nu_{k,r}' X_k \rightleftarrows \sum_{k=1}^{n_k} \nu_{k,r}'' X_k \quad for \quad k = 1,....,n_r \tag{3.78}$$

Where $\nu_{k,r}'$ is the stoichiometric coefficient of the reactants and $\nu_{k,r}''$ of the products. From the scheme the formation rate $\dot{\omega}_k$ of species k is obtained by [26]:

$$\dot{\omega}_k = \sum_{k=1}^{n_k} (\nu_{k,r}'' - \nu_{k,r}') \left[k_{f,r} \prod_{k=1}^{n_k} [X_k]^{\nu_{k,r}'} - k_{b,r} \prod_{k=1}^{n_k} [X_k]^{\nu_{k,r}''} \right] \tag{3.79}$$

where $k_{f,r}$ and $k_{b,r}$ are the forward and backwards reaction rate, respectively, and can be determined by the Arrhenius law in its three-parameter form and the equilibrium constant of the

reaction K_{eq} [26]:

$$k_{f,r}(T) = A_r T^b exp\left(\frac{-E_a}{\bar{R}T}\right) \tag{3.80}$$

$$k_{b,r} = \frac{k_{f,r}}{K_{eq}} \tag{3.81}$$

The activation energy E_a, the pre-exponential factor A_r and b need to be found empirically or from theoretical considerations and are provided by the reaction scheme [61]. The calculated species reaction rate $\dot{\omega}_k$ is then used to calculate the formation or consumption of species k in a cell and the change in temperature according to the reactions [82]:

$$\frac{dY_k}{dt} = \dot{\omega}_k \frac{M_k}{\rho} \tag{3.82}$$

$$\frac{dT}{dt} = -\frac{1}{\rho c_{v,mix}} \sum_{k=1}^{n_s} \left(\frac{U_i}{M_i}\frac{dY_k}{dt}\right) \tag{3.83}$$

The change of the internal energy of species U_k equals the product of temperature and the change in entropy for a constant volume. This product can be expressed using the fundamental equation of thermodynamics for enthalpy and a closed system:

$$dh = Tds + Vdp \tag{3.84}$$

So that for a cell in the computational domain yields [8]:

$$\frac{dT}{dt} = \frac{1}{M_{mix} c_{v,mix}} \left(V\frac{dp}{dt} - \sum_{k=1}^{n_s} h_k \dot{\omega}_k\right) \tag{3.85}$$

The advantage of the WSR model is that the species source terms are calculated using cell mean values. Different than for other models in turbulent combustion modeling, no closure is done. The most important drawback of this simplification is that the model does not include turbulence-chemistry interactions. Long computational times due to the solution of the chemistry in each cell can be reduced by using clustering techniques as the multi-zone model in Converge [8]. In such models, cells with similar thermodynamic conditions are grouped by, for example, equivalence ratio and temperature. The solution for the cluster center is then mapped back to the individual cells.

3.4 The Stochastic Reactor Model for SI Engines

The Stochastic Reactor Model (SRM) is a zero-dimensional engine simulation tool, that is developed for the efficient prediction of in-cylinder combustion process using detailed chemistry [88, 89, 90, 91]. The reduction in dimensions decreases the computational costs

compared to CFD simulations from hours per cycle to minutes for chemistry solved on the fly and seconds for tabulated chemistry [92]. Therefore, it can be used to analyze cycle-to-cycle variations and be integrated in one-dimensional full cycle or system simulations [89].

In the SRM, the in-cylinder mass is discretized into virtual packages that are called particles. Each of those particles has its own chemical composition, mass and enthalpy. Each of the particles is a discrete realization of the joint PDF of species and enthalpy. The model approach accounts for inhomogeneity. The solution of a kinetic scheme for each particle allows to study chemistry effects in detail. The mixing between the particles governs the physical and chemical combustion processes. In the SRM, the flow field is not solved due to the reduction is spatial dimensionality. Particles have no spatial position or motion. As consequence there are no convection and diffusion terms or processes. The mixing is on molecular level only. The mixing time determines the mixing rate of the particles and therefore represents the turbulent flow and the turbulence-chemistry interaction. The mixing time needs to be provided as input, either from a CFD simulation or from a parameterized model [91]. The provided mixing time determines the particle-particle mixing intensity for the mixing model. Beside mixing with each other, random selected particles can exchange heat with the wall. The distributions can be compared to experiments and three-dimensional simulations [90, 93, 94].

3.4.1 Physical Model

In the SRM, the evolution of a mass density function (MDF) instead of a PDF is solved since the system follows a mass-based description. The MDF is given by $F_\varphi(\psi_1, \psi_2, ..., \psi_k, \psi_{k+1}, t)$ with [90]:

$$\varphi(t) = (\varphi_1, \varphi_2, ..., \varphi_k, \varphi_{k+1}, t) = (Y_1, Y_2, ..., Y_k, h, t), \tag{3.86}$$

where in the following the notation $F_\varphi = F_\varphi(\psi_1, \psi_2, ..., \psi_k, \psi_{k+1}, t)$ is used for readability. The SRM is based on the model of a partially stirred plug flow reactor [90, 95]. Statistical homogeneity is assumed. The MDF does not vary in space [96].
The mixing and the heat transfer are governed by stochastic models. To introduce stochastic in the heat transfer a set of randomly chosen particles can transfer heat to the wall in each time step only. The source term of a property ψ governs the change of the MDF. It consists of terms for reactions, volume work S_i and heat transfer to the walls S_{trans}. The heat transfer is modeled according to Woschni [97] with the heat transfer coefficient h_g. To model fluctuations in this term, a finite difference scheme is introduced. The stochastic process is introducing fluctuation. The temperature becomes therefore a fluctuation and modeling parameter. The following set of

equations results [90, 95]:

$$\frac{\partial F_\varphi}{\partial t} + \frac{\partial}{\partial \psi_i}\left[S_i(\psi)F_\varphi\right] + \frac{\partial}{\partial \psi_{k+1}}\left[S_{trans}(\psi_{k+1})F_\varphi\right] = \text{mixing term} \tag{3.87}$$

$$S_i = \frac{M_i}{\rho}\dot{\omega}_{ij} \quad \text{with } i = 1,...,k \text{ and } j = 1,...,r \tag{3.88}$$

$$S_{k+1} = \frac{1}{C_p}\sum_{i=1}^{k} h_i \frac{M_i}{\rho}\dot{\omega}_{ij} - V\frac{1}{C_p}\frac{dp}{dt} \tag{3.89}$$

$$S_{trans} = -\frac{h_g A}{C_p}(T - T_{wall}) \tag{3.90}$$

where the last term in equation (3.87) replaced by [90, 95]:

$$\frac{1}{h}\left[S_{trans}(\psi_{k+1})F_\varphi - S_{trans}(\psi_{k+1}-h)F_\varphi(\psi_1,....,\psi_k,\psi_{k+1}-h,t)\right] \text{ if } S_{trans}(\psi_{k+1}) < 0$$
$$\frac{1}{h}\left[S_{trans}(\psi_{k+1})F_\varphi - S_{trans}(\psi_{k+1}+h)F_\varphi(\psi_1,....,\psi_k,\psi_{k+1}+h,t)\right] \text{ if } S_{trans}(\psi_{k+1}) > 0$$

The MDFs is solved with operator splitting [90, 95]:

$$\frac{\partial F_\varphi}{\partial t} = \left(\frac{\partial F_\varphi}{\partial t}\right)_{\Delta V} + \left(\frac{\partial F_\varphi}{\partial t}\right)_{\text{mix}} + \left(\frac{\partial F_\varphi}{\partial t}\right)_{\text{chem}} + \left(\frac{\partial F_\varphi}{\partial t}\right)_{\text{trans}} + \left(\frac{\partial F_\varphi}{\partial t}\right)_{\text{vap}} \tag{3.91}$$

where the indices stand for ΔV - piston movement, mix - mixing, chem - chemical reactions and trans - heat transfer, vap - vaporization (only for direct injection, not applied in this work). The single terms are given by [90, 95]:

$$\left(\frac{\partial F_\varphi}{\partial t}\right)_{\Delta V} = p_{c,\Delta V} \tag{3.92}$$

$$\left(\frac{\partial F_\varphi}{\partial t}\right)_{\text{mix}} = \frac{C_\varphi \beta}{\tau_{mix}}\left(\int_{\Delta\varphi} F_\varphi(\psi - \Delta\psi, i)F_\varphi(\psi + \Delta\psi)d(\Delta\psi) - F_\varphi\right) + p_{c,\text{mix}} \tag{3.93}$$

$$\left(\frac{\partial F_\varphi}{\partial t}\right)_{\text{chem}} = \frac{\partial}{\partial \psi_{k+1}}\left(\frac{1}{C_p}\sum_{i=1}^{k} h_i \frac{M_i}{\rho}\dot{\omega}(\varphi)F_\varphi\right) - \sum_{i=1}^{k}\frac{\partial}{\partial \psi_i}\left(\frac{M_i}{\rho}\dot{\omega}(\varphi)F_\varphi\right) + p_{c,\text{chem}} \tag{3.94}$$

$$\left(\frac{\partial F_\varphi}{\partial t}\right)_{\text{trans}} = \frac{\partial}{\partial \psi_{k+1}}\left(\frac{h_g A}{C_p}(\psi_{k+1} - T_{wall}F_\varphi)\right) + p_{c,\text{trans}} \tag{3.95}$$

$\frac{\partial F_\varphi}{\partial t}$ is solved under the assumption of constant pressure. Therefore a pressure correction at the end of the time step is necessary. The terms $p_{c,x}$ are given by [90]:

$$p_{c,x} = \frac{\partial}{\partial \psi_{k+1}} \left(V \frac{1}{C_p} \left[\frac{dp}{dt} \right]_x F_\varphi \right) \tag{3.96}$$

For the solution of the different steps a mixing model (section 3.4.2), equations for piston movement, heat transfer and the calculation of the combustion chemistry is needed. Details are given in [90, 95].

3.4.2 Mixing Time and Model

Turbulence is an important process of all turbulent combustion processes and characterized by its stochastic nature and three-dimensionality. Due to the zero-dimensional model approach, in contrast to the earlier discussed three-dimensional approach, the flow field is not solved, but instead the mixing is modeled, which is a result of the turbulence. From the consideration of the energy cascade and dimensional analysis, the velocity fluctuation u' is given by the ratio of the integral length scale l and the turbulent mixing time $\tau_{t,mix}$. Integral length scale and velocity fluctuations can be related to the turbulent kinetic energy k and dissipation of the turbulent kinetic energy ϵ, which results in [17, 96]:

$$\tau_{t,mix} = \frac{l}{u'} \approx \frac{k}{\epsilon} \tag{3.97}$$

Consequently, the turbulent mixing time can be estimated from CFD RANS simulations and applied to the SRM. However, in the SRM the scalar mixing time τ_{mix} is needed. Turbulent and scalar mixing time can be related using the mixing time constant C_φ, that represents the velocity scalar decay time [96, 98]:

$$\tau_{mix} = \frac{\tau_{t,mix}}{C_\varphi} \tag{3.98}$$

Figure 3.7 shows an example of turbulent kinetic energy k and turbulent dissipation ϵ in a closed motored and a fired cycle of a port-injected SI engine CFD simulation. In Figure 3.8, the corresponding turbulent mixing time $\tau_{t,mix}$ is shown. At top dead center (TDC), the compression of the charge is the highest, the turbulence and mixing increase, k and ϵ reach their maximum. The mixing time, a measure of turbulence intensity and mixing, decreases. While combustion (ignition shortly before TDC), the mixing time decreases as mixing is increased due to the flame propagation.

The interaction by exchange with the mean (IMEM) [99], the multi-weighted coalescence/dispersal (C/D) model by Curl [100] and the modified (C/D) model by Janicka et al. [101] are available for the SRM [88, 95]. In this work, the C/D model is applied and therefore discussed in the following.

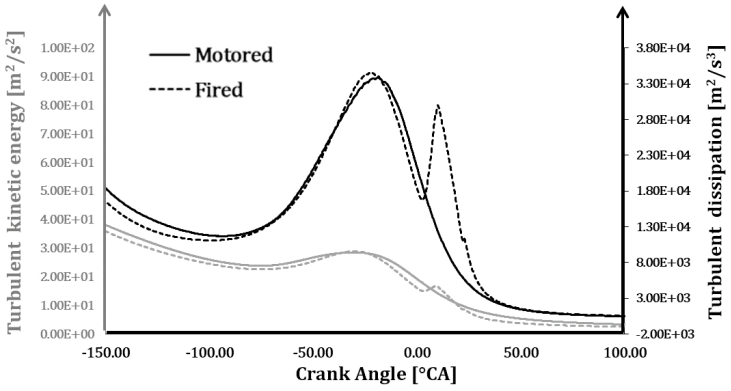

Figure 3.7: Exemplary trends of the turbulent kinetic energy k (gray) and dissipation of the turbulent kinetic energy ϵ (black) extracted from a motored and a fired RANS simulation.

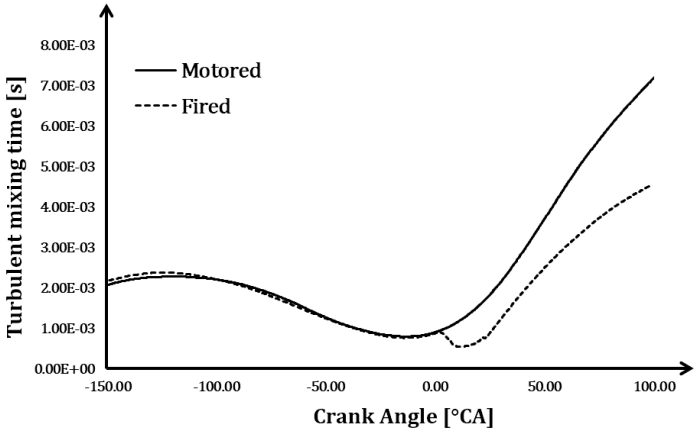

Figure 3.8: Exemplary turbulent mixing time $\tau_{t,mix}$ calculated using the turbulent kinetic energy k and turbulent dissipation ϵ from Figure 3.7.

The basic idea of the C/D model is, that two randomly chosen particles from a set of particles n, where $n < N$ and N is the total number of particles, are mixed to their mean. Figure 3.9 illustrates the model: the randomly chosen particle (a) with its properties $\Psi^{(a)}$ at $t = 0$ is mixed with the randomly chosen particle (b). At the time setup $t + \Delta t$, their properties are equal and the mean of their sum at $t = 0$ is given [88]:

$$\Psi^{(a)}(t+\Delta t) = \Psi^{(b)}(t+\Delta t) = \frac{1}{2}\left(\Psi^{(a)}(t=0) + \Psi^{(b)}(t=0)\right) \tag{3.99}$$

In the next mixing step, the particles are mixed with another particle (n) if again chosen to be in the set n. The mean values of a property of the computational domain and the number of particles are not changed during the mixing. The mixing term for the C/D model is given by

[95]:

$$\text{mixing term} = \frac{C_\varphi \beta}{\tau_{mix}} \left(\int_{\Delta\varphi} F_\varphi(\psi - \Delta\psi, t) F_\varphi(\psi + \Delta\psi) d(\Delta\varphi) - F_\varphi \right) \tag{3.100}$$

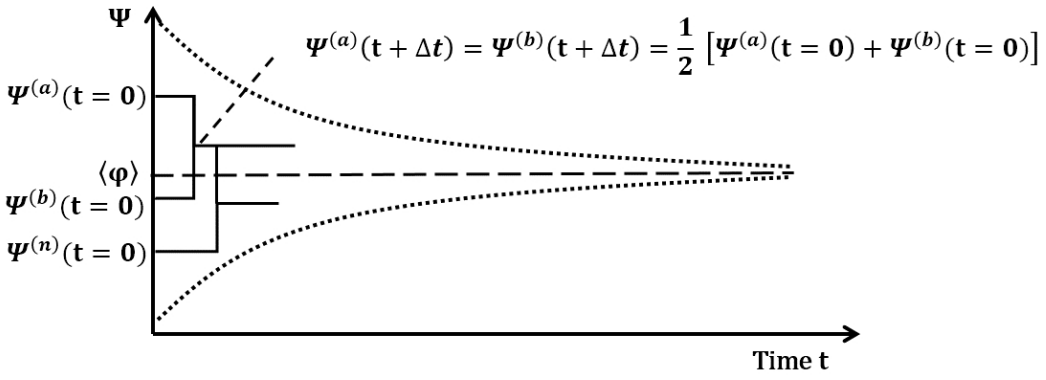

Figure 3.9: Mixing step in the C/D model. Figure according to [88].

The frequency of how often particles are chosen and mixed within a global time step Δt depends on the scalar mixing time τ_{mix}. Randomly chosen, but depending on the scalar mixing time τ_{mix}, sub time steps are calculated. In each sub-time step, particles are chosen and mixed to their mean. The smaller the mixing time, the smaller the sub-time steps and the more mixing steps are carried out within the global time step Δt. If the mixing is faster, the distribution in species concentrations and temperature become homogeneous faster [90].

3.4.3 Two Zone Approach

For the Spark Ignition Stochastic Reactor Model (SI-SRM), a two-zone approach is used for the combustion prediction. Particles in the unburnt and the burnt zone can mix with particles in their own zone, but not with particles in the other zone. There is no interaction between unburnt and burnt zone, except for mass transfer from the unburnt to burnt zone. This mass transfer is governed by the turbulent flame propagation, which can be modeled using equation (3.57) or the model based on the correlation by Kolla et al. [102], introduced for the SI-SRM by Bjerkborn et al. [103]:

$$\begin{aligned} \frac{s_t}{s_l} = \Bigg(& \left[b - a \left(1 + \left(\frac{u'}{s_l} \right)^{1.5} \left(\frac{\delta}{l} \right)^{0.5} \right)^{-0.4} \right] \frac{(T_f - T_u)}{T_f} \frac{\delta}{l} \frac{u'}{s_l} \\ & + d \left[\left(\frac{u'}{s_l} \right)^2 + \left(\frac{\delta}{l} \right)^{-0.25} \left(\frac{u'}{s_l} \right)^{-2.25} \right]^{-1} \Bigg)^{0.5} \end{aligned} \tag{3.101}$$

Here, u' and the unburnt temperature T_u are calculated by the SI-SRM and T_f is the adiabatic flame temperature. The other parameters are provided by the user, the values are given in Table 3.5. The laminar flame speed is retrieved as in CFD by using a global EGR value form laminar flame speed look-up tables (4.3). The varying EGR composition therefore affects the auto-ignition prediction, but is neglected for the laminar flame speed retrieval. Starting from the spark, the flame front is tracked to give quasi-dimensional information about the spatial development of the flame [96, 103, 104]. Detailed chemistry is solved in the burnt zone to predict emissions as well as to predict auto-ignition in the fresh gas zone. Cycle-to-cycle variations are predicted based on the stochastic mixing of the particles, the random choice of particles for heat transfer with the wall and variation of inlet temperature and EGR composition according to the previous engine cycle [90]. The model concept is illustrated in Figure 3.10.

Table 3.5: Parameters for the flame propagation prediction within the SI-SRM.

Parameter	**Source**	**Applied value**
Laminar flame speed s_l	look-up table	
Laminar flame thickness δ	given by user	0.6 mm
Integral length scale l	given by user	4.0 mm
Correlation parameter a	$a = \frac{1.1}{d}$ [103]	0.665
Correlation parameter b	$b = \frac{1.6}{d}$ [103]	0.967
Correlation parameter d	$d = \frac{(2C_m - 1)\beta'}{18C_\mu}$ [103]	1.654
Bray parameter C_m	[102]	0.7
Modell parameter β'	[102]	6.7
Turbulent viscosity coefficient C_μ	[102]	0.09

Gogan et al. [105] found that using this approach it is possible to account for the inhomogeneities in gas composition and temperature, and the fluctuations in the wall-gas heat transfer interaction. The availability of detailed information of the reactions in the unburnt zone, enables to analyze abnormal combustion based on detailed reaction schemes [104, 106, 107, 108]. The information about the conditions in the unburnt zone are of importance for the knock prediction. Stenlåås et al. [106] found that nitrogen monoxide NO has a strong influence on engine knock, since it delays the first stage of the ignition process (the low temperature reactions). The released heat is hereby limited by the transfer from NO to NO_2. Overall, NO promotes the ignition process. The impact of NO was found to be more dominant in lean mixtures.

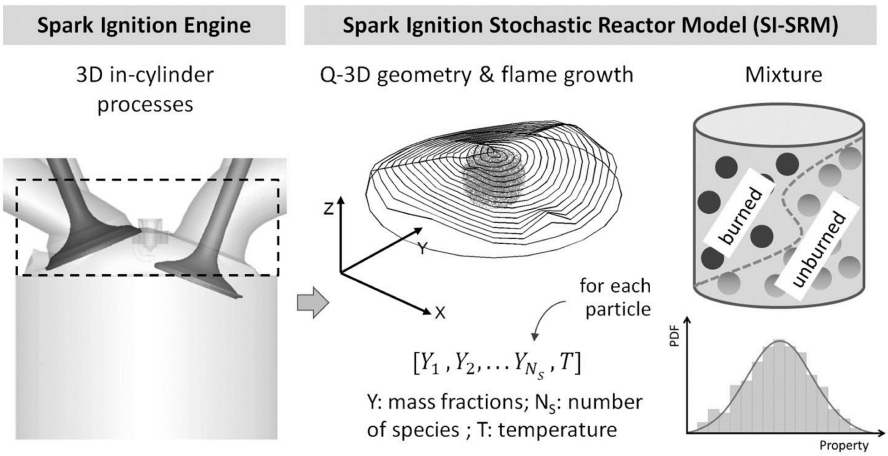

Figure 3.10: Model concept of the SI-SRM. Figure reprinted from [96].

3.5 Model Choice and Interaction

For the CFD simulations, the RANS approach has been chosen for knock prediction due to several reasons: The RANS simulations are used to characterize and investigate the mean auto-ignition tendency of an operating point. Beside the assessment of the impact of the operating conditions and spark timing, the work aims to investigation the impact of octane rating and formulation of the surrogate. For those studies, detailed chemistry is needed since it can reproduce the impact of different chemical properties, such as ignition delay time, C:H:O-ratio or octane sensitivity, of the surrogate. For these investigations the same operating point needs to be simulated for each investigated surrogate. Chemical properties do not vary over cycles, so that the mean tendency of an operating point is of interest. Further, the CPU demand for the solution of the detailed reaction scheme with more than 180 species is high even for RANS, but still acceptable for engineering purposes. A CPU time comparison is given in Table 3.6. From this table can be seen that LES is much more expensive than RANS, but since LES is the more physical approach, the developed methodology is verified using LES.

It was decided to use the G-equation model, since it provides a detailed model for the turbulent flame propagation based on properties of macro- and microsales. Further, allows the G-equation model for a turbulent flame speed model based on provided laminar flame speed tables, which provides a direct connection between the detailed chemistry and flame propagation prediction. The laminar flame speeds obtained from the detailed mechanisms have been validated over a wide range of conditions and for different surrogates. This enables to predict the impact of the surrogate formulation on the propagation of the flame front. In order to make the combustion model complete, the WSR model is used in the unburnt zone. The WSR models enables to

predict auto-ignition based on detailed chemistry. Further, a consistent model formulation for the LES context is available for verification purposes.

Table 3.6: CPU costs of the different model approaches using the 188 species mechanisms by Seidel [29]. CPU times include the simulation of the combustion only (-20°CA aTDC to EVO) for CFD using Converge 2.4.9 [8] and the full closed cycle for the SI-SRM.

	LES	**RANS**	**SI-SRM**
CPU time [h]	2558.2	127.2	0.32

Cycle-to-cycle variations are important to consider in SI engine development. Therefore, the investigation of the mean auto-ignition is obtained with RANS complemented by zero-dimensional simulations using the SI-SRM. Thanks to the PDF based concept, the SI-SRM can reproduce inhomogeneity in the unburnt zone. The solution of the chemistry governs auto-ignition prediction with low CPU costs. This allows to calculate several consecutive cycles. The stochastic mixing of the particles and stochastic heat transfer to the walls mimic the stochastics of the flow. Cyclic variations can further be imposed by applying EGR compositions based on the previous cycle and by imposing a PDF for the inflammation time and the mixing time. The same chemistry and laminar flame speed tables as in CFD can be applied. Further, the mixing time from CFD is imposed. Using this interaction, the SI-SRM can support the details known from CFD, such as size, shape and number of ignition kernels, with the knocking tendency of the whole pressure range of an operating point.

4 Detailed Chemistry

To support engine development, accurate and efficient simulation tools are needed. These tools shall reproduce the chemical and physical processes that governs the flame propagation and lead to auto-ignition in the unburnt gases.

The laminar flame speed is an important input parameter for the flame propagation prediction. Often, this parameter is taken from correlations, as for example by Gülder et al. [109] or Metghalchi and Keck [110]. Those correlations can replicate the change of the reference laminar flame speed s_l^0 on pressure p, unburnt temperate T_u, equivalence ratio ϕ or dilution. Very specific fuel effects such as the location of the maximum laminar flame speed that depends on the ongoing reactions and oxygen demand or the impact of aromatic or alcohol content, cannot be covered by generalized correlations. Therefore, in this work, the laminar flame speed is calculated using the flame speed scheme from Seidel [29] and the freely propagation flame module in LOGEsoft [9]. This module follows the model described in section 3.3.1. The laminar flame speeds are calculated for a specific surrogate and stored in look-up tables.

Since the fuel octane rating has a major impact on auto-ignition, the surrogate fuel must be formulated in a way that it represents the octane rating of the commercial gasoline fuel. To consider fuel blend effects, modeling approaches with varying detail are available in literature. The use of a global chemical mechanism and an adequate fitting procedure for auto-ignition prediction are, for instance, proposed in the Shell model [111, 112, 113]. Through the use of (reduced) reaction mechanisms, the oxidation of the fuel species is described in more detail. Frequently, Primary Reference Fuels (PRF) are applied to predict engine knock. Their composition of *iso*-octane (RON=100, MON=100) and *n*-heptane (RON=0, MON=0) can be used to compose a surrogate that represents the RON of a commercial gasoline fuel, but never at the same time the correct MON or octane sensitivity S. With this rather simple surrogate fuel model, auto-ignition can be reproduced, for instance, demonstrated in Teodosio et al. [114], but the PRF model does not capture the major chemical and physical properties of commercial gasoline such as ethanol and aromatic content or C:H:O-ratio. To reproduce these properties, the use of ethanol toluene reference fuels (ETRFs) was suggested [39, 115, 116]. This surrogate

fuel is a blend of *n*-heptane, *iso*-octane, toluene and ethanol. A reaction mechanism describing the combustion of a surrogate caters for the prediction of the impact of chemical and physical gasoline properties on auto-ignition in engine simulations. In contrast to fitted correlation, detailed chemistry can also capture the impact of exhaust gas recirculation (EGR) and radicals or NOx in the residual gas discussed, for example, in the works by Stenlåås et al. [106] and Hoffmeyer et al. [117] and references therein. Therefore, ETRF reaction schemes are today the best compromise to define a flexible surrogate fuel for gasoline with high accuracy [117] while keeping the number of surrogate components low.

4.1 Kinetic Model

A reaction mechanism is a set of elementary reactions. In combustion applications, the combustion is governed by the interaction of those reactions. To reduce the number of elementary reactions, they can be merged using the concepts of quasi-steady state or partial equilibrium. Applying those concepts, a net or global reaction of the considered elementary reactions results [61]. As discussed before, chemistry happens at various scales. Of special interest is therefore the rate of a certain reaction or how fast a species is formed or consumed. The reaction rate of species A can be obtained exemplary by [61]:

$$A + B + C + ... \xrightarrow{k} D + E + F + ... \tag{4.1}$$

$$\begin{aligned} &\text{forward reaction} && \frac{d[A]}{dt} = -k_{f,r}[A]^a[B]^b[C]^c + ... \\ &\text{backward reaction} && \frac{d[A]}{dt} = \quad k_{b,r}[D]^d[E]^e[F]^f + ... \end{aligned} \tag{4.2}$$

Where k_r denotes the rate coefficient, $[x]$ the concentration of species x and ^{x} the reaction order. The forward and backward rate coefficients are connected via the equilibrium constant K_{eq}. The rate coefficients are strongly temperature dependent, described by the Arrhenius law [61]:

$$k_r = A_r T^b exp\left(-\frac{E_a}{RT}\right) \tag{4.3}$$

The activation energy E_a represents the energy barrier, that needs to be overcome to initialize the progress of a reaction. A_r is called the pre-exponential factor and b is the temperature correction of A_r. The parameters A_r, b and E_a can be obtained from experiments or theoretical considerations. In a reaction scheme, they need to be listed for each included reaction. Dissociation and recombinations reactions are also pressure dependent. This pressure dependency is apparent and indicate, that those reactions are not elementary, but a sequence of very fast

reactions [61]. Anyhow, this dependency is described by the Lindemann model. It says, that for breaking up the bond sufficient energy needs to be available and that this energy can be provided by the collision with another molecule M. The collision leads to the excitation of the considered species A, which can then decompose or rearrange. One needs to distinguish between low and high pressure dependency. At low pressures, the concentration of the collision partner *M* and there for the collision probability is small. The reaction rate depends on [A] and [M]. For this regime the Arrhenius coefficients are corrected. In the mechanism this is indicated with the keyword "LOW" [61]. At elevated pressures, the concentration of M is high. The molecules collide frequently. In this regime the reaction rate depends on the excited molecule only. The apparent reaction order is one. In the reaction mechanism the center of the fall off curves are given after the key word "TROE" instead of the Arrhenius coefficients.
Thermal properties (heat capacity, specific enthalpy and entropy) are calculated using NASA polynomials. The transport properties (viscosity, conductivity and diffusion coefficient) are retrieved based on provided molecule specific properties such as the collision diameter or polarizability. In three-dimensional simulations those transport data are not needed, the species diffusion coefficient is here assumed to be the same for all species. Transport is governed from the solved flow. In contrast, for one dimensional flame calculations, used for the laminar flame speed, those properties are important. More details are given, for instance, in [21, 61, 118].

Reaction schemes are carefully validated against ignition delay time, laminar flame speed and speciation experiments. However, those experiments (i.e. burner stabilized flames, shock tubes, jet stirred reactors, rapid compression machines) are limited in operating pressure and temperature. This circumstance, leads to the concerns for the use of detailed chemistry schemes for engine simulations. With pressures $>$40 bar and temperatures $>$800 K, their operating conditions are often above the range of fundamental experiments. The leading question here is: can under different conditions validated reaction schemes be extrapolated to higher pressures and temperatures? Though, if the trends over wide ranges of equivalence ratio, pressure and temperature are well predicted, there is a certain confidence that they can be used outside the validated region. Further, they can give a deep inside and understanding of the ongoing chemistry.

In this work, the ETRF reaction scheme by Seidel [29] is applied. For the development of the detailed mechanism, the reaction scheme core model was taken from Seidel et al. [119], and a sub-mechanism for NO_x formation was included. The sub-mechanism for *iso*-octane was developed following the rates used by Ahmed et al. [120] and from the *n*-heptane core model. The horizontal lumping technique described in Seidel et al. [121] was applied to pool chemical isomers into representative pseudo-species. The detailed scheme consists in total of

386 species and 4511 reactions. Since auto-ignition and the flame propagation are physically independent (as discussed in section 3.3) and modeled as separate processes, it was decided to split up the reduction process to these two targets (see Figure 4.1). For both skeletal schemes, a reduction procedure using the chemistry-guided reduction concept introduced by Zeuch et al. [122], which was further developed with special emphasis on engine simulation by Seidel et al. [121], was applied. The early oxidation pathways of the fuel species are formulated independently from each other. During the reduction process, the single fuel species as well as the equimolar mixture of them are controlled within a wide range of initial conditions. This concept enables to define the surrogate composition after the reduction process and to exchange the fuel composition in the engine simulations.

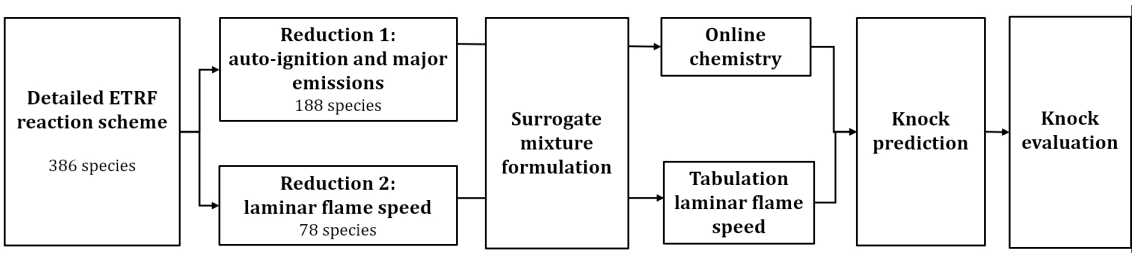

Figure 4.1: Scheme of the chemistry modeling and reduction strategy.

The reduced scheme for prediction of auto-ignition and major emissions consists of 188 species. In Figure 4.2 predicted ignition delay times τ of the detailed and the reduced scheme are compared against values obtained in shock tube experiments.
The reaction scheme for laminar flame speed s_l is reduced to 78 species. The predicted laminar flame speeds using the reduced and detailed scheme are compared against experimental values obtained from heat-flux burner experiments, exemplary shown in Figure 4.3). All simulations have been performed with LOGEsoft 1.08 [9].

4.2 Surrogate Formulation

Seidel [29] developed a surrogate formulation method based on published correlations from Morgan et al. [39] and Anderson et al. [126]. The correlation from Morgan et al. [39] is used to formulate the toluene reference fuel (TRF) surrogate for the gasoline fraction. The linear by molar fraction mixing rule for oxygenated fuels with gasoline suggested by Anderson et al. [126] is applied to determine the impact of the ethanol fraction. To compose the surrogates, the aromatic content is represented by toluene. The ethanol fraction and the RON of the gasoline are imposed as well. The *iso*-octane and *n*-heptane fractions of the surrogate are calculated to

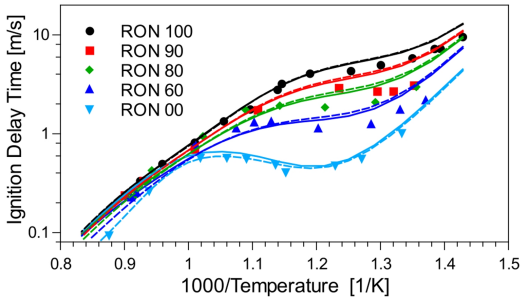

(a) Stoichiometric mixture of *iso*-octane/*n*-heptane-air mixtures. Experimental data from Fieweger et al. [123] for $\phi = 1.0$ and $40+/2$ *bar*. Simulations performed using the upper pressure limit.

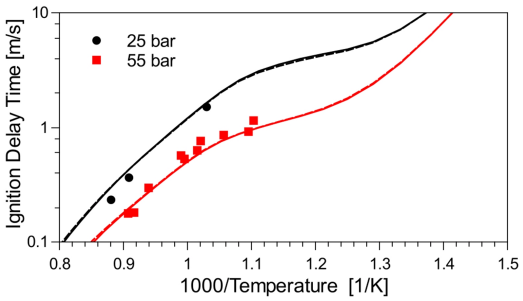

(b) Mixture of: 0.63 *iso*-octane, 0.20 toluene and 0.17 *n*-heptane (mole fraction) mixed with artificial air at $\phi = 1.0$. Experimental data from Gauthier et al. [115] (Surrogate B). See publication for scatter in initial pressure.

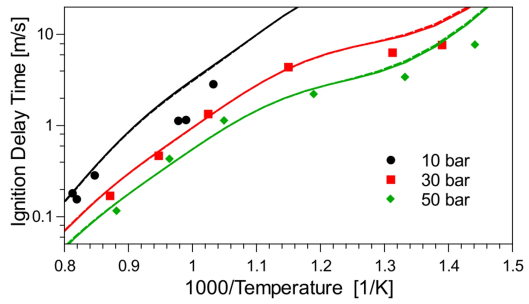

(c) Mixture of 0.18 *n*-heptane, 0.62 *iso*-octane and 0.2 ethanol (liquid volume fraction). Experimental data from Fikri et al. [124] for $\phi = 1.0$.

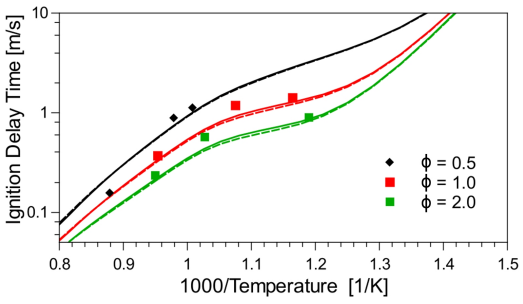

(d) Mixture of 0.56 *iso*-octane, 0.28 toluene and 0.17 *n*-heptane (mole fraction) at 52 *bar* mixed with artificial air at $\phi = 1.0$. Experimental data from Gauthier et al. [115] (Surrogate A). See publication for scatter in initial pressure.

Figure 4.2: Ignition delay time over the inverted temperature. Symbols: Experimental data. Solid lines: Detailed mechanism [29]. Dashed lines: 188 species mechanism [29]. Figures are reprinted from [12].

match the RON of the gasoline. To correlate the TRF mixture a renormalization of the PRF mixture from the space [0,100] to [0,1] is needed. Since the RON of a PRF is directly given by the mole fraction of *iso*-octane $X_{iso\text{-}octane}$ and *n*-heptane $X_{n\text{-}heptane}$, the renormalization is given by [39]:

$$P = \frac{X_{iso\text{-}octane}}{X_{iso\text{-}octane} + X_{n\text{-}heptane}} \tag{4.4}$$

The Modified Linear by Volume (MLbV) approximation for the RON of a TRF mixture is [39]:

$$RON = a_{R,P}P + a_{R,tol}X_{toluene} + a_{R,tol^2}X_{toluene}^2 + a_{R,tol,P}X_{toluene}P \tag{4.5}$$

To find the composition of a TRF surrogate with a specific toluene content, RON and the sur-

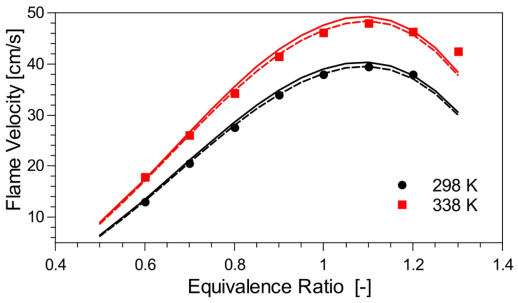

(a) Mixture of 0.333 *n*-heptane, 0.334 *iso*-octane, and 0.333 ethanol (liquid volume fraction) with air as oxidizer at atmospheric pressure. Symbols: Experimental data from van Lipzig et al. [125].

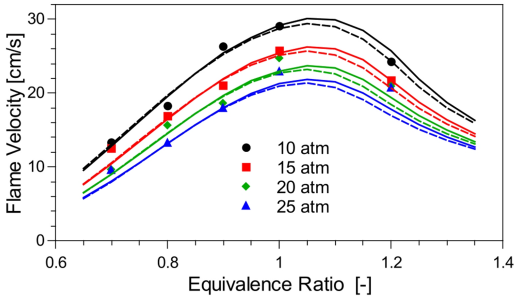

(b) Laminar flame speeds for PRF 87 / air at 373 *K* and different ambient pressures. Experimental data from Jerzembeck et al. [28].

Figure 4.3: Laminar flame speeds over ϕ. Symbols: Experiments. Solid lines: Detailed mechanism [29]. Dashed lines: 78 species mechanism [29]. Figures are reprinted from [12].

rogate sensitivity, the MLbV method can be inverted. The following equations result [39] (the coefficients are listed in Table 4.1):

$$P = \frac{RON - a_{R,tol}X_{toluene} + a_{R,tol^2}X_{toluene}^2}{100 + a_{R,tol,P}X_{toluene}} \tag{4.6}$$

$$S = a_{S,tol}X_{toluene} + a_{S,tol^2}X_{toluene}^2 + \frac{a_{S,tol,P}X_{toluene}\left(RON - a_{R,tol}X_{toluene} + a_{R,tol^2}X_{toluene}^2\right)}{100 + a_{R,tol,P}X_{toluene}} \tag{4.7}$$

Table 4.1: coefficients for the calculation of octane rating and the composition of a surrogate [39].

Coefficient	$\mathbf{a_{x,P}}$	$\mathbf{a_{x,tol}}$	$\mathbf{a_{x,tol^2}}$	$\mathbf{a_{x,tol,P}}$
RON ($x = R$)	100.0	142.79	-22.651	-111.95
MON ($x = M$)	100.0	128.00	-19.207	-119.24
S ($x = S$)	0.0	14.79	-3.444	7.29

To respect the ethanol content, the linear molar based blending rule, in detail investigated and extended by a scaling parameter P_g by Anderson et al. [126], is applied. In this approach, the octane rating ON (valid for both RON and MON) are mixed based on the ethanol mole fraction $X_{ethanol}$ [126]:

$$\begin{aligned} ON_{blend} = (1 - X_{ethanol})ON_{gasoline} + (1 - X_{ethanol})ON_{ethanol} \\ + P_g X_{ethanol})(1 - X_{ethanol})(ON_{ethanol} - ON_{gasoline}) \end{aligned} \tag{4.8}$$

P_g is a scaling parameter that needs to be determined from measurement. In case P_g is not known, it is set to $P_g = 0$, so that the last term in equation (4.8) is neglected. The surrogates are composed using the properties in Table 4.2. Once the ETRF surrogate is defined, physical and chemical properties of the surrogate such as C:H:O-ratio, MON, lower heating value (LHV) and density can be calculated in close agreement with the commercial gasoline fuels. The validation and agreement to commercial gasoline can be found in detail in [29] and in Tables 6.2 and 6.1.

Table 4.2: Properties of the surrogate species [29].

Species	**Formula**	**RON**	**MON**	**Density**	**LHV**
		[-]	[-]	$[kg/m^3]$	$[MJ/kg]$
iso-Octane	C_8H_{18}	100.0	100.0	692.01	44.427
n-Heptane	C_7H_{16}	0.0	0.0	683.81	44.566
Toluene	C_7H_8	120.0	109.0	866.89	40.589
Ethanol	C_2H_5OH	109.0	90.0	789.67	28.865

4.3 Laminar Flame Speed Tables

A well established approach to model laminar flame speeds is the use of correlations. Those correlations are build based on experiments. Frequently used correlations are from Metghalchi and Keck [110] published in 1982, developed for methanol, *iso*-octane, indolene and their mixtures and from Gülder et al. [109] published in 1984 for, among others, *iso*-octane and ethanol as well as their mixtures. Both methods calculate a reference laminar flame speed as function of the equivalence ratio ϕ, which is in a second step corrected for unburnt temperate T_u, pressure p and dilution. Predicted flame speeds for pure *iso*-octane are compared against experiments and the prediction using the 78 species skeletal mechanism for laminar flame speed prediction from Seidel [29] in Figure 4.4. The trends in pressure and temperature are kept by all models. The correlation from Metghalchi and Keck [110] cannot reproduce the gradient change at higher fuel equivalence ratios ϕ. The correlation from Gülder et al. [109] tends to over predict the laminar flame speed. Overall the detailed chemistry agrees the best in comparison to the experiment, particularly with increasing temperatures and pressures.
The different approaches have been compared in a stoichiometric initialized engine simulation (except the laminar flame speed model, the initialization and model constants are for all calculations the same). The correlations for pure *iso*-octane are applied since to the gasoline used in the experiment no ethanol has been added. In comparison, flame speed tables for pure *iso*-octane and for a TRF mixture (formulated using detailed information from the commercial gasoline) have been tested. The results are shown in Figure 4.5. It has to be noted that the CFD simulation

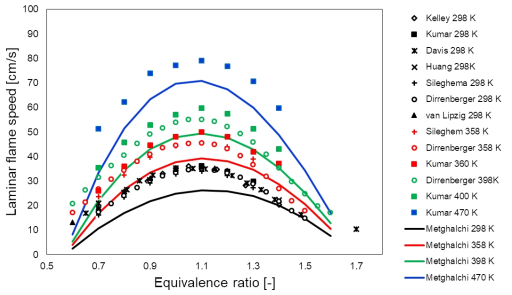

(a) Temperature dependency Metghalchi and Keck [110].

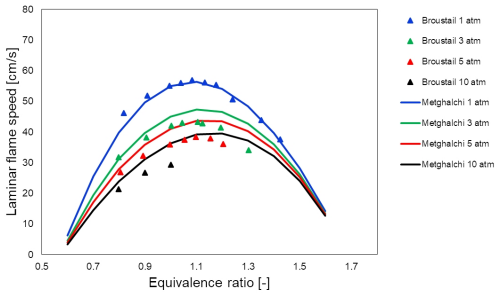

(b) Pressure dependency Metghalchi and Keck [110].

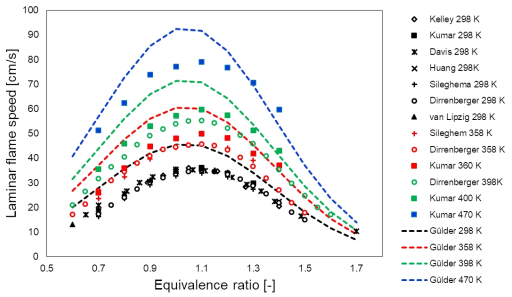

(c) Temperature dependency Gülder et al. [109].

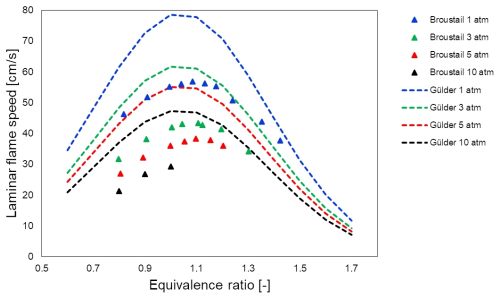

(d) Pressure dependency Gülder et al. [109].

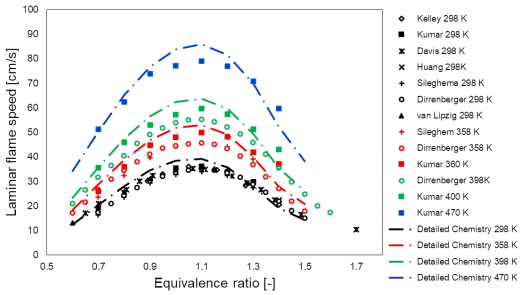

(e) Temperature dependency Seidel [29].

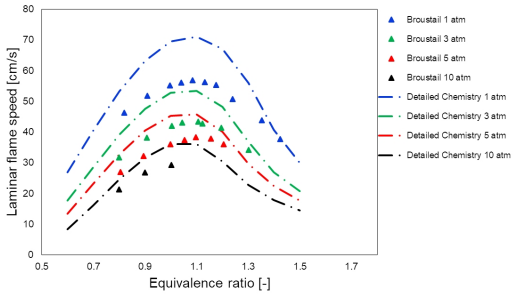

(f) Pressure dependency Seidel [29].

Figure 4.4: Comparison of the prediction of the flame speed correlations by Metghalchi and Keck [110] and Gülder [109] versus experiments and detailed chemistry [29]. Experiments *iso*-octane in air from Kelley et al. [127], Kumar et al. [128], Davis et al. [129], Huang et al. [130], Sileghem et al. [27], Dirrenberger et al. [131], van Lipzig et al. [125] and Broustail et al. [132].

has been calibrated using the TRF surrogate, therefore no conclusion on the accuracy should be drawn, rather the trends should be considered. Figure 4.6 provides a quantification of the difference in flame propagation. For that purpose, the peak pressure and its location and the combustion phasing at 5%, 10%, 50% and 90% burn duration normalized to the experiment are calculated. Using the correlation by Metghalchi and Keck [110] leads to the fastest flame propagation, the flame speed table to the slowest as expected from the laminar flame speed (Figure

4.5 (a)). The difference in predicted peak pressure between the pure *iso*-octane models is 12 bar, the difference in combustion phasing at center (50%) is 4°CA. This big deviation points out how important the choice of the laminar flame speed model is. The comparison of the tables generated using *iso*-octane and the TRF surrogate show that the flame speed prediction accounting for *n*-heptane and toluene is not negligible. Even though the simulations using one of the correlations could be calibrated to the experiment adjusting the constants of the turbulent flame propagation or the spark timing, they should only be applied within their development range, extrapolations to PRF, TRF or ETRF mixtures are not covered by the approach. The use of the flame speed tables is more flexible since every validated mechanism can be used to build up the surrogate sensitive tables. This approach therefore allows to investigate and predict changes in flame propagation due to certain characteristics of the surrogate.

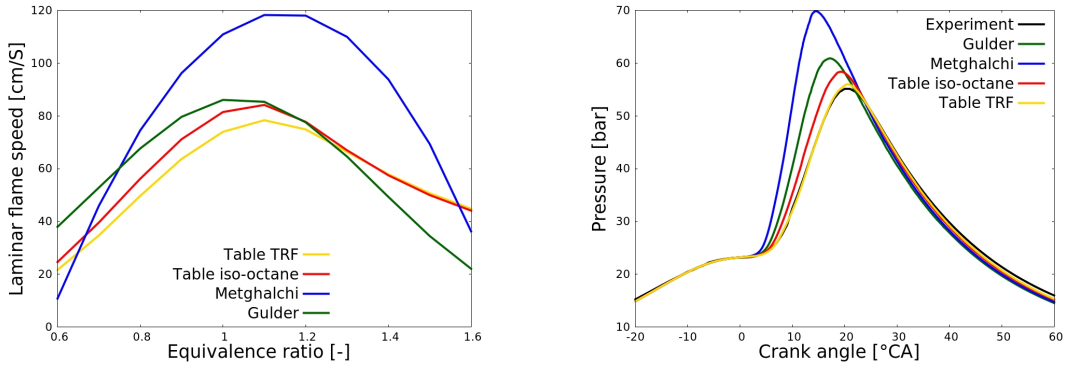

(a) Predicted laminar flame speed at 800 K and 60 bar.

(b) Predicted mean pressure.

Figure 4.5: Comparison using flame speed correlations and a flame speed table in engine simulations.

In both approaches, using correlations or a flame speed table, the flame speed is retrieved cell local depending on temperature, pressure and global dilution. During the flame speed table generation, it can be decided if the recirculated exhaust gas/diluent consists of nitrogen (N_2) only or of a mixture of air and the main combustion products water (H_2O) and carbon dioxide (CO_2). However, in the flame speed retrieval only the global dilution factor is considered independent of the diluent definition in the table. Diluent stratification in the charge is neglected. Different than in the CFM or ECFM model, the unburnt composition is not directly available in the G-equation model since it is not needed for the model formulation. By transporting non-reactive tracers for the composition of the unburnt zone, the impact of single species could be implemented. Anyhow, those species would needed to be accounted for in the table generation as well.

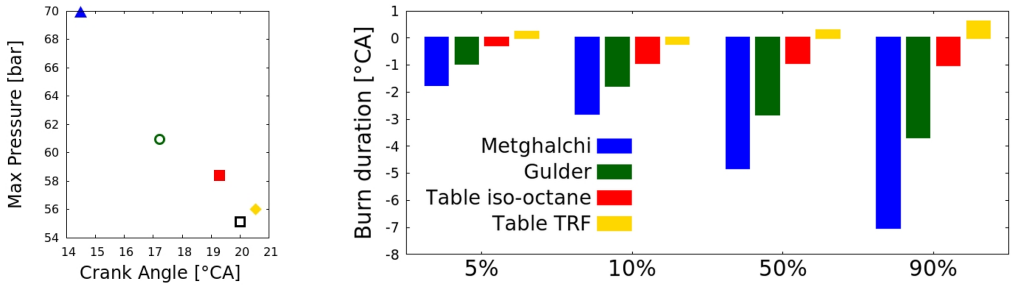

(a) Location of the maximum of the mean pressure.

(b) Combustion phasing.

Figure 4.6: Predicted location of the peak pressure and the combustion phasing related to the experiment. Analysis of the combustion prediction using different methods for the laminar flame speed (corresponding to Figure 5.20 (d).

Table 4.3: Ranges of the laminar flame speed look-up tables.

Property	**Minimum**	**Maximum**	**Step size**
Pressure p	1 *bar*	10 *bar*	1 *bar*
	10 *bar*	150 *bar*	10 *bar*
Unburnt temperature T_u	350 *K*	1600 *K*	50 *K*
Fuel/air equivalence ratio ϕ	0.5	1.5	0.05
EGR level	0.0 %	30.0 %	10.0 %

Due to the benefits of a model based on detailed chemistry, in this work, prior to the engine simulations the 78 species skeletal mechanism is used to calculate the laminar flame speeds for specific surrogates. The small size of the mechanism allows building up laminar flame speed tables over wide ranges of inlet pressure p, unburnt temperature T_u, fuel-air equivalence ratio ϕ and EGR levels efficiently (Table 4.3). The ranges have been chosen to cover the unburnt conditions in modern SI engines. To calculate the flame speed for a given p, T_u and ϕ, a planar steady state flame normal to the x_1-coordinate is considered. For the laminar flame speed prediction, models for variable Lewis numbers, thermo diffusion and radiation losses are applied. The calculated laminar flame speeds are stored in look-up tables build up using LOGEsoft 1.08 [9]. The table is read via user coding to the CFD code Converge [8] where the look-up parameters are the same as listed in Table 4.3. The same tables are applied in the SI-SRM.

5 Resonance Theory in Three-Dimensional Engine Simulations

5.1 Methodology

In the post-processing approach, the physical and chemical properties of the predicted auto-ignition kernels are related to the properties to the works by Bradley and colleagues [2, 4, 5, 3] and Peters et al. [6, 7] to analyze the regime of the predicted auto-ignition. In these works, the hotspot size r_0 and the temperature gradient $(\partial T/\partial r)$ were assumed to have a certain value; in the present post-processing method, the hotspot size is calculated from the reaction progress. With respect to the limitations of the RANS framework, the present approach analyzes the regime of the predicted auto-ignition and evaluates if a developing detonation could be initialized without taking the predicted pressure gradients or pressure wave into account. To evaluate whether the predicted auto-ignition in the three-dimensional simulations is harmless or whether a developing detonation may be formed, the auto-ignition is analyzed in detail: as the spark is induced and the flame propagates, the pressure and the temperature in the end gases increase. Depending on the local pressure and temperature history in the unburnt gases, auto-ignition is predicted. A steep increase in the calculated pressure rise rate indicate an auto-ignition event. The ignition events are predicted based on the aforementioned reaction scheme (section 4.1). Hence, species that are typically involved in an ignition process can be studied (see also discussion in section 3.4). Locally, elevated temperatures allow for the first formation of radicals, which promote the ignition process by the oxidation of the fuel molecules. In this temperature regime, typical low-temperature species such as formaldehyde (CH_2O) are produced. An example of a hotspot with high concentrations of CH_2O is shown in Figure 5.1. The oxidation process propagates and leads to the formation of an ignition kernel. The ignition is characterized by the sudden production of OH radicals, which is a typical high temperature chemistry marker. Simultaneously, with this increased OH radical concentrations, formaldehyde is rapidly

consumed in this region (Figure 5.1).

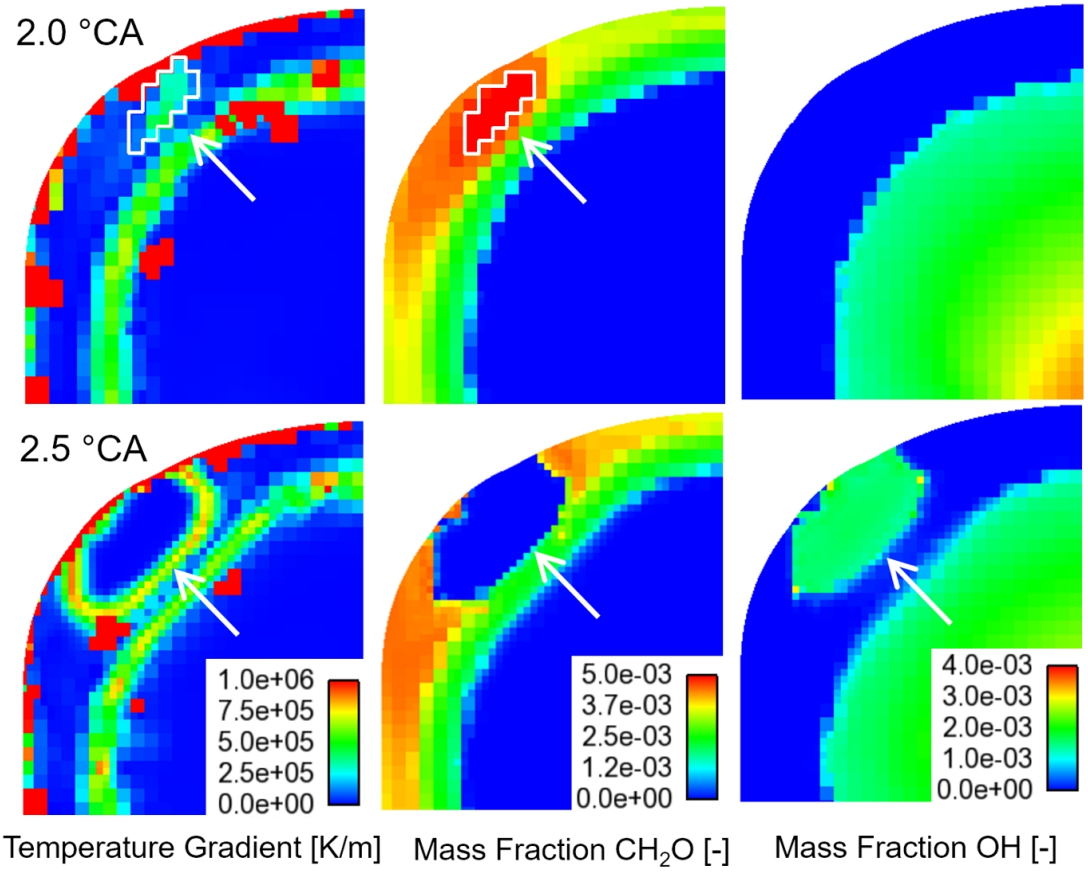

Figure 5.1: Ignition kernel prior to auto-ignition at 2.0°CA aTDC (top row) and after auto-ignition at 2.5°CA aTDC (bottom row) close to an intake valve. View from top. Reprinted from [12].

In the post-processing, prior to the auto-ignition process, a kernel with almost constant temperature is observed in the same region as the formaldehyde is formed (Figure 5.1). Some areas with very high-temperature gradients are visible. These result from the post-processing and are numerical artifacts and physically meaningless. To reliably determine the severity of the ignition, the ignition kernel size is calculated from the CH_2O concentration that aligns well with the temperature gradient but provides a clear cutoff. From the latter, the ignition kernel size r_0, and from the OH concentration profile in space, the reaction path length can be extracted. The length, that the reaction front traveled, is measured in the direction of the highest imposed gas velocity as result of the auto-ignition process. In this way, the maximum reaction front velocity is found. Figure 5.2 to 5.4 exemplify predicted ignition processes. In Figure 5.2 there is one auto-ignition event predicted that consumes the whole ignition kernel during one time step. This auto-ignition imposes a certain gas velocity that decreases after the ignition event. In some cases after a first auto-ignition, a second stronger auto-ignition is induced in

the following time step, which can be identified considering the imposed gas velocities (Figure 5.3). The first auto-ignition heats up the hotspot further, the second auto-ignition event is therefore stronger. Figure 5.4 shows a large stretched ignition kernel with two auto-ignitions in the following time steps. In this example, the first auto-ignition is not directly imposing the second stronger auto-ignition. Those sequential auto-ignitions are typical for engine knock occurrence [47, 133]. In case of appearance, the second stronger auto-ignition is evaluated. In the discussed figures, the size of the ignition kernel is highlighted and marked with "r_0", the way that the reaction velocity traveled in the direction of the fastest imposed gas velocity with "dx".

The additional required parameters, such as ignition delay time τ and excitation time τ_e, are calculated separately according to the local thermodynamic conditions using homogeneous constant volume reactors in LOGEsoft 1.08 [9]. For the excitation time, the maximum kernel temperature and pressure prior to the ignition event are used under the assumption that the kernel will auto-ignite in the region with the highest temperature. The ignition delay time is calculated for the maximum kernel temperature prior to the auto-ignition event and the mean temperature of the surrounding unburned gases. For those calculations, the composition of the charge prior to the appearance of the low-temperature chemistry is used since the species concentrations and thermodynamic state are defined for a homogeneous unburnt mixture [3]. If several ignition kernels are predicted, each ignition kernel is analyzed separately.

For the assessment of the predicted auto-ignitions in the detonation diagram it is distinguished between to classes: "harmless auto-ignition", which includes the regimes deflagration and no knock conditions and developing detonation or "harmful engine knock", which means mild and super knock events. The thermal explosion regime will not be entered. Since the upper and lower transition boundaries are mean values, the transition region is assumed to be $\pm 10\%$ of ξ_u. The harmless auto-ignition class is defined by $\xi > 1.1\xi_u$ and $\varepsilon < 1.6$ if $\xi < 1.1\xi_u$. The engine knock class includes the transition range to give a security margin for engine development. Therefore, it is given by $\varepsilon > 1.6$ and $\xi < 1.1\xi_u$. The knock strength increases with decreasing resonance parameter ξ and increasing reactivity parameter ε. Figure 5.5 illustrates the two classes.

5.2 Sensitivity to Spark Timing

The model has been applied to a Renault gasoline fueled passenger car engine with port injection operated at the KLSA (see Table 5.1 for the specification). A full-cylinder model including the intake and exhaust ports is used for the simulation. The ports and the cylinder are

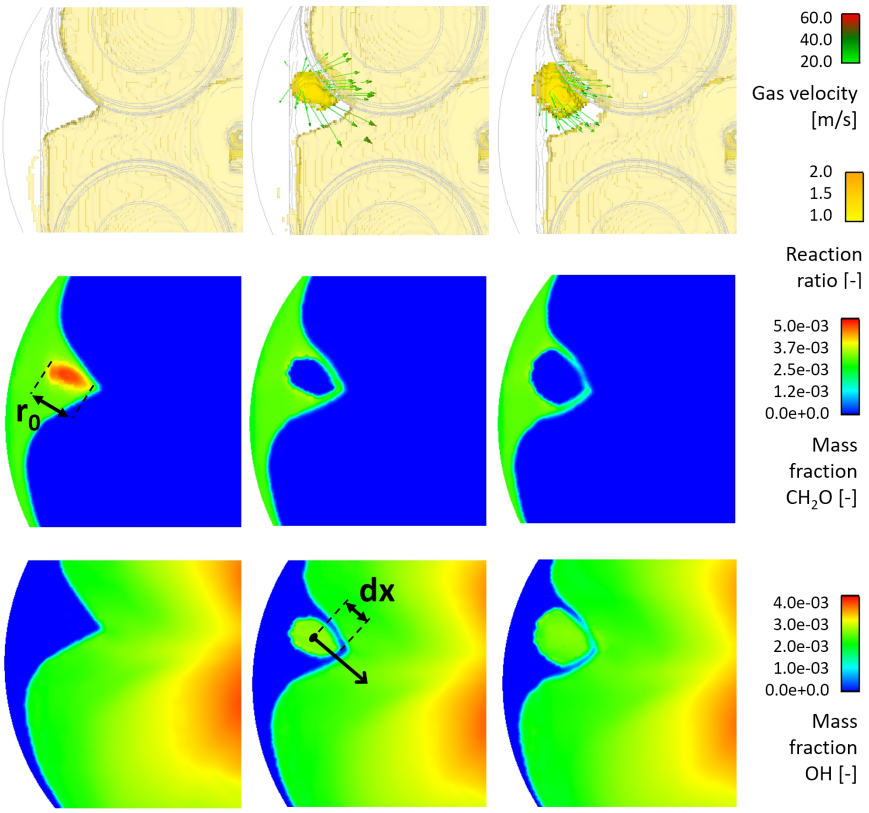

Figure 5.2: Example of an auto-ignition that consumes the hotspot. The kernel size is highlighted with dashed lines. The solid arrow shows the direction of the highest imposed gas velocity.

initialized homogeneously. The port fuel injection is not simulated. The base mesh size of the in-cylinder volume is set to 2.5 mm. Based on local differences in velocity and temperature, the mesh is refined down to 0.625 mm. The time step is set to 5.0 μs during the flame propagation. This spatial and temporal discretization prevents that the sound wave at its maximum at 2500 K travels further than one cell. Summarizing, given the limitations of the RANS framework, the discretization is of sufficient accuracy for this study.

The operating point given in Table 5.1 was taken as a reference case for the numerical simulations. Figure 5.6 (a) shows the predicted versus the experimental pressure trace. While the reference case is close at the transition to knock, advancing the spark timing about 1°CA leads to mild knock (Figure 5.6 (b)). This agrees with the experimentally found KLSA.

Based on the reference case, a sensitivity study analyzing the spark timing and surrogate fuel 1 (RON 87 as defined in Table 5.3) has been carried out. All remaining parameters are left unchanged. The predicted pressure rise rates for the spark timing sweep are shown in Figure

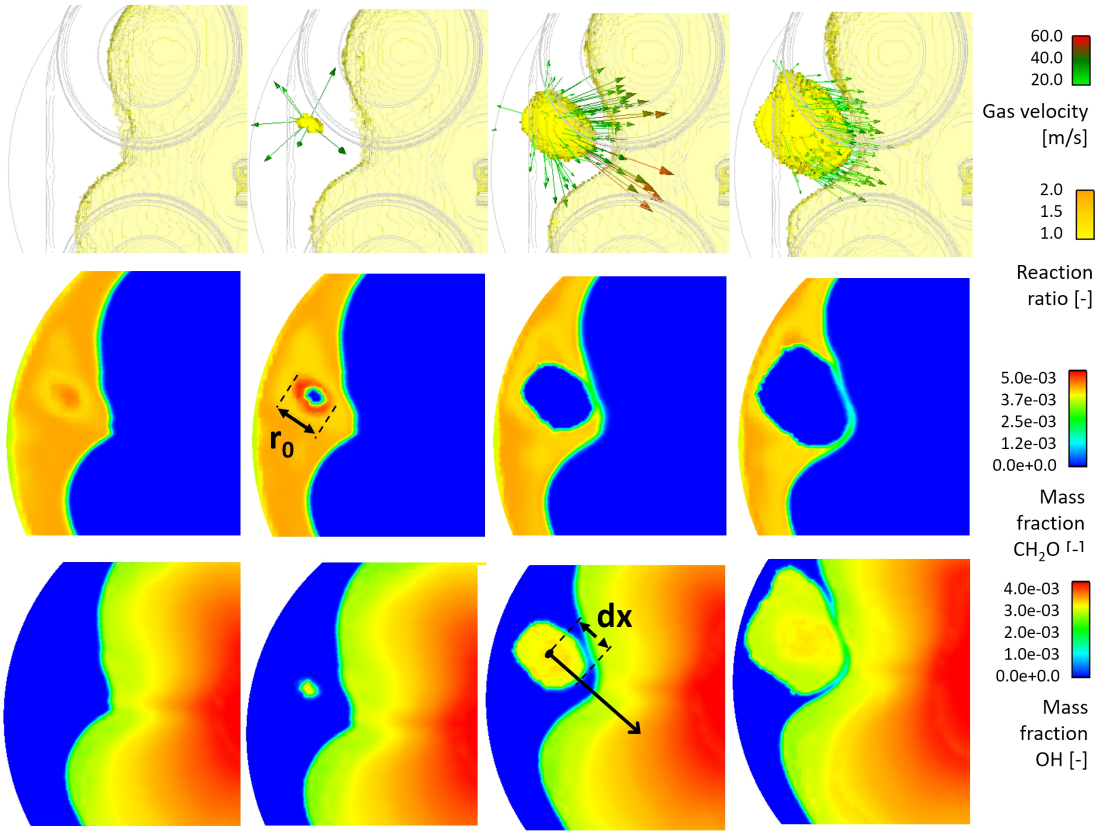

Figure 5.3: Example of an induced sequential auto-ignition after a prior auto-ignition. The kernel size is highlighted with dashed lines. The solid arrow shows the direction of the highest imposed gas velocity.

Table 5.1: Engine geometry and operating conditions.

Bore	72.0 mm
Stroke	82.0 mm
Connecting rod length	128.0 mm
Compression ratio	10.9
Gross IMEP	10.6 bar
Speed	2000 rpm
Spark timing	-4.0°CA aTDC
EGR (only internal, estimated)	4.0 %

5.7 (a). For the spark timing reference +4°CA, a "smooth" combustion process is predicted. Advancing the spark-induced ignition, steep gradients in the pressure rise rate are found. The more the spark timing is advanced, the higher local pressure gradients are predicted. The pressure rise traces suggest that several auto-ignition events are predicted in each simulation with

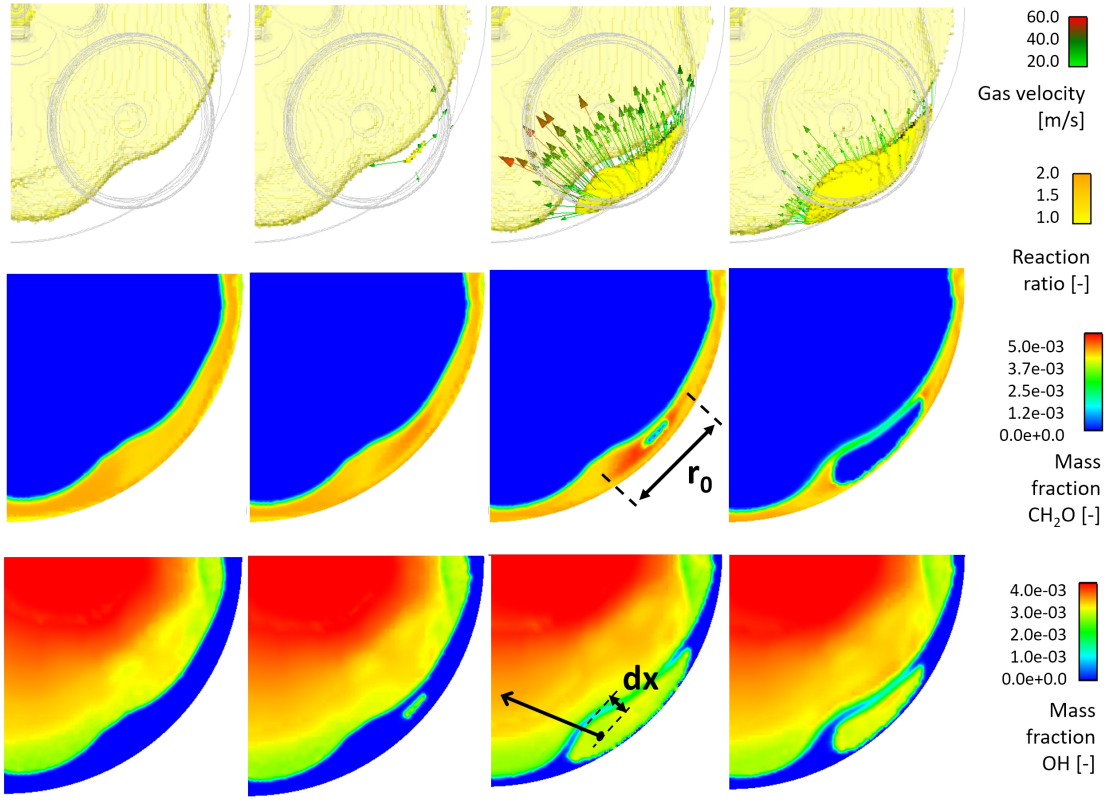

Figure 5.4: Example of a two auto-ignitions in the same ignition kernel. The kernel size is highlighted with dashed lines. The solid arrow shows the direction of the highest imposed gas velocity.

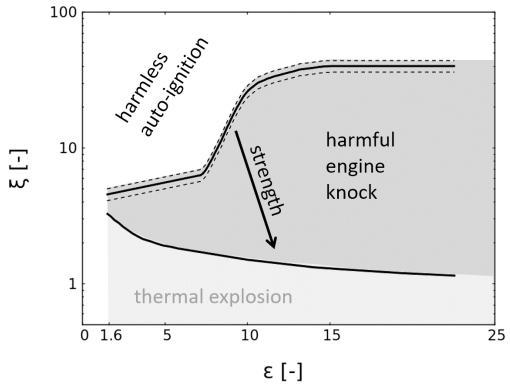

Figure 5.5: Classes for the assessment of the predicted auto-ignitions. The broken lines indicate the transition range $\pm 10\%$ of ξ_u, which is accounted to the engine knock class.

advanced spark timing. Each ignition kernel is analyzed separately. The results are shown in the detonation diagram in Figure 5.7 (b). The predicted ignition kernel size r_0 is analyzed. Kernel which do not lead to a developing detonation are predicted between 2 mm up to 4.5 mm

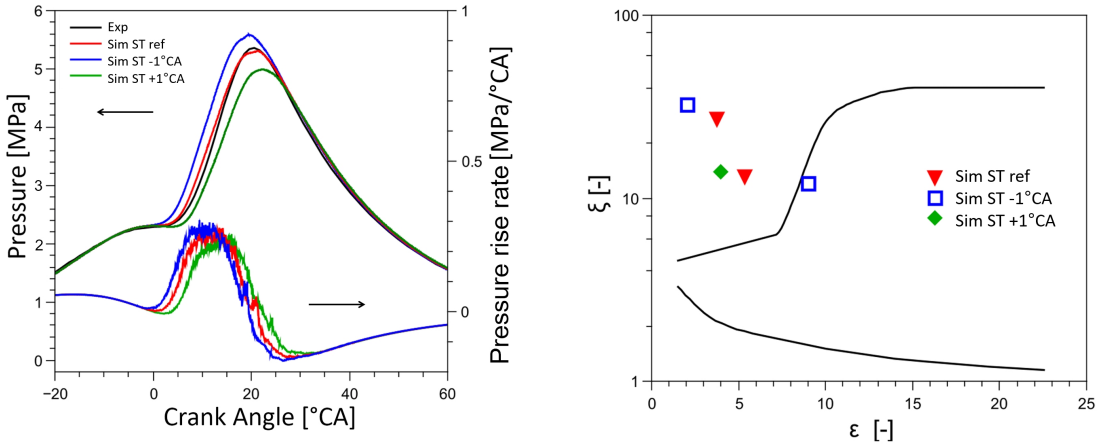

(a) Experimental mean pressure over 300 cycles and mean predicted pressure and pressure rise rate.

(b) Evaluation of the predicted auto-ignitions in the detonation diagram.

Figure 5.6: Spark timing sweep of the reference case and shifted spark timing ± 1°CA. Figure reprinted from [12].

close to the transition border. In the developing detonation regime, kernel sizes up to 8.5 mm are found. For the case with spark timing -12°CA, five ignition kernels are predicted. Four of them are evaluated to be mild to strong knock. The first occurring kernel is found to be in the subsonic auto-ignition regime. With decreasing pressure rise rate, the knock events are evaluated consistently to be weaker. For the reference spark timing, auto-ignition events that lead to a pressure rise are predicted, but the intensity of the auto-ignition is too low to induce a developing detonation.

In Figure 5.8, the predicted pressure wave is illustrated for reference spark timing -12°CA and surrogate fuel 1. In these plots, the squared normalized pressure is shown versus crank angle. At 2.5°CA, the first ignition kernel appears. The kernel is characterized by local, very high pressure gradients. The resulting pressure wave is traveling through the cylinder. At 4.0°CA, the second and third auto-ignition event can be observed. These kernels are evaluated to be strong knock incidents. The local pressure gradients are predicted to be higher than for the first auto-ignition. The generated pressure waves induce a fourth and fifth auto-ignition kernel (4.5°CA and 5.0°CA). The series of auto-ignition events lead to a pressure wave that hits the right wall at 5.5°CA, is reflected (6.0°CA), and hits the right wall again at 6.5°CA. This goes well together with literature. In comparison, the pressure wave induced by the first auto-ignition vanishes after 1.0°CA. The order of the auto-ignition events is added to Figure 5.7 (b).

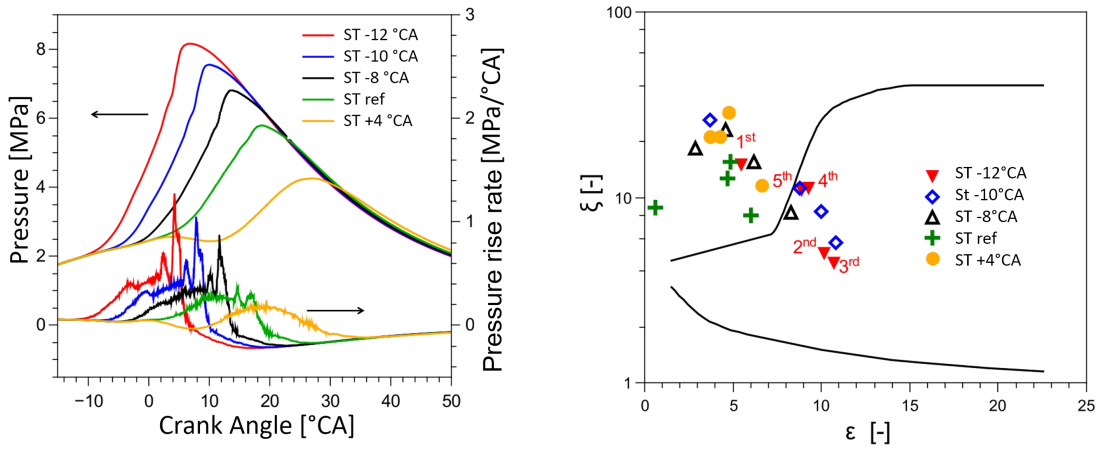

(a) Mean predicted pressure and pressure rise rate.

(b) Evaluation of the predicted auto-ignitions in the detonation diagram.

Figure 5.7: Spark timing sweep using surrogate fuel 1. Figure reprinted from [12].

5.3 Sensitivity to Octane Rating

The engine test case (Table 5.1) is further used to investigate if the model can predict the knock tendency as function of the octane rating. For this study, six fuel surrogates with different octane ratings (RON 87.0 – RON 106.9) at a spark timing of -12°CA are investigated. The properties of the commercial gasoline and the corresponding surrogates are given in Table 5.2 and Table 5.3.

The predicted mean pressure and pressure rise rates using the six different surrogates are shown in Figure 5.9 (a) and (b). With increasing RON, the magnitude of the maximum pressure rise rate is decreasing, and the appearance of the first and the heaviest auto-ignition is delayed (Figure 5.9 (d)). The assessment is illustrated in Figure 5.9 (c). The strongest knock is observed for fuel 1 (RON 87). The transition from harmless subsonic auto-ignition to knocking combustion is found to be between fuel blend 4 (RON 94.5) and fuel blend 3 (RON 93.6). Using fuel blend 6 (RON 106.9), a “smooth” combustion event is predicted. An auto-ignition is observed, but the kernel is evaluated to be in the harmless subsonic deflagration regime. Fuels 4 and 5 exhibit a similar behavior. These two fuel blends have the same base composition, but ethanol (5 vol%) is added to fuel 4 to obtain fuel 5. The fuel injection is not simulated, therefore the effect of different vaporization enthalpies of the surrogates is not considered in this study.

The increase in the fuel octane rating and subsequently of ignition delay time leads to a decrease of the first ignition kernel size, a delay in the appearance of the first ignition kernel and a decrease in the imposed gas velocity (Figure 5.10). The shown ignition kernels are the first kernels occurring in the engine cycle, but they are not the strongest. These kernels appear

Table 5.2: Fuel test bench data.

	RON	**MON**	**Aromatic content**	**Ethanol content**	**Density**	**LHV**	**C:H:O-ratio**
	[–]	[–]	$[vol\%]$	$[vol\%]$	$[kg/m^3]$	$[MJ/kg]$	$[mass\%]$
fuel 1	87.0	77.5	24.0	0.0	744.2	43.2	86.8:13.4:0.0
fuel 2	91.0	81.2	26.2	0.0	747.4	44.4	86.0:14.0:0.0
fuel 3	93.6	82.4	11.7	22.8	744.0	39.6	77.7:13.9:8.4
fuel 4	94.5	84.1	32.6	0.0	747.5	42.9	86.9:13.1:0.0
fuel 5	Fuel 4 + 5 vol% ethanol						
fuel 6	106.9	95.3	35.2	0.0	756.2	41.3	84.1:12.7:3.2

Table 5.3: Composition in mass fractions and physical properties of the surrogates corresponding to the fuel test bench data in Table 5.2.

	RON	**MON**	***iso*-Octane**	***n*-Heptane**	**Ethanol**	**Toluene**	**Density**	**LHV**	**C:H:O-ratio**
	[–]	[–]	$[mass\%]$	$[mass\%]$	$[mass\%]$	$[mass\%]$	$[kg/m^3]$	$[MJ/kg]$	$[mass\%]$
fuel 1	87.0	82.4	53.2	18.4	0.0	28.4	731.5	43.3	86.0:14.0:0.0
fuel 2	91.0	85.9	54.2	14.9	0.0	30.9	735.8	43.2	85.4:14.6:0.0
fuel 3	93.6	83.5	45.7	16.2	25.0	13.1	746.0	39.5	77.0:14.4:8.7
fuel 4	94.5	88.2	49.5	12.7	0.0	37.8	747.3	42.9	86.8:13.3:0.0
fuel 5	96.0	91.1	46.0	12.3	5.3	36.4	747.7	42.1	83.1:13.1:3.8
fuel 6	106.9	98.7	57.5	2.0	0.0	40.5	753.3	42.8	87.1:12.9:0.0

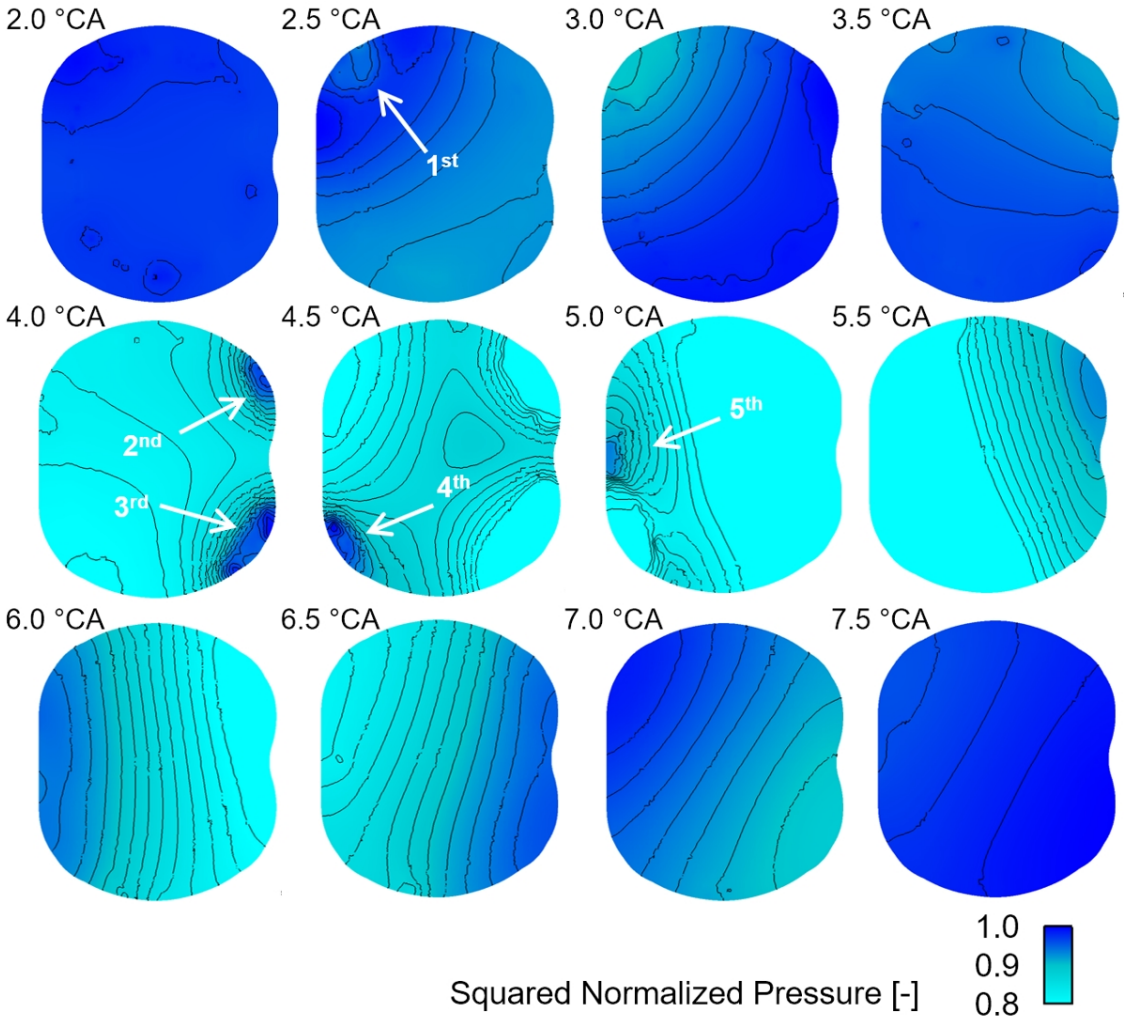

Figure 5.8: Sequence of the squared normalized pressure and its contour lines at a horizontal clip plane. View from top of the cylinder. Case: spark timing ref-12°CA aTDC, surrogate fuel 1. Figure reprinted from [12].

in the same location, which is explained by the flow field. Surrogate fuel 1 auto-ignites around 2.5°CA and surrogate fuel 6 at 8.0°CA. The mean temperature of the unburnt zone is about 850 K and the pressure is about 60 bar. Since the engine is operated at 2000 rpm, this shift corresponds to 0.47 ms and follows directly from the increased ignition delay time (Figure 5.11).

Since in SI engine knock shall not appear, in a second step the impact of the surrogate octane rating on the KLSA is analyzed. To find the KLSA, a spark timing sweep has been simulated and the predicted ignition kernels evaluated using the detonation diagram. For fuel 1 and the reference spark timing are four auto-ignitions predicted (Figure 5.7 (a) and (b)). However, the evaluation in the detonation diagram determines them to be in subsonic deflagration mode.

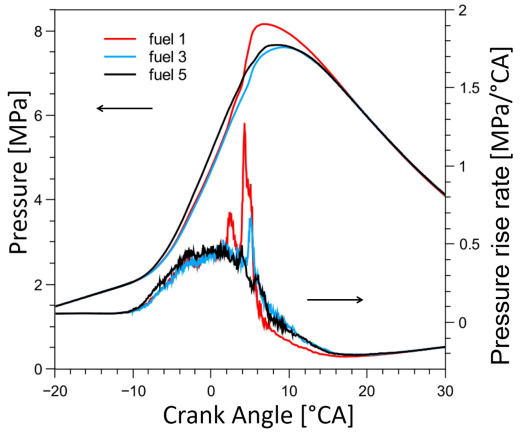

(a) Mean predicted pressure and pressure rise rate of fuel 1, 3 and 5.

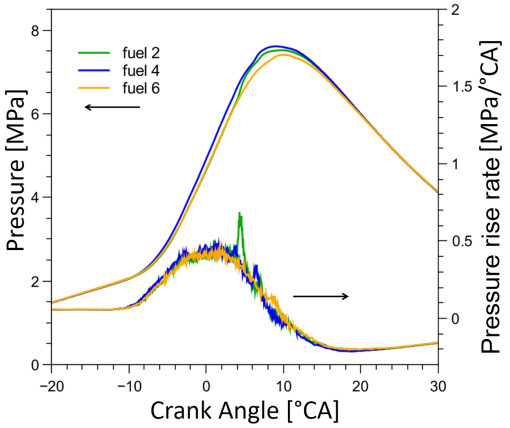

(b) Mean predicted pressure and pressure rise rate of fuel 2, 4 and 6.

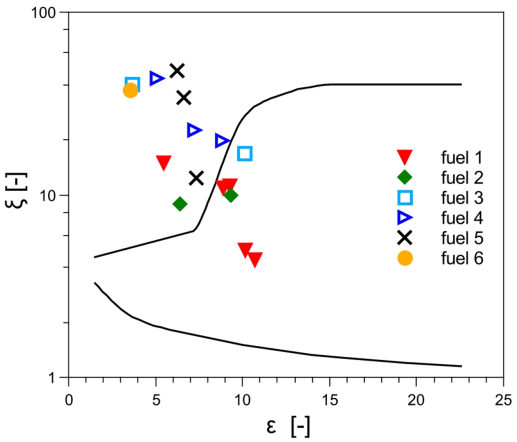

(c) Evaluation of the predicted auto-ignitions in the detonation diagram.

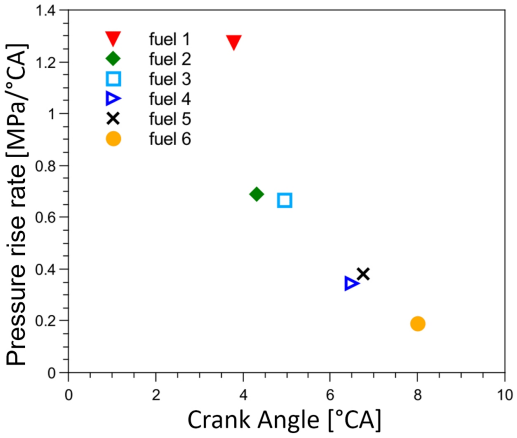

(d) Maximum predicted pressure rise rate and corresponding crank angle of the pressure rise rate maximum.

Figure 5.9: Perdiction for spark timing ref-12°CA aTDC and different surrogates. Figures reprinted from [12].

Therefore, the spark timing was advanced further. For the spark timing -3°CA the severest acceptable auto-ignition is predicted. All auto-ignition events are in no-knock conditions. Further spark time advancing (-4°CA) leads to the prediction of mild knock. Therefore, for fuel 1 ST -3°CA is the maximum acceptable spark timing and the engine is operating at the KLSA. The same methodology was applied using the five other surrogates. Figure 5.12 shows the mean pressure and the mode of the predicted ignition kernels at the KLSA. All auto-ignition events are located in the harmless subsonic deflagration area and no-knock regime. The found KLSA are given in Table 5.4. The trend of the found KLSA is as expected: the higher the octane rating, the further the spark can be advanced. At rather low octane ratings, the KLSA

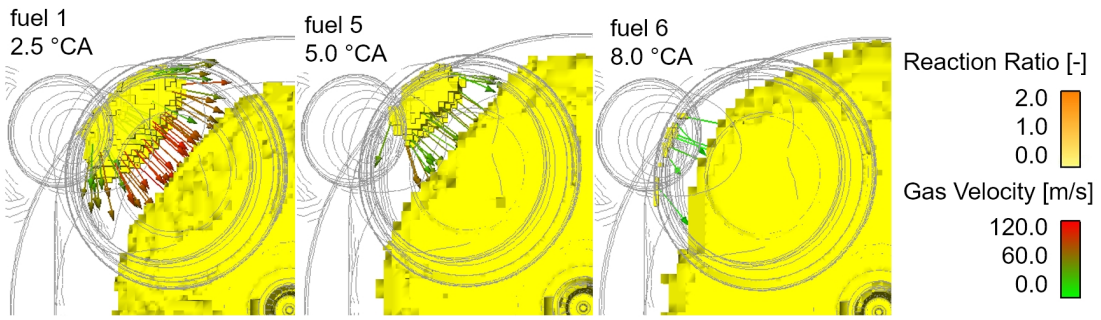

Figure 5.10: First predicted ignition kernel for selected surrogates close to an intake valve. View from top. Figure reprinted from [12].

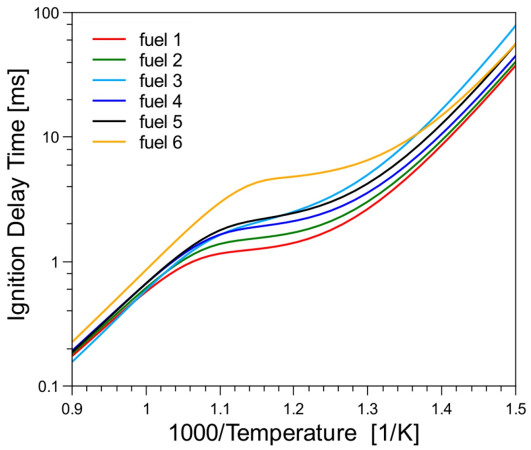

Figure 5.11: Ignition delay time of the surrogate fuels at stoichiometric conditions and at 60 bar. Figure reprinted from [12].

is more sensitive to this rating. A difference of 4 points in RON (fuel 1 and fuel 2) leads to a shift of 7°CA, whereas at very high octane ratings (fuel 5 and fuel 6) a difference of 10 points in RON earns only 5°CA in KLSA. By the use of a fuel with higher RON/MON and thus the possibility to ignite the charge earlier leads to a higher maximum pressure and higher gross IMEP (Table 5.4). At low octane ratings the IMEP increases with advanced spark timing. Even though the spark is further advanced, starting from fuel 3 (RON 93.6) the earned IMEP is stagnating. Therefore, it can be observed that this operating point does not benefit significantly from octane ratings higher than 93.6.

Summarizing, based on this section and section 5.2 some conclusions regarding the introduced methodology and approach to predict auto-ignitions based on detailed chemistry can be drawn: The evolution of the auto-ignition event can be studied in detail, thanks to the use of reaction

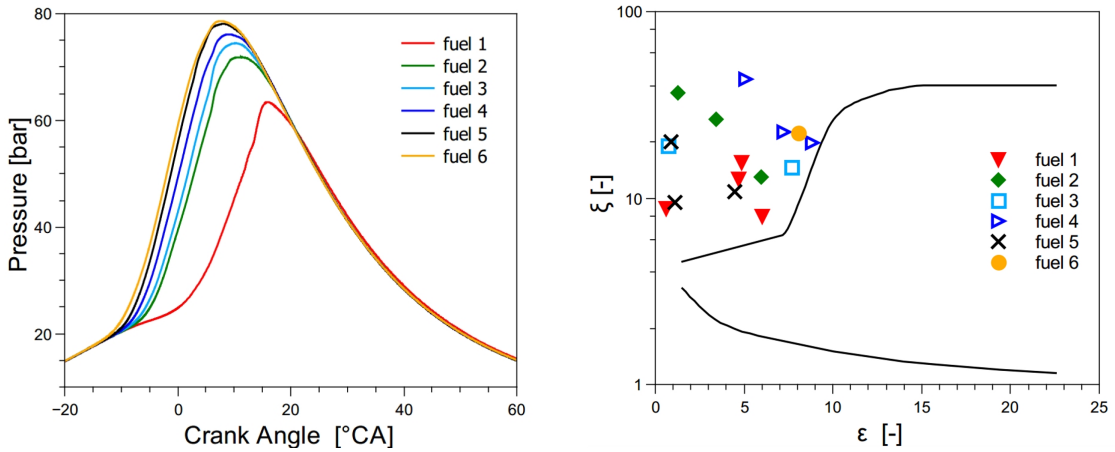

(a) Mean predicted pressure.

(b) Evaluation of the predicted auto-ignitions in the detonation diagram.

Figure 5.12: Optimized KLSA for the different surrogates.

Table 5.4: Optimized Knock Limit Spark Advance (KSLA) and Gross Indicated Mean Effective Pressure (IMEP) of the closed cycles for the different surrogates.

Surrogate	**RON**	**MON**	**KLSA**	**IMEP**
	[-]	[-]	[°CA aTDC]	[bar]
fuel 1	87.0	82.4	-3.0	10.72
fuel 2	91.0	85.9	-10.0	10.99
fuel 3	93.6	83.5	-11.0	11.06
fuel 4	94.5	88.2	-12.0	11.06
fuel 5	97.0	91.1	-13.0	11.07
fuel 6	107.0	98.7	-18.0	11.08

kinetics and low- and high-temperature markers. The pressure rise rate is an indicator for auto-ignition events. Using the detonation diagram, the mode of the ignition and therefore the severity of the auto-ignition event can reliably be determined. Sensitivity studies toward spark advancing and different octane ratings were performed. The model responds to the changes as expected from theory and practical observations. With advanced spark timing or reduced surrogate octane rating, the local pressure gradients and the knock strength increase and a transition toward possible harmful developing detonation is observed.

CFD based tracking of the KLSA can be realized as function of different surrogates very efficiently (less than 4 hours per CFD run in the optimization step using a workstation with

24 cores and a restarting strategy). Sensitivity studies with respect to different fuel qualities and octane ratings can be performed easily thanks to a flexible formulation of the reduced mechanism and pre-compiled laminar flame speed tables. With the proposed approach it is possible to find the optimal ignition timing of the average cycle of an operating point for a given gasoline fuel quality in terms of IMEP and knocking tendency.

Even if RANS calculations cannot resolve the sub-grid structure of a developing detonation, the application of the detonation theory showed the trends expected for gasoline engines at the knock limit. This was shown for octane number as well as for spark timing variations. The results indicate that the application of the detonation diagram can be meaningful for post-processing RANS simulations. However, details of LES calculations should be analyzed to understand the possible limitations of the RANS calculations (next section). Furthermore, the comparison to cycle-resolved measurements (section 6.4) and the application to model setups including the fuel injection and local inhomogeneity are needed to validate and further investigate the suggested model strategy.

5.4 Verification of the RANS Methodology using LES

RANS provides the ensemble average of the flow and the mean location of the flame front over several cycles. Also the predicted auto-ignition events need to be understood as the mean location and strength of auto-ignition kernels. As discussed in section 3.2, this is due to the modeling approach. However, turbulent SI engine combustion exhibits instabilities and an unsteady nature that cannot be computed with RANS [134]. Regarding the resonance theory, there are further concerns: the RANS approach can usually not handle acoustic waves, since the solvers apply large turbulent and numerical viscosities. Those prohibit acoustic waves to develop [134]. The detonation diagram has been developed using DNS [2, 3] and was applied for engines using LES [60, 135]. It has been found that the transition to detonation depends on the local instantaneous gradients of temperature and the resonance parameter ξ. This local dependency cannot be resolved by RANS that is derived at the integral length scale and that provides mean gradients. Gradients that lead to a developing detonation are averaged and therefore not present in a RANS simulation.

Given the limitations of the RANS framework, it needs to be stated, that no developing detonation is predicted in this work. The resonance theory is used to classify the strength of a predicted ignition kernel at the time step of ignition. The predicted dimensions of the kernel and chemical properties are compared to the given and imposed boundary conditions of the simulations in [2, 3] on which the detonation diagram was built. In this way, no developing

detonation is predicted, but the potential of the kernel to form a developing detonation is estimated. This methodology overcomes the use of global or local pressure and pressure fluctuations that are typically used to evaluate knock in RANS [48]. Considering the limitation of RANS, the pressure fluctuations are no reliable estimate for a developing detonation. In this section, it is investigated if the assumption holds and the detonation diagram can give reasonable estimates within the RANS framework.

The comparison is performed using typical operating conditions for knocking combustion of a passenger car (Table 5.5). The aim of this study is to compare the evaluation of predicted auto-ignition in the detonation diagram. To limit the CPU costs of the LES simulation, the chemistry is not solved in the burnt zone and a restart strategy from -20°CA aTDC is applied. The spark is initialized as in RANS for the LES simulation (by initializing a progress for G). In this way no cycle-to-cycle variations are accounted for. The discretization of RANS and LES simulations and the applied models are listed in Table 5.6. For both turbulence models, a spark timing sweep to force different auto-ignition regimes is performed. The results for the spark timing sweep using LES and RANS are shown versus experimental data in Figure 5.13.

Table 5.5: Engine geometry and operating conditions for the LES verification.

Bore	72.2 mm
Stroke	73.2 mm
Connecting rod length	132.5 mm
Displacement per cylinder	300 cm^3
Compression ratio	9.8
Speed	2500 rpm

In the LES simulations, the spark ignition has a longer induction time to initiated the flame. As discussed before, the local flow field stretches the induced spark. Further, the slope of the pressure traces differs from the RANS results. The LES simulations are restarted form the same simulation at -20.0°CA aTDC, which causes that the flow field does not differ before this time step. This explains, why the early flame development is similar delayed for all cases. Compared to the experiment, the pressure slope of the early flame development of the LES results agree better than RANS with the experiment. For each simulation type, a result in the range of slow, mean and fast cycles of the experimental range and with advanced spark timing to force strong auto-ignitions are predicted. . The fundamental differences between the two turbulence model are shown in Figure 5.14: in the LES prediction the flame front is wrinkled, whereas in RANS the mean flame position is obtained, and compared to LES the flame appears

Table 5.6: Spatial discretization and applied models for RANS and LES.

	LES	**RANS**
Turbulence model	Dynamic Smagorinsky [72]	RNG k-ϵ
Wall model	Werner and Wengle [136]	law-of-the wall assumption
Combustion model	G-equation with WSR in unburnt zone [17, 67]	
Turbulent flame speed model	Pitsch [67]	Peters [17]
Base mesh size	0.25 mm	1.0 mm
Minimum cell size	31.25 μm	125.0 μm
Cell count TDC	2,500,000	90,000

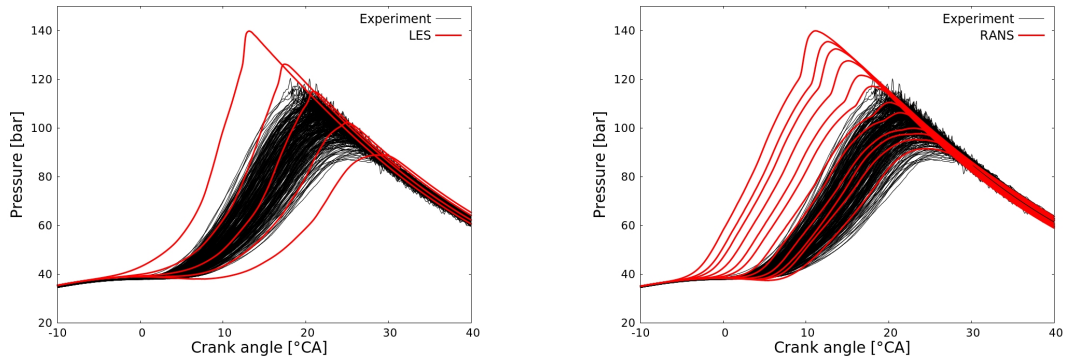

(a) LES, 5 realizations.

(b) RANS, 12 cycles.

Figure 5.13: LES and RANS pressure predicted versus 500 cycles from the experiment.

uniform.

To compare the auto-ignition prediction and validate the assessment method, comparable auto-ignitions have to be analyzed. For this purpose, not the overall combustion prediction have to be similar, which cannot be given by using the fundamental different turbulence models, but the conditions in the unburnt zone in the time step of the predicted auto-ignitions needs to be similar. To find comparable cases for the LES prediction, several RANS simulations with different spark timing have been run (Figure 5.13 b)). From this sweep, for each LES result a comparable RANS case is assigned. For this assignment, the case shall have similar conditions in the unburnt gases. The decision criteria are the maximum value of predicted mean pressure p_{max} and the ignition delay τ_{CA} until an auto-ignition occurs. For this ignition delay time τ_{CA}, the time in crank angle degree between 5% burn duration (CA_5) and auto-ignition onset (AI onset) is taken. The selected cases are given in Table 5.7.

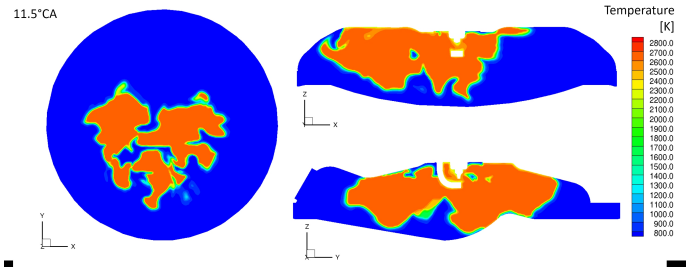

(a) LES.

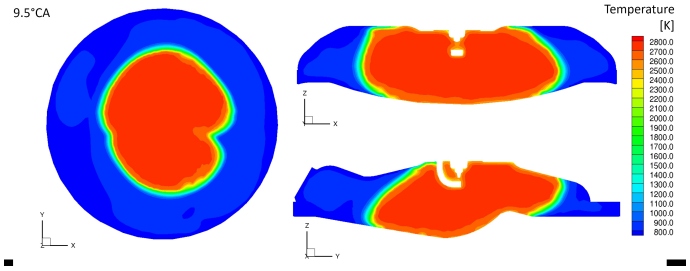

(b) RANS.

Figure 5.14: Exemplary temperature prediction at CA_{10}.

Table 5.7: Selection of RANS simulations corresponding to the LES results. Timings are in °CA aTDC.

LES				**RANS**			
ST [°CA]	$\mathbf{p_{max}}$ [bar]	**AI onset** [°CA]	τ_{CA} [°CA]	**ST** [°CA]	$\mathbf{p_{max}}$ [bar]	**AI onset** [°CA]	τ_{CA} [°CA]
-15.0	140.0	13.0	11.4	-10.0	139.9	9.5	11.7
-10.0	127.7	17.0	12.3	-7.0	132.6	13.0	12.2
-8.0	115.1	20.5	13.6	-4.0	111.7	17.5	13.4
-7.0	100.0	24.5	15.3	-2.0	102.4	21.5	15.0
-5.0	91.6	29.5	17.8	2.0	89.1	27.5	18.4

The mean pressure, local maximum pressure and rate of heat release for some selected cases are shown in Figure 5.15. In the time step of a predicted auto-ignition in the unburnt gases, the rate of heat release and the maximum pressure have steep rise rates. The maximum pressure is oscillating and fades over several crank angle. In RANS, the pressure rise and the oscillations are smaller and fade faster. The heat is released in a shorter time period in LES than in RANS. To understand if anyway the predicted ignition kernels in RANS can be interpreted to be meaningful, all predicted ignition kernels are evaluated in the detonation diagram (Figure 5.16).

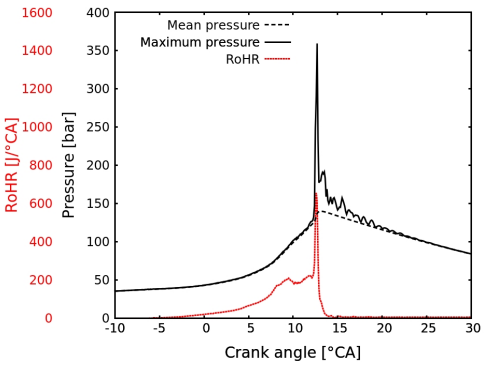

(a) LES ST -15°CA.

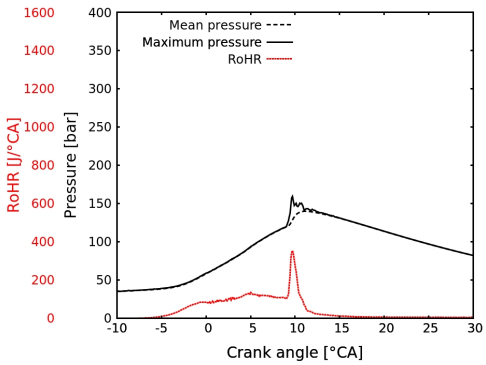

(b) RANS ST -10°CA.

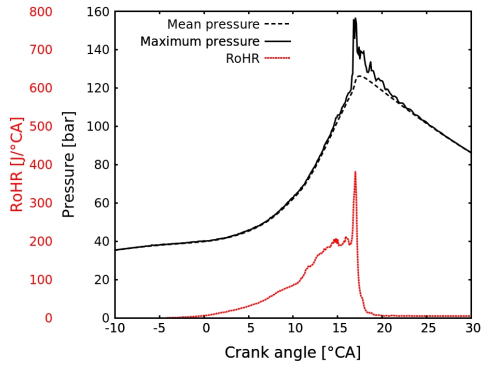

(c) LES ST -8°CA.

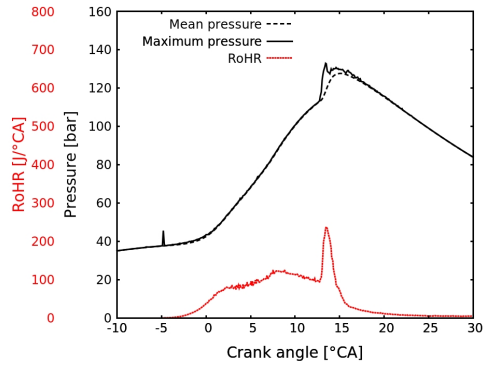

(d) RANS ST -4°CA.

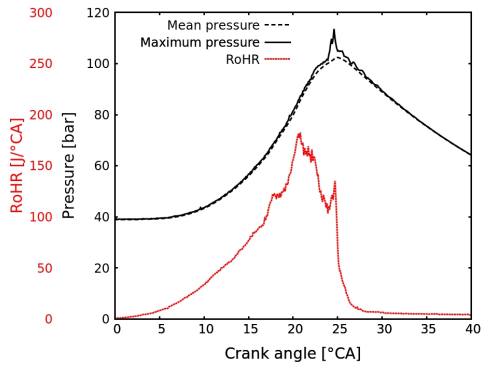

(e) LES ST -7°CA.

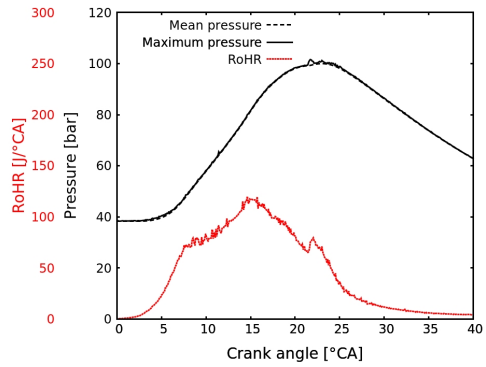

(f) RANS ST -2°CA.

Figure 5.15: Predicted mean, maximum pressure and rate of heat release (gray lines) using LES and RANS for selected spark timings.

The LES prediction for spark timing ST -15°CA has a rise rate of the local maximum pressure of 1000.8 bar/°CA. The maximum local pressure is >350 bar. The pressure is oscillating over

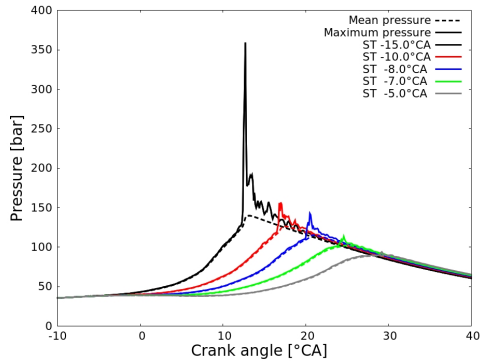

(a) Pressure prediction LES.

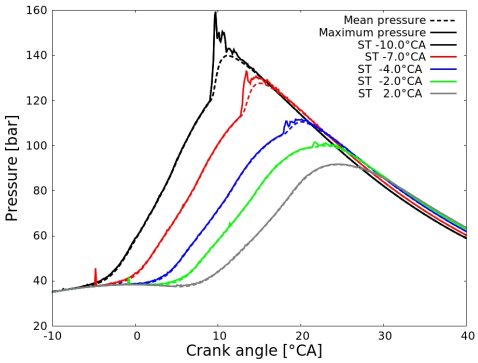

(b) Pressure prediction RANS.

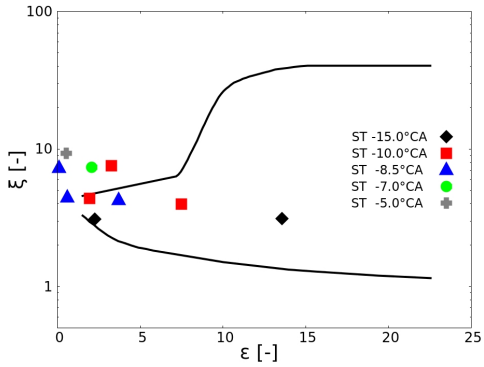

(c) Detonation diagram LES.

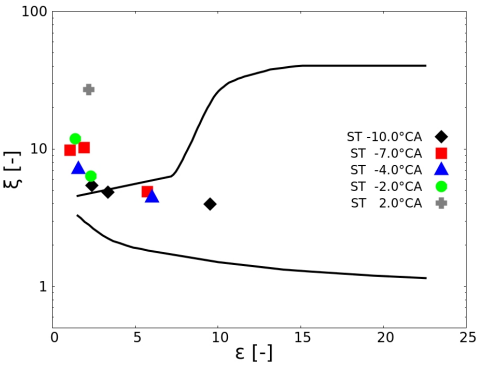

(d) Detonation diagram RANS.

Figure 5.16: Predicted mean and maximum pressure and evaluation of the auto-ignitions in the unburnt zone for LES and RANS.

a time interval corresponding to 20°CA. From those numbers, it can be stated that knocking combustion is predicted. Two ignition kernels are predicted. The maximum imposed gas velocity by the auto-ignition is about 270 m/s. The evaluation in the detonation diagram estimates both kernels to be in developing detonation regime. The found regime corresponds well to the predicted pressure gradients and fluctuations of the maximum pressure. With later spark timing, the peak pressures and pressure fluctuations are predicted to be lower. The evaluation in the detonation digram estimates weaker auto-ignition events. For the cases ST -7.0°CA and ST -5.0°CA, the maximum pressure rise rates are <40 bar/°CA. The pressure oscillations are smaller and vanish faster than for the earlier spark timings. All predicted auto-ignitions are found to be in deflagration mode. The combustion characteristics and the assessment in the detonation diagram agree well for LES. The discussed numbers are given in Table 5.8.

Table 5.8: Predicted parameters for the regime classification. Ignition kernel parameters for the strongest auto-ignition event of a simulation. Abbreviations: dd - developing detonation, def - deflagration.

	ST [°CA aTDC]	$\mathbf{p_{rise,max}}$ [bar/°CA]	$\mathbf{r_0}$ [mm]	$\mathbf{u_{a,max}}$ [m/s]	ξ [-]	ε [-]	**Regime**
LES	-15.0	1000.8	10.5	269.5	3.1	13.6	dd
	-10.0	282.9	11.9	194.3	4.0	7.5	dd
	-8.0	147.5	6.5	179.5	4.3	3.7	dd
	-7.0	37.8	3.6	104.3	7.4	2.1	def
	-5.0	31.9	1.5	79.6	9.3	0.5	def
RANS	-10.0	121.5	9.5	157.8	4.0	9.5	dd
	-7.0	77.9	5.6	147.0	4.9	5.7	dd
	-4.0	41.8	6.0	144.0	4.4	6.0	dd
	-2.0	37.7	4.3	102.0	6.4	2.3	def
	2.0	10.8	2.9	25.7	27.0	2.2	def

The pressure rise rates and pressure oscillations are predicted to be smaller in the RANS calculations due to the modeling assumptions in RANS (Figure 5.15. Considering the pressure rise rates and oscillations it cannot reliable be determined if engine knock is predicted or not. In contrast, the evaluation of the ignition kernel sizes and the induced reaction velocities in the detonation diagram predicted with RANS agree well with the estimations for LES and the experiment. The first three spark timings are found to be in the developing detonation regime, the later two in deflagration mode. In general, the resulting gas velocities are higher in LES than in RANS. For both models there is a clear cut-off in the predicted gas velocities that are estimated to lead to a developing detonation or deflagration. In LES $u_{a,max} \geq 180 m/s$ and in RANS $u_{a,max} \geq 140 m/s$, whereas $u_{a,max} \approx 100 m/s$ lead to deflagration. This also follows from Table 5.9, that gives all predicted ignition kernels located in the developing detonation regime, and from Table 5.10, that gives the kernels located in the deflagration regime. Based on the assessment in detonation diagram ignition kernels with $r_0 \geq 6mm$ have the potential to form a developing detonation for both LES and RANS. The resonance parameter ξ is smaller and the reactivity parameter ε larger for LES. For kernels between $3mm \geq r_0 \leq 6mm$, the local conditions as temperature and resulting decreased excitations time and chemical reactivity of the spot decided on the auto-ignition regime.

Figures 5.17 and 5.18 show the velocity vectors for LES and RANS simulations for which the auto-ignition was found to be in the same regime. In the LES simulations, the imposed gas velocities are higher and the velocity fluctuations more pronounced. In the LES results,

Table 5.9: Predicted kernels in developing detonation regime.

Turbulence model	$\mathbf{r_0}$ [mm]	$\mathbf{u_{a,max}}$ [m/s]	ξ [-]	ε [-]
LES	10.5	269.5	3.1	13.6
LES	9.6	245.9	3.1	2.2
LES	11.9	194.3	4.0	7.5
LES	6.5	179.5	4.3	3.7
LES	3.6	175.0	4.4	1.9
RANS	9.5	157.8	4.0	9.5
RANS	8.0	155.4	4.9	3.3
RANS	5.6	147.0	4.9	5.7
RANS	6.0	144.0	4.4	6.0

Table 5.10: Predicted kernels in deflagration regime.

Turbulence model	$\mathbf{r_0}$ [mm]	$\mathbf{u_{a,max}}$ [m/s]	ξ [-]	ε [-]
LES	3.6	104.3	7.4	2.1
RANS	4.3	102.0	6.4	2.3
LES	5.2	101.7	7.6	3.3
RANS	4.1	97.4	7.2	1.6
LES	1.0	96.4	7.3	0.1
LES	1.5	79.6	9.3	0.5
RANS	2.3	74.6	9.8	1.1
RANS	2.5	68.7	10.2	1.9
RANS	2.3	54.7	11.9	1.4
RANS	2.9	25.7	27.0	2.2

the velocity field homogenized after 4°CA, in the RANS results after only 1.5°CA. In case of a deflagration in the RANS simulation the velocity field remains homogeneous and almost unaffected by the auto-ignition event.

Despite the given limitations of the RANS concept, this analysis shows that the detonation diagram gives reasonable estimates for the regime of the auto-ignition events, even though the following pressure waves cannot be predicted in RANS. The knock strength using RANS is under-predicted compared to LES. For the use in engine development, a safety margin for the

predicted gas velocities u_a of 30 % should be applied. To calculate the full engine cycle in LES on a workstation with 36 cores and CONVERGE 2.4.9 [8] 7.5 days are needed, using RANS 0.8 days. The benefit in computational costs of a factor 10 using RANS is especially important for the applicability in engine development, where huge parameter studies and different designs need to be investigated in short time frames and for the use of detailed reaction schemes. RANS cannot capture all physics, but is an useful and efficient engineering tool using the obtained information on the mean cycle and the estimation of the knock probability.

Summarizing, the analysis of the predicted local pressure gradients and the pressure oscillation independent evaluation of the auto-ignition using the resonance theory agree for the LES. In addition, the detonation diagram gives detailed information of kernels in the transition regime ($3mm \geq r_0 \leq 6mm$). The predicted ignition kernel sizes and imposed gas velocities for the different regimes are comparable in the RANS and LES simulations. Hereby the gas velocities are predicted higher in LES than in RANS. By applying a safety margin for the reaction front velocity, the evaluation of the predicted ignition kernels in RANS is feasible in engine simulations. Thanks to the lower computational cost, the RANS methodology can be used for simulations using detailed chemistry. In the RANS simulation a developing detonation is not predicted, but the potential of the predicted auto-ignition to initiate a developing detonation is estimated.

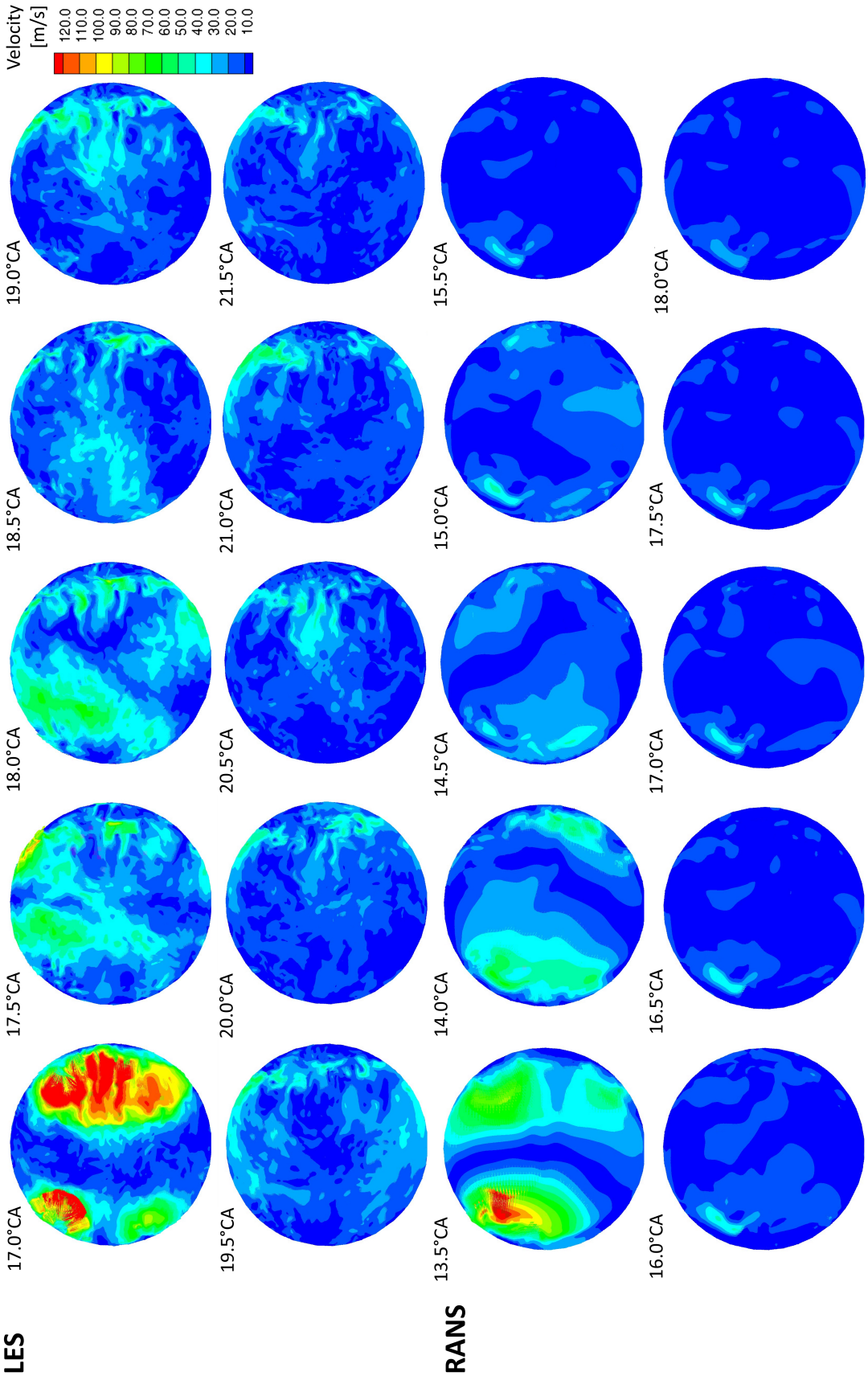

Figure 5.17: Example for predicted kernels in developing detonation regime. Top two rows LES prediction, bottom rows RANS.

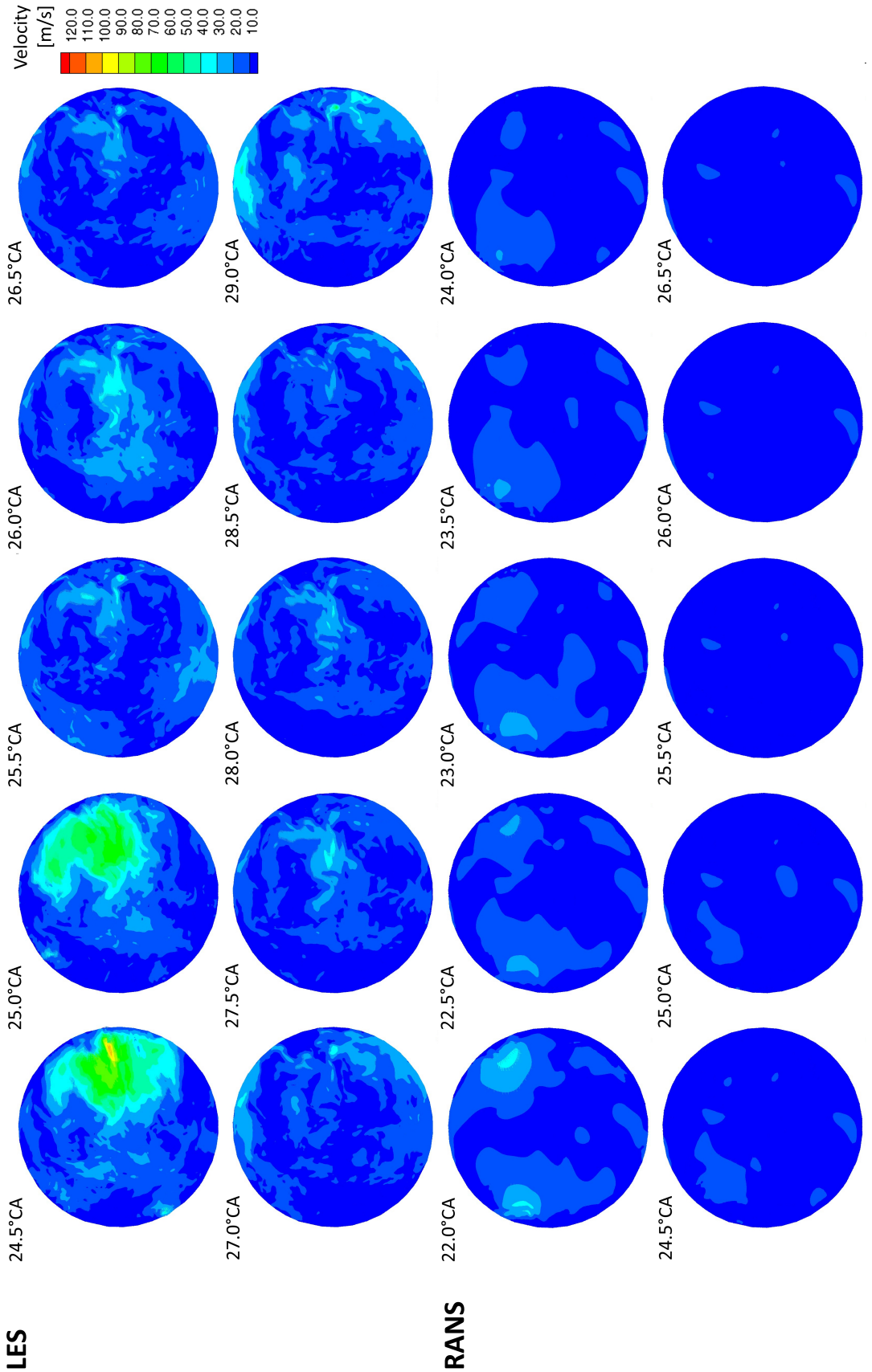

Figure 5.18: Example for predicted kernels in deflagration regime. Top two rows LES prediction, bottom rows RANS.

5.5 Impact of the Surrogate Formulation

In this section, the effect of the surrogate composition on engine knock prediction in RANS is analyzed. Surrogates composed of different fuels (PRF, TRF, ETRF) are compared to each other. The applied surrogates have all the same RON, but differ in MON and other characteristics such as C:H:O–ratio, LHV and density. Through this analysis, the effect of the different gasoline surrogates characteristics on engine knock prediction is evaluated. The aim is to understand the impact of the surrogate composition on the predicted knock intensity, the knock onset and the knock limit spark advance (KLSA).

Different surrogates with same RON, but different number of surrogate fuel species and therefore different MON are composed using the methodology discussed in section 4. In the experiment a commercial gasoline without ethanol content was used. Representing the aromatic content of this gasoline by toluene and setting the ethanol content in the surrogate to zero results in a TRF surrogate that agrees well in density, LHV and C:H:O-ratio with the commercial gasoline (gasoline F9 in Table 6.1). However, the octane sensitivity is under-predicted. To investigate different surrogate formulations, a PRF is composed neglecting the aromatic content of the commercial gasoline. As discussed before, the PRF surrogate has no octane sensitivity. The LHV for this surrogate is the highest compared to the other analyzed surrogates. Since gasoline fuels usually contain ethanol, ETRF surrogates adopting the properties of the commercial gasoline with 5% and 10% ethanol by volume are composed, here named “ETRF 1” and “ETRF 2”. To match the target RON, the *iso*-octane and toluene content need to be aligned. To generate a surrogate with the same sensitivity as the commercial gasoline “ETRF 3” with an increased toluene content is formulated. However, this results in the lowest LHV among the surrogates. The physical and chemical properties of the different surrogates are given in Table 5.11. The surrogate compositions are shown in Figure 5.19 (b).

In a first step, the impact of the surrogate properties on the flame propagation is investigated. For this purpose a flame speed look-up table for each surrogate is compiled. The laminar flame speeds of the surrogate components and the surrogates are shown at 60 bar, that corresponds typical conditions in a SI engine, in Figure 5.20. At stoichiometric conditions the PRF surrogate has the highest laminar flame speed (Figure 5.20 (b)). At stoichiometric conditions the PRF surrogate has the highest laminar flame speed. The TRF and ETRF surrogates have slower flame speeds due to their toluene content. To analyze the impact on flame propagation, chemistry dependencies of the surrogate in unburnt and burnt zone are excluded. This is achieved by initializing all cases with the same surrogate, but applying different flame speed tables. Surrogate “TRF” is chosen to be initialized since it is composed according to the fuel

Table 5.11: Properties of the commercial gasoline (fuel analysis) and the surrogates (calculated) all with RON=94.5.

	MON	**S**	**Aromatic content**	**Ethanol content**	**Density**	**LHV**	**C:H:O –ratio**
	$[-]$	$[-]$	$[vol\%]$	$[vol\%]$	$[kg/m^3]$	$[MJ/kg]$	$[mass\%]$
Gasoline	84.1	10.4	32.6	0.0	747.5	42.9	86.9.13.1:0.0
PRF	94.5	0.0	0.0	0.0	691.3	44.4	84.2:15.8:0.0
TRF	88.2	6.3	32.6	0.0	747.3	42.9	86.9:13.1:0.0
ETRF 1	88.1	6.4	22.5	5.1	735.3	42.4	84.3:13.8:1.9
ETRF 2	87.6	7.0	15.8	10.1	728.5	41.7	82.0:14.2:3.8
ETRF 3	84.3	10.1	39.5	10.2	769.6	40.9	84.0:12.4:3.6

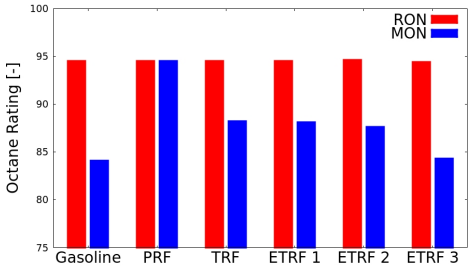

(a) Octane rating of the commercial gasoline and the surrogates.

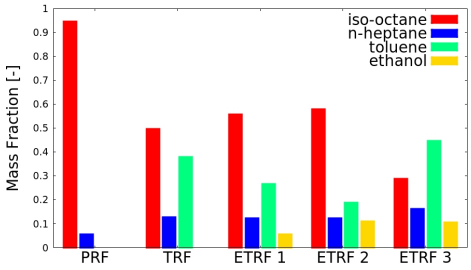

(b) Composition of the surrogates in mass fraction.

Figure 5.19: Illustration of the characteristics of the analyzed surrogates.

used in the experiment. The operating conditions and engine geometry are the same as in Table 5.1, apart from the cylinder head. The same clear difference between the PRF surrogate and the other surrogates are found in the engine simulation (Figure 5.20 (d)). It has to be noted that the CFD simulation has been calibrated using the TRF surrogate, therefore no conclusions on which surrogate leads to the most accurate combustion prediction should be drawn, instead the trends should be considered. Figure 5.21 provides a quantification of the difference in flame propagation. For that purpose, the peak pressure and its location and the combustion phasing at 5%, 10%, 50% and 90% burn duration normalized to the experiment are calculated. The simulation using surrogate "TRF" shows the best agreement with the experiment thanks to the discussed setup choice. Surrogate "PRF" over-predicts the combustion rate, whereas the other surrogates under-predict. At the center of combustion (CA_{50}, in Figure 5.21 (b): 50%) the maximum difference between the fastest (PRF) and the slowest (ETRF 1) surrogates are 1.5°CA. The maximal difference in peak pressure is about 3.5 bar. From this analysis, it can

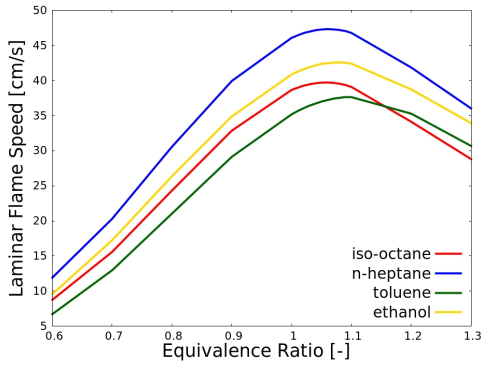

(a) s_l of the surrogate components.

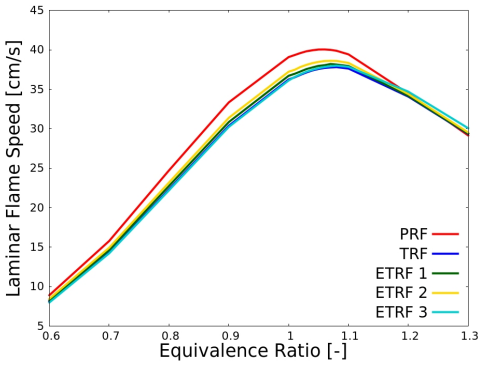

(b) s_l of the analyzed surrogates.

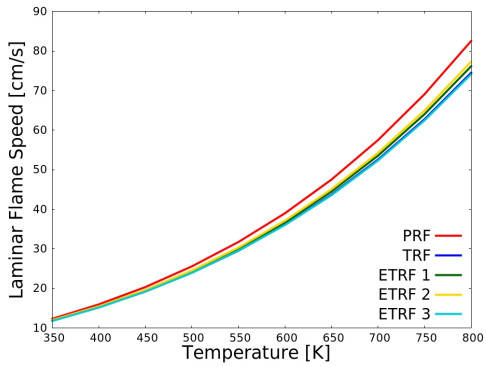

(c) Temperature dependency of the surrogates.

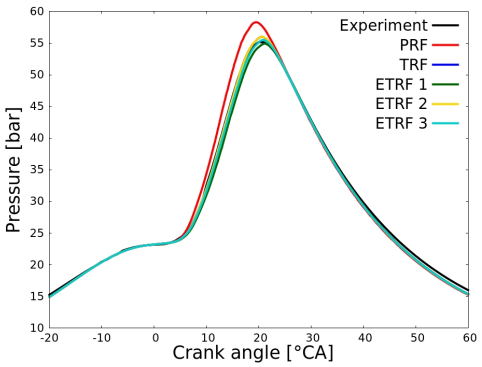

(d) Impact on flame propagation in CFD.

Figure 5.20: Predicted laminar flame speed for the surrogate components and the analyzed surrogates at 60 bar and their impact on the combustion prediction.

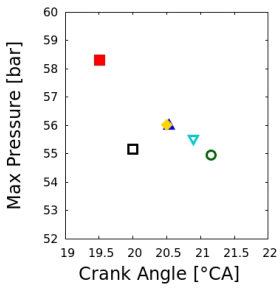

(a) Location of the maximum of the mean pressure.

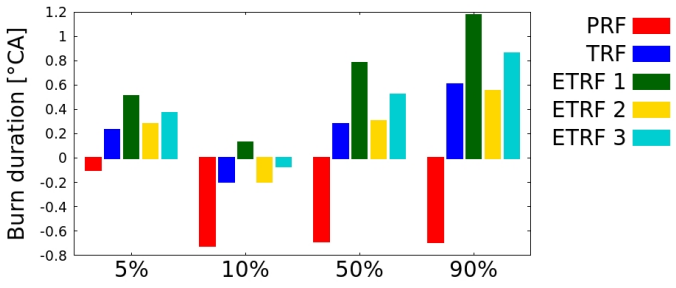

(b) Combustion phasing.

Figure 5.21: Predicted location of the peak pressure and the combustion phasing related to the experiment. Analysis of the combustion prediction using different flame speed tables (corresponding to Figure 5.20 (d)).

be concluded that it is important to consider the fuel surrogate composition on the flame speed prediction in engine simulations.

In a second step, the impact of the surrogate formulation on engine knock is examined. This section does not aim to optimize a fuel or surrogate, but to understand how the surrogate composition may affect the knock prediction. Two different studies that keep all operating parameter the same, are carried out: first the fuel surrogate mass is kept constant and secondly the equivalence ratio is kept constant. Load change and port-injection are not modeled to reduce the number of influencing factors. All simulations are started with same initial mean temperature and pressure. The operating conditions are kept the same. These assumptions lead to a carburetor-type setup, analyzing the same surrogate applying a direct injection might change the results. According to [43], this simulation setup causes the MON value to be more significant than in direct injection gasoline engines. In the first part of the study, the air and fuel mass in the cylinder for all surrogates are set to the same amount. The simulation is initialized homogeneous at IVC, masses are not changed, all differences can be attributed to the chemistry. Since all surrogates have different C:H:O-ratios and consequently a different stoichiometric air demands, the fuel/air equivalence ratios ϕ differ about $\phi = 1 \pm 0.05$. There are also small deviations in trapped energy due to differences in LHV of the surrogates. The second part of the study explores the alternative to adjust the fuel surrogate mass so that all mixtures are stoichiometric. This leads to different trapped masses.
The differences in ignition delay time τ prediction using constant volume reactors versus equivalence ratios ϕ are shown in Figure 5.22 (b), the surrogate components in Figure 5.22 (a). The ignition delay time of surrogate "PRF" has a different trend than the TRF and ETRF surrogates. Whereas for $\phi = 1$ (dashed lines), the ignition delay time of the TRF and ETRF surrogates converge at 870 K and invert the trends at this temperature, this cross-over temperature for the actual trapped mixtures with different equivalence ratios (solid lines) appears at about 820 K. For those predictions, the difference in ignition delay time are more pronounced at 900 K. The predicted ignition delay times are converted from milliseconds to crank angle degree assuming 2000 rpm (Figure 5.22 (c)). At temperatures >900 K, the differences in ignition delay are about 1°CA and higher. This would suggest a distinctive deviation in KLSA in the engine simulations due to the surrogate formulation if only considering ignition delay times.

The predicted mean pressure from CFD for the different surrogates at the reference (ref) spark timing from the experiment are shown in Figure 5.23 (a). Since the same flame speed table is used for all calculations the flame propagation prediction is similar and the thermodynamic conditions in the unburned zone are comparable. For all surrogates a spark sweep from -2°CA to +1°CA related to the reference spark timing is performed. Exemplary, the predicted maximum

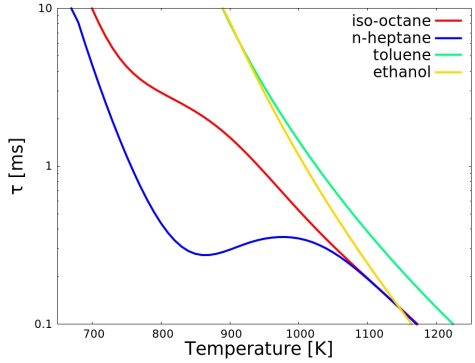

(a) Ignition delay time of the surrogate species for $\phi = 1$ and 60 bar.

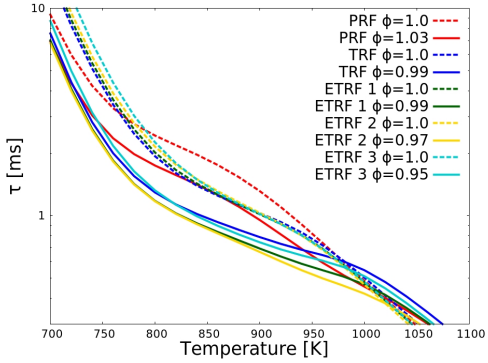

(b) $\phi = 1$ and ϕ in the CFD simulations.

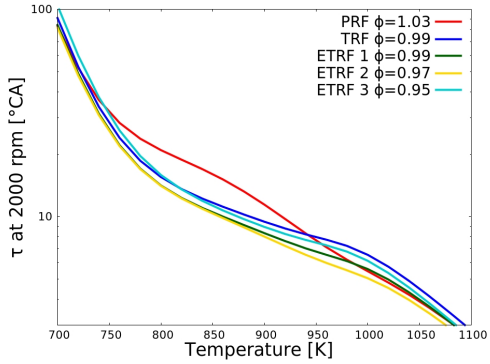

(c) τ in crank angle degree for a speed of 2000 rpm.

Figure 5.22: Predicted ignition delay time τ for different mixtures with air as oxidizer at 60 bar using constant volume reactors.

pressure in the cylinder is shown for the spark sweep using "ETRF 2" (Figure 5.23 (c)). At TDC the modeled spark is visible. Shortly before the maximum pressure is reached, fluctuations resulting from auto-ignitions in the unburned zone occur. The onset of those fluctuations delays and the amplitude decreases with delayed spark timing as it is expected from literature.

For all calculated spark timings, the predicted auto-ignitions in the unburned zone are evaluated using the detonation diagram (Figure 5.23 (d)). "ETRF 2" shows the strongest auto-ignition events in the developing detonation regime. For surrogate "TRF" and "PRF" the ignition kernels for ST -2°CA are very close to the transition line and therefore accounted to the developing detonation regime. Figure 5.24 provides more information on the auto-ignition onset and the ignition kernel size. For surrogate "PRF" the autoignition onset is the latest. This agrees well with the theory since it has the highest MON. Surrogates "TRF" and "ETRF

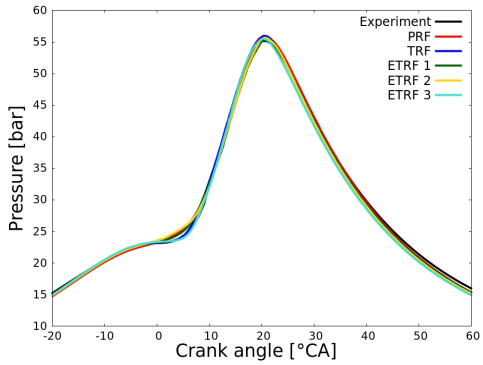

(a) Predicted pressure at the reference spark timing.

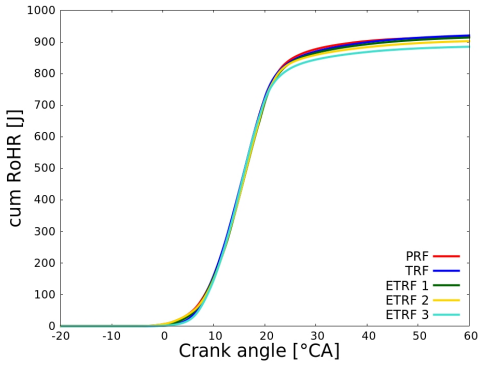

(b) Chemical heat release at the reference spark timing.

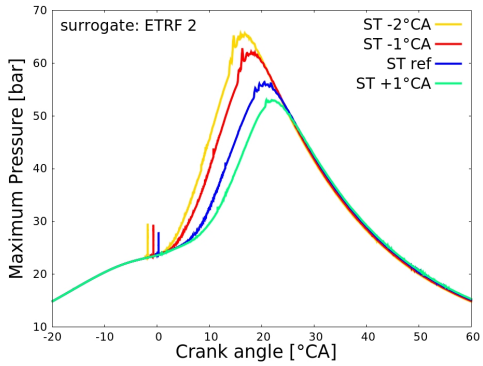

(c) Maximum predicted pressure for the spark timing sweep and “ETRF 2”.

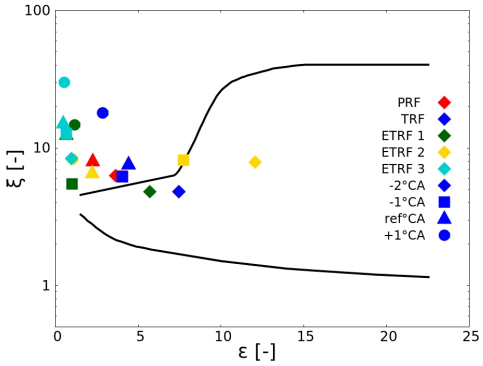

(d) Evaluation in the detonation diagram.

Figure 5.23: Results for the different surrogates using the same fuel mass and flame speed table.

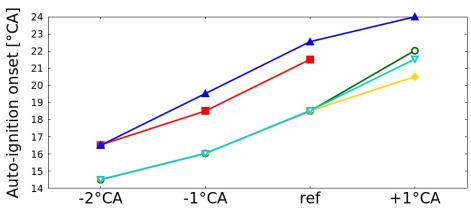

(a) Predicted auto-ignition onset.

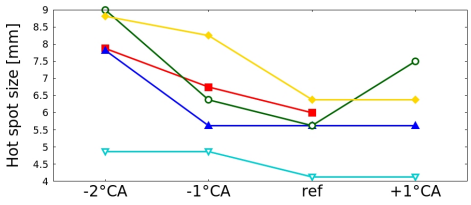

(b) Ignition kernel size r_0.

Figure 5.24: Analysis of the predicted auto-ignition onset and auto-ignition kernel sizes corresponding to Figure 5.23 (d).

1” differ in their composition, but have the same MON and equivalence ratio in the engine simulation. However, the evaluation using the detonation diagram shows noticeable differences

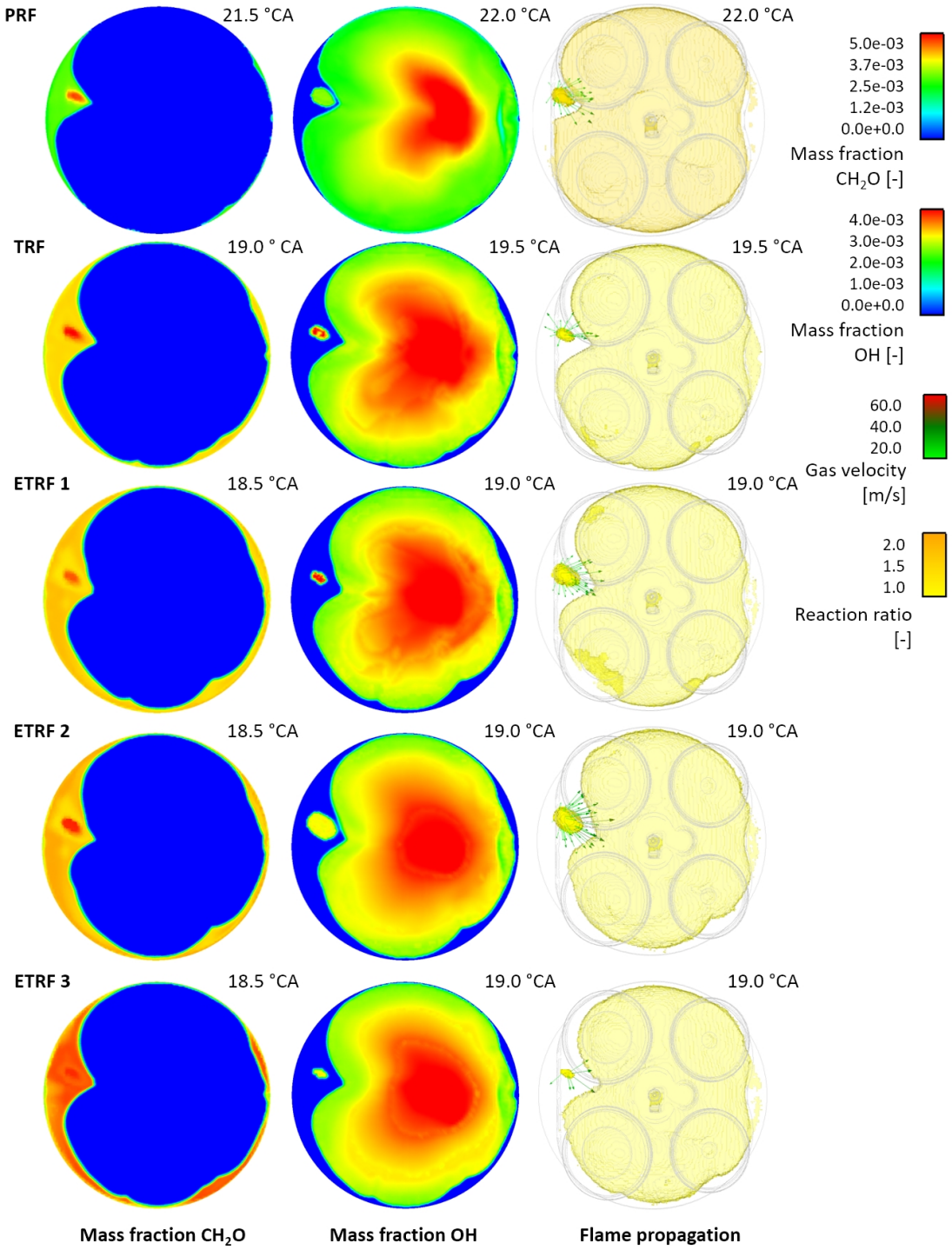

Figure 5.25: Predicted ignition kernels for the different surrogates corresponding to Figure 5.23 (a). View from top on a clip plane.

in the strengths of the auto-ignitions. The auto-ignition onset is earlier for all spark timings. Comparing the three ETRF surrogates, "ETRF 2" forms the strongest auto-ignition kernels and

"ETRF 3" the weakest. This finding agrees with the trend in ignition delay time τ, but disagrees in terms of MON. "ETRF 3" has the lowest, "ETRF 1" the highest MON. Considering only this characteristic number the trends in auto-ignition tendency are unexpected. Several reasons might contribute to this finding: The suggested MON values for toluene differ in literature from MON=104.0 [137] to MON=109.0 [138]. To calculate the MON in this work MON=109.0 is applied as it is reported by Heywood [31] and following the rules from Morgan et al. [39]. Further the difference in MON= 88.1 ("ETRF 1") and MON=87.6 ("ETRF 2") are within the reproducibility and repeatability limits discussed in [34, 137, 138]. Additionally, the engine operating point with a boost pressure of 1.8 bar and 2000 rpm differs to the MON test conditions as discussed in section 2.3. The predicted ignition delay times >820 K show a different trend in auto-ignition tendency than the MON numbers suggest (Figure 5.22). "ETRF 2" leads to the biggest ignition kernels and highest maximum temperatures in those ignition kernels even though they are very similar in RON and MON. Moreover, effects from differences in equivalence ratios, in heat capacity and local flow field may superpose the effect of MON. This becomes clearer when studying the kernel development with the "ETRF 3" surrogate.

Figure 5.25 shows the dimensions of the ignition kernel using CH_2O, the propagation of the imposed reaction front using the mass fraction of OH and the imposed gas velocity as vector arrows. The level of CH_2O in the unburned zone in the time step prior to auto-ignition is the lowest for the PRF and increases with increasing *n*-heptane content, which has a pronounced low temperature chemistry, up to "ETRF 3". In those figures, it can also be seen that the ignition kernels appear in the same region for all calculations at reference spark timing since the flame propagation and flow field are similar. The reactivity of the ignition kernels is illustrated using the OH radical as high temperature marker and the gas velocity vectors. Both agree with the evaluation of the auto-ignition event in the detonation diagram. "ETRF 2" has clearly the strongest auto-ignition event. Surrogate "PRF" has an ignition kernel size that is similar to the ones of "TRF", "ETRF 1" and "ETRF 2", but is less reactive. Even though "ETRF 3" shows the highest concentration of the low temperature marker CH_2O, it shows the lowest concentration of OH and the smallest reacted burned volume (Figure 5.25, bottom row center). It is very likely that there is less energy available in the ignition kernel due to the lower ϕ and lower LHV. This follows also from the cumulative heat release at reference spark timing (Figure 5.23 (b)). At this crank angle, the energy released by auto-ignition competes against the quenching by expansion and it may be possible that the kernel cannot release sufficient energy needed to develop knocking combustion. Using surrogate "ETRF 2" and spark timing ST -2°CA a much stronger knock event than for the other surrogates and spark timings is predicted. This is because the position of the auto-ignition kernel changes. After the first ignition kernel on the

side of the intake valves, the flame and the induced pressure gradient lead to a second stronger knock event close to the exhaust valves (Figure 5.31).

In the third step, the different surrogates are initialized and the flame speed tables generated for the specific surrogate are applied. The fuel masses are adjusted to give the same fuel/air equivalence ratio ($\phi = 1 \pm 0.01$) for all surrogates. The results of this simulations are shown in Figure 5.26. As observed in the flame speed analysis above (Figure 5.20), surrogate "PRF" leads to the fastest flame propagation, "ETRF 3" to the slowest. To match the predicted peak pressure of the experiment, the spark timing was calibrated for the surrogates "PRF" and "ETRF 3". The necessary shift in spark timing is given in Table 5.12. The comparison of predicted pressure traces with reference and calibrated spark timing are shown in Figure 5.26 and in Figure 5.27. The prediction of the peak pressure location and value is improved with adjusted spark timing (Figure 5.27 (a) and (c)). However, the prediction of the combustion phasing at CA_{50} is better for the uncalibrated cases (Figure 5.27 (b) and (d)). For the cases with adjusted spark timing the same analysis as for the cases with the same fuel mass has been performed.

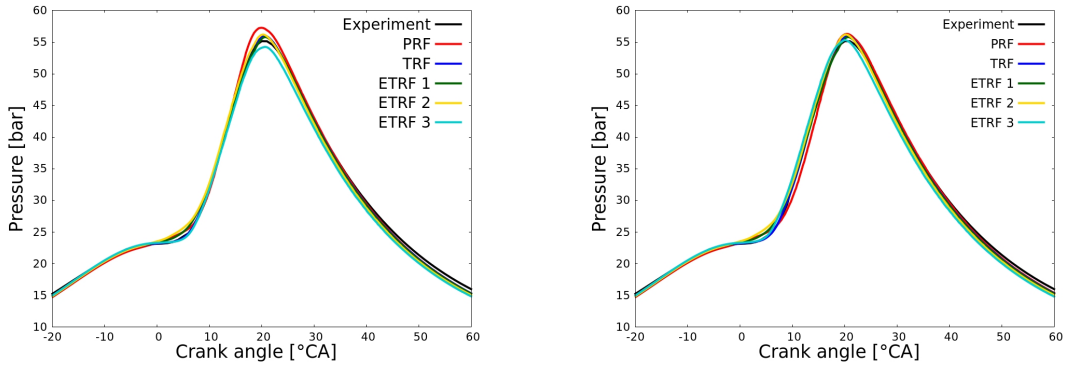

(a) Reference spark timing.

(b) Calibrated spark timing.

Figure 5.26: Predicted pressure using the surrogate specific flame speed table and $\phi \approx 1$.

Table 5.12: Shift in spark timing to match the combustion process of the experiment (compare Figure 5.26).

PRF	TRF	ETRF 1	ETRF 2	ETRF 3
+2.0°CA	-	-	-	-0.5°CA

Figure 5.28 shows the evaluation in the detonation diagram of this study. Conspicuous is that "ETRF 2" leads to much weaker auto-ignitions than observed in Figure 5.23 (d). The ignition

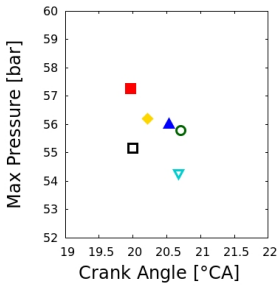

(a) Location of the maximum of the mean pressure reference spark timing.

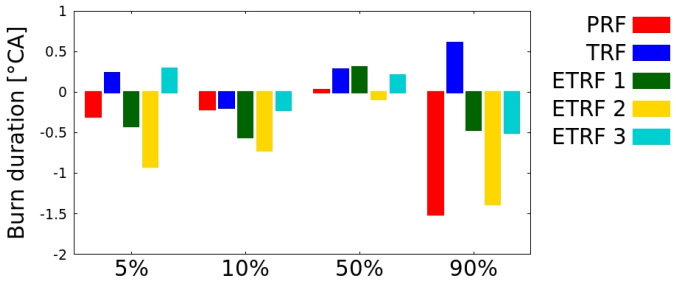

(b) Combustion phasing reference spark timing.

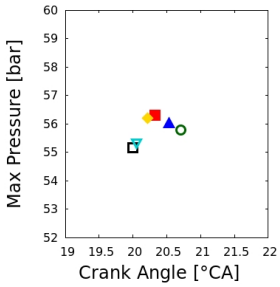

(c) Location of the maximum of the mean pressure calibrated spark timing.

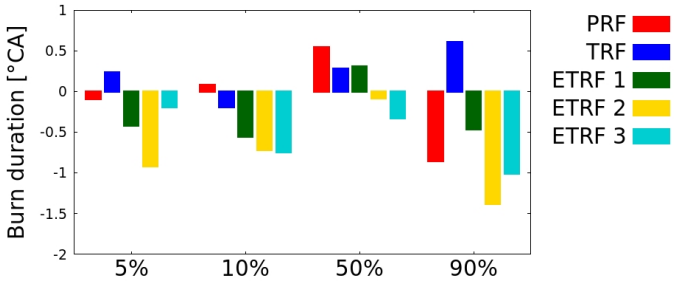

(d) Combustion phasing calibrated spark timing.

Figure 5.27: Predicted location of the peak pressure and the combustion phasing related to the experiment. Analysis of the combustion prediction using different methods for the laminar flame speed (corresponding to Figure 5.26).

kernels occur in the same region (at the side of the intake vales). However, the transition of the strongest auto-ignition event to the exhaust valve side is not predicted. The ignition delay times in the charge with $\phi \approx 1$ are longer than in the previous studies $\phi = 0.97$ (Figure 5.22 (b)). The same trend is found for the PRF surrogate. The predicted auto-ignitions are the weakest in comparison to the other surrogates, the strongest auto-ignition (predicted for the spark timing ST -2°CA) is clearly in deflagration mode. “TRF” and “ETRF 1” with the same MON, show a very different transition to a possible developing detonation. Whereas for surrogate “TRF” with advanced spark timing ξ decreases, ε increases, for surrogate “ETRF 1”, decreases ξ much less (logarithmic scale). The same trends and reason for this can be found in the maximum temperatures in the ignition kernel just prior the high temperature ignition and the excitation times (Figure 5.29 (c) and (d)).

Table 5.13 presents the auto-ignition onset and the latest spark timing of predicted knock

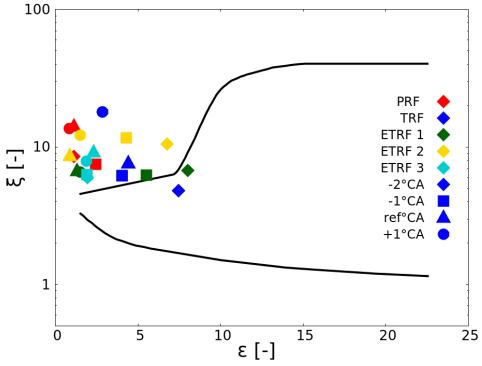

Figure 5.28: Evaluation of the predicted auto-ignitions performing a spark variation corresponding to Figure 5.26 (b).

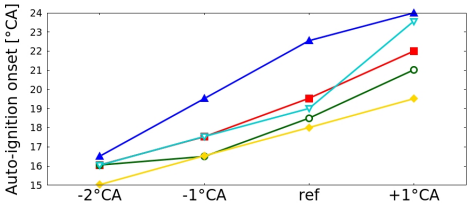

(a) Auto-ignition onset.

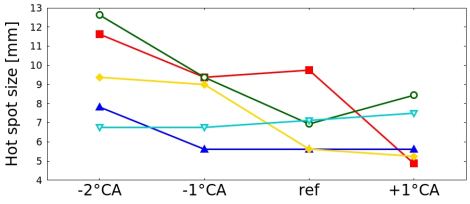

(b) Ignition kernel size r_0.

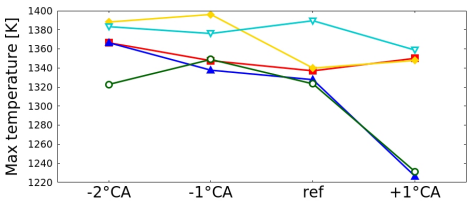

(c) Maximum temperature prior ignition.

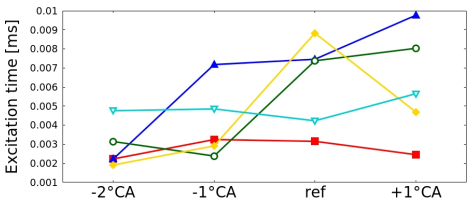

(d) Excitation time τ_e.

Figure 5.29: Analysis of the predicted auto-ignition onset and auto-ignition kernel sizes corresponding to 5.26 (b).

for the two CFD studies. Whereas, except for the PRF, the auto-ignition onset is close for the complex surrogates, varies the tendency to form a developing detonation. The results show, that even though a similar flame propagation and flow filed are predicted, the surrogates auto-ignite different. The ignition onset, kernel sizes as well as the imposed gas velocities differ between the surrogates. This finding is independent from the fuel/air equivalence ratio. The differences in KLSA due to the differences in the surrogate composition are found to be up to 2°CA. The cooling due to vaporization may increase predicted differences. The ranking of the ETRF surrogates may depend on the properties used for the surrogate composition and the accuracies of the chemical and numerical models. However, it is evident that the

Table 5.13: Predicted auto-ignition onset of the reference spark timing and latest spark timing of predicted knock corresponding to Figure 5.23 and Figure 5.28.

	First auto-ignition event [°CA]		**First knock event** [ST in °CA]	
	$m_{fuel} = const$	$\phi = const$	$m_{fuel} = const$	$\phi = const$
PRF	22.0	22.5	-2	/
TRF	19.5	20.0	-1	-1
ETRF 1	19.0	19.0	-2	-1
ETRF 2	19.0	18.5	-1	/
ETRF 3	19.0	19.5	/	/

predictions using the PRF surrogate are outliers. The auto-ignition onset is predicted later, the ignition event weaker. Using this simplified surrogate underestimates the knock tendency compared to the more complex surrogate formulations. This finding goes well together with the MON numbers. However, in homogenous zero-dimensional reactors that are used for the development of reaction mechanism and to validate against ignition delay time measurements those effects are also neglected. The conditions are closer to the MON test than to the RON test. To understand if the different knock tendency can be estimated with homogeneous reactors, so that computationally expensive CFD simulations can be avoided, the auto-ignition tendency of the surrogates is investigated in constant volume reactors (CVR) and zero-dimensional rapid compression machine (RCM) simulations.

Figure 5.30 shows two typical low temperature chemistry species CH_2O, an early *iso*-octane decomposition product C_8H_{17} and the temperature of the domain. The species mass and temperature profiles are shown for different simulation methods:

a) Constant volume reactors (CVR) that are typically used to calculate ignition delay times.

b) Homogeneous rapid compression machine (RCM) simulations imposing the engine volume profile and species concentrations as in the engine simulation to consider the transient effects. Calculations with an initial temperature of 600 K that do not ignite, but show the evolution of the low temperature chemistry.

c) As b), but with an initial temperature of 800 K to study auto-ignition.

d) Three-dimensional CFD SI engine simulations with constant fuel mass.

The ignition delay time estimated from the OH gradient ranks the auto-ignition tendency. If no auto-ignition is predicted, the surrogate with the highest concentration of low temperature

species, earliest formation of OH and the highest compression end temperature is assumed to auto-ignite the first, the others in descending order. For the CFD simulation, the ranking from auto-ignition onset (AI onset) and the evaluation from the detonation diagram are shown. The auto-ignition tendency of the surrogates differs in the predicted order as well as in sensitivity. In the CVR simulations the maximum deviation, expressed in crank angle degree assuming 2000 rpm, is 2.0 °CA, in the RCM simulations it is 1.0 °CA. Analyzing the same operating point with the ETRF mechanism by Cai and Pitsch [44] leads to maximum deviations of 4.0 °CA and 1.5 °CA, respectively. This deviation is proportional with speed. The stationary CVR simulations are more sensitive to changes in the chemistry than the RCM simulations, in which pressure and unburned temperatures change. The CVR simulations are therefore more meaningful to understand the differences in ignition delay. In contrast, the RCM simulations give the conclusion that differences between CVR and CFD rankings are not only explained by transient effects. In both simulations where auto-ignition is observed (Figure 5.30 (a) and (c)), the low temperature chemistry occurs the earliest for surrogate “PRF”, which is not the case in the transient and non-igniting RCM and in the mean CFD simulation output (Figure 5.30 (d)). The CH_2O concentration is lower as for the other surrogates as it is also predicted in the transient simulations. “ETRF 2” has the earliest CH_2O formation in the transient calculations and leads to the strongest knock events in the CFD simulation. “ETRF 1” has a lower tendency to auto-ignite than “ETRF 2” in the RCM and CFD simulation, but not in the CVR calculations. From the RCM calculation, it can be seen that “ETRF 3” reaches a higher compression pressure and temperature, but releases the least energy in the expansion. The TRF mixture has longer ignition delay times in the CVR calculations, but is on the second rank in knock tendency in the engine simulation. This points out, that solely from homogeneous calculations (CVR or RCM) no conclusion on the knock tendency can be drawn. The same study was performed using the ETRF mechanism from Cai and Pitsch [139]. Even though this scheme ignites earlier, the same trends for the ETRF surrogates have been found, but no clear connection between the homogeneous calculations and the knock tendency in the CFD calculation. In literature, studies relating ignition delay times from 0D simulations to the octane rating can be found. They emphasize that their relation is not straight forward, e.g. [140]. The different auto-ignition tendencies are ranked in Table 5.14. It needs to be pointed out, that this ranking depends on the initial temperature and pressure. As it can be seen from Figures 6 to 8, the predicted ignition delay time of surrogate “PRF” crosses the predicted ignition delay times of the other surrogates in the range from 900 K to 1050 K. However, as demonstrated this also changes with the applied model approach (transient in the RCM or stationary in the CVR simulations). Small changes in fuel/air equivalence ratio (Figure 18 a) and b)) lead to a different ranking. In the CFD simulations, local gradients in unburnt temperature as well as species concentrations are predicted. Those gradients affect the occurrence of predicted of the auto-ignition events.

Overall surrogate “ETRF 2” is ranked to auto-ignite the most likely, “PRF” is ranked to be the most auto-ignition resistant. Not every auto-ignition leads to engine knock. It is essential to distinguish a harmless auto-ignition in deflagration mode from an auto-ignition that leads to a developing detonation. The comparison of the AI onset and knock tendency of the different CFD simulations show this. Regarding the AI onset only, the TRF and ETRF surrogates are close; the ranking in terms of the transition to developing combustion shows bigger deviations. “ETRF 3” ignites in the same crank angle, but does not from a developing detonation. By considering the ignition delay times from homogeneous stationary or transient simulations, this distinction cannot be made since no gradients in temperature or ignition delay time are present. For this kind of analysis, simulation approaches that account for inhomogeneity are necessary, i.e. CFD simulations or zero-dimensional stochastic reactor models. Figure 5.25 shows that even though the auto-ignition is predicated in the same time step (ETRF surrogates), only “ETRF 2” turns to a developing detonation. This conclusion cannot be drawn from a homogeneous calculation. Summarizing this study, it was found that even though the surrogates have the same RON, the tendency to auto-ignite in the engine simulations is very different. No clear connections between MON and knock tendency or ignition delay time in homogeneous reactors and knock tendency was found. The predicted sensitivities may also depend on the specific surrogate properties and the resulting small differences in the initial charge such as density, heat capacity, LHV and C:H:O-ratio. It was found that it is not possible to estimate the knock tendency of different surrogates in the CFD simulation from homogeneous reactor calculations. The ranking in terms of auto-ignition onset and transition to developing detonation are different, since not every auto-ignition turns to engine knock. This finding is irrespective of the used reaction scheme, but may be influenced by the physical properties of the analyzed surrogates. There is a complex interaction between turbulence, physical phenomena and combustion chemistry.

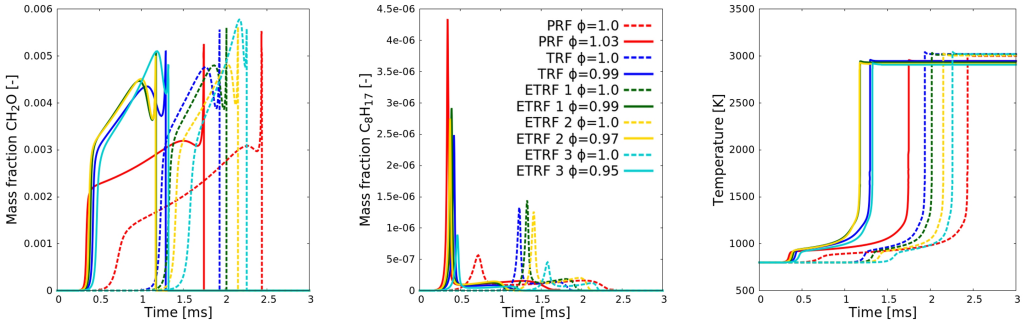

(a) Constant volume reactor - 800 K and 60 bar.

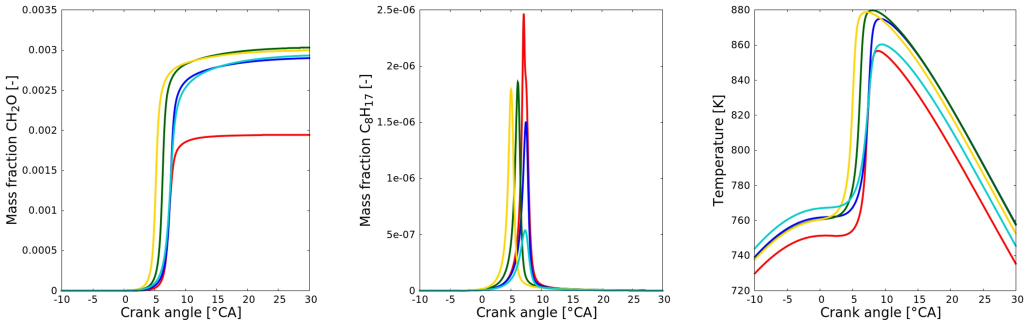

(b) Rapid compression machine - 600 K.

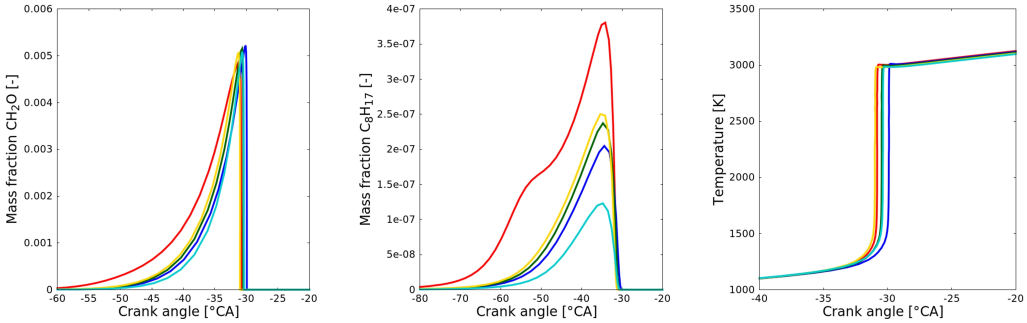

(c) Rapid compression machine - 800 K.

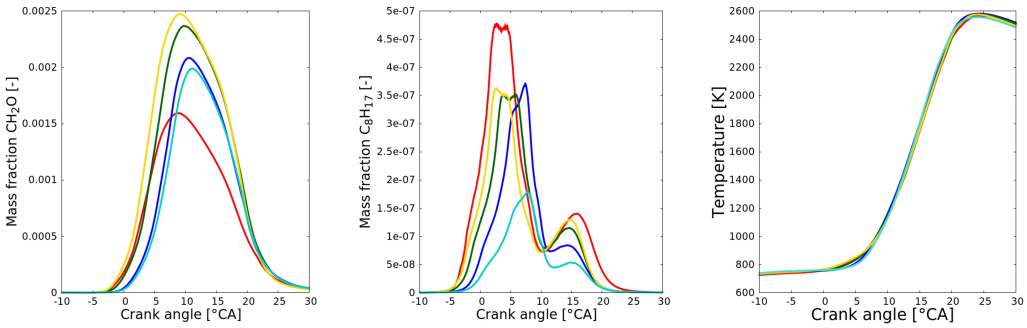

(d) Three-dimensional engine simulation.

Figure 5.30: Predicted mass fractions of typical low temperature chemistry species and temperature profiles for different simulation methods.

Table 5.14: Knock tendency estimated from different simulation methods and MON value. RCM^1 is initialized with 600 K, RCM^2 with 800 K.

	ϕ	**Auto-ignition tendency ranking**								
MON		ETRF 3	>	ETRF 2	>	ETRF 1	|	TRF	>	PRF
CVR	1.0	TRF	>	ETRF 1	>	ETRF 2	>	ETRF 3	>	PRF
CVR	1 ± 0.05	ETRF 1	|	ETRF 2	>	TRF	>	ETRF 3	>	PRF
RCM^1	1 ± 0.05	ETRF 2	>	ETRF 1	>	TRF	|	ETRF 3	>	PRF
RCM^2	1 ± 0.05	ETRF 2	>	PRF	>	ETRF 1	|	ETRF 3	>	TRF
CFD (AI onset)	1 ± 0.05	ETRF 1	|	ETRF 2	|	ETRF 3	>	TRF	>	PRF
CFD (AI onset)	1 ± 0.05	ETRF 2	>	ETRF 1	>	ETRF 3	>	TRF	>	PRF
		Knock tendency ranking								
CFD (knock)	1 ± 0.05	ETRF 2	>	TRF	>	ETRF 1	>	PRF	>	ETRF 3
CFD (knock)	1 ± 0.01	TRF	>	ETRF 1	>	ETRF 2	>	PRF	|	ETRF 3

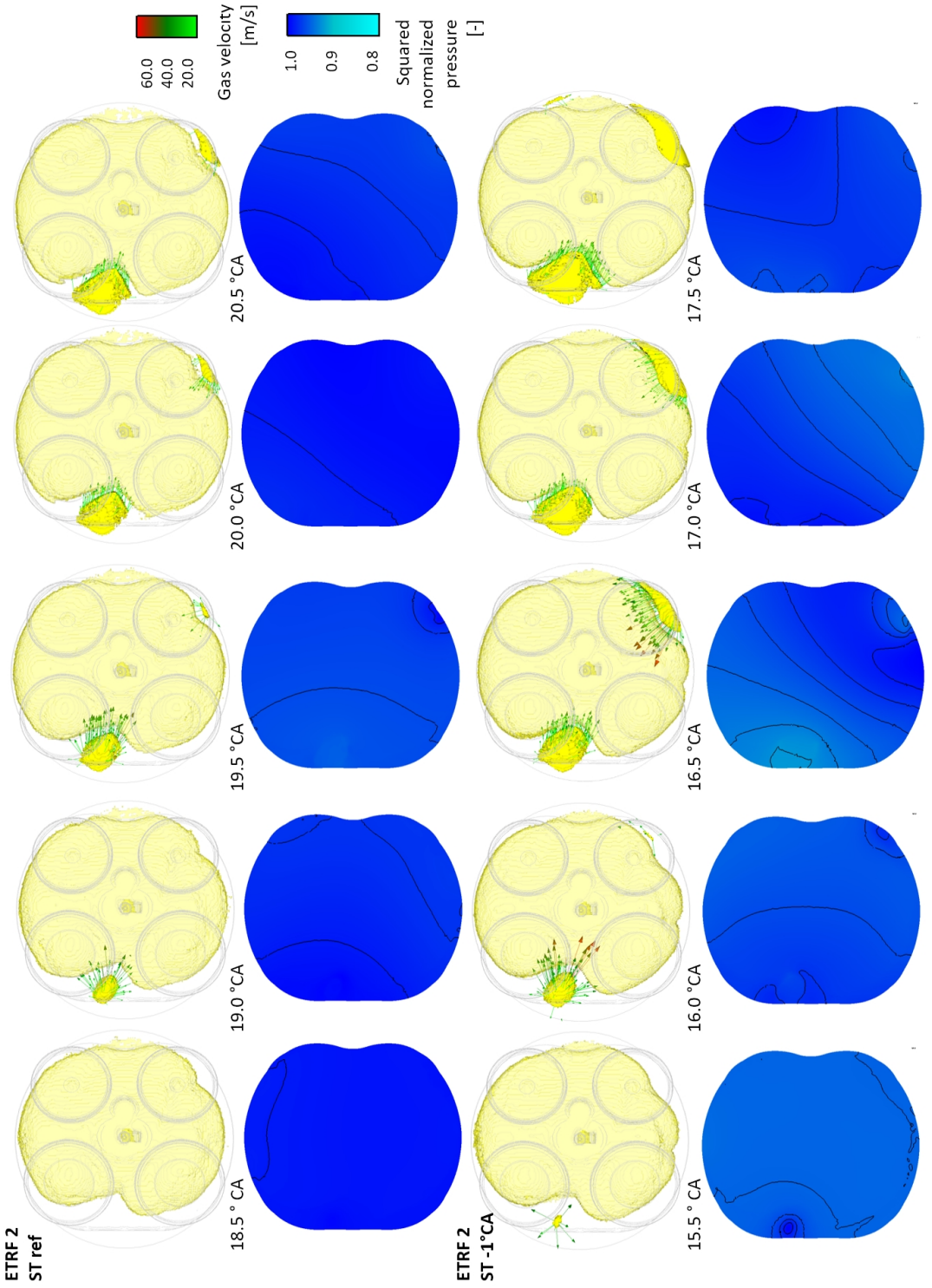

Figure 5.31: Predicted ignition kernels for the different surrogates corresponding to Figure 5.23 (a). View from top on a clip plane.

6 Resonance Theory in Zero-Dimensional Engine Simulations

6.1 Methodology

In this chapter, he resonance theory (discussed in section 2.5) is transferred to the quasi-dimensional engine model (SI-SRM). Auto-ignitions in the unburnt zone can be identified using the rate of heat release. The ignition event in the unburnt gases for regular hydrocarbon fuel blends typically consists of two stages. This is discussed on an example using a RON 87.0 surrogate. First, during the low temperature pre-reactions the decomposition of the alkane fuel species starts. An example for a low temperature intermediate species is the oxygenated *iso*-$C_{18}H_{17}O_2$, which is formed by the addition of O_2 to *iso*-octyl at temperatures below $\sim$1000 K. This species shows its maximum concentration (Figure 6.1 (a)) at around 8°CA before TDC. At the same time typical low temperature markers such as formaldehyde (CH_2O) are formed (Figure 6.1 (b)). The concentration of CH_2O increases as the auto-ignition process propagates between the low temperature pre-ignition and the high temperature excitation. At around 35°CA aTDC the main auto-ignition event or high temperature excitation is observed. It is characterized by the consumption of all fuel molecules and the formation of the typical high temperature combustion products such as hydroxyl radical OH (Figure 6.1 (d)). Since the majority of these reactions are exothermic, the two ignition stages can also be characterized by the heat release in the unburnt zone. The two peaks from low temperature pre-reactions and high temperature excitation are visible in the apparent rate of heat release for the whole domain (Figure 6.1 and 6.2). During the occurrence of the low temperature chemistry event the whole combustion domain corresponds to the unburnt zone since the charge will be ignited at 4°CA aTDC. The heat release rates, calculated for the whole combustion domain and for the unburnt zone are equal (Figure 6.2 (a)). The released energy during the main auto-ignition in the unburnt zone at 35°CA after TDC is visible in the apparent rate of heat release for the whole domain and

leads to a steep rise of the pressure in the combustion chamber (Figure 6.2 (b)). Therefore, the heat release in the unburnt zone is an indicator for auto-ignitions in this zone. To evaluate if the detected auto-ignition event leads to knocking combustion the detonation diagram by Bradley and co-workers [2, 3] is applied.

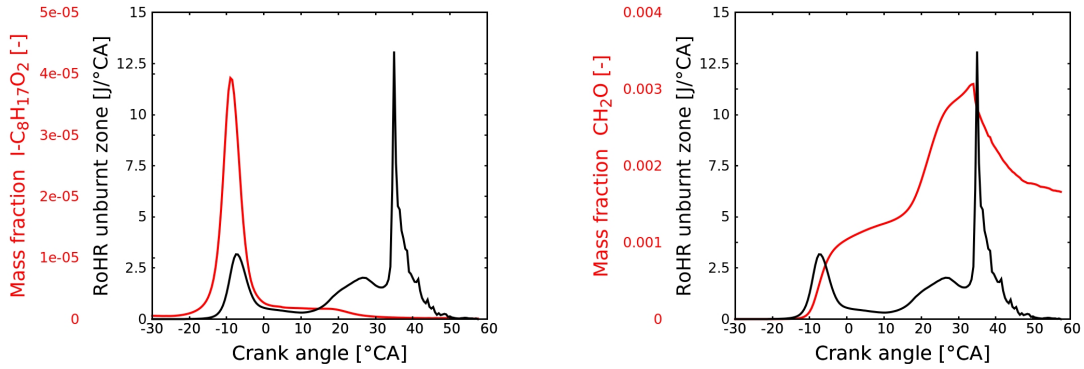

(a) Low temperature, *iso*-$C_8H_{17}O_2$.

(b) Low temperature, CH_20.

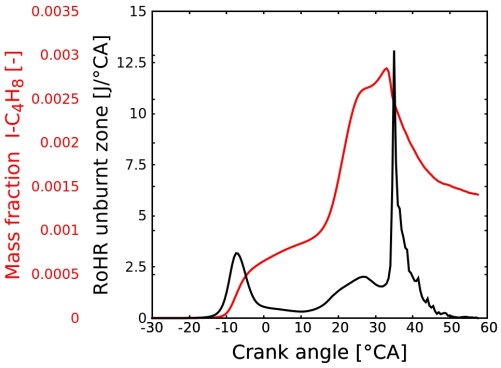

(c) Low temperature, *iso*-C_4H_8.

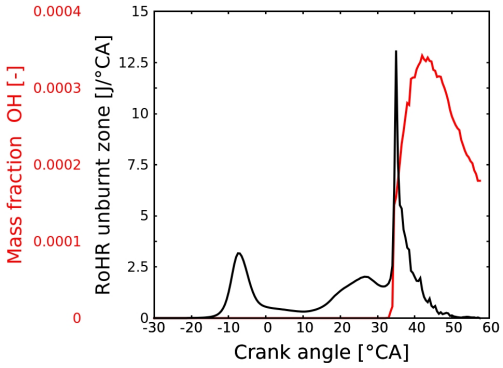

(d) High temperature, OH.

Figure 6.1: Rate of heat release in the unburnt zone (black line) and mass fraction of selected species. Figure according to [15].

The resonance theory is applies based on the heat release and the local conditions in the unburnt zone the methodology is applied during post-processing. Since there is no spatial resolution for the particles, all particles that contribute to the investigated high temperature peak are collected and treated as one ignition kernel. The total volume of the ignition kernel is calculated from the apparent volumes of the identified particles. The apparent volumes are calculated from the mass and density of each particle. To determine the maximum knock intensity of the current cycle, the time step of the maximum gradient in the rate of heat release of the total domain is selected. All particles, that ignite in the analyzed time step, are identified and accounted to the ignition kernel. The ignition of the particles is identified by their maximum heat release

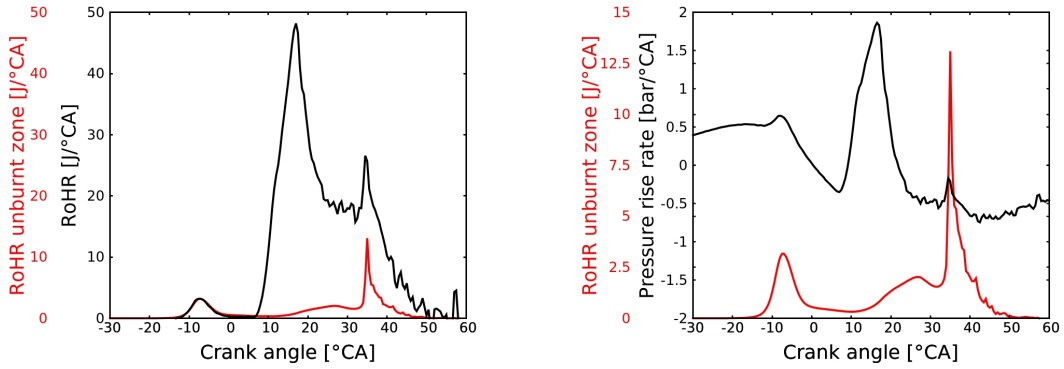

(a) Rate of heat release.

(b) Pressure rise rate.

Figure 6.2: Relation between heat release in the unburnt zone and combustion properties of the total domain. Figure according to [15].

rise rate. The term "time step" refers here to a time step of the operator splitting loop, which is used to solve the mass density equation, introduced by the SRM (see reference [90] and references therein or section 3.4). Particles that ignite in an earlier or later time step (time step size 0.5°CA) are accounted to a different auto-ignition kernel and not further treated in this study. In this way, the most severe auto-ignition event (steepest heat release gradient) of the current cycle is investigated and evaluated.

To calculate the reaction front velocity, the ignition kernel is assumed to be a sphere. Due to the auto-ignition the temperature of the kernel is increased, the volume increases accordingly. The difference of the radius of the ignition kernel before and after ignition gives the length for the reaction velocity calculation. The ignition delay time τ gradient is calculated using the maximum particle temperature of the ignition kernel (sum of all selected particles) before the ignition occurs and the mean temperature of the unburnt zone. The speed of sound a is calculated as function of the mean properties of the end gas. To estimate ε, r_0 is set to the diameter of the kernel prior ignition. The excitation time is calculated for the maximum temperature of the ignition kernel prior the ignition event (analog to RANS). Fuel characteristics, such as ignition delay time and excitation time, are calculated based on the 188 species mechanism using homogeneous constant volume reactors. These calculations are carried out as post-processing step and are performed with the LOGEsoft 1.08 [9]. The species concentrations and thermodynamic conditions (T_u and p), of the ignition kernel at one time step prior the ignition are used as initial conditions.

6.2 Verification of the Methodology

The engine case specified in Table 5.1 servers as reference case. In the modeling, the cylinder volume is represented by 1000 dimensionless particles. For each operating point, 30 consecutive cycles with a time step size of 0.5°CA are calculated. The determined EGR composition of the prior cycle is feed as inlet to the next cycle according to the EGR level. Figure 6.3 compares the mean predicted pressure and apparent rate of heat release against the measurement (300 consecutive cycles).

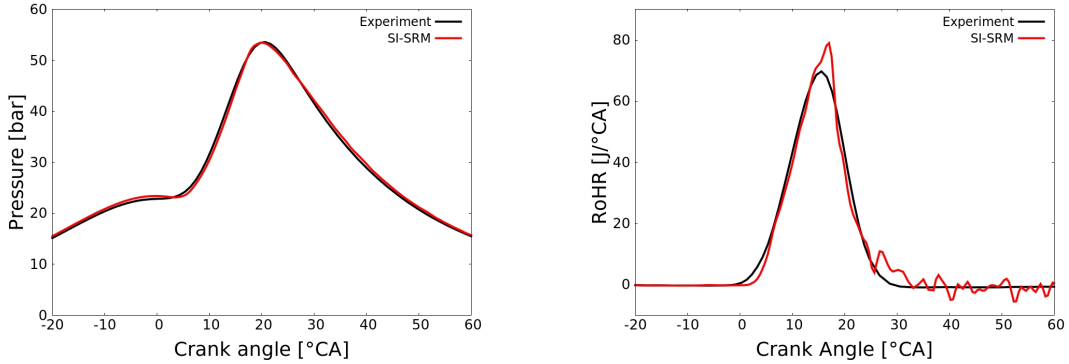

(a) Pressure.

(b) Rate of heat release.

Figure 6.3: Comparison of experimental (black line) and prediction (red). Figure according to [15].

Based on the zero-dimensional application of the detonation diagram the reference operating point is evaluated for the reference fuel blend with RON 96.0 / MON 91.1. In the experiment, this operating point was found to be at the KLSA, further spark advancing would result in knocking combustion. The predicted results are evaluated in Figure 6.4. Two major modes can be identified: whereas some cycles are in subsonic deflagration mode, some are in the mild knock area. Delaying the spark timing about 1°CA shows a more homogeneously distribution with the majority of the events in subsonic auto-ignition regime. Therefore, ST +1°CA is accounted to be at the KLSA.

To study the capabilities of the zero-dimensional evaluation of the knock event, two different modeling studies have been carried out to investigate the transition from deflagration to knocking combustion: first knocking combustion is forced by advancing the spark timing and secondly by varying the composition and therefore the octane rating of the surrogate at a fixed spark timing.

First, the results obtained for different spark timings are discussed. All other parameters are

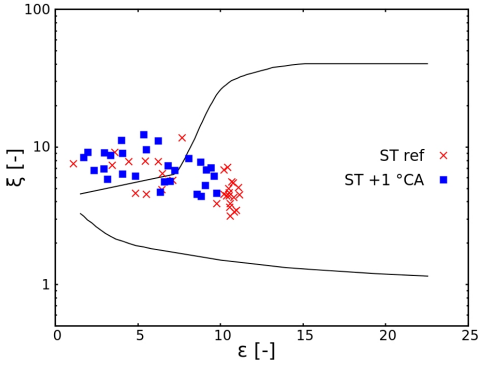

Figure 6.4: Detonation diagram for the reference engine case and the reference fuel (RON 96.0 and MON 91.1) and for 1°CA delayed spark timing. Figure according to [15].

kept unchanged. The predicted pressure rise rates using the surrogate with RON 87.0 are shown in Figure 6.5 (a). The operating point at reference spark timing (-4°CA aTDC) shows a significant pressure rise at about 20°CA. By delaying the spark timing, the mean pressure rise due to the auto-ignition events decreases from 1 bar/°CA down to 0.1 bar/°CA for spark timing ref +5°CA. For the operating points +6°CA and +7°CA delayed spark timing, no steep rise in the pressure is observed, while +5°CA to +2°CA show an increasing gradient in pressure rise. The knock evaluation for these calculations are shown in Figure 6.5 (b). With a higher predicted mean pressure rise rate, the cycle-to-cycle evaluation in the detonation diagram moves towards smaller ξ and larger ε values. This behavior is expected. The predicted gradients in pressure and the results from the detonation diagram are consistent. Of special interest is the spark timing ref +6°CA. Even though, no steep mean pressure rise is predicted, there are auto-ignition events detected. Delaying the spark timing about 1°CA leads to the elimination of auto-ignition events; advancing about 1°CA to mild knock. This suggests that with Ref +6°CA spark timing the engine operates at the knock limit.

By analyzing the heat release in the unburned zone, the transition from no auto-ignition event to knocking combustion can be followed up in detail. Figure 6.6 shows the evolution of the heat release in the unburned zone for three different spark timings. Shown are the cycle-to-cycle variations for 30 consecutive cycles. Based on the single pictures the transition from no auto-ignition in the unburned zone (spark timing ref +7°CA) over harmless deflagration after auto-ignition to mild knock (spark timing ref +5°CA) can be studied. If there is no auto-ignition event (spark timing ref +7°CA), the cycle-to-cycle variations are small. As soon as an auto-ignition occurs (spark timing ref +6°CA) the combustion becomes more unstable.
Knocking combustion can develop over several cycles and often do not occur with the same severity at each appearance [31]. The scattered distribution of the single engine cycles in the

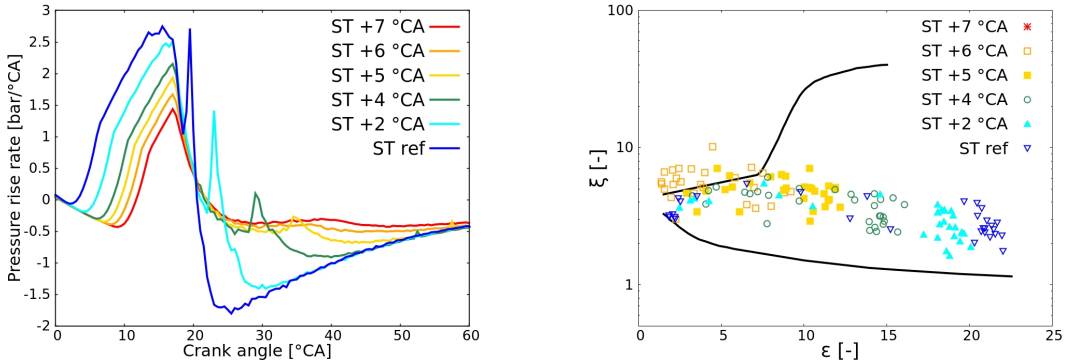

(a) Pressure rise rate.

(b) Detonation diagram.

Figure 6.5: Predicted mean pressure rise rate for reference engine case and surrogate F1 (RON 87.0 and MON 82.4) and different spark timings and evaluation of the predicted auto-ignitions in the detonation diagram. Figure according to [15].

detonation diagram indicates that the model is able to predict this behavior. To evaluate the irregularity of the combustion, the mean values for ξ and ε and their variance over 30 cycles are shown in Figure 6.7. The variance in ξ appears to be about the same for all investigated operating points. The magnitude of ξ is mainly a function of the reaction front velocity. According to that, it is reasonable to find only a small range of variance. The mean values of ξ decrease with advanced spark timing, the knock intensity increases. In contrast, the variance in ε increases significantly with an increase of the knock severity. The conditions that lead to auto-ignition events are spread wider. This indicates that operating points with a stronger knock tendency are accompanied by increasingly unstable combustion. The mean ε values increase with advancing of the spark ignition. The operating conditions close to the knock limit appear to be particularly homogeneous with an especially stable combustion.

The second performed study is the simulation of the reference operating point applying surrogates with different octane ratings. Four different ETRF surrogates and their corresponding laminar flame speed look-up tables are applied. Figure 6.8 (a) shows the predicted mean pressure gradients for this study. It can be seen that with increased RON and MON the mean pressure rise due to auto-ignition decreases. For RON 87.0 this peak is around 1 bar/°CA, whereas for RON 96.0 only 0.2 bar/°CA are predicted. In case of RON 106.9 no sudden change in the pressure trace is found. With the increasing octane rating the occurrence of the mean auto-ignition event in the unburnt zone is delayed.
Figure 6.8 (b) shows the corresponding evaluation based on the detonation diagram. For RON 106.9 just in a few cycles an auto-ignition is predicted. If an auto-ignition occurs, it is in sub-

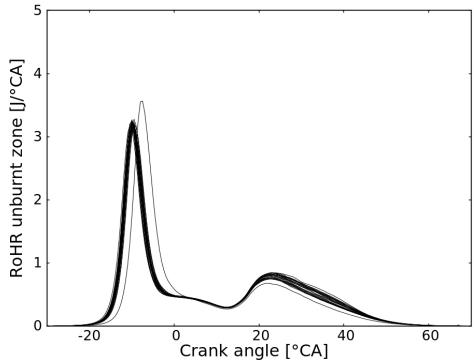

(a) ST +7°CA.

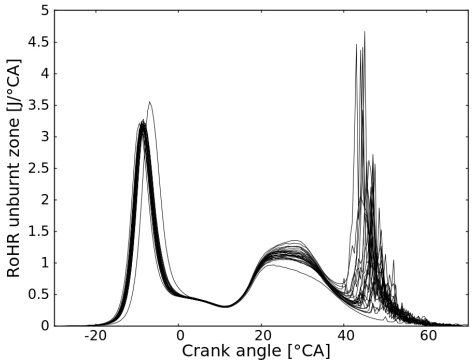

(b) ST +6°CA.

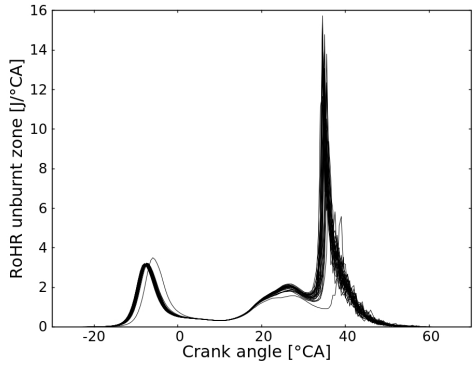

(c) ST +5°CA.

Figure 6.6: Rate of heat release in the unburnt zone for different spark timings in comparison to reference spark timing delayed about 5 to 7 CAD. Cycle-to-cycle variations are shown for 30 consecutive cycles in colored lines. Figure according to [15].

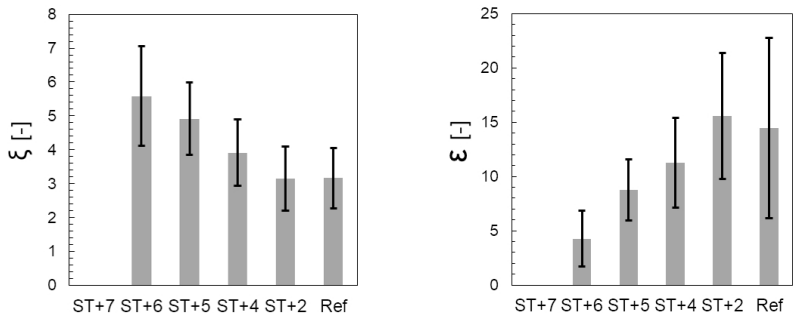

Figure 6.7: Mean value (gray bars) and variance (black error bars) for ξ and ε corresponding to Figure 6.5 (b). Figure according to [15].

sonic deflagration mode and harmless for the engine. For the reference surrogate wiht RON 96.0 and below an auto-ignition event occurs in each cycle. The intensity increases with decreasing RON. For RON 96.0 and RON 94.5 two different regimes emerge. On the one hand, there are knocking cycles, on the other hand there are auto-ignition events in subsonic deflagration mode. For RON 87.0 every cycle shows strong knock.

In Figure 6.9 the mean calculated values for ξ and ε as well as the variance of these values are shown. The mean values for ξ increase exponentially. Whereas the variance in ξ for the calculations used different RON is of the same magnitude. In contrast, for ε the variance gets wider with decreasing RON. Similarly, to the investigations for a fixed surrogate fuel at different spark timings, it is also found that the more the fuel tends to knock, the more unstable the combustion develops.

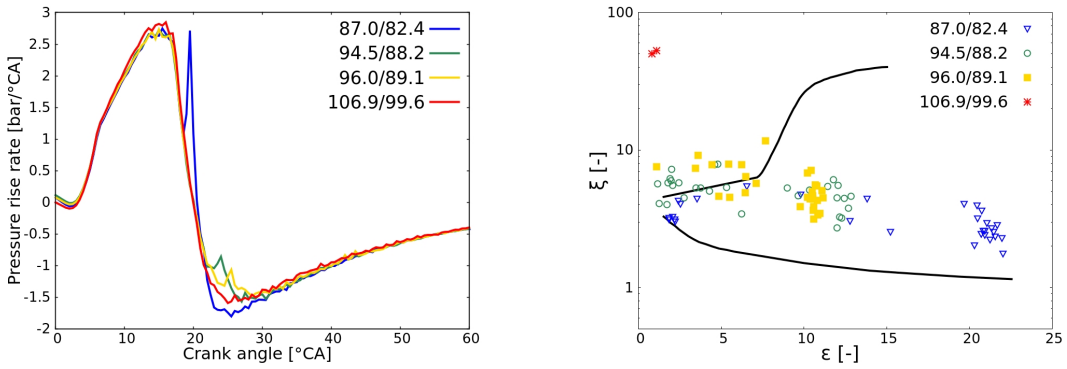

(a) Pressure rise rate.

(b) Detonation diagram.

Figure 6.8: Predicted mean pressure rise rate for reference engine case and surrogates with different octane rating and evaluation of the predicted auto-ignitions in the detonation diagram. The legend gives the RON/MON values of the analyzed surrogate. Figure according to [15].

Summarizing, the model corresponds to the changes as expected from theory and practical observations: with advanced spark timing or reduced surrogate octane rating, the rise rates of the mean pressure increase and thereby the knock strength. It was further found, that the variance of ε is a good measure for the cycle-to-cycle combustion stability and shows a strong correlation with the knock tendency.

6.3 Analysis of Surrogates

The data from 14 commercial gasolines have been used to compose TRF and ETRF surrogates applying the methodology by Seidel [29]. The physical and chemical properties such as C:H:O-ratio, MON, LHV and density of the surrogates (Table 6.2) are in close agreement to

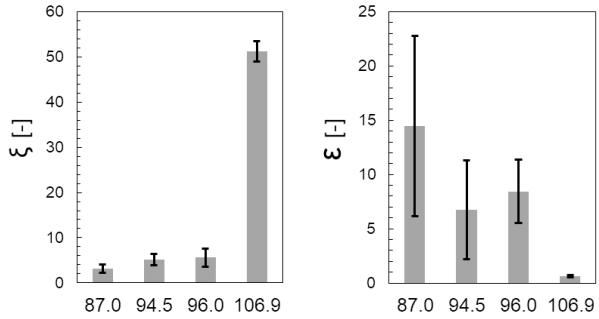

Figure 6.9: Mean value (gray bars) and variance (black error bars) for ξ and ε corresponding to Figure 6.8. Figure according to [15].

the commercial gasoline fuels (Table 6.1).

A sensitivity study to the surrogate composition is performed. The surrogate composition (Table 6.2) in the engine calculation is exchanged and the corresponding laminar flame speed table is applied. The equivalence ratio is set to $\phi = 1$, all remaining parameters are not changed. Figure 6.10 (a) shows the mean predicted pressure over 30 consecutive cycles using different TRF mixtures. The steep changes in the pressure rise rates and rate of heat release indicates an auto-ignition in the end gas. As expected, these peaks decrease with increasing octane number until it vanishes for F14 (RON 106.9/MON 95.3). With this decrease, the occurrence of auto-ignition in the engine cycle is delayed as well. This can be explained by considering the ignition delay time τ for the different applied surrogates (Figure 6.11). The higher RON/MON, the longer is the ignition delay time. The increase in ignition delay time with increasing RON/MON, predicted in constant pressure reactors at 60 bar and 800 K, correlates with the delay of the auto-ignition in crank angle degree that was found in the engine simulations.

The auto-ignitions are evaluated for all surrogates and for each cycle using the detonation diagram (Figure 6.10 (d)). The knock intensity is decreasing with increasing RON/MON. Applying F1, every cycle shows strong knock. The knock strength is shifted towards mild knock up to F12. For F14 no auto-ignition is predicted. Especially for the surrogates that lead to mild knock (F9 – F12), two different combustion regimes emerge. Whereas some of the cycle show mild knock, an increasing number of cycles operates in the no-knock and subsonic deflagration regime. The mean and the variance of these scattered auto-ignition events is shown in Figure 6.12. The mean value of ξ and ε determine the mean strength of the knock event. The smaller the mean value of ξ and the bigger the mean value of ε, the stronger the engine knock.

Table 6.1: Fuel test bench data [11].

	RON	**MON**	**Aromatic content**	**Ethanol content**	**Density**	**LHV**
	[–]	[–]	$[vol\%]$	$[vol\%]$	$[kg/m^3]$	$[MJ/kg]$
F1	87.0	77.5	24.0	0.0	744.2	43.16
F2	87.9	80.5	36.0	0.0	751.7	-
F3	90.1	80.2	26.0	0.0	753.0	43.12
F4	91.0	81.2	26.0	0.0	747.4	44.44
F5	91.0	82.0	15.0	0.0	744.2	43.49
F6	91.4	82.4	37.0	0.0	761.5	44.39
F7	93.6	82.4	12.0	23.0	744.0	39.55
F8	94.0	80.9	26.0	0.0	750.6	42.02
F9	94.5	84.1	33.0	0.0	747.5	42.94
F10	95.6	84.0	23.0	0.0	746.0	42.43
F11	Fuel 9 + 5 vol% ethanol					
F12	96.2	85.1	0.37	0.0	763.7	42.95
F13	96.7	85.8	0.28	9.5	744.0	41.51
F14	106.9	95.3	0.35	0.0	756.2	41.26

Table 6.2: Composition in mass percent and physical properties of the surrogates corresponding to the fuel test bench data in Table 6.1.

	RON	**MON**	***iso*-Octane**	***n*-Heptane**	**Ethanol**	**Toluene**	**Density**	**LHV**
	[–]	[–]	$[mass\%]$	$[mass\%]$	$[mass\%]$	$[mass\%]$	$[kg/m^3]$	$[MJ/kg]$
F1	87.0	82.4	53.1	18.4	0.0	28.4	731.5	43.30
F2	87.9	81.2	38.5	19.7	0.0	41.8	752.8	42.79
F3	90.1	85.0	53.2	15.9	0.0	31.0	735.9	43.19
F4	91.0	85.9	54.2	15.0	0.0	30.9	735.8	43.20
F5	91.0	88.0	69.3	12.7	0.0	18.0	716.4	43.68
F6	91.4	84.5	41.1	16.4	0.0	42.5	754.4	42.76
F7	93.6	83.5	45.7	16.2	25.0	13.1	746.0	39.50
F8	94.0	88.8	57.3	12.0	0.0	30.6	753.8	43.20
F9	94.5	88.2	49.5	12.7	0.0	37.8	747.3	42.93
F10	95.6	91.0	63.1	9.9	0.0	27.1	730.6	43.30
F11	96.0	89.1	46.0	12.2	5.4	36.4	747.7	42.75
F12	96.2	88.1	45.9	11.7	0.0	42.4	754.9	41.37
F13	96.7	98.7	46.0	11.9	10.1	32.0	752.0	42.80
F14	106.9	82.4	57.5	2.0	0.0	40.5	753.3	43.30

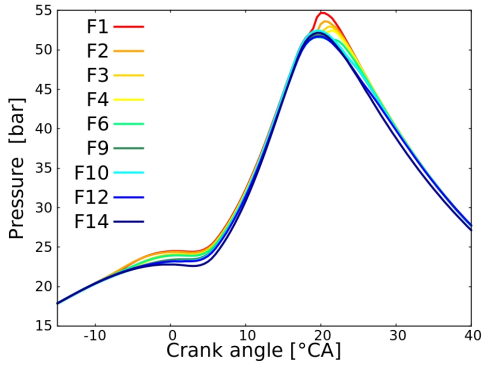

(a) Pressure.

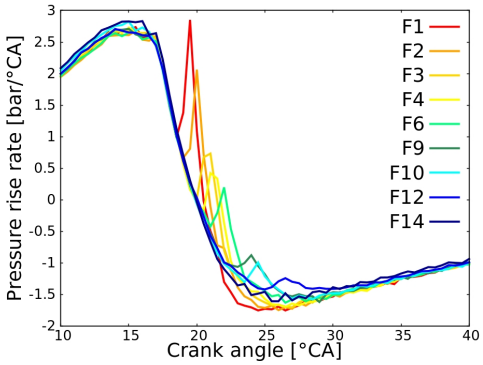

(b) Pressure rise rate.

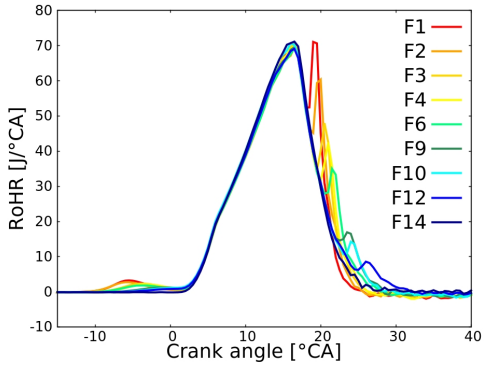

(c) Rate of heat release total domain.

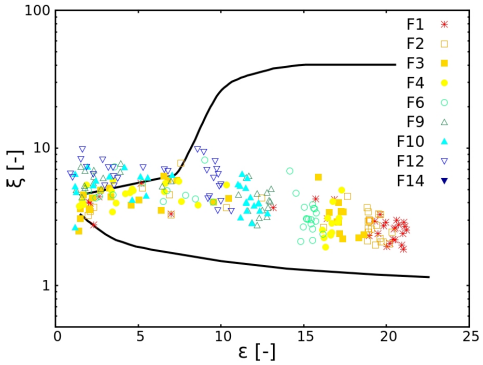

(d) Detonation diagram.

Figure 6.10: Result using TRF surrogates with different octane rating.

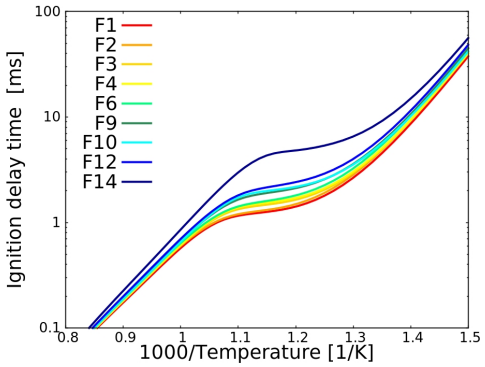

Figure 6.11: Ignition delay times τ of the TRF surrogates for stoichiometric fuel/air mixtures at 60 bar.

By applying ETRF surrogates, the effect of ethanol on the knock severity can be analysed. For this study TRF and ETRF surrogates with close RON/MON are compared (F7: 93.6/83.5 vs F8: 94.0/80.9 and F12: 96.2/88.1 vs F13: 96.7/98.7). Cooling effects due to evaporation

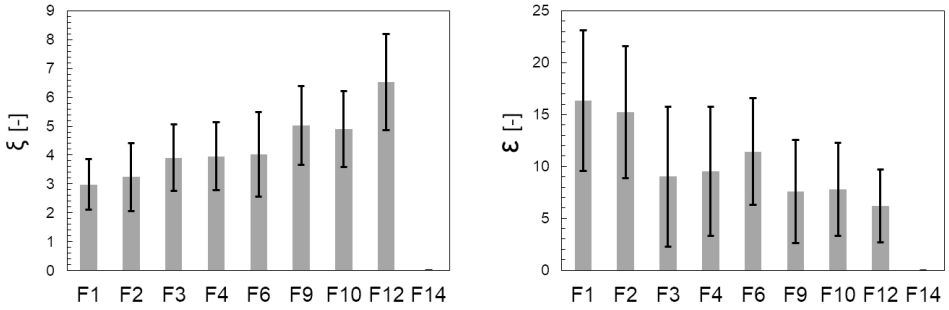

Figure 6.12: Mean value (gray bars) and variance (black error bars) for ξ and ε corresponding to Figure 6.10.

are not included in this analysis. The surrogates F7 and F8 operate in the regime of strong knock. For the ETRF mixture (F8) milder knock than for the TRF mixture (F7) is predicted. The reduction in knock severity can have two reasons: the increase in RON (Δ0.4) and the presence of ethanol. Compared to F1 and F2 (Figure 6.10 (d)) with a difference in RON of Δ0.9, the decrease in knock intensity is bigger even though the difference in RON is smaller. Following, the additional reduction can be accounted to the presence of ethanol. The comparison of F12 and F13 does not show this clear reduction of knock intensity. Whereas the mean value for ξ remains unchanged, the mean for ε is increased (Figure 6.13). The reaction velocity is about the same, but the ignition kernel size is reduced by the presents of ethanol. For the ETRF mixtures two clusters emerge: one in the sub-sonic and one in the mild knock area. To investigate this trend further some more consecutive cycles may be needed.

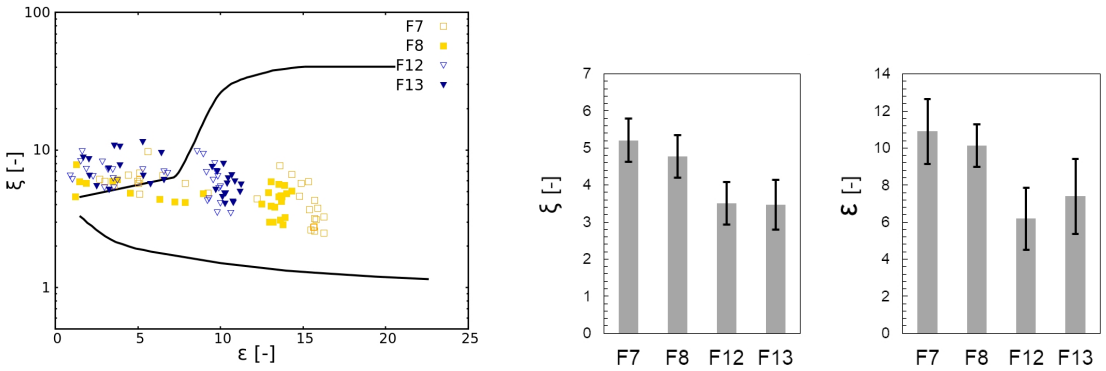

Figure 6.13: Evaluation of predicted auto-ignitions for surrogates with and without ethanol content and their mean value (gray bars) and variance (black error bars) for ξ and ε.

In Figure 6.14 surrogates with same RON, but different MON are shown (F4: 91.0/85.9 vs F5: 91.0/88.0). F5 shows according to the higher MON milder knock. Whereas the reactivity

parameter ε is not affected, ξ is increased (Figure 6.14. F8 and F9 differ slightly in RON (Δ0.5) and MON (Δ0.6). F9 with a higher RON and MON shows milder knock (F8: 94.0/88.8 vs F9: 94.5/88.2).

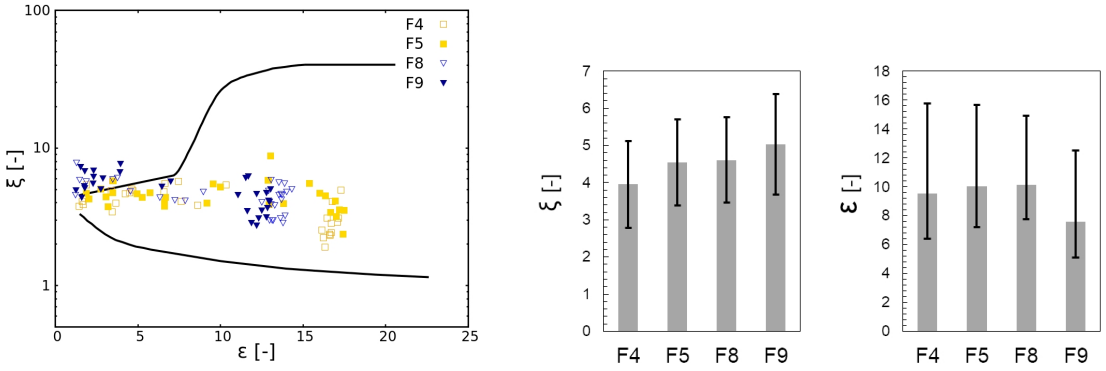

Figure 6.14: Evaluation of predicted auto-ignitions for surrogates with same RON, but different MON and their mean value (gray bars) and variance (black error bars) for ξ and ε.

Summarizing this study, for surrogates with increasing RON and MON, milder auto-ignition is predicted. The apparent reaction velocity increases, whereas the ignition kernel size decreases. The presence of ethanol or increasing MON seems to slow down the apparent reaction velocity. Further analysis including more surrogates and more consecutive engine cycles are needed to understand the impact of small variations in octane rating of ETRF surrogates on engine knock.

6.4 Analysis of Cycle-to-Cycle Variations

In internal combustion engines, cycle-to-cycle variations (CCV) are referred to as the lack of the repeatability of engine performance parameters between different working cycles [31]. CCV are associated with various combustion concepts in internal combustion engines [141], but they are a dominating phenomenon in spark ignition (SI) engines. CCV are an undesired phenomenon that increase fuel consumption and exhaust out emission [142, 143]. In extreme situations, they might negatively influence the stability of engine operation [142] and may cause knocking [143]. Hence, the occurrence of CCV is considered as one of the main obstacles to further efficiency improvement of SI engines. To characterize CCV pressure related parameters, such as the indicated mean effective pressure (IMEP), the maximum cylinder pressure and its location or combustion related parameters such as the start of combustion and burn duration, are typically used [144, 145, 146]. The major causes for CCV are attributed to mixture formation, charge ignition and flow field and are usually broken down into following phenomena [31, 141, 142,

144, 145, 146, 147, 148, 149, 150, 151, 152, 153]:

- Mixing homogeneity: particularly crucial in GDI
- Spark plug flow: rising of the early flame kernel and turn into turbulent flame front
- Long combustion: low flame front propagation velocity due to high turbulence or fuel characteristics (low laminar flame speed)
- High Karlovitz combustion: local increasing of the flame thickness

The biggest impact has the different charge motion, particularly at the spark plug [31]. The flow field can promote, retard or even extinct the spark ignition and early development of the flame kernel. This variation in the ignition process and early combustion phase is significant and has a bigger impact on CCV than other factors later in the cycle [141, 142], e.g. such as the burn duration [154]. As indicated by CFD simulations, which provide detailed information about the flow characteristic, the CCV is mainly governed by the structure of the turbulence field at the spark. In [155], LES were performed for operating points with low and high cyclic variability. In agreement with previous findings in literature [147], they found that the initial growth of the flame kernel (until 2 % of the mass is burned, CA_2) dominates the overall combustion phasing of the cycle and the location of the tumble residual motion at spark timing to be of special importance. The reason for a slow burning cycle is, according to their findings, a non-centered tumble that drives the flame into the spark plug cavity. This leads to higher heat losses and less exposure to turbulence. Further, the flow motion can drive the kernel to cylinder walls where it undergoes partial quenching. In the work reported in [152], 2D DNS were applied to investigate the influencing factors on the early flame propagation. They ranked the impact in descending order to be the initial kernel size, the turbulence structure, turbulence intensity and integral length scale. The reduction of cyclic variability with increasing initial kernel size was also reported in [149].

In SI engines, the spark timing is optimized to obtain the maximum torque for certain operating conditions. Both, fast and slow burning cycles cause deviations from the optimum and lead therefore to losses in power and efficiency. Knocking cycles limit the KLSA and the compression ratio. Slow burning cycles determine the lean limit and the amount of EGR [31, 156].

For CFD simulations employing detailed chemistry, RANS based turbulence modeling is usually first choice since it ensures shorter computational time compared to LES and DNS. However, RANS simulations cannot capture the stochastic of the flow leading to CCV due to the time averaging and its formulation at integral length scale [23]. Therefore, RANS always

predicts an average cycle. To overcome this drawback, in the presented approach, RANS is combined with the 0D Spark Ignition Stochastic Reactor Model (SI-SRM) to predict the full range of CVV. Thanks to the 0D formulation, the SI-SRM shortens the simulation time to a fraction of time needed for CFD simulations even if detailed reaction mechanisms are employed for the modeling of combustion and pollutants formation. This allows calculating several consecutive cycles. The SI-SRM can support the details known from CFD, such as size, shape and number of ignition kernels, post-processed using the same methodology, with the knocking tendency of the whole pressure range of an operating point. The stochastics of the flow is a 3D phenomenon that, in contrary to LES or DNS, cannot be resolved in the 0D SI-SRM and must be modeled. The stochastic mixing of the particles and stochastic heat transfer to the walls mimic the stochastics of the flow [90]. EGR compositions based on the previous cycle lead to variations of the composition of each cycle. In this chapter, additionally two imposed PDFs for the inflammation time and the mixing time constant C_φ are introduced.

As discussed above, the cyclic variation of the charge motion is an important impact factor for CCV. To predict varying turbulence levels, the mixing time obtained from a single RANS calculation is combined with an imposed PDF for the mixing time constant C_φ In this way, cycles with faster and slower mixing can be reproduced. This PDF enters the mixing process of the particles directly, the smaller the provided value, the shorter is the scalar mixing time, the more frequent are particles mixed within a time step. Experimental data indicate that the combustion progress of operating points with CCV are until CA_{50} normally distributed [157]. The analysis of the CA_{50} distribution in the experiment of the analyzed engine gives a normal distribution with a standard deviation of $\sigma = 2.0$ (Figure 6.15). This distribution is adopted to the C_φ-PDF since it represents the global mixing. That results in a variation of the scalar mixing time (Figure 6.16) and the cycles will burn faster or slower accordingly.
However, the early flame development is affected by the local flow field of the spark plug and the vicinity of the cylinder head walls. The turbulence around the spark plug can lead to an over-advanced start of combustion of fast burning cycles and retarded start of combustion for slow cycles [31]. To account for this phenomenon an additional PDF is introduced for the delay between Spark Timing (ST) and the inflammation time. The inflammation time is defined as the crank angle degree (°CA) between ST and the 5% burn point (CA_5) [156]. By introducing a PDF for the inflammation time, a variation in CA_5 is achieved that replicates the promoted or retard flame kernel development. The PDF for the inflammation time gives directly the starting crank angle of the turbulent flame initiation since no spark model is applied. For the inflammation time PDF, the CA_5 distribution is analyzed (Figure 6.15). It can be represented using a normally distributed PDF with a standard deviation of $\sigma = 0.8$.

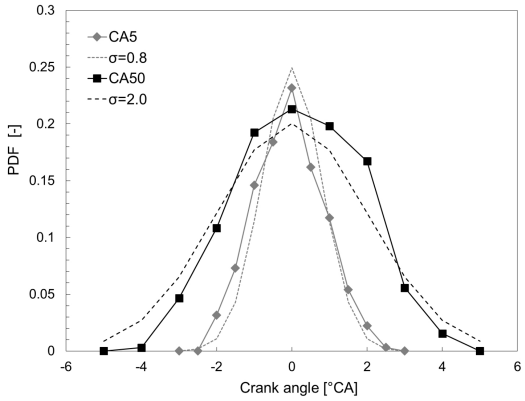

Figure 6.15: Analysis of the distribution of CA_5 and CA_{50} in the analyzed experiments using normal distributions. Locations are normalized to top dead center for plotting.

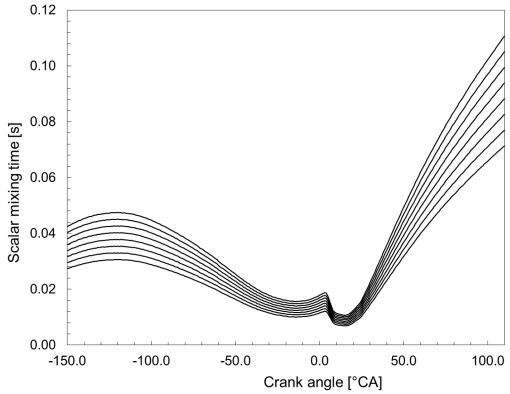

Figure 6.16: Example of the imposed mixing times following the found normal distribution and predicted mixing time from CFD.

In this section, the auto-ignition tendency of a four cylinder passenger car engine is analyzed. For this purpose, first RANS simulations have been performed to analyze the auto-ignition of the mean cycles. Second, the mixing time of the CFD simulation is transfered to the SI-SRM to study cycle-to-cycle variations.

In the experiments, provided by Renault [11], 500 consecutive cycles have been recorded for each cylinder. It is found, that under the listed operating conditions in Table 6.3, the engine operates at the KLSA. The engine has a port injection system and is operated stoichiometric using the commercial gasoline F9 from Table 6.1.

Figure 6.17 shows the mean pressure and the Matekunas diagram [144] for the 4 cylinders. Cylinder 2 has the earliest combustion phasing and highest pressures, cylinder 4 the latest phas-

Table 6.3: Engine geometry and operating conditions.

Bore	72.2 mm
Stroke	73.2 mm
Connecting rod length	132.5 mm
Displacement per cylinder	300 cm^3
Compression ratio	9.8
IMEP	23.4 bar
Speed	2500 rpm
Spark timing	-5.3 aTDC

ing. Hence, those two cylinders have been chosen for the investigations.

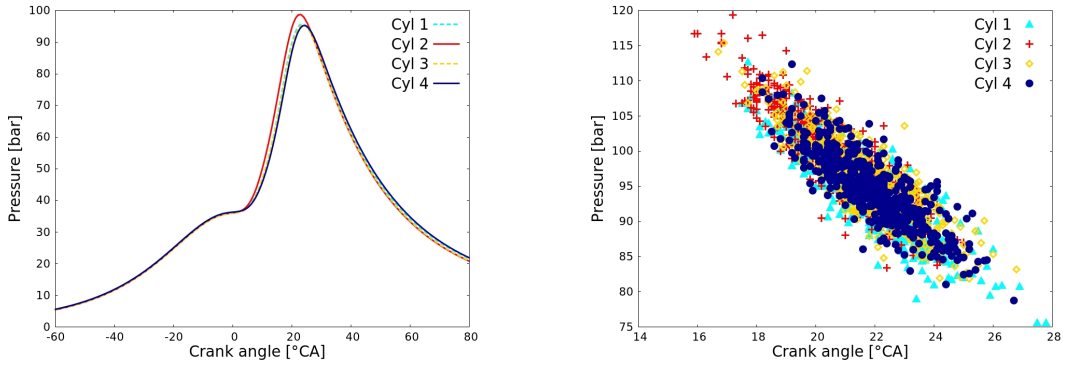

(a) Mean pressure.

(b) Matekunas diagram.

Figure 6.17: Experimental results over 500 consecutive cycles.

In a first step, the conditions at IVC are analyzed using an optimizer built in LOGEengine [10]. For cylinder 1, 3 and 4 uniform conditions have been found (Table 6.4). However, cylinder 2 has less estimated internal EGR and trapped mass compared to the remaining cylinders. Its mean temperature is 15 K higher at IVC. Using the combustion model approach and discretization discussed in section 5, those different conditions are reproduced for cylinder 2 and 4 in CFD. The dilution factor for the laminar flame speed retrieval is set to the according EGR amounts. To govern results in the whole range of measured pressures, the spark timing is varied in the range [-3.0 to -1.0°CA aTDC] in 0.5°CA steps. Figure 6.18 shows the pressure prediction for cylinder 2. In Figure 6.19, the corresponding predicted pressure rise rates and the evaluation of the auto-ignitions in the unburnt zone for this reference spark timing, and for advanced spark timings (-3.5 and -4.0°CA) are shown. The auto-ignitions using the reference spark timing range lead to comparable small peaks in the pressure and are found in the deflagration regime. Different

ignition kernel sizes between 2.5 and 6.0 mm are predicted. Advancing the spark timing, leads to the prediction of ignition kernels in the mild knock area. The prediction agrees well with the experiment that found the operating point to be at the KLSA.

Table 6.4: Estimated temperature and EGR amount at IVC.

	Cylinder 1	**Cylinder 2**	**Cylinder 3**	**Cylinder 4**
Trapped mass	778.7 mg	767.5 mg	776.6 mg	774.6 mg
Temperature at IVC	333.3 K	351.8 K	336.5 K	336.3 K
Internal EGR (mass based)	3.9 %	2.5 %	3.7 %	3.4 %

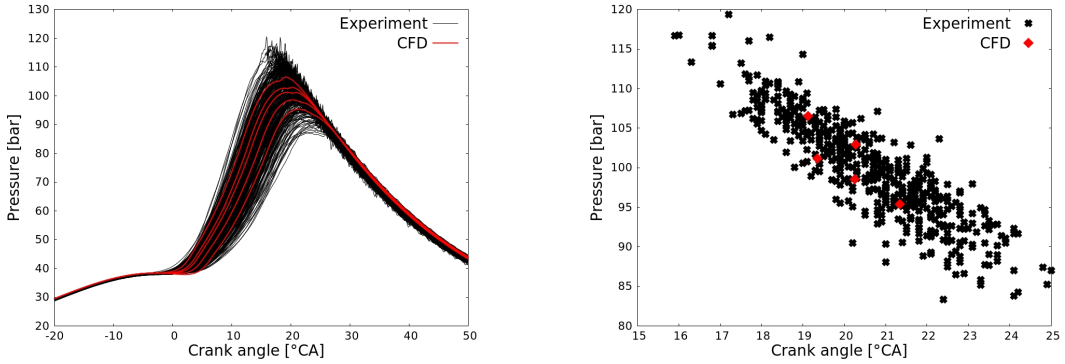

(a) In-cylinder pressures.

(b) Matekunas diagram.

Figure 6.18: Comparison of the experiment and RANS prediction of cylinder 2.

The same analysis is carried out for cylinder 4 (Figure 6.20). The combustion phasing is predicted to be slower than for cylinder 2. The evaluation in the detonation diagram estimates for one ignition kernel the possible transition to developing detonation. The predicted auto-ignition for the cases with advanced spark timing, show stronger knock than the same spark timing for cylinder 2. The knock onset for cylinder 2 is predicted at 19.0°CA, for cylinder 4 at 20.5°CA. Cylinder 2 has higher mean pressures, but also a faster flame propagation. However, in cylinder 4 the unburnt zone exists some crank angle longer due to the slower flame propagation, which leads to a longer, available time to form auto-ignitions. Further, due to the slightly higher EGR amount, more small radicals as NO that promote auto-ignitions are present [106].

The differences in auto-ignition occurrence is further illustrated in Figure 6.21. Shown are the time steps at the strongest predicted auto-ignition for the earliest spark timing within the reference range (-3.0°CA) and the latest spark timing of the advanced range (-3.5°CA). In both

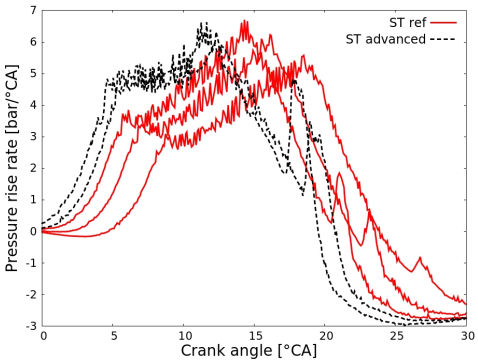

(a) Predicted pressure rise rate.

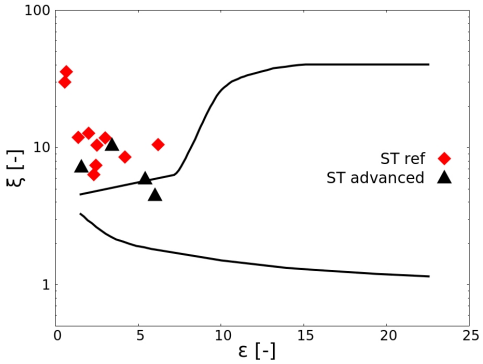

(b) Detonation diagram.

Figure 6.19: Comparison of the pressure rise rate and the auto-ignition predictions for the reference spark timing [-3.0; -2.5; -2.0; -1.5 ; -1.0°CA aTDC] and advance spark timing [-4.0 and -3.5°CA aTDC] using RANS.

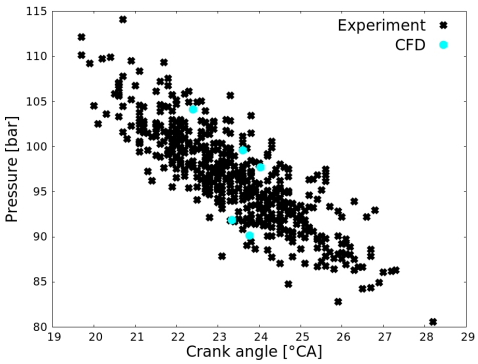

(a) Matekunas diagram.

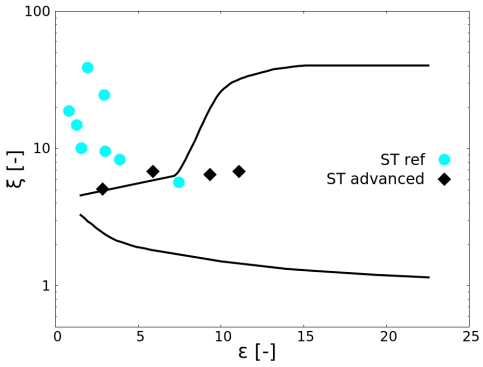

(b) Detonation diagram.

Figure 6.20: RANS prediction for cylinder 4. Spark timing as in Figure 6.19.

cylinders occur three ignition kernels. For cylinder 2 and ST -3.0°CA, equal strong ignitions at the side of the intake and exhaust valves are predicted. For the spark timing ST -3.5°CA, the ignition kernel at the intake valves (left side) turns stronger and to a possible developing detonation. In contrast, for cylinder 4 are the two main ignition kernels located close to the exhaust valves. The imposed gas velocities are higher than predicted for the same spark timing for cylinder 2. Advancing the spark about 0.5°CA, leads to the formation of a large ignition kernel, that is located in the developing detonation regime. At the intake valve side of cylinder 2, a certain volume is not consumed, an ignition kernel can form. In the same area is the unburnt zone in cylinder 4 widely consumed, only a small ignition kernel occurs. On the side of the exhaust valve, is the situation opposite. For cylinder 4 a larger volume for the formation

of an ignition kernel remains.

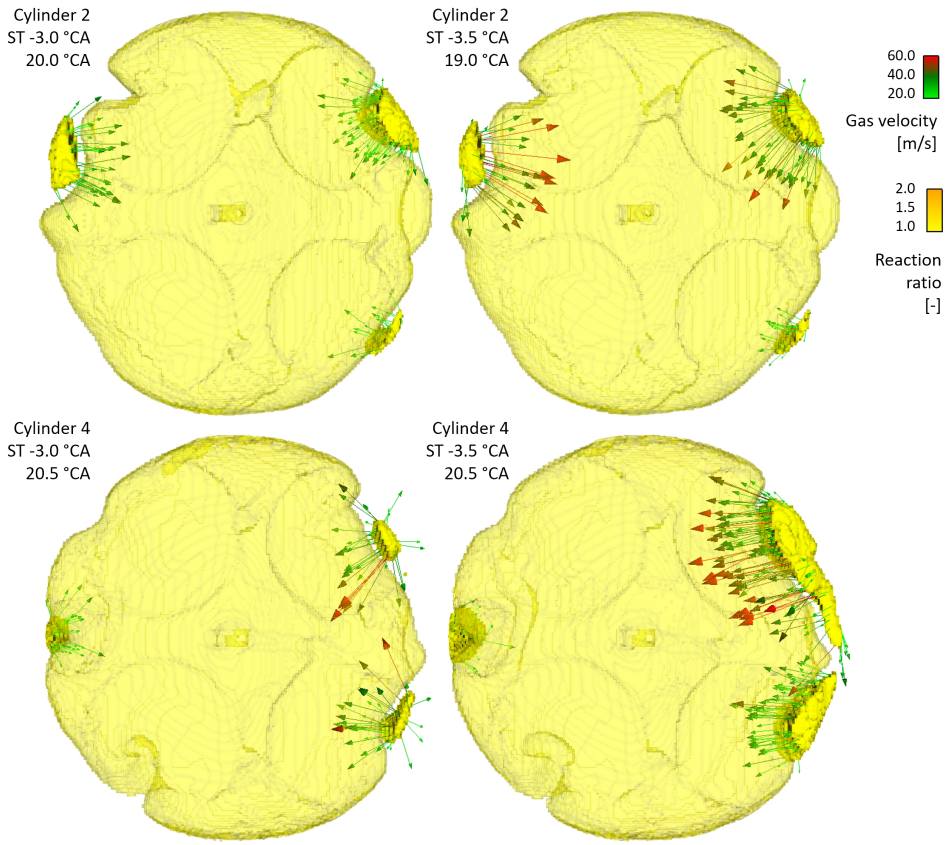

Figure 6.21: Predicted ignition kernels for cylinder 2 and 4 using CFD for the reference spark timing (-3.0 aTDC) and advance spark timing (-3.5°CA aTDC).

In the second step of the analysis, the mixing times from CFD have been extracted and provided for the SI-SRM simulations (Figure 6.22). To reproduce the cyclic variations of the turbulence, the normally distributed PDF of the mixing time constant is applied. Following the findings from Figure 6.15, for the SI-SRM a normal distribution for $C_\varphi$using $\sigma = 2.0$ is imposed. The ranges of [12.7 to 19.7] for cylinder 2 and [13.7 to 20.7] for cylinder 4 are calibrated to match the measured pressure. Further, a normal distribution of the inflammation time is imposed. For both cylinders, the inflammation time was set to be normally distributed using $\sigma = 0.8$ and a range of [-1, 1] °CA. The mean spark timing has been optimized to match the average cycle of the experiment. 130 consecutive cycles are calculated using 1000 particles and time step of 0.5°CA.

Figure 6.23 shows the predicted pressures and validation for cylinder 2. The distribution of the cycles and the location of the maximum pressures are well matched. To analyze if the

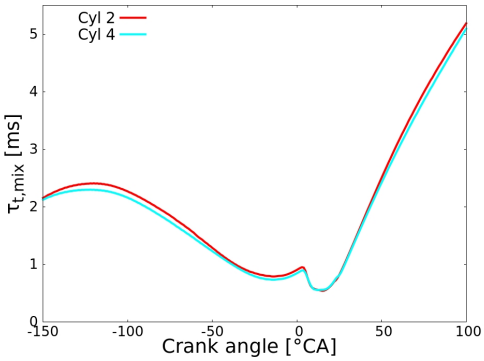

Figure 6.22: Predicted turbulent mixing time using RANS for Cylinder 2 and 4.

predicted combustion is at the KLSA as in the experiment and in the CFD simulation, a spark timing sweep [-2°CA, -1°CA, ref, +1°CA] is performed. The predicted combustion progress is shown in Figure 6.24. As expected, the combustion phasing is advanced or delayed with the spark timing. For each spark timing, the auto-ignitions are evaluated in the detonation diagram (Figure 6.25).

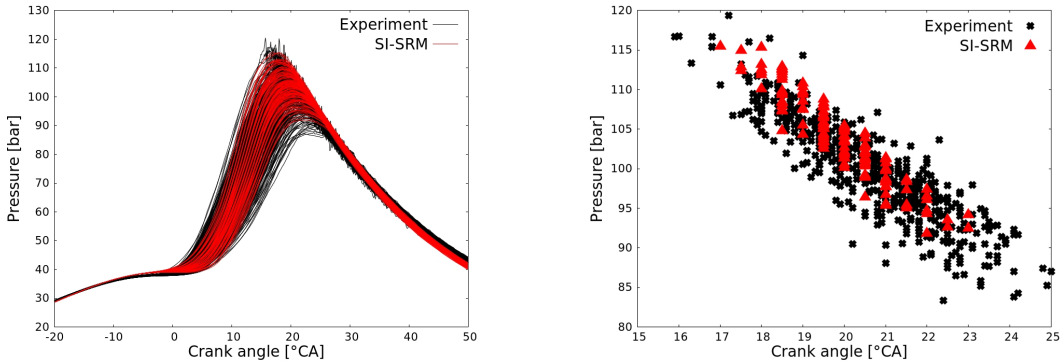

(a) Predicted pressure.

(b) Matekunas diagram.

Figure 6.23: SI-SRM pressure prediction of cylinder 2.

In the simulations using ST +1°CA and the reference spark timing, only some cycles have an auto-ignition. The number of auto-ignitions increases with advanced spark timing, so that ST -1°CA and ST -2°CA predict in every cycle an auto-ignition. The predicted auto-ignitions for ST +1°CA are all found in deflagration mode. The distribution in ε is the smallest (Figure 6.26). The case at reference spark timing, has some auto-ignitions close to the transition border and in the mild knock region. However, they are less than 10%, so that this spark timing is

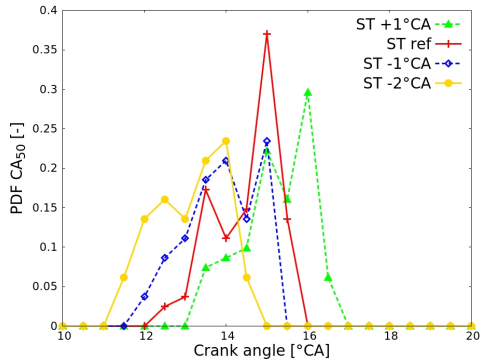

(a) 50% burn duration.

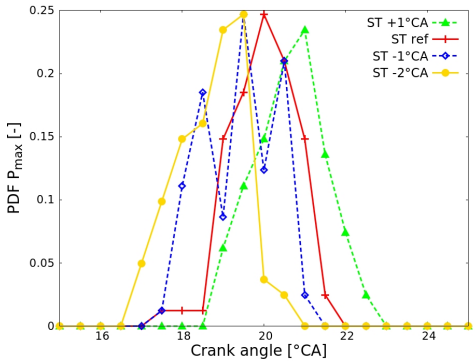

(b) Maximum pressure.

Figure 6.24: Comparison of the predicted combustion progress cylinder 2 and the spark sweep.

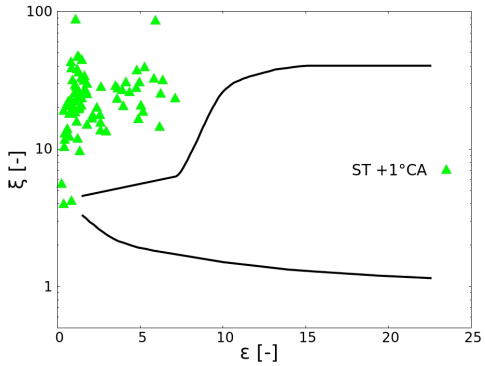

(a) ST +1°CA.

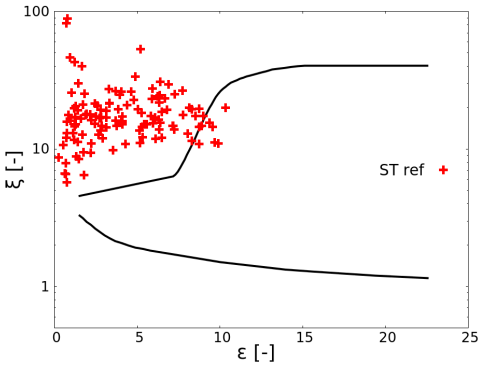

(b) Reference ST.

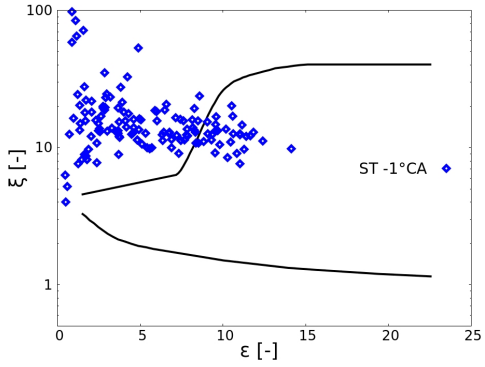

(c) ST -1°CA.

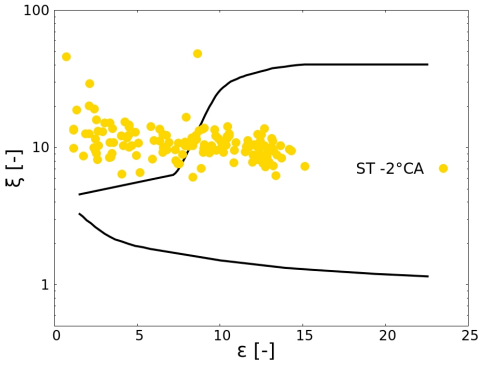

(d) ST -2°CA.

Figure 6.25: Evaluation of the predicted auto-ignitions of the spark timing sweep for cylinder 2.

considered to be acceptable and at the KLSA. With further advanced spark timing, the knock

strength and the distribution in ε increases (Figure 6.25 and 6.26). In contrast, to the findings in section 6.2, the variation in ξ is decreasing clearly with increased knock tendency. Overall, the resonance parameter ξ is wider spread as result of the varying mixing times and corresponding pressures and temperatures.

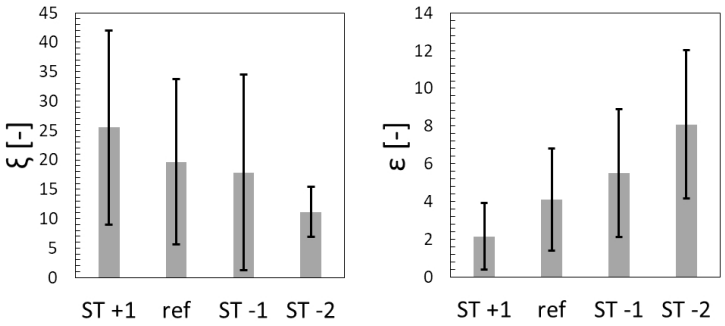

Figure 6.26: Mean value (gray bars) and variance (black error bars) for ξ and ε corresponding to Figure 6.23.

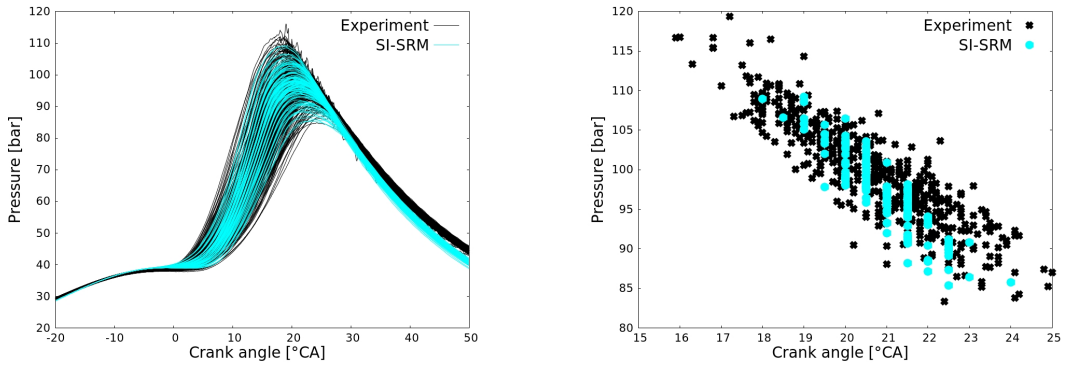

(a) Predicted pressure.

(b) Matekunas diagram.

Figure 6.27: SI-SRM pressure prediction of cylinder 4.

For the prediction of cylinder 4, the PDF of C_φ is shifted to higher constants to slow down the mixing. The pressure prediction is shown in Figure 6.27. Simulation and experiment align well. To further analyze the different behavior of the two cylinders, the prediction of cylinder 2 and 4 are compared in Figures 6.28 and 6.29. Cylinder 2 has an earlier and faster combustion phasing. The shift within the Matekunas diagram is well reproduced.

The evaluation in the detonation diagram of both cylinders and the prediction in CFD and SI-SRM align well. Cylinder 2 is less prone to knocking combustion than cylinder 4. For cylinder 4, the knock onset is later (cylinder 4: 20.5°CA in CFD and SI-SRM, cylinder 2:

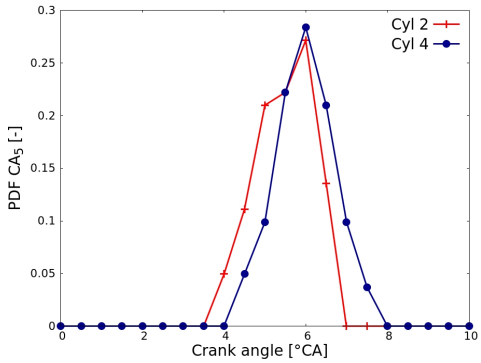

(a) 5% burn duration.

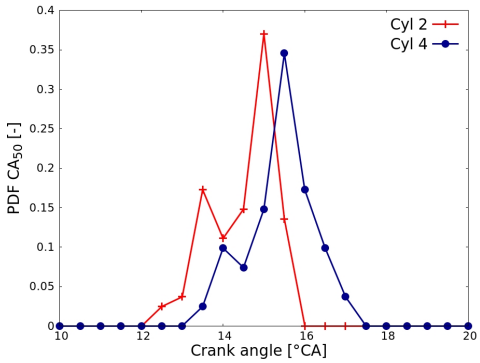

(b) 50% burn duration.

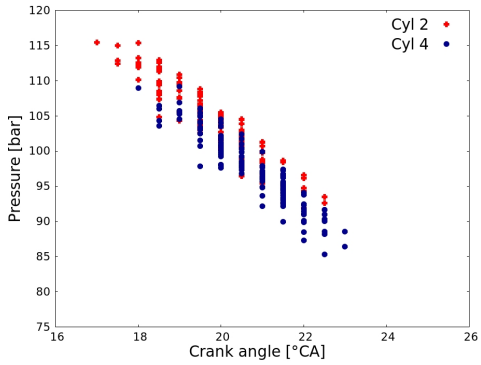

(c) Matekunas diagram SI-SRM.

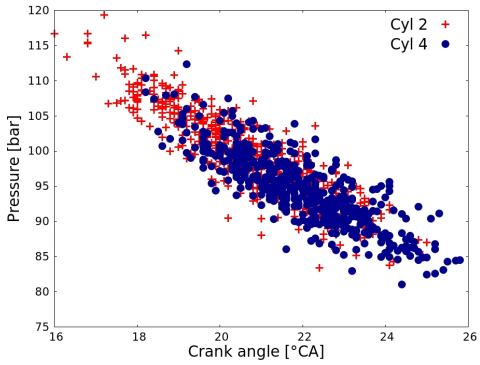

(d) Matekunas diagram experiment.

Figure 6.28: Comparison of the predicted combustion progress using the SI-SRM for cylinder 2 and 4.

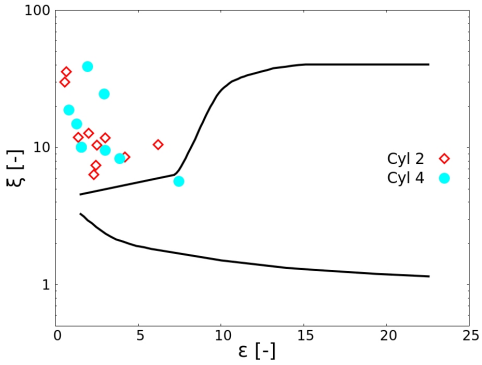

(a) CFD.

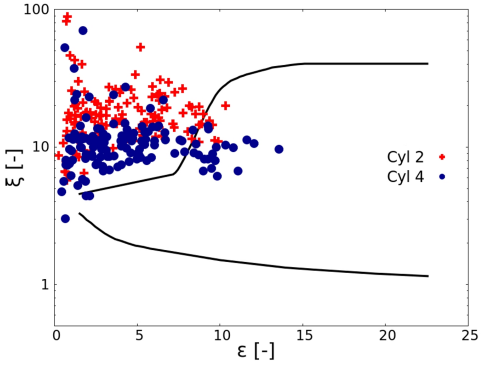

(b) SI-SRM.

Figure 6.29: Comparison of the predicted auto-ignitions for cylinder 2 and 4.

19.0°CA/19.5°CA CFD/SI-SRM), but the ignition is stronger. The absolute values of ξ and

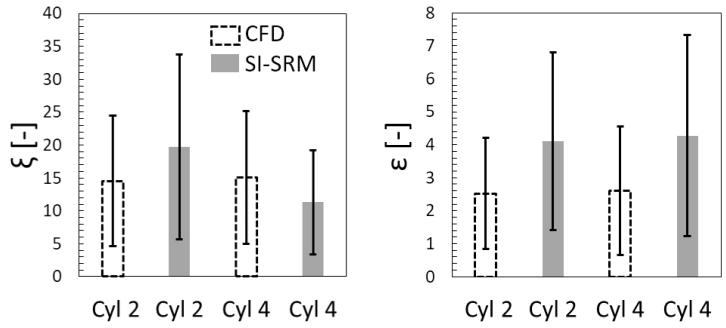

Figure 6.30: Mean value (gray bars) and variance (black error bars) for ξ and ε corresponding to Figure 6.29.

ε are in the same range, their distribution are comparable (Figure 6.30). In the SI-SRM, the ignition kernels are predicted bigger. This is due to the introduced assumptions: it is assumed that all particles, that contribute to the steepest heat release gradient, form one ignition kernel. As can be seen in the CFD simulation (Figure 6.21), it is likely that two or more ignition kernels ignite in the same time step. However, this detailed information is not available in zero-dimensions. Further, it is assumed that the kernels in the SI-SRM are spherical, which is a rough assumption considering the stretched and elliptic kernels predicted in CFD. Therefore, both assumptions lead to an over-estimation of the kernel size. Hence, in the SI-SRM, larger reactivity parameters ε are acceptable at the KLSA.

This analysis demonstrates that the combination of the detailed analysis using RANS and cycle-to-cycle phenomena in the SI-SRM act jointly. Detailed information on the impact of flow field and flame propagation on the occurrence of auto-ignition kernels and their size can be obtained from RANS. The SI-SRM accounts for cyclic variations and chemistry effects, such as varying NO and other radical contents in the residual gases. Both approaches account for octane rating (sections 5.3 and 6.2). Both tools applied together can give insides in the knocking tendency of different operating points and cylinders. RANS simulations are computational cheap compared to LES and only one CFD simulation is necessary for this analysis per cylinder, instead of at least 30 consecutive cycles for a LES study. Further, one cycle with maximum 20 minutes on a single core using the 188 species mechanism applied in the SI-SRM allows to simulate all performed 130 cycles with less computational cost than a single CFD RANS simulation. This low CPU cost, make this approach applicable within optimization tools.

Summarizing this study: The RANS results deliver detailed information on the average cycle. The impact of differences in internal EGR amount and cylinder mass have been analyzed. Using detailed chemistry, the interaction of flow, flame propagation and auto-ignitions are

investigated. The mean mixing time is transferred to the SI-SRM where the full CCV range is investigated. The auto-ignition tendency of the different cylinders agree between RANS and SI-SRM. Delaying the spark timing in the SI-SRM leads to stronger auto-ignitions the distribution in ε increases, in ξ decreases. Ignition kernels are compared to RANS and over-estimated due to the introduced assumptions.

The combination of RANS and SI-SRM gives a detailed insight into the possible locations and kernel sizes and a picture of the full operating point. With RANS being the fastest CFD approach and the 0D framework of the SI-SRM the computational times allow to study several consecutive cycles computationally efficient. The on the fly solved chemistry can be replaced by a tabulated approach [92], which will reduce the costs of a predicted cycle in the SI-SRM down to seconds and significantly for RANS.

7 Summary and Outlook

This work presented a methodology to predict and classify auto-ignition in the unburnt gases of SI engines. The methodology is based on the application and interaction between detailed chemistry in three-dimensional CFD and zero-dimensional SI-SRM simulations. The ETRF scheme from Seidel [29] is used to compile flame speed look-up tables for the flame propagation prediction and the prediction of auto-ignitions in the unburnt gases. For both models, the classification of the predicted auto-ignitions using the detonation diagram by Bradley and colleagues [2, 3, 4, 5, 6, 7] has been introduced.

The three-dimensional RANS simulations are used to predict and investigate the impact of the local thermodynamic conditions and local species concentrations on the auto-ignition kernel formation. The kernel location and dimensions are affected by the propagation of the main flame and the local chemistry. The appearance of an auto-ignition can promote the formation of a second stronger auto-ignition. It has been demonstrated, that the KLSA can be determined as function of octane rating. Further, it has been shown that the formulation of the surrogate is an important model parameter that leads to a difference of the predicted KLSA of 2°CA and more. Based on varying initial conditions and EGR, the different behavior of cylinders in an engine can be reproduced and investigated. Further, it has been shown that the resonance theory, originally developed using DNS, can be applied to interpret results within the RANS framework by comparing to LES.
In Netzer et al. [158], the methodology has been applied to investigate the impact of water injection on combustion and thermodynamics with special emphasis on the auto-ignition strength and KLSA. The impact of the water vapor on the combustion chemistry and its cooling effect in a port and direct injection strategy have been analyzed.

The zero-dimensional SI-SRM is used to study cycle-to-cycle variations and to perform parameter studies. The knock prediction has been shown to be sensitive for spark timing, octane rating and EGR amount. The cycle-to-cycle prediction agrees well with measurements if a PDF for the mixing model time constant and inflammation time is imposed. If strong knock is forced by advancing the spark timing, two groups of ignition kernels are found. A part of

the cycles is evaluated to have strong knock events, the other groups has smaller reactivity parameters ε and is therefore found in non- or mild knocking regime. The distribution of the resonance and reactivity parameter has been introduce to characterize the stability of an operating point.
In Pasternak et al. [159], the methodology to evaluate the knock limit in the SI-SRM has been applied to investigate the effects of spark timing and the external EGR composition under knock-limited operation at high speed and load. Further, the impact of the EGR composition on the KLSA was investigated.

The surrogates and therefore the octane rating is interchangeable. The flame speed look-up tables are applicable to both models. Applying RANS and SI-SRM to study the same engine, gives information and understanding of the details of the ignition kernel formation and cycle-to-cycle variations with low computational costs. The resonance theory has been shown to provide a reasonable assessment of the classification of the auto-ignition events compared to experiments.

The knocking tendency in the SI-SRM is, compared to the CFD results, over-predicted as result of the introduced assumptions: (1) All particles that ignite in one time step are collected to from one ignition kernel. (2) The ignition kernel is spherical. There is no spatial information, different kernels cannot be distinguished as in CFD. However, the kernels could be assumed to be elliptic, which would agree better with the findings in CFD. Further, the evaluation in this work is limited to the time-step exhibiting the strongest ignition event in the cycle. The method can be extended to analyze all time steps.

In the CFD simulations using the G-equation model, a global dilution (EGR) mass fraction is used due to limitations in the implementations of the G-equation model. This could be replaced by a cell local look-up based on the actual dilution in the cell. For concepts, such as water injection, it is of interest to predict the impact of a certain species, for this example H_2O, on the flame speed. For such a specific look-up, tracer species that allow to restore the unburnt conditions, as for example in the ECFM model, would need to be introduced. In the flame speed table generation those species would also need to be accounted for.

To improve the early flame propagation prediction within CFD and SI-SRM, a spark ignition model should be applied, e.g. as suggested in [81].

For both CFD and SI-SRM the chemistry is solved in the unburnt and burnt zone on the fly for clustered cells or each particle. This could be changed by the use of tabulated chemistry

as suggested for the combustion progress variable (CPV) model [92, 160]. The idea of the CPV approach is to use the chemical enthalpy h_{298} as progress variable. Chemistry is solved for homogeneous zero-dimensional reactors and stored in look-up tables. For the Well-Stirred Reactor (WSR) combustion model for each cell or in the SI-SRM for the particles source terms according to the combustion progress are retrieved. This concept is adopted from transient flamelet models and cell local Conditional Moment Closure [161] approaches. In this approach, not only the combustion solver is replaced and outsourced prior to the simulation, but also the number of scalars to transport are reduced and are the same, regardless of the chemical mechanism size. By tabulating the state just after the flame front, emissions prediction could be included.

Nomenclature

Symbol	Description	Unit
A	area	m^2
A_r	pre-exponential factor	$1/s$
a	speed of sound	m/s
a_4	model constant turbulent flame speed	-
α	thermal diffusivity	m^2/s
α_p	pressure coefficient laminar flame speed	-
α_T	temperature coefficient laminar flame speed	-
α_x	coefficient mixing rules by Morgan	-
b_1	model constant turbulent flame speed	-
b_3	model constant turbulent flame speed	-
β	RNG model constant	-
C	model constant turbulent flame speed	-
C_p	isobaric heat capacity	$J/(K)$
c_p	specific isobaric heat capacity	$J/(kgK)$
c_v	specific isochoric heat capacity	$J/(kgK)$
$C_{\epsilon,1}/C_{\epsilon,2}$	turbulent dissipation constants	-
C_μ	turbulent viscosity coefficient	-
C_φ	mixing time constant	-
$C_{s,dyn}$	model constant dynamic Smagorinsky model	-
D	diffusion coefficient	m^2/s
Da	Damköhler number	-
d	model constant flame propagation model SI-SRM	-
Δ	LES filter size	m
δ	laminar flame thickness	m
δ_{ij}	Kronecker delta	-
E	energy	J
E_a	activation energy	J/mol

$\sum$	flame surface density	$1/m$
e	specific energy	J/kg
ϵ	dissipation of turbulent kinetic energy	m^2/s^3
ε	reactivity parameter detonation theory	-
F_φ	MDF of φ	-
$f_{k,i}$	external forces on species k	$kg/(m^2 s)$
H	enthalpy	J
h	specific enthalpy	J/kg
h_g	heat transfer coefficient Woschni model	-
h_s	sensible enthalpy	J/kg
j_q	heat flux vector	W/m^2
j_k	vector of diffusive flux of species k	m^2/s
$k_{f,r}/k_{b,r}$	forward / backward reaction rate	$mol/(m^3 s)$;
K_{eq}	chemical equilibrium constant	-
Ka	Karlovitz number	-
k	turbulent kinetic energy	m^2/s^2
$k_{w,c}$	critical / filter wave number	$1/m$
k_w	wave number	$1/m$
κ	curvature	$1/m$
$L_{i,j}$	Leondard stress tensor	$kg/(ms^2)$
Le	Lewis number	-
l	integral length scale	m
l_{eddy}	eddy size	m
l_t	turbulent length scale	m
$\mathscr{L}$	Markstein length	m
λ	thermal conductivity	$W/(mK)$
M_k	molar mass of species k	kg/mol
m	mass	kg
μ	dynamic viscosity	$kg/(ms)$
μ_t	turbulent viscosity	$kg/(ms)$
n_i	normal vector	-
n_r	number of reactions	-
n_k	number of species	-
η_0	RNG model constant	-
η_K	Kolmogorov scale	m
OI	octane index	-
p	pressure	Pa

$p_{c,x}$	pressure correction of x	-
ϕ	fuel/air equivalence ratio	-
Re	Reynolds number	-
$\dot{Q}$	external energy source	J
r_0	ignition kernel radius	m
ρ	density	kg/m^3
$\rho_{k,s}$	mass source term of species k	kg/m^3
S	fuel octane sensitivity	-
S	strain rate	-
S_{ij}	stress tensor	$kg/(ms^2)$
s_l	laminar flame speed	m/s
s_d	displacement speed	m/s
s_t	turbulent flame speed	m/s
$\dot{s}_{u,i}$	momentum source term	$kg/(ms)$
Sc	Schmidt number	-
σ	Prandtl number	-
$\sigma_{i,j}$	stress tensor	$kg/(ms^2)$
T	temperature	K
T_i	ignition temperature	K
T_f	adiabatic flame temperature	K
T_{wall}	wall temperature	K
T_{ij}	test filter range	m
t	time	s
t_c	chemical time scale	s
t_t	turbulent time scale	s
τ	ignition delay time	s
τ_e	excitation time	s
τ_{ij}	viscous stress tensor	$kg/(ms^2)$
$\tau_{t,mix}$	turbulent mixing time	s
τ_{mix}	scalar mixing time	s
U	inner energy	J
u	specific inner energy	J/kg
u_a	imposed burning velocity	m/s
u_i	velocity vector	m/s
V	volume	m^3
V_c	control volume	m^3
$V_{k,i}$	diffusion velocity vector of species k	m/s

$\nu'_{k,r}/\nu''_{k,r}$	stoichiometric coefficient product / reactant of reaction r	-
$\dot{\omega}_k$	chemical source term of species k	$mol/(m^3 s)$
$\dot{\omega}_T$	heat release due to combustion	$J/(m^3 s)$
Y_k	mass fraction of species k	-
X_k	mole fraction of species k	-
x_i	spatial vector (three-dimensional)	m
ξ	resonance parameter detonation theory	-
ξ_l	lower limit of the resonance parameter	-
ξ_u	upper limit of resonance parameter	-

Bibliography

[1] European Automobile Manufacturers Association. The Automobile Industry Pocket Guide 2018/2019, 2018.

[2] D. Bradley, C. Morley, X. J. Gu, and D. R. Emerson. Amplified Pressure Waves During Autoignition: Relevance to CAI Engines. *SAE Technical Paper 2002-01-2868*, 2002.

[3] Modes of reaction front propagation from hot spots. *Combust Flame*, 133(1):63 – 74, 2003.

[4] D. Bradley and G.T. Kalghatgi. Influence of autoignition delay time characteristics of different fuels on pressure waves and knock in reciprocating engines. *Combust Flame*, 156(12):2307 – 2318, 2009.

[5] G.T. Kalghatgi and D. Bradley. Pre-ignition and 'super-knock' in turbo-charged spark-ignition engines. *Int J of Engine Res*, 13(4):399–414, 2012.

[6] N. Peters, B. Kerschgens, and G. Paczko. Super-Knock Prediction Using a Refined Theory of Turbulence. *SAE Int J Engines*, 6:953–967, 2013.

[7] N. Peters. Mega-knock in super-charged gasoline engines interpreted as a localized developing detonation. *In: 4th conference knocking in gasoline engines, Berlin, 9–10 October 2013*, page 23–40, IAV Automotive Engineering GmbH, 2013.

[8] K.J. Richards, P.K. Senecal, and E. Pomraning. *CONVERGE v2.4 Manual*. Convergent Science, Inc., 2017.

[9] LOGEsoft v1.10, LOGE AB http://www.logesoft.com, 2018.

[10] LOGEengine v3.0. LOGE AB, http://www.logesoft.com, 2018.

[11] F. Ravet. Renault S.A.S, Lardy, France.

[12] C. Netzer, L. Seidel, M. Pasternak, H. Lehtiniemi, C. Perlman, F. Ravet, and F. Mauss. Three-dimensional computational fluid dynamics engine knock prediction and evaluation based on detailed chemistry and detonation theory. *Int J Engine Res*, 19(1):33–44, 2018.

[13] C. Netzer, L.Seidel, F. Ravet, and F. Mauss. Assessment of the validity of rans knock prediction using the resonance theory. *Int J Engine Res*, 2019 - in Press, doi 10.1177/1468087419846032.

[14] C. Netzer, L. Seidel, F. Ravet, and F. Mauß. Impact of the surrogate formulation on 3d cfd engine knock prediction using detailed chemistry. *Fuel*, 254:115678, 2019.

[15] C. Netzer, L. Seidel, M. Pasternak, C. Klauer, C. Perlman, F. Ravet, and F. Mauss. Engine Knock Prediction and Evaluation Based on Detonation Theory Using a Quasi-Dimensional Stochastic Reactor Model. *SAE Technical Paper 2017-01-0538*, 2017.

[16] C. Netzer, M. Pasternak, L.Seidel, F. Ravet, and F. Mauss. Computationally efficient prediction of cycle-to-cycle variations in spark-ignition engines. *Int J Engine Res*, 2019 - in Press, doi 10.1177/1468087419856493.

[17] N. Peters. *Turbulent Combustion*. Cambridge University Press, 2000.

[18] D. Bradley, M. Lawes, and M.S. Mansour. Measurement of turbulent burning velocities in implosions at high pressures. *P Combust Inst*, 33(1):1269 – 1275, 2011.

[19] M. Huth and A. Heilos. 14 - Fuel flexibility in gas turbine systems: impact on burner design and performance. In P. Jansohn, editor, *Modern Gas Turbine Systems*, Woodhead Publishing Series in Energy, pages 635 – 684. Woodhead Publishing, 2013.

[20] M. Tsunekane, T. Inohara, K. Kanehara, and T. Taira. *Micro-solid-state laser for ignition of automobile engines*. Advances in Solid-State Lasers: Development and Applications, M. Grishin, editor, 195–212, 2010.

[21] I. Glassmann. *Combustion*. Academic Press, Inc., 3 edition, 1996.

[22] E. Mallard and H.L. Le Chatelier. Thermal Model for Flame Propagation. *Ann Mines*, 4:397, 1883.

[23] T. Poinsot and D. Veynante. *Theoretical and Numerical Combustion*. R.T Edwards, Inc., 2 edition, 2005.

[24] The Asymptotic Structure of Stoichiometric Methane-Air Flames. *Combust Flame*, 68(2):185 – 207, 1987.

[25] Analytic approximations of burning velocities and flame thicknesses of lean hydrogen, methane, ethylene, ethane, acetylene, and propane flames. *P Combust Inst*, 24(1):129 – 135, 1992.

[26] S.R. Turns. *An Introduction to Combustion: Concepts and Applications*. McGraw-Hill Education, 3 edition, 2012.

[27] L. Sileghem, V.A. Alekseev, J. Vancoillie, K.M. Van Geem, E.J.K. Nilsson, S. Verhelst, and A.A. Konnov. Laminar burning velocity of gasoline and the gasoline surrogate components iso-octane, n-heptane and toluene. *Fuel*, 112:355 – 365, 2013.

[28] S. Jerzembeck, N. Peters, P. Pepiot-Desjardins, and H. Pitsch. Laminar burning velocities at high pressure for primary reference fuels and gasoline: Experimental and numerical investigation. *Combust Flame*, 156(2):292 – 301, 2009.

[29] L. Seidel. *Development and Reduction of a Multicomponent Reference Fuel for Gasoline*. PhD thesis, Brandenburg University of Technology Cottbus-Senftenberg, 2017.

[30] R. Cracknell, B. Head, S. Remmert, Y. Wu, A. Prakash, and M. Luebbers. Laminar burning velocity as a fuel characteristic: Impact on vehicle performance. In IMechE, editor, *Internal Combustion Engines: Performance, Fuel Economy and Emissions*, pages 149 – 156. Woodhead Publishing, 2013.

[31] J.B. Heywood. *Internal Combustion Engine Fundamentals*. McGraw-Hill Education, 1988.

[32] Z. Wang, H. Liu, T. Song, Y. Qi, X. He, S. Shuai, and J. Wang. Relationship between super-knock and pre-ignition. *Int J Engine Res*, 16(2):166–180, 2015.

[33] H.R. Ricardo. *Schnellaufende Verbrennungsmaschinen*. Heidelberg: Springer-Verlag GmbH, 1926.

[34] G.P. Merker, C. Schwarz, and R. Teichmann. *Combustion Engines Development: Mixture Formation, Combustion, Emissions and Simulation*. Springer-Verlag Berlin Heidelberg, 2012.

[35] B. Durst, G. Unterweger, S. Rubbert, A. Witt, and M. Böhm. Thermodynamic effects of water injection on Otto Cycle engines with different water injection systems. *The Working Process of the Internal Combustion Engine*, Graz, September 24th/25th, 2015.

[36] F. Hoppe, M. Tewes, H. Baumgarten, and J. Dohmen. Water injection for gasoline engines: Potentials, challenges, and solutions. *Int J Engine Res*, 17(1):86–96, 2016.

[37] A. Prakash, C. Wang, A. Janssen, A. Aradi, and R. Cracknell. *SAE Int J Fuels Lubr*.

[38] F. Bozza, V. De Bellis, and L. Teodosio. Potentials of Cooled EGR and Water Injection for Knock Resistance and Fuel Consumption Improvements of Gasoline Engines. *Appl Energ*, 169:112–125, 2016.

[39] N. Morgan, A. Smallbone, A. Bhave, M. Kraft, R. Cracknell, and G.T. Kalghatgi. Mapping surrogate gasoline compositions into RON/MON space. *Combust Flame*, 157(6):1122 – 1131, 2010.

[40] A.D.B. Yates, A. Swarts, and C.L. Viljoen. Correlating Auto-Ignition Delays And Knock-Limited Spark-Advance Data For Different Types Of Fuel. *SAE Technical Paper 2005-01-2083*, 2005.

[41] W.R. Leppard. The Chemical Origin of Fuel Octane Sensitivity. *SAE Technical Paper 902137*, 1990.

[42] G.T. Kalghatgi. Fuel Anti-Knock Quality - Part I. Engine Studies. *SAE Technical Paper 2001-01-3584*, 2001.

[43] G.T. Kalghatgi.

[44] N. van Dam, Z. Yue, P. Pal, and S. Som. Simulations Enabling Co-Optimization of Engines and Fuels. *Converge User Conference North America, Dearborn, MI, 26-27 September, 2017*, 2017.

[45] K. Kohse-Höinghaus, P. Oßwald, T.A. Cool, T. Kasper, N. Hansen, F. Qi, C.K. Westbrook, and P.R. Westmoreland. Biofuel Combustion Chemistry: From Ethanol to Biodiesel. *Angew Chem Int Edit*, 49(21):3572–3597, 2010.

[46] US Departement of Energy. https://www.energy.gov/eere/bioenergy/co-optimization-fuels-engines, 2018-06-15.

[47] Z. Wang, H. Liu, and R.D. Reitz. Knocking combustion in spark-ignition engines. *Prog Energ Combust*, 61:78 – 112, 2017.

[48] X. Zhen, Y. Wang, S. Xu, Y. Zhu, C. Tao, T. Xu, and M. Song. The engine knock analysis – An overview. *Appl Energ*, 92:628 – 636, 2012.

[49] M.D. Checkel and J.D. Dale. Computerized Knock Detection from Engine Pressure Records. *SAE Technical Paper 860028*, 1986.

[50] G.T. Kalghatgi, M. Golomok, and P. Snowdon. Fuel Effects on Knock, Heat Release and "CARS" Temperatures in a Spark Ignition Engine. *Combust Sci Technol*, 110-111(1):209–228, 1995.

[51] Knock measurement for fuel evaluation in spark ignition engines. *Fuel*, 80(3):395 – 407, 2001.

[52] A new indicator for knock detection in gas SI engines. *Int J Therm Sci*, 42(5):523 – 532, 2003.

[53] C. Forte, E. Corti, G.M. Bianchi, S. Falfari, and S. Fantoni. A RANS CFD 3D Methodology for the Evaluation of the Effects of Cycle By Cycle Variation on Knock Tendency of a High Performance Spark Ignition Engine. *SAE Technical Paper 2014-01-1223*, 2014.

[54] A. d'Adamo, S. Breda, S. Fontanesi, A. Irimescu, S.S. Merola, and C. Tornatore. A RANS knock model to predict the statistical occurrence of engine knock. *Appl Energ*, 191:251 – 263, 2017.

[55] R. Worret and U. Spicher. Klopfkriterium. In *Heft 741-2002*. FVV-Abschlussbericht, 2002.

[56] D. Linse, A. Kleemann, and C. Hasse. Probability density function approach coupled with detailed chemical kinetics for the prediction of knock in turbocharged direct injection spark ignition engines. *Combust Flame*, 161(4):997 – 1014, 2014.

[57] E. Corti, C. Forte, G. Cazzoli, D. Moro, S. Falfari, and V. Ravaglioli. Comparison of Knock Indexes Based on CFD Analysis. *Energy Procedia*, 101:917 – 924, 2016. ATI 2016 - 71st Conference of the Italian Thermal Machines Engineering Association.

[58] Regime classification of an exothermic reaction with nonuniform initial conditions. *Combust Flame*, 39(2):211 – 214, 1980.

[59] Nonuniformities in initial temperature and concentration as a cause of explosive chemical reactions in combustible gases. *Combust Flame*, 87(3):347 – 356, 1991.

[60] L. Bates, D. Bradley, G. Paczko, and N. Peters. Engine hot spots: Modes of auto-ignition and reaction propagation. *Combust Flame*, 166:80 – 85, 2016.

[61] J. Warnatz and U. Maas and R.W. Dibble. *Combustion: Physical and Chemical Fundamentals, Modelling and Simulation, Experiments, Pollutant Formation*. Springer-Verlag Berlin Heidelberg, 4 edition, 2006.

[62] A. Dewan. *Tackling Turbulent Flows in Engineering*. Springer Verlag Berlin Heidelberg New Work, 2011.

[63] N. Peters. Multiscale combustion and turbulence. *P Combust Inst*, 32(1):1 – 25, 2009.

[64] J.H. Ferziger and M. Péric. *Computational Methods for Fluid Dynamics*. Springer-Verlag Berlin Heidelberg New York, 1996.

[65] M. Schmitt. *Direct Numerical Simulations in Engine-like Geometries*. PhD thesis, ETH Zurich, 2014.

[66] C.J. Rutland. Large-eddy simulations for internal combustion engines – a review. *Int J Engine Res*, 12(5):421–451, 2011.

[67] H. Pitsch. A consistent level set formulation for large-eddy simulation of premixed turbulent combustion. *Combust Flame*, 143(4):587 – 598, 2005.

[68] H. Martin. *Numerische Strömungssimulation in der Hydrodynamik: Grundlagen und Methoden*. Springer-Verlag Berlin Heidelberg, 2011.

[69] J. Smagorinsky. General Circulation Experiments with the Primitive Equation 1 the Basic Experiment. *Monthly Weather Review*, 91:99 – 164, 1963.

[70] M. Germano, U. Piomelli, P. Moin, and W.H. Cabot. A Dynamic Subgrid-scale Eddy Viscosity Model. *Phys Fluids A*, 3:1760 – 1765, 1991.

[71] D.K. Lilly. A proposed modification of the Germano subgrid-scale closure method. *Phys Fluids A*, 4:633–633, 1992.

[72] C. Meneveau. Statistics of turbulence subgrid-scale stresses: Necessary conditions and experimental tests. *Phys Fluids*, 6:815–833, 1994.

[73] G. Stiesch. *Modeling Engine Spray and Combustion Processes*. Springer Verlag Berlin Heidelberg New Work, 2003.

[74] Mixing and chemical reaction in steady confined turbulent flames. *P Combust Inst*, 13(1):649 – 657, 1971.

[75] On mathematical modeling of turbulent combustion with special emphasis on soot formation and combustion. *P Combust Inst*, 16(1):719 – 729, 1977.

[76] K.N.C. Bray, P.A. Libby, and J.B. Moss. Flamelet Crossing Frequencies and Mean Reaction Rates in Premixed Turbulent Combustion. *Combust Sci Technol*, 41(3-4):143–172, 1984.

[77] F.E. Marble and J.E. Broadwell. TRW-29314-6001-RU-00. Project SQUID.

[78] J.M. Duclos and M. Zolver. 3D Modeling of Intake, Injection and Combustion in a DI-SI Engine under Homogeneous and Stratified Operating Conditions. In *The Fourth International Symposium COMODIA 98*, 1998.

[79] O. Colin, A. Benkenida, and C. Angelberger. 3D Modeling of Mixing, Ignition and Combustion Phenomena in Highly Stratified Gasoline Engines. *Oil Gas Sci Technol*, 58(1):47–62, 2003.

[80] A. Yoshizawa, H. Fujiwara, H. Abe, and Y. Matsuo. Mechanisms of countergradient diffusion in turbulent combustion. *Phys Fluids*, 21:015107, 2009.

[81] L. Liang and R.D. Reitz. Spark Ignition Engine Combustion Modeling Using a Level Set Method with Detailed Chemistry. *SAE Technical Paper 2006-01-0243*, 2006.

[82] F. Perini, Y. Ra, K. Hiraoka, K. Nomura, A. Yuuki, Y. Oda, C. Rutland, and R.D. Reitz. An Efficient Level-Set Flame Propagation Model for Hybrid Unstructured Grids Using the G-Equation. *SAE Int J Engines*, 9:1409–1424, 2016.

[83] Z. Tan and R.D. Reitz. Modeling Ignition and Combustion in Spark-ignition Engines Using a Level Set Method. *SAE Technical Paper 2003-01-0722*, 2003.

[84] P. Pal, Y. Wu, T. Lu, S. Som, Y. See, and A. Le Moine. Multi-Dimensional CFD Simulations of Knocking Combustion in a CFR Engine. In *Emissions Control Systems; Instrumentation, Controls, and Hybrids; Numerical Simulation; Engine Design and Mechanical Development:V002T06A017*. ASME. Internal Combustion Engine Division Fall Technical Conference, Volume 2, 2017.

[85] G. Damköhler. Der Einfluß der Turbulenz auf die Flammengeschwindigkeit in Gasgemischen. *Z Elektrochemie*, 46:601 – 652, 1947.

[86] F.A. Sethian. Level Set Methods. In *Cambridge Monographs on Applied and Computational Mathematics*. Cambridge University Press, 1996.

[87] F.A. Williams. Turbulent Combustion. In J. Buckmaster, editor, *The Mathematics of Combustion*, pages 97 – 131. SIAM, Philadelphia, 1985.

[88] M. Balthasar. *Detailed Soot Modelling in Laminar and Turbulent Reacting Flows*. PhD thesis, LTH Lund University, 2000.

[89] A. Gogan. *Full Cycle Engine Simulations with Detailed Chemistry*. PhD thesis, LTH Lund University, 2006.

[90] M. Tunér. *Stochastic Reactor Models for Engine Simulations*. PhD thesis, LTH Lund University, 2008.

[91] M. Pasternak. *Simulation of the Diesel Engine Combustion Process Using the Stochastic Reactor Model*. PhD thesis, Brandenburg University of Technology Cottbus-Senftenberg, 2015.

[92] A. Matrisciano, T. Franken, C. Perlman, A. Borg, H. Lehtiniemi, and F. Mauss. Development of a Computationally Efficient Progress Variable Approach for a Direct Injection Stochastic Reactor Model. *SAE Technical Paper 2017-01-0512*, 2017.

[93] M. Pasternak, F. Mauss, C. Perlman, and H. Lehtiniemi. Aspects of 0D and 3D Modeling of Soot Formation for Diesel Engines. *Combust Sci Technol*, 186(10-11):1517–1535, 2014.

[94] T. Nilsson. Development of a simulation methodology for gas turbine combustion. Master's thesis, LTH Lund University, 2014.

[95] LOGEsoft v1.10, LOGE AB, Manual Book 3 - Engine Models, 2018.

[96] M. Pasternak, F. Mauss, M. Sens, M. Riess, A. Benz, and K.G. Stapf. Gasoline engine simulations using zero-dimensional spark ignition stochastic reactor model and three-dimensional computational fluid dynamics engine model. *Int J Engine Res*, 17(1):76–85, 2016.

[97] G. Woschni. A Universally Applicable Equation for the Instantaneous Heat Transfer Coefficient in the Internal Combustion Engine. *SAE Technical Paper 670931*, 1967.

[98] PDF methods for turbulent reactive flows. *Prog Energ Combust*, 11(2):119 – 192, 1985.

[99] C. Dopazo. Relaxation of initial probability density functions in the turbulent convection of scalar fields. *Phys Fluids*, 22(1):20–30, 1979.

[100] R.L. Curl. Dispersed phase mixing: I. Theory and effects in simple reactors. *AIChE Journal*, 9(2):175–181, 1963.

[101] J. Janicka, W. Kolbe, and W. Kollmann. Closure of the Transport Equation for the Probability Density Function of Turbulent Scalar Fields. *J Non-Equil Thermody*, 4(1):47–66, 2009.

[102] H. Kolla, J.W. Rogerson, N. Chakraborty, and N. Swaminathan. Scalar Dissipation Rate Modeling and its Validation. *Combust Sci Technol*, 181(3):518–535, 2009.

[103] S. Bjerkborn, K. Frojd, C. Perlman, and F. Mauss. A Monte Carlo Based Turbulent Flame Propagation Model for Predictive SI In-Cylinder Engine Simulations Employing Detailed Chemistry for Accurate Knock Prediction. *SAE Int J Engines*, 5:1637–1647, 2012.

[104] M. Pasternak, F. Mauss, F. Xavier, M. Rieß, M. Sens, and A. Benz. 0D/3D Simulations of Combustion in Gasoline Engines Operated with Multiple Spark Plug Technology. *SAE Technical Paper 2015-01-1243*, 2015.

[105] A. Gogan, B. Sundén, H. Lehtiniemi, and F. Mauss. Stochastic Model for the Investigation of the Effect of Inhomogeneities on Engine Knock. ASME. Internal Combustion Engine Division Fall Technical Conference, 2004.

[106] O. Stenlåås, A. Gogan, R. Egnell, B. Sundén, and F. Mauss. The Influence of Nitric Oxide on the Occurrence of Autoignition in the End Gas of Spark Ignition Engines. *SAE Technical Paper 2002-01-2699*, 2002.

[107] A. Gogan, B. Sundén, L. Montorsi, S.S. Ahmedand, and F. Mauss. Knock Modeling: an Integrated Tool for Detailed Chemistry and Engine Cycle Simulation. *SAE Technical Paper 2003-01-3122*, 2003.

[108] A. Gogan, B. Sundén, H. Lehtiniemi, and F. Mauss. Stochastic Model for the Investigation of the Influence of Turbulent Mixing on Engine Knock. *SAE Technical Paper 2004-01-2999*, 2004.

[109] Ö.L. Gülder. Correlations of Laminar Combustion Data for Alternative S.I. Engine Fuels. *SAE Technical Paper 841000*, 1984.

[110] Burning velocities of mixtures of air with methanol, isooctane, and indolene at high pressure and temperature. *Combust Flame*, 48:191 – 210, 1982.

[111] The autoignition of hydrocarbon fuels at high temperatures and pressures - Fitting of a mathematical model. *Combust Flame*, 30:45 – 60, 1977.

[112] The shell autoignition model: a new mathematical formulation. *Combust Flame*, 117(3):529 – 540, 1999.

[113] The Shell autoignition model: applications to gasoline and diesel fuels. *Fuel*, 78(4):389 – 401, 1999.

[114] L. Teodosio, V. De Bellis, and F. Bozza. Fuel Economy Improvement and Knock Tendency Reduction of a Downsized Turbocharged Engine at Full Load Operations through a Low-Pressure EGR System. *SAE Int J Engines*, 8:1508–1519, 2015.

[115] B.M. Gauthier, D.F. Davidson, and R.K. Hanson. Shock tube determination of ignition delay times in full-blend and surrogate fuel mixtures. *Combust Flame*, 139(4):300 – 311, 2004.

[116] J.C.G. Andrae, P. Björnbom, R.F. Cracknell, and G.T. Kalghatgi. Autoignition of toluene reference fuels at high pressures modeled with detailed chemical kinetics. *Combust Flame*, 149(1):2 – 24, 2007.

[117] H. Hoffmeyer, E. Montefrancesco, L. Beck, J. Willand, F. Ziebart, and F. Mauss. CARE – CAtalytic Reformated Exhaust Gases in Turbocharged DISI-Engines. *SAE Int J Fuels Lubr*, 2:139–148, 2009.

[118] K.K. Kuo. *Principles of Combustion*. Wilet & Sons: Hoboken, HJ, 2005.

[119] L. Seidel, K. Moshammer, X. Wang, T. Zeuch, K. Kohse-Höinghaus, and F. Mauss. Comprehensive kinetic modeling and experimental study of a fuel-rich, premixed n-heptane flame. *Combust Flame*, 162(5):2045 – 2058, 2015.

[120] S.S. Ahmed, F. Mauss, G. Moreac, and T. Zeuch. A comprehensive and compact n-heptane oxidation model derived using chemical lumping. *Phys Chem Chem Phys*, 9:1107–1126, 2007.

[121] L. Seidel, C. Netzer, M. Hilbig, F. Mauss, C. Klauer, M. Pasternak, and A. Matrisciano. Systematic Reduction of Detailed Chemical Reaction Mechanisms for Engine Applications. *J Eng Gas Turb Power*, 139:091701–9, 2017.

[122] T. Zeuch, G. Moréac, S.S. Ahmed, and F. Mauss. A comprehensive skeletal mechanism for the oxidation of n-heptane generated by chemistry-guided reduction. *Combust Flame*, 155(4):651 – 674, 2008.

[123] Self-ignition of S.I. engine model fuels: A shock tube investigation at high pressure. *Combust Flame*, 109(4):599 – 619, 1997.

[124] M. Fikri, J. Herzler, R. Starke, C. Schulz, P. Roth, and G.T. Kalghatgi. Autoignition of gasoline surrogates mixtures at intermediate temperatures and high pressures. *Combust Flame*, 152:276–281, 2008.

[125] J.P.J. van Lipzig and E.J.K. Nilsson and L.P.H. de Goey and A.A. Konnov. Laminar burning velocities of n-heptane, iso-octane, ethanol and their binary and tertiary mixtures. *Fuel*, 90(8):2773–2781, 2011.

[126] J.E. Anderson, T.G. Leone, M.H. Shelby, T.J. Wallington, J.J. Bizub, M. Foster, M.G. Lynskey, and D. Polovina. Octane Numbers of Ethanol-Gasoline Blends: Measurements and Novel Estimation Method from Molar Composition. *SAE Technical Paper 2012-01-1274*, 2012.

[127] A.P. Kelley, W. Liu, Y.X. Xin, A.J. Smallbone, and C.K. Law. Laminar flame speeds, non-premixed stagnation ignition, and reduced mechanisms in the oxidation of iso-octane. *P Combust Inst*, 33(1):501 – 508, 2011.

[128] K. Kumar, J. E. Freeh, C. J. Sung, and Y. Huang. Laminar Flame Speeds of Preheated iso-Octane/O2/N2 and n-Heptane/O2/N2 Mixtures. *J Propul and Power*, 23(2):428–436, 2007.

[129] S.G. Davis and C.K. Law. Determination of and Fuel Structure Effects on Laminar Flame Speeds of C1 to C8 Hydrocarbons. *Combust Sci Technol*, 140(1-6):427–449, 1998.

[130] Y. Huang, C.J. Sung, and J.A. Eng. Laminar flame speeds of primary reference fuels and reformer gas mixtures. *Combust Flame*, 139(3):239 – 251, 2004.

[131] P. Dirrenberger, P.A. Glaude, R. Bounaceur, H. Le Gall, A.P. da Cruz, A.A. Konnov, and F. Battin-Leclerc. Laminar burning velocity of gasolines with addition of ethanol. *Fuel*, 115:162 – 169, 2014.

[132] G. Broustail, F. Halter, P. Seers, G. Moréac, and C. Mounaïm-Rousselle. Experimental determination of laminar burning velocity for butanol/iso-octane and ethanol/iso-octane blends for different initial pressures. *Fuel*, 106:310 – 317, 2013.

[133] X. Ma, Z. Wang, C. Jiang, Y. Jiang, H. Xu, and J. Wang. An optical study of in-cylinder CH2O and OH chemiluminescence in flame-induced reaction front propagation using high speed imaging. *Fuel*, 134:603 – 610, 2014.

[134] T. Poinsot, D. Veynante, F. Nicoud, B. Cuenot, L. Selle, G. Lartigue, L. Gicquel, V. Moureau, and S. Candel. *Simulation tools for 3D reacting flows*. Lectures Notes Princeton University, 2013.

[135] A. Robert, S. Richard, O. Colin, and T. Poinsot. LES study of deflagration to detonation mechanisms in a downsized spark ignition engine. *Combust Flame*, 162(7):2788 – 2807, 2015.

[136] H. Werner and H. Wengle. Large Eddy Simulation of Turbulent Flow Over and Around a Cube in a Plane Channel. In *Proceedings of the Eighth Symposium on Turbulent Shear Flows*, volume 2. Technical University of Munich, 1991.

[137] F. Spausta. *Eigenschaften und Untersuchungen der flüssigen Treibstoffe: die gasförmigen Treibstoffe* . Springer-Verlag Wien, 2 edition, 1953.

[138] V. Knop, M. Loos, C. Pera, and N. Jeuland. A linear-by-mole blending rule for octane numbers of n-heptane/iso-octane/toluene mixtures. *Fuel*, 115:666 – 673, 2014.

[139] L. Cai and H. Pitsch. Optimized chemical mechanism for combustion of gasoline surrogate fuels. *Combust Flame*, 162(5):1623 – 1637, 2015.

[140] N. Naser, S.M. Sarathy, and S.H. Chung. Estimating fuel octane numbers from homogeneous gas-phase ignition delay times. *Combust Flame*, 188:307 – 323, 2018.

[141] P. Kyrtatos, C. Brückner, and K. Boulouchos. Cycle-to-cycle variations in diesel engines. *Appl Energy*, 171:120 – 132, 2016.

[142] S.K. Gupta and M. Mittal. Effect of Compression Ratio on the Performance and Emission Characteristics, and Cycle-to-Cycle Combustion Variations of a Spark-Ignition Engine Fueled with Bio-Methane Surrogate. *Appl Therm Eng*, 2018.

[143] M. Balthasar. *Investigation of knock in an industrial spark-ignition engine by Large-Eddy Simulation*. PhD thesis, Université Paris-Sacaly, 2018.

[144] F.A. Matekunas. Modes and Measures of Cyclic Combustion Variability. *SAE Technical Paper 830337*, 1983.

[145] R.K. Maurya and A.K. Agarwal. Experimental investigation of cyclic variations in HCCI combustion parameters for gasoline like fuels using statistical methods. *Appl Energy*, 111:310 – 323, 2013.

[146] H.G. Zhang, X.J. Han, B.F. Yao, and G.X. Li. Study on the effect of engine operation parameters on cyclic combustion variations and correlation coefficient between the pressure-related parameters of a CNG engine. *Appl Energy*, 104:992 – 1002, 2013.

[147] M.B. Young. Cyclic dispersion in the homogeneous-charge spark-ignition engine - a literature survey. *SAE Technical Paper 810020*, 1981.

[148] J.H. Whitelaw and H.M. Xu. Cyclic variations in a lean-burn spark ignition engine without and with swirl. *SAE Technical Paper 950683*, 1995.

[149] M. Ghaderi Masouleh, K. Keskinen, O. Kaario, H. Kahila, Y.M. Wright, and V. Vuorinen. Flow and thermal field effects on cycle-to-cycle variation of combustion: scale-resolving simulation in a spark ignited simplified engine configuration. *Appl Energy*, 230:486 – 505, 2018.

[150] O. Vermorel, S. Richard, O. Colin, C. Angelberger, A. Benkenida, and D. Veynante. Towards the understanding of cyclic variability in a spark ignited engine using multi-cycle LES. *Combust Flame*, 156(8):1525 – 1541, 2009.

[151] A.K. Sen, S.K. Ash, B. Huang, and Z. Huang. Effect of exhaust gas recirculation on the cycle-to-cycle variations in a natural gas spark ignition engine. *Appl Therm Eng*, 31(14):2247 – 2253, 2011.

[152] C. Pera, V. Knop, and J. Reveillon. Influence of flow and ignition fluctuations on cycle-to-cycle variations in early flame kernel growth. *P Combust Inst*, 35(3):2897 – 2905, 2015.

[153] B.L. Salvi and K.A. Subramanian. Experimental investigation and phenomenological model development of flame kernel growth rate in a gasoline fuelled spark ignition engine. *Applied Energy*, 139:93 – 103, 2015.

[154] Cyclic variations and turbulence structure in spark-ignition engines. *Combust Flame*, 72(1):73 – 89, 1988.

[155] B. Enaux, V. Granet, O. Vermorel, C. Lacour, C. Pera, C. Angelberger, and T. Poinsot. LES study of cycle-to-cycle variations in a spark ignition engine. *P Combust Inst*, 33(2):3115 – 3122, 2011.

[156] D. Jung, K. Sasaki, and N. Iida. Effects of increased spark discharge energy and enhanced in-cylinder turbulence level on lean limits and cycle-to-cycle variations of combustion for si engine operation. *Appl Energy*, 205:1467 – 1477, 2017.

[157] S. Richard, A. Dulbecco, C. Angelberger, and K. Truffin. Invited Review: Development of a one-dimensional computational fluid dynamics modeling approach to predict cycle-to-cycle variability in spark-ignition engines based on physical understanding acquired from large-eddy simulation. *Int J Eng Research*, 16(3):379–402, 2015.

[158] C. Netzer, T. Franken, L. Seidel, H. Lehtiniemi, and F. Mauss. Numerical Analysis of the Impact of Water Injection on Combustion and Thermodynamics in a Gasoline Engine using Detailed Chemistry. *SAE Technical Paper 2018-01-0200*, 2018.

[159] M. Pasternak, C. Netzer, F. Mauss, M. Fischer, M. Sens, and M. Riess. Simulation of the effects of spark timing and external EGR on gasoline combustion under knock-limited operation at high speed and load. In M. Guenther and M. Sens, editors, *Knocking in Gasoline Engines*, IAV Automotive Engineering, pages 121–142. 2017.

[160] A. Werner, C. Netzer, H. Lehtiniemi, A. Borg, A. Matrisciano, L. Seidel, and F. Mauss. A Computationally Efficient Combustion Progress Variable (CPV) Approach for Engine Applications. In *Joint Meeting of the German and Italian Sections of the Combustion Institute*, 2018.

[161] H. Lehtiniemi, A. Borg, and F. Mauss. Combustion Modeling of Diesel Sprays. *SAE Technical Paper 2016-01-0592*, 2016.